AD-A147 917 PLASMA STUDIES IN ION DIODES(U) MASSACHUSETTS INST OF TECH CAMBRIDGE RESEARCH LAB OF ELECTRONICS G BEKEFI SEP 84 N00014-83-K-2024 1/4

UNCLASSIFIED F/G 20/9 NL

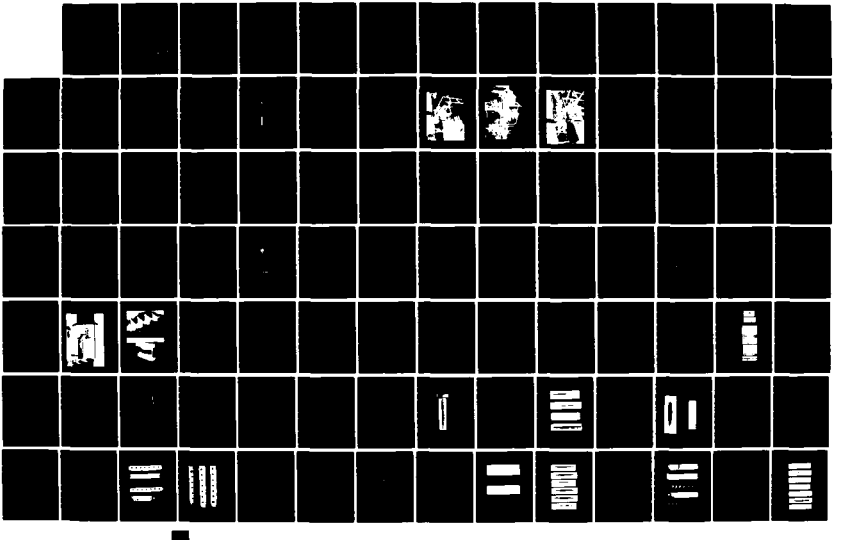

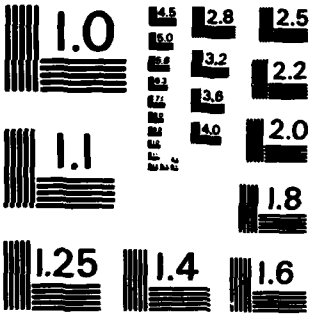

MICROCOPY RESOLUTION TEST CHART
NATIONAL BUREAU OF STANDARDS-1963-A

(12)

FINAL REPORT

Plasma Studies in Ion Diodes

Office of Naval Research
Contract N00014-83-K-2024

covering the period
3 November 1980 - 31 August 1984

Submitted by
George Bekefi

September 1984

MASSACHUSETTS INSTITUTE OF TECHNOLOGY
Research Laboratory of Electronics
Cambridge, Massachusetts 02139

EXPLOSIVE EMISSION CATHODE PLASMAS IN INTENSE RELATIVISTIC ELECTRON BEAM DIODES

by

David Dickson Hinshelwood

Submitted to the Department of Physics
on August 31, 1984 in partial fulfillment of the
requirements for the Degree of
Doctor of Philosophy in Physics

Abstract

An experimental study of cathode plasmas in planar diodes driven by a Sandia Nereus accelerator (270 kV, 60 kA, 70 ns), with particular attention devoted to plasma uniformity and expansion velocity, has been carried out.

The diode current density was varied over a factor of ten and the rate of rise dE/dt of the applied field was varied over a factor of six. Different cathode materials, coatings, and surface roughnesses were used and the effects of glow discharge cleaning and *in situ* heating were examined. Framing photography, electron beam dosimetry, perveance measurements, optical interferometry, and (spatially and temporally resolved) spectroscopy were used to diagnose the plasma uniformity, electron beam uniformity, plasma front motion, electron density, plasma composition, motion of distinct species, electron temperature, and ion (and neutral) densities.

Electron beam uniformity is seen to be related to cathode plasma uniformity; this uniformity is enhanced by a high value of (the microscopic) dE/dt, which is determined both by the rise time of the applied field and by the cathode surface roughness. The significance of dE/dt is believed to be related to the screening effect of the emitted electrons.

The motion of the plasma front is seen to be affected by two phenomena. To begin with, all species of the cathode plasma are seen to expand at the same rate. The ions are believed to be accelerated to velocities on the order of 2–3 cm/μs in dense cathode spot regions at the cathode surface. Plasma expansion is also seen to be inhibited by electric pressure effects, which are influenced by the shape of the driving power pulse.

A simple cathode plasma model, which explains the similarity of plasmas in diodes with greatly differing parameters, is proposed.

The relevance of these results to inductively driven diodes, repetitively pulsed diodes, and magnetically insulated transmission lines is also discussed.

Thesis Supervisor: Dr. George Bekefi
Title: Professor of Physics

Acknowledgements

I thank my thesis supervisor, George Bekefi, for his support, encouragement, and many helpful suggestions over the years.

This work was supported jointly by Sandia National Laboratories and by the Naval Research Laboratory, during which time I have had a close working relationship with the contract monitors, Regan Stinnett of Sandia and Gerry Cooperstein of NRL, and their constant support, interest, and advice has contributed greatly to this work. Thanks also go to Gerry for encouraging me to pursue this topic for my thesis.

Most of this work was carried out with the aid of Ren-Jun Li of the Institute of Atomic Energy, Academia Sinica in Peking, PRC, and it is a pleasure to acknowledge his many contributions.

One of the joys of this work has been the close contact with two large experimental groups. I have benefitted from many helpful conversations with members of the Fusion Research Department at Sandia. Particular thanks go to Dillon McDaniel for his pulsed power advice and to Nancy Dhooge and Dave Huskisson, who performed the electron microscopy and surface analysis described in Ch. 5.

A helpful and pleasant association with the entire Plasma Technology Branch at NRL over the years is also gratefully acknowledged. Bob Commisso, in particular, aided in the spectrometer calibration.

Particular thanks go to Shyke Goldstein of Jaycor/G T Devices for his inspiration, encouragement, and advice.

Dwight Duston of NRL supplied many of the rate coefficients and performed the CRE modeling described in Ch. 9. In addition, he was kind enough to answer many of my atomic physics questions.

Many helpful conversations with Dave Bacon of SAI are also acknowledged.

Thanks go to the other members of the electron beam group at MIT for their pleasant companionship, to the members of the Versator group for their gracious gifts of equipment and film, and to the Research Laboratory of Electronics support staff.

Finally, it is a pleasure to acknowledge the help I have received from the three wizards: Ron Boller of NRL, who answered my countless questions concerning electrical monitors and pulsed power in general; Ed Fitzgerald of the Versator group, for teaching me the subtleties of Unistrut; (and most of all) Ivan Mastovsky, whose technical acumen made this work a lot easier (or at least less difficult).

Sometimes the light's all shining on me.
Other times I can barely see.
Lately it occurs to me...
What a long, strange trip it's been.

The Grateful Dead

Contents

List Of Figures

List of Tables

Chapter 1

Introduction

This chapter consists of discussion of the motivation for the present work, a brief description of the experiments, and an outline of the remainder of this thesis.

1.1. Background

Intense charged particle beam generators[1] have been developed during the past twenty years to the point where beam currents of 10 MA, powers of 10^{13} W, and energies of 10^6 J are presently available.[2] These devices consist of a series of energy compression (and hence power multiplication) stages which deliver a high power pulse, with a typical rise time of 10 ns, to a pulsed high current vacuum diode (also variously referred to as an explosive emission, field emission, or cold cathode diode). This diode in its simplest form consists of a pair of electrodes separated by vacuum; when an electric field on the order of 10^5 V/cm is impressed across the gap, a plasma is formed on the cathode, constituting a zero work function surface from which intense electron current may be drawn. It is this plasma cathode which allows current densities in excess of 10^7 A/cm^2 to be drawn from the cathode surface, exceeding by orders of magnitude those available from thermionic or photoelectric cathodes. An anode plasma may also be formed, either by the electric field directly or by the heating effect of impinging electrons from the cathode: in this case a large flux of ions may be drawn from the anode. Finally, since either electrode may be made largely transparent, intense electron or ion beams can be extracted from the diode.

Intense relativistic electron beams were first developed to provide sources for flash x-radiography. There are presently many applications of intense charged particle beams, such as x-ray production,[3] microwave generation,[4] laser pumping,[5] electron beam controlled switching,[6] and material response studies.[7] Perhaps the most important potential application concerns inertial confinement fusion (ICF): both electron[8,9] and ion[10] beams have been proposed as ICF drivers. There is currently a vigorous effort in the United States directed towards light ion beam driven

ICF,[11,12,13] and similar efforts are underway in France,[14] Japan,[15,16] China[17] and (most recently) West Germany.[18] Electron beam driven ICF, which has been largely abandoned in the West in recent years, is still being pursued in the Soviet Union.[19]

Intense charged particle beam applications to magnetic confinement fusion[20] such as plasma heating,[21] field reversal,[22] and current drive[23] are also being investigated; in addition, there are possible industrial uses for slightly lower power beams, such as heat treatment,[24] ion implantation[25] and radioisotope production through target activation,[26] which remain largely unexplored.

1.1.1. Significance of the Cathode Plasma

The formation and subsequent dynamics of the cathode plasma are perhaps the most significant factors affecting the behavior of high power vacuum diodes. The three most important characteristics of the cathode plasma are the formation time, expansion velocity and uniformity. Plasma formation is not instantaneous, with typical delays of 3–10 ns, and once formed the plasma does not remain stationary but expands toward the anode. This expansion in effect reduces the cathode-anode gap which alters the diode impedance and eventually terminates the pulse due to shorting of the gap. Finite formation time is the principle limitation on short pulse diodes while the expansion velocity is more significant for longer pulses. In addition to a delay time for plasma formation, the plasma may not be formed uniformly. This reduces the total current available from the cathode, but more important, gives rise to a 'bumpy' surface which can disturb the electron trajectories in the diode, causing beam filimentation or imparting a finite transverse velocity to the electrons. As a relatively cool, uniform electron beam is vital to the operation of all of the aforementioned devices, in particular ion beam diodes (since the ion and electron beam trajectories are coupled) and beam driven microwave devices, plasma uniformity is a critical requirement.

Of course, formation time, uniformity, and expansion velocity are not necessarily independent. As will be shown in Ch. 4, the plasma uniformity increases as the formation time decreases. Also, a nonuniform plasma may have regions

of locally high current density, causing increased heating and thus (presumably) increased expansion velocity.

The physics of cathode plasma formation is also directly relevant to the problem of electromagnetic power flow. The electric fields associated with high power densities will break down any material used as an insulator in a transmission line. Vacuum will also break down, with the resulting formation of a cathode plasma. However, if the current is high enough, its own self magnetic field will return (in principle) all electrons emitted from the cathode plasma back to the cathode.[27] These so-called magnetically insulated transmission lines[28] (MITL's) are an integral part of most high power particle beam systems as well as pulsed power systems (such as those used to drive imploding foils[29]) that do not involve particle beams as such.

1.2. Description of the Experiments

1.2.1. Experimental Goals

The objective of the work reported here is to characterize the cathode plasma with regard to uniformity, expansion velocity, density, composition, and (electron) temperature as a function of several experimental parameters such as the cathode material and the diode current density. The plasma formation time was too short to be measured accurately in these experiments, although the effect of increased formation time on plasma uniformity was investigated and is discussed in Ch. 4. Plasma density, composition, and temperature measurements are desirable in that they provide information on the underlying physics of cathode plasma behavior. For example, these properties determine growth rates of instabilities that can increase plasma expansion velocity and plasma nonuniformities. Also, measurement of these properties improves the data base for theoretical modeling of the plasma.

While diode plasmas have been observed for over a decade, no attempt has been made until now at either a relatively complete characterization of the plasma or a determination of the effect of variations of the experimental parameters on the plasma properties.

The experiments described here have both practical and physics related goals. It is of immediate importance to determine the influence of various specific parameters that can be varied in practice, such as the electric field rise time or the cathode surface preparation, on the plasma properties. In particular, there exists a large body of (generally unpublished) folklore concerning cathode surface preparation which will now be evaluated. As an example of the importance of such an evaluation, the Sandia PBFA II ion beam generator, which will hopefully be used to achieve pellet ignition and is now in the design phase, will include large aluminum MITL's. According to the present folklore aluminum emits better when coated with a commercially available graphite coating. However, the non-permanent nature of this coating coupled with the increased outgassing from coated surfaces would necessitate major (and expensive) design changes if the coating is to be used. Hence, it is necessary to determine precisely how beneficial (if at all) this coating is.

Beyond this, determination of the plasma properties, and their dependence on the diode parameters, will provide insight into the fundamental physics of the cathode plasma formation and subsequent dynamics. From knowledge of this fundamental physics, it is possible to assess limits on the performance of explosive emission cathodes. The macroscopic nature of the experimental investigation places limits, however, on the information which can be obtained concerning the basic physics, which (as discussed in Ch. 2) is to some degree dominated by very small, high density plasma regions near the cathode surface.

1.2.2. Experimental Description

This thesis describes studies of plasmas formed on the cathodes of parallel plate diodes pulsed by a Sandia Nereus accelerator. A schematic of the experimental arrangement is shown in Fig. 1.1. The experiment had an extensive diagnostic arrangement which allowed electron density measurements with a two frame interferometer, time integrated spectroscopy with a 0.5 M spectrograph, time resolved spectroscopy with 0.3 M and 0.1 M monochromators, single frame framing photography, and time resolved measurement of the total light to be made on a single shot. Framing photography was used to diagnose the plasma uniformity:

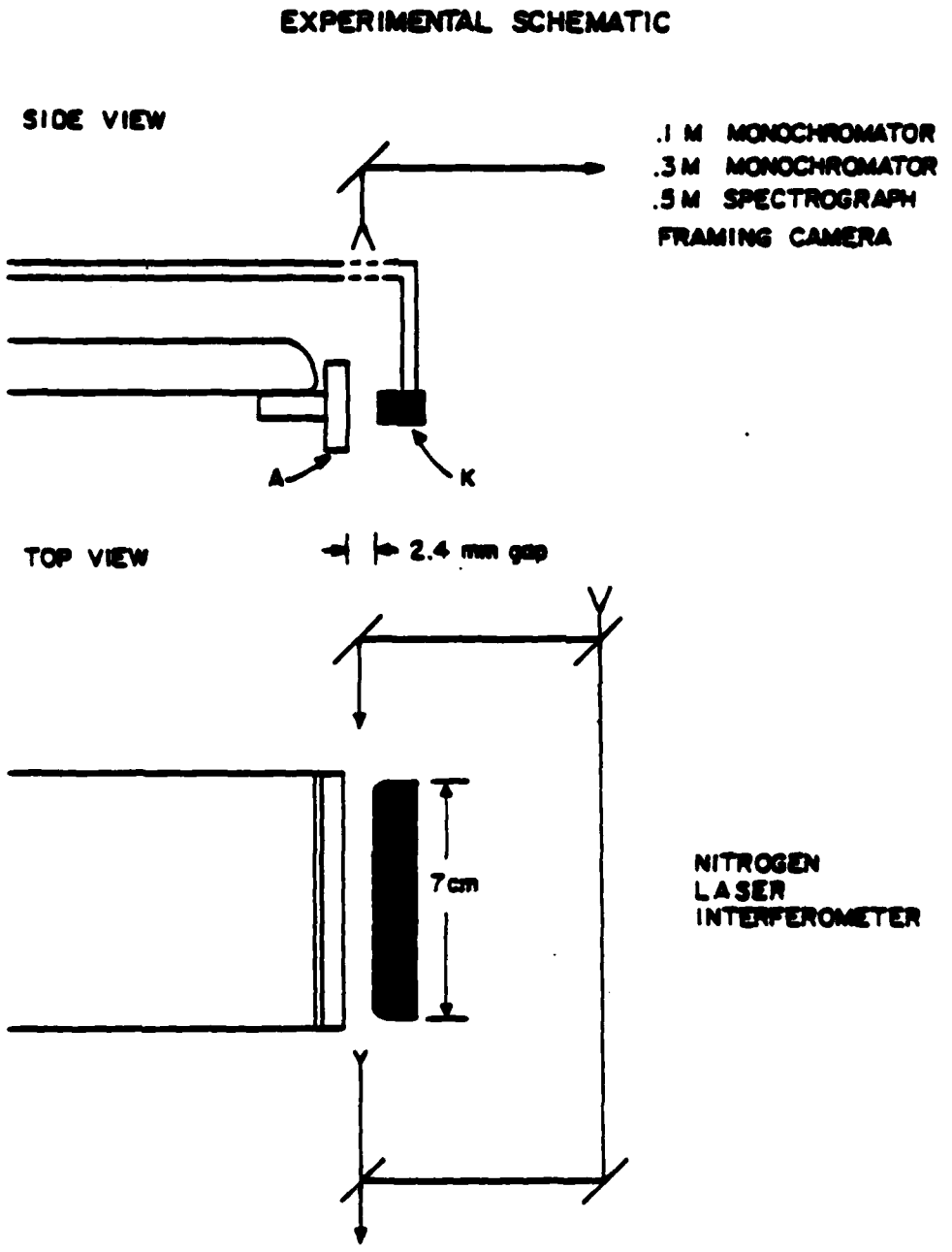

Fig. 1.1: A schematic of the experimental arrangement.

the spectroscopic diagnostics provided information on the plasma composition, ion density, electron temperature, and the expansion of specific ionic species. In addition, a powerful dosimetric diagnostic which measured the electron beam uniformity and emittance was used on some shots, as was an x-ray pinhole camera. The principal diagnostics are summarized in Table 1.1.

The cathode plasma was characterized as a function of the cathode characteristics and electrical parameters. Cathodes of graphite, aluminum, brass and stainless steel were used; the effect of surface roughness was examined; surface coatings of graphite and (silicone and hydrocarbon) oil were used; the current density was varied over a factor of ten; the electric field risetime was varied over a factor of four; the effects of glow discharge cleaning and *in situ* heating to >700°C were also examined.

Photographs of the experimental set-up are shown in Figs. 1.2–1.4.

The results of this study are also relevant to phenomena other than field induced cathode plasma formation. Although anode plasma formation was not treated directly, many aspects of the physics involved may be similar to that for cathode plasmas. Also, it is often desirable to use active electrode plasma sources, for example by using laser induced plasmas or external electrodes, in order to decouple plasma formation from the primary electric field and again, the physics involved will have aspects in common with that for field produced plasmas.

1.3. Thesis Outline

The outline of this thesis is as follows: Chapter 2 consists of a review of previous work relevant to cathode plasma formation, including a discussion of the results of previous studies of cathode plasma microphysics. The accelerator, diode, and electrical monitors are described in chapter 3.

Chapters 4–6 describe (more or less) direct measurements of the plasma uniformity and expansion velocity. Framing camera and dosimetry measurements of plasma uniformity are presented in chapter 4. Surface analytic studies of the cathodes, both before and after shots, which aid in interpretation of the results of Ch. 4, are described in chapter 5. Chapter 6 consists of the analysis of the current

Table 1.1

Cathode Plasma Diagnostics

Diagnostic	Plasma Property Measured
Framing photography	Uniformity
Dosimetry	Uniformity
Electrical monitors	Expansion
Interferometry	Electron Density
Time integrated spectroscopy	Composition
Time resolved spectroscopy	Composition
	Expansion of different species
	Electron temperature
	Ion density

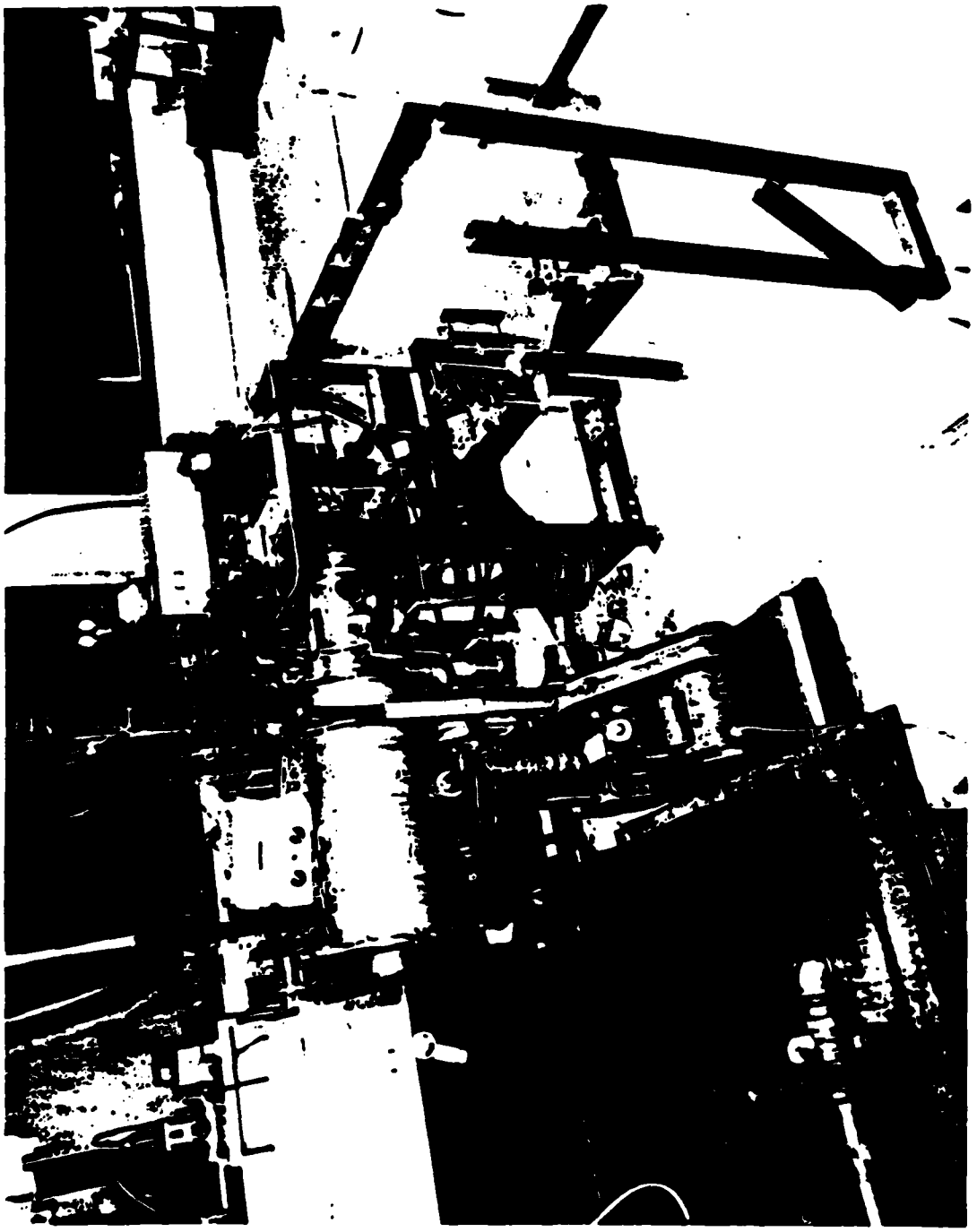

Fig. 1.2: Photograph of the experimental set-up, with the accelerator at left and interferometer exit optics (see Ch. 7) in foreground.

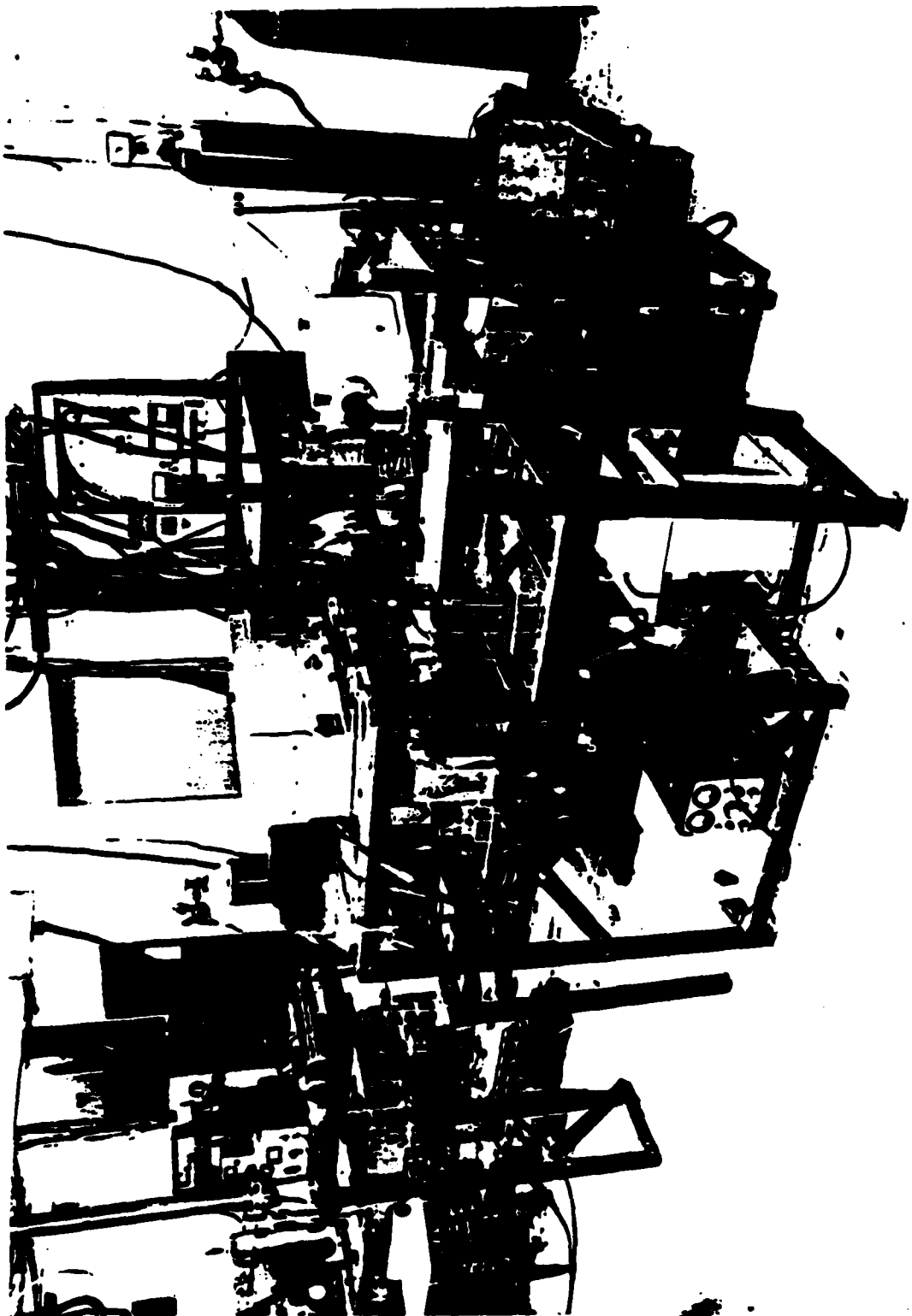

Fig. 1.3: Photograph of the experimental set-up, with the interferometer entrance optics (see Ch. 7) in foreground and 0.3 M monochromator system at center right.

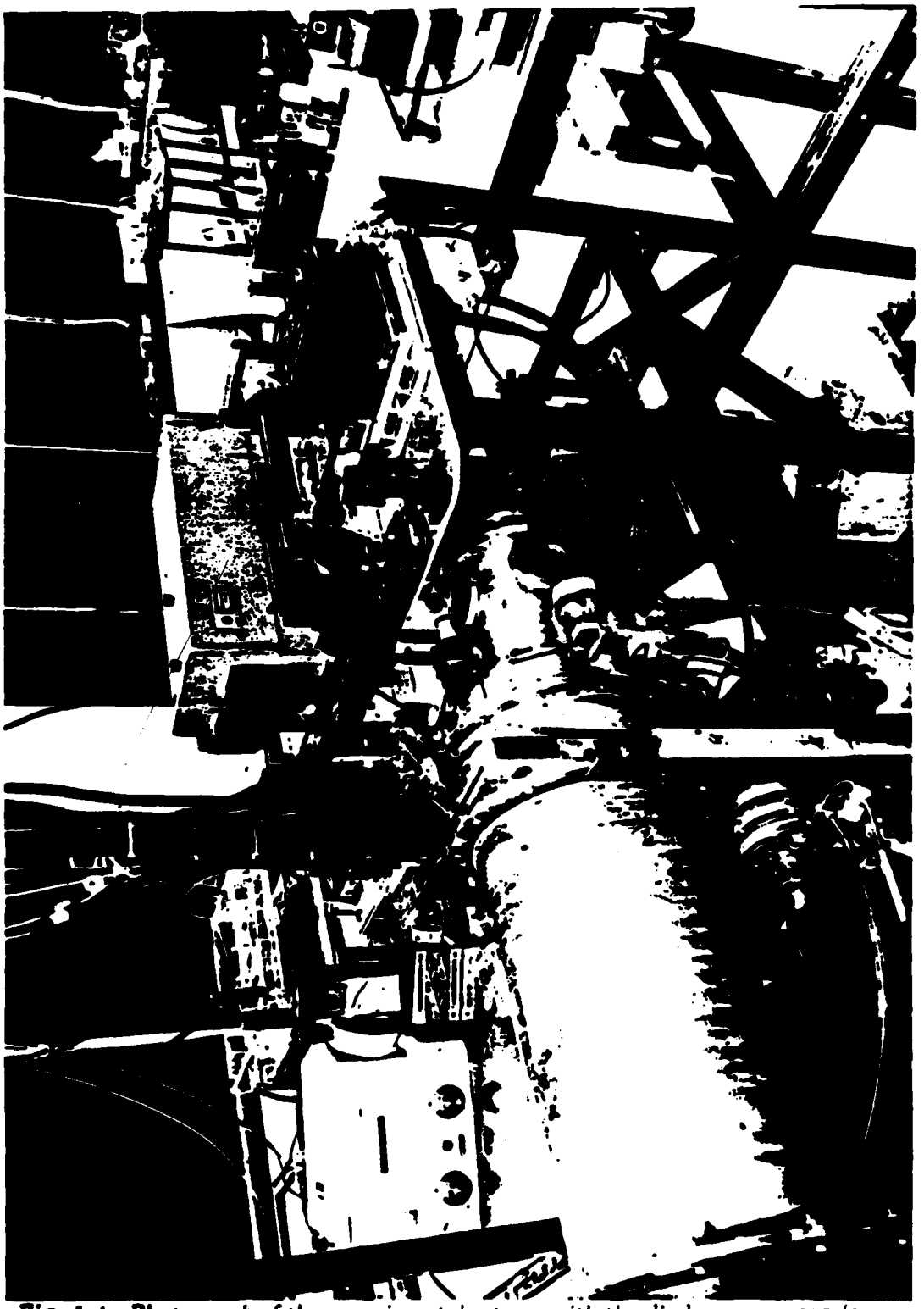

Fig. 1.4: Photograph of the experimental set-up, with the diode vacuum can (see Ch. 3) in center, surrounded by the interferometer optics, and laser at upper left (see Ch. 7). The optics above the vacuum can are described in Chs. 4 and 8.

and voltage waveforms as a function of the experimental parameters, where the rate of change of the diode perveance ($I/V^{3/2}$) is used to infer the characteristics of plasma motion. In these chapters, particular attention is given to evaluation of cathode surface preparation folklore.

Chapters 7–9 describe measurements of the 'bulk' plasma properties: interferometric measurements of the electron density in chapter 7; qualitative spectroscopy, which identifies the constituents of the cathode plasma and measured minimum expansion velocities of these constituents, in chapter 8; quantitative spectroscopy, which gives estimates of the relative concentrations of different species in the cathode plasma and of the electron temperature, in chapter 9.

In chapter 10, a rough global model of the cathode plasma is presented, based on the results of Chs. 7–9, and simple calculations of plasma-surface interaction and thermal processes in the plasma are given.

Conclusions are given in chapter 11. These conclusions are discussed in regard to five cases of particular future relevance: short pulse diodes, long pulse, low current diodes, repetitively pulsed diodes, inductively driven diodes, and MITL's.

1.4. Note on Units

Unless otherwise noted, all equations are in cgs-Gaussian units with the exception of temperatures, which are given in electron volts.

Chapter 2

Review of Previous Work

2.1. Introduction

When an electric field is applied across the gap between two conductors in vacuum, a current of electrons is drawn from local regions on the cathode. This current is observed to flow at electric field strengths 100–1000 times smaller than is consistent with the basic theories of field and Schottky enhanced thermionic emission. For sufficiently high field strengths, this so called field emission current heats the cathode in these localized regions, vaporizing and ionizing material from the cathode, resulting in the formation of local plasma flares. These plasma flares have surfaces of essentially zero work function from which macroscopic currents may be drawn. In time, more and more regions of the cathode are 'turned on' until the plasma surface covers the entire cathode. At this point, the current drawn from the cathode is generally described by space charge limited flow from the entire cathode area.

With further passage of time, the plasma surface expands toward the anode, reducing the space charge limited impedance of the gap until the gap is completely shorted by the plasma. In typical intense beam diodes with electric fields of $\sim$1 MV/cm, initial turn-on occurs in a few ns, complete plasma formation requires 5–20 ns and the plasma expands with velocities of $\sim$2–3 cm/μs.

The terminology used here is described in Sec. 2.1.1. Sec. 2.2 consists of a brief historical overview, followed by a summary of previous work.

Previous experiments have furnished information concerning both the macroscopic plasma properties (such as the density or expansion velocity), with which the results of this present work may be directly compared, and the fundamental microphysics of plasma formation. While the microprocesses were not observed directly in this work, the findings presented here will give some insight into these microprocesses.

The current knowledge regarding cathode microprocesses is reviewed in Secs. 2.3–2.5. Sec. 2.3 deals with the physics of the initial breakdown and Sec. 2.4 is concerned with the subsequent plasma flare. Interactions between the plasma flare and the cathode surface leading to the formation of new sites are discussed in Sec. 2.5. Previous microscopic observations are summarized in Sec. 2.6. Previous observations of macroscopic properties will be reviewed in the appropriate experimental sections.

2.1.1. Terminology

As the terminology used by different investigators is not entirely consistent, that used here will now be defined. The formation of emission sites (i.e., plasma flares) capable of supplying space charge limited currents will be referred to as the *initial breakdown* or *turning on* of the cathode surface. *Field emission* will be used only in reference to the *prebreakdown current*, drawn by the action of an imposed field, that flows prior to breakdown. The micron sized cathodes used in early breakdown experiments, that were of the same size as the typical dimensions of an emission site, will be referred to as *single emitters*. Many experiments have involved cathodes of 10–500 micron size that are much smaller than those in diodes but still large compared to the typical dimensions of an emission site, and these will be referred to as *needle cathodes*. The term *broad area cathodes* will be used to refer to the ~cm^2 area cathodes in typical intense beam diodes.

2.2. Historical Overview

Vacuum breakdown has been studied at least since the 1920's.[30] In the early experiments (as well as many to this day), breakdown was studied on a sufficiently long timescale that the sequence of initial plasma formation, plasma expansion, and gap closure was regarded as a single instantaneous event. One motivation for such studies was the developement of high voltage devices, such as x-ray tubes, for which vacuum breakdown was a fault mode to be avoided if possible.

Other studies (also carried out since the early part of the century[31]) concerned the short circuit phase following breakdown, namely, the so-called vacuum

or metal vapor arc. These arcs, often produced by separating two current carrying contacts in vacuum, have been investigated primarily in connection with the development of devices for commercial electric power, such as high current vacuum interrupters. They have been subject to extensive experimental investigation, generally on timescales ranging from microseconds to DC and at current densities ranging from 100–1000 A/cm^2. Good reviews of vacuum arc phenomena are given by Lyubimov and Rakhovshiĭ,[32] Lafferty,[33] and Boxman *et al.*[34]

Dyke and co-workers were the first to investigate vacuum breakdown under pulsed (μs) voltages and controlled conditions in the 1950's, with studies of single crystal emitters.[35,36,37] Alpert and co-workers[38] extended the results of those experiments to the breakdown of broad area electrodes.

Sources of high current, high voltage particle beams rely on the intermediate phase of vacuum breakdown, between initial plasma formation and gap closure: the cathode plasma is needed to supply the high current densities and the gap must remain open in order to support the high applied voltages. Thus, the development of these sources required the technology capable of switching and transmitting high power densities on nanosecond timescales (with more severe insulation requirements since the short timescales required lower inductances and hence more compact geometries) as well as the means of making measurements on these timescales. Much of the early work in this so-called pulsed power field took place at the Atomic Weapons Research Establishment in the United Kingdom under Martin[39] in the 1960's. The most significant contribution of Martin's group was the development of pulse forming line technology which compressed the microsecond pulse lengths supplied by high voltage pulse generators, such as Marx banks, to the timescale of tens of nanoseconds required for proper operation of intense beam diodes.

The first experimental investigation of intense relativistic electron beams was reported by Graybill and Nablo[1] in 1966 and intense beam experiments were soon carried out in many places. The intense emission from the cathode which ocurred under the action of an applied electric field was attributed to field emission

processes — the significance of the plasma layer was apparently not immediately appreciated.

The processes of plasma formation and intense electron emission were clarified in an extensive set of experiments in the Soviet Union from the mid 1960's to the present, at Lenningrad State University under Fursei and at the Institute of High Current Electronics (formerly the Institute of Atmospheric Optics) at Tomsk under Mesyats. These experiments for the most part involved small (~100 μm) cathodes at high current densities. The Tomsk group has authored several useful review papers.[40,41,42]

In the early 1970's, Parker and coworkers[43] at the Air Force Weapons Laboratory studied the electrical behavior of broad area diodes and concluded that this was consistent with the results of Mesyats' group and with previous microscopic vacuum breakdown studies. They affirmed the central role of the cathode plasma in affecting the diode properties.

Since then there have been a limited number of studies of broad area diode plasmas, principally at Sandia National Laboratories. The work described in this thesis represents an extension of these studies.

2.2.1. Summary of Previous Work

Electrode plasma studies to date may be loosely grouped into three categories. The first consists of studies of plasmas on single emitter and needle cathodes. In these experiments the small cathode sizes permitted detailed microscopic measurements not possible with broad area cathodes, but the possible lack of relevance of these results to broad area cathodes must be kept in mind. The second category consists of the vacuum arc studies. In this case the dimensions are comparable to those of broad area diodes, and the long time scales and low voltages facilitate plasma measurements (for example, as the vacuum arc voltage is roughly equal to the cathode plasma potential drop, this quantity can be measured directly in a vacuum arc). However, the long timescale also causes fundamental differences between the operational regimes of arcs and diodes, as will be discussed. Finally,

measurements of plasmas in diodes are of the most relevance, but these measurements are the most difficult to make and as stated above, relatively few studies have been performed.

2.3. Initial Breakdown

Initial breakdown has been the most widely studied aspect of electrode plasma phenomena, and reviews are given by Mesyats,[44] Farrall,[45] and Noer,[46] as well as in Refs. 40–42. Until recently, breakdown was thought to proceed via the so-called "whisker model", where turn-on originates at the sites of metallic microprotrusions on the cathode surface. In recent years, however, an increasing body of evidence has suggested that there is a nonmetallic nature to this breakdown. The whisker model will be discussed first.

A typical plot of the potential energy of an electron as a function of distance from a metal-vacuum boundary, in the absence of an applied field, is shown in Fig. 2.1 a. For an electron to leave the metal, an energy equal to the work function must be supplied to it. This can be accomplished by heating the metal so that an appreciable fraction of the conduction electrons have such energies, giving rise to thermionic emission. The imposition of an electric field alters the potential barrier as shown in Fig. 2.1 b. One effect of the field is to lower the barrier height, leading to enhanced emission (the Schottky effect[47]). More important, the barrier now has a finite width so that electrons may tunnel through. This quantum mechanical effect, which is to first order independent of temperature, is described by the Fowler-Nordheim (FN) equation[48]

$$j = 1.5 \times 10^{-2} \frac{E^2}{v t^2} e^{-6.8 \times 10^7 \phi^{3/2} v / E} \tag{2.1}$$

where j is the emitted current density in A cm^{-2}, E is the electric field in V/cm, ϕ is the work function, and v and t are slowly varying functions of $E^{1/2}/\phi$ which are close to unity. In reality, the emission is caused by a mixture of field and thermionic effects, particularly inasmuch as the high field emission currents cause strong resistive heating. Murphy and Good have given a unified treatment of the emission process, obtaining a general expression for so-called thermo-field emission

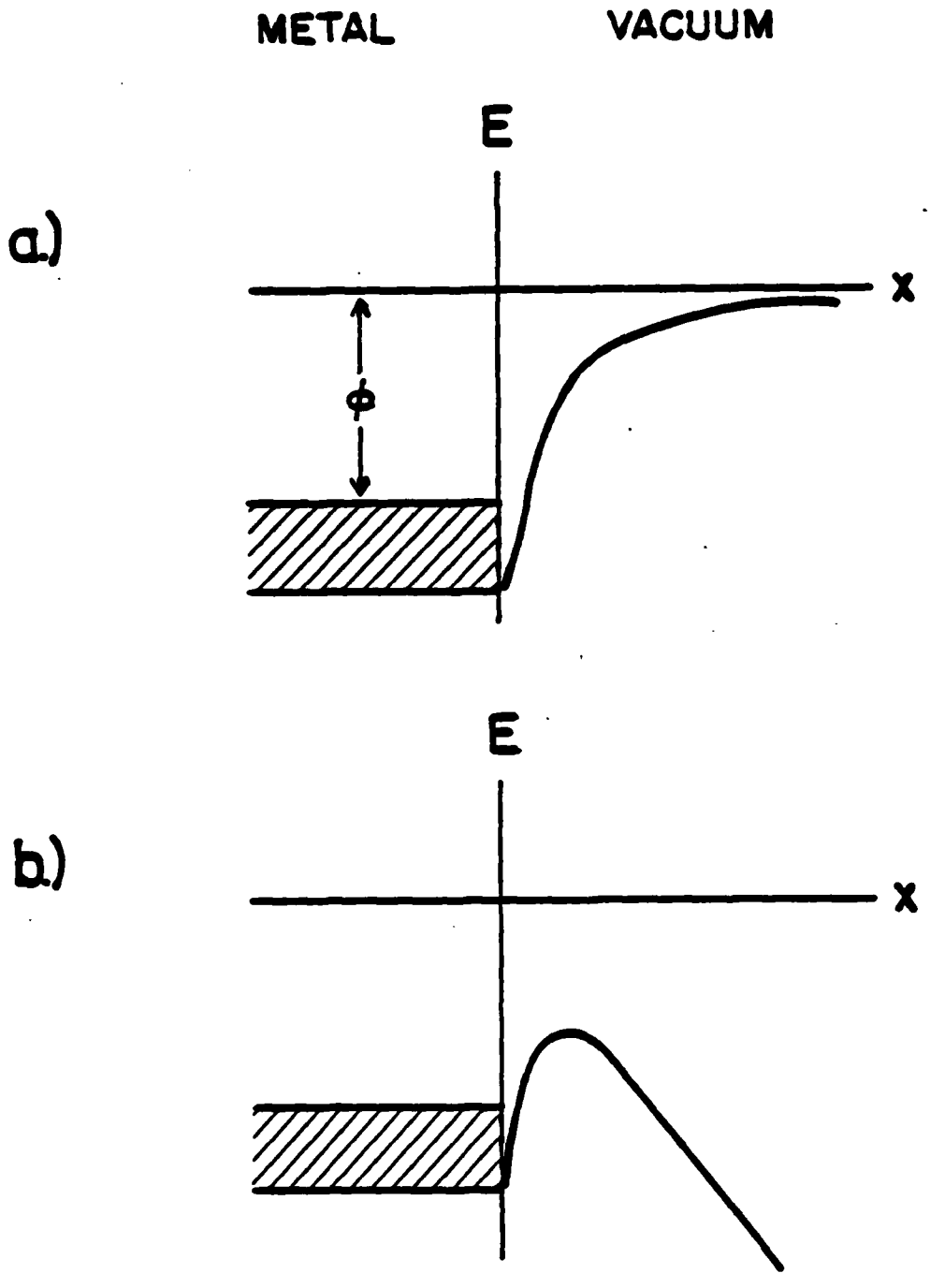

Fig. 2.1: Plot of the potential energy of an electron as a function of distance from a metal-vacuum boundary (ϕ is the work function).

as a function of field strength and temperature.[49] In order to obtain substantial currents at room temperature, electric fields exceeding 10^7 V/cm are required, and the emitted current increases rapidly with the applied field.

The first vacuum breakdown experiments under controlled conditions with clean surfaces and relatively short pulse lengths ($\sim$1 μs) were performed in the 1950's by Dyke and coworkers.[35–37] They studied the breakdown of the gap between a microscopic point cathode and a planar anode. They found that currents drawn from the cathode could be described well by the temperature corrected FN equation, and that at current densities on the order of 10^8 A/cm^2 a breakdown of the gap ocurred. Breakdown was attributed to a regenerative thermal instability caused by the increase of thermo-field emission due to resistive heating of the emitter, leading to increased heating, and so on. Space charge effects would tend to limit the current, and it was concluded that vaporization and ionization of the emitter material led to a partial neutralization of this space charge, permitting the instability to grow.

Charbonier *et al.*[50,51] pointed out that stable field emission at electric fields below the critical breakdown field could be explained by the Nottingham effect.[52] This effect arises because as electrons leave the metal they are replaced by electrons from the metal interior which 'travel' at the Fermi energy. Depending on whether the average energy of the emitted electrons is greater or less than this, there is either a net heating or cooling effect. Initially with a cold cathode heating occurs, but above the so-called inversion temperature, the Nottingham effect tends to cool the emitter. At this point there is a competition between resistive heating ($\propto j^2$) and Nottingham cooling ($\propto j$) so that the emitter will either remain stable or continue to heat, depending on j (and hence on E).

Further studies of small emitter breakdown were carried out by Fursei and coworkers in the early 1960's.[53,54] Based on their experiments it was concluded that space charge neutralization could not explain the rapid breakdown. Rather, it was concluded that emitter destruction was of an explosive nature, analagous

to the explosion of wires. In this explosion, there was a virtually instantaneous formation of a cloud of dense, highly ionized plasma.

Mesyats' group refined the model of Fursei, which they dubbed "explosive emission". In Ref. 55, the temporal behavior of breakdown was studied under nanosecond pulsed conditions, with typical behavior as that shown in Fig. 2.2. Initially, a level field emission current was observed (stage I), followed after some delay by explosive destruction of the emitter with a rapid rise in current (stage II). After this, the current rose slowly (stage III), which was attributed to a decrease in the (space charge limited) impedance due to plasma expansion, followed by a rapid current increase once the gap shorted (stage IV). The time required for breakdown τ_d was related to the plateau current, j, by $j^2\tau_d = const.$ As j strongly depended on the electric field, so did the breakdown time. An increase in the field from just above the critical field for DC breakdown to twice that resulted in a decrease in the breakdown time to a few nanoseconds.

These results were explained theoretically by Litvinov *et al.*, where the heating of an emitter was calculated for the time dependent case, including the Nottingham effect and the dependence of resistivity on temperature.[56] They calculated that

$$j^2\tau_d = \gamma\frac{c_p}{\rho_0} \tag{2.2}$$

where c_p and ρ_0 are the heat capacity and temperature coefficient of resistivity and γ is a factor of order unity that depends on the emitter geometry.

An interesting point mentioned in Ref. 40 is that the current raises the emitter electron temperature while the lattice temperature is raised by the electron-lattice interaction. Thus, for sufficiently short pulse lengths (10^{-10}-10^{-11} sec) it should be possible to draw 10^{10}-10^{11} A/cm^2 without emitter destruction.

In another interesting experiment.[57] Litvinov *et al.* studied the breakdown of a superconducting cathode, for which resistive heating should be absent. It was found that while the breakdown voltage did not increase, (which could be attributed to Nottingham heating), the breakdown delay time increased significantly when the cathode was in the superconducting state.

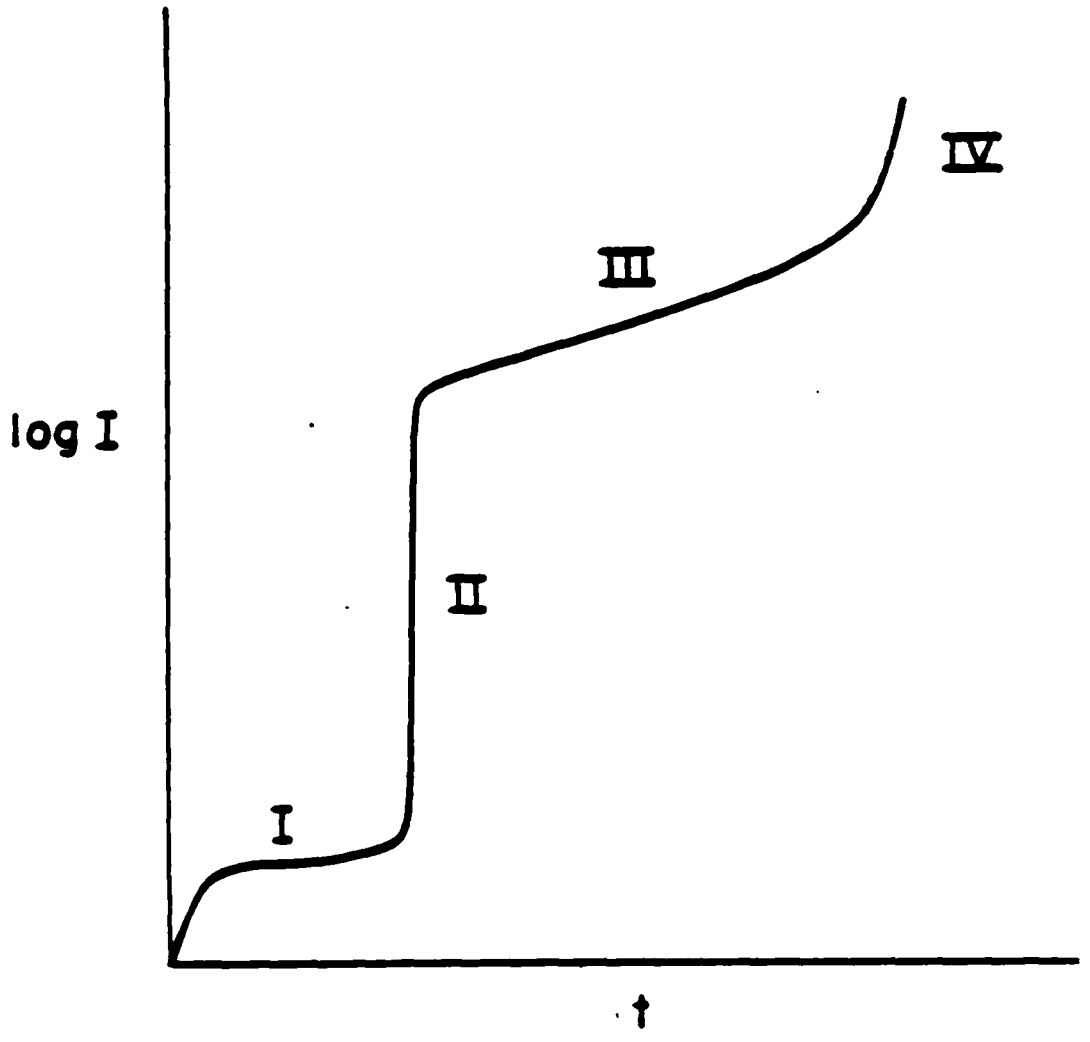

Fig. 2.2: Stages in current growth observed by Mesyats' group (from Ref. 55): (I) field emission: (II) breakdown: (III) expanding plasma: (IV) gap closure.

The breakdown of semiconducting emitters made of silicon and germanium was examined by Zhukov *et al.*[58] In contrast to the metallic case, breakdown was thought to initiate with an avalanche-type breakdown of the semiconductor leading to intense carrier generation, after which field emission occured leading to thermal explosion as in the case of a metal. The initial carrier generation was attributed to field induced tunelling from the metal into the semiconductor. Breakdown reproducibility was observed to be greater than for metallic emitters. Liquid gallium emitters were studied in Ref. 59, where the turn-on was observed to be more reproducible, and require less delay, than with tungsten emitters.

Further theoretical investigations into explosive emission were carried out by Martynyuk,[60] who compared emitter destruction to exploding wires as examples of nonstationary phase explosion of superheated metal, and by Dmitriev and Sinkevich,[61] who considered thermoelastic whisker destruction.

2.4. Extension to Broad Area Diodes

When broad area cathodes are subjected to a sufficiently high electric field, prebreakdown current and breakdown are observed to occur, just as in the case of a single emitter. However, these phenomena occur at electric fields about 10–1000 times lower than those in the experiments of Dyke *et al.* Alpert *et al.* extended the results of Dyke to planar electrodes by assuming that breakdown initiated at "whiskers" — local regions of high field enhancement (denoted by the coefficient β).[38]

There are several facts to support this. A series of experiments, described in Ref. 46, have shown that prebreakdown currents and breakdown originate from discrete sites. Electron microscopic observations, such as those by Little and Whitney,[62] have shown the existence of micron sized whiskers on the cathode, and these are often correlated with emission site locations.

A powerful technique used in breakdown studies involves measuring the voltage dependence of the prebreakdown current. From these I-V curves, called FN plots, three things may be determined — whether the functional dependence fits the FN equation, what the field enhancement factor, β would have to be, and

what the emission site area is. A series of experiments, also described in Ref. 46, have shown that prebreakdown currents from broad area electrodes exhibit FN behavior, with calculated β' s of 10–1000 and emission areas of 10^{-10}– 10^{-14} cm^2. In addition, Boyle *et al.* showed that the measured beta decreases at small gap lengths, approaching unity at distances comparable to the theoretical whisker dimensions, as would be expected from the whisker model.[63]

Several relatively recent experiments have cast doubt on this model, however. A variety of site-tagging techniques (again, reviewed in Ref. 46) have been employed to locate and characterize emission sites, during both the prebreakdown current phase and breakdown. These have shown that while the sites exhibit FN behavior, there are often no whiskers present with the necessary field enhancement and/or area. Instead, emission sites are often observed to be associated with the locations of non or semiconducting inclusions, surface impurity concentrations, or pits, scratches, and grain boundaries (which are themselves known to be favored sites of impurity concentration).

Hurley and coworkers[64] found that when DC or microsecond pulsed fields were applied to a cathode, small points of *prebreakdown* light appeared in the vicinity of emission sites, and it was concluded that this light was electroluminescence from semiconducting inclusions. Latham and coworkers[65] measured the energy spectra of prebreakdown emission electrons. From their measurements, it was concluded that this emission was of a nonmetallic nature.

In two experiments.[66,67] 5–50 micron sized nonconducting inclusions were intentionally added to cathodes and breakdown voltages were observed to be lower, with breakdown originating from metal-insulator boundaries.

Finally, in perhaps the most relevant experiment to nanosecond breakdown, Achtert *et al.* compared breakdown of small needle cathodes under nanosecond pulsed conditions in both clean and dirty vacuum systems.[68] In the former case, the surfaces were shown by surface analytic techniques to be free of all but a single monolayer of chemisorbed hydrogen. It was found that breakdown with clean

cathodes occured at voltages about three times greater, and with less reproducibility, than with contaminated (i.e., standard) cathodes.

There have been several theories proposed to explain the effect of impurities on breakdown, as shown in Fig. 2.3. The absence of surface features with sufficient β's can be explained by the existence of further field enhancement by submicroscopic subtips, with sizes of a few hundered Angstroms, as seen by Mesyats.[69] However, emission from such small tips would be inconsistent with the area measurements obtained from FN plots.

Farrall suggests that breakdown is caused by field enhancement at impurity metal juctions[67] (Fig. 2.3 a). Zhelzhnikov has proposed a method where the impurities spontaneously acquire a surface charge, presumably by field emission, and that this charge leads to an internal field causing increased emission of electrons from the metal into the inclusion, leading to avalanche breakdown[70] (Fig. 2.3 b). Hurley has proposed a model where the electric field causes small filaments to be switched on in the dielectric[64] (Fig. 2.3 c). These filaments are small conducting channels which then resemble whiskers embedded in the dielectric and so breakdown can then occur due to a thermal destruction mechanism analagous to that with metallic whiskers. Latham has proposed a model involving band bending[65] — initially the inclusion is nonconducting, and the imposition of an electric field causes a transition to a state like that shown in Fig. 2.3 d, where emission can occur by tunneling both into the impurity from the metal and from the impurity into vacuum. In this case breakdown can also be caused by a thermal destructive mechanism. It is not clear, however, how this model can explain the dependence of β on gap length, as observed by in Ref. 63.

The latter three theories all involve the breakdown of non or semiconducting particles, reminiscent of the previously mentioned semiconductor emitter studies of Zhukov *et al.*

Another possibility involves the desorption of adsorbed gasses by the applied field. This can occur because in the neighborhood of a protrusion, the field has a large gradient which can act on the dipole moment of an adsorbed molecule and pull it from the surface. In this way a field with sufficient intensity can give rise

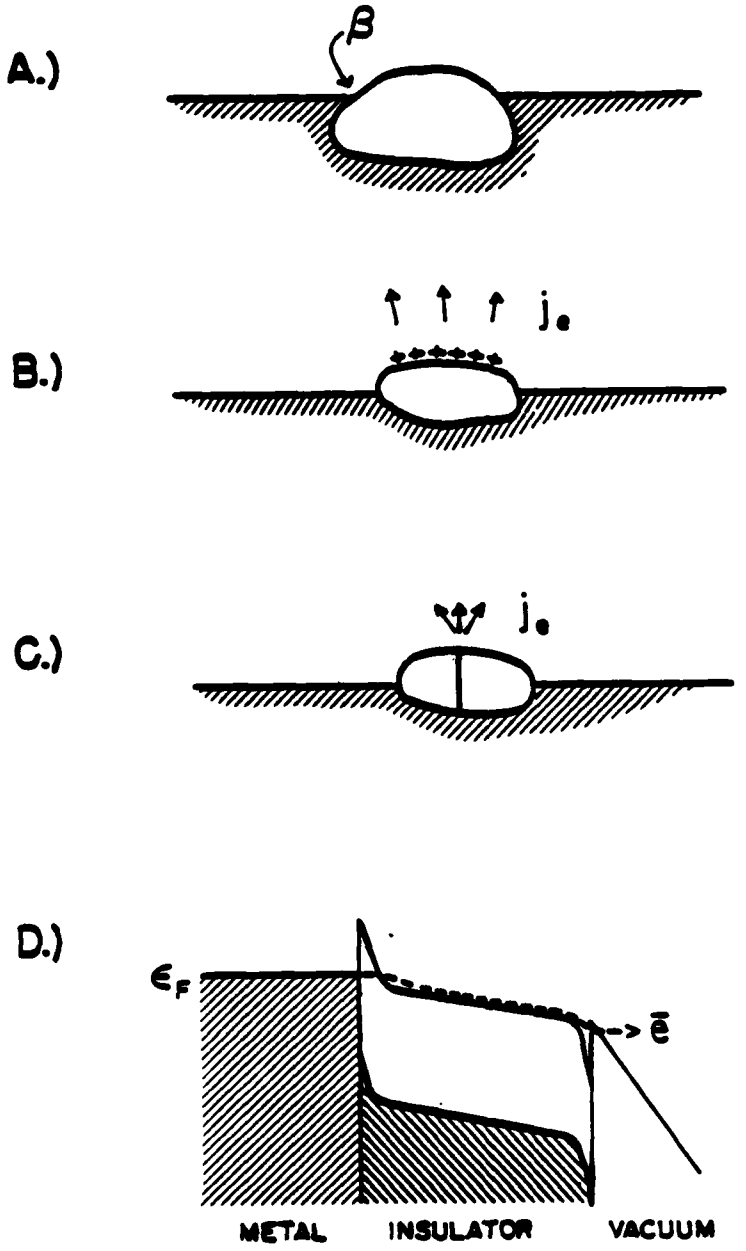

Fig. 2.3: Proposed mechanisms of impurity-enhanced breakdown: (a) field enhancement at the impurity-metal junction; (b) self-charging of the impurity: (c) electroformed filament: (d) band bending transition.

to a dense layer of gas on the cathode surface. This gas can be ionized by the prebreakdown current, partially compensating the field emission space charge and allowing an increase in current and subsequent breakdown. Originally proposed by Tarasova,[71] this was analyzed in Refs. 72 and 42. Both authors concluded that this effect could cause an effective field enhancement of about a factor of three, similar to the effect found by Achtert *et al.*

In evaluating these alternate possibilities, there are several points to consider. First, most of the detailed prebreakdown current measurements were carried out on a DC, or at best microsecond, timescale. It is questionable whether the solid state switching mechanisms proposed by Latham and Hurley can explain the sub-nanosecond breakdown times observed by Mesyats' group. (Switching times for these mechanisms are discussed in Refs. 73–75).

Also, these experiments were concerned only with the most strongly emitting sites, of which there were only a few per cm^2, whereas the rapid plasma formation observed in pulsed broad area diodes requires the simultaneous formation of at least several hundered sites/cm^2.

Finally, all of the above measurements may not be concerned with the same phenomena. The inclusions examined in Refs. 65 and 66 are 1–2 orders of magnitude larger than the submicron inclusions examined by Latham *et al.* and their effect may well be due to an entirely different mechanism than that of the smaller inclusions.

In conclusion, surface impurities, whether they be 10μ inclusions, submicron concentrations, or adsorbed films, are associated with enhanced breakdown. The exact mechanism is not yet known. none of the theories so far proposed can explain all of the data. and indeed it seems likely that different mechanisms may be involved with different types of impurites.

However. because of the observed FN plots. it can be said that *phenomenologically* breakdown may be considered to initiate from localized whiskers with β's of 100–1000. whether of not such whiskers actually exist.

If the correct microphysics of breakdown is ever known, there is the attractive possibility of producing a surface that either exhibits improved hold-off, or that turns on quicker, and at lower voltages, either of which would be extremely beneficial.

2.5. Cathode Flare Phenomena

2.5.1. Sheath Electric Field

In order to maintain current continuity, the electron current emitted by the plasma flare (toward the anode) must be balanced by a current flow from the cathode into the plasma. Since the plasma cloud will shield the surface from the applied field, Fursei suggested that charge transfer from the cathode to the plasma is maintained by the action of the sheath field at the cathode-plasma interface.[54]

Plasma adjacent to a surface is generally at a different potential than the surface; the two are separated by a thin, electron rich, electrically non-neutral sheath region with an associated electric field. The field at the cathode surface will be calculated. The geometry is indicated in Fig. 2.4. The plasma is assumed to be at positive potential V_c with respect to the cathode. In the general case there will be current j_c of electrons emitted from the cathode and a thermal ion current j_i from the plasma. Both the electrons and ions are assumed to have initial velocities which are small compared to the sheath drop. In addition, there will be a thermal electron current j_e from the plasma, with a Maxwellian distribution of initial velocities. Integration of the Poisson equation (assuming a collisionless sheath, Boltzmann electron distribution, and vanishing electric field at the plasma boundary) results in an equation for the electric field E at the cathode surface, in terms of j_c, j_i, and the electron temperature T

$$E^2 = 16\pi\sqrt{\frac{mV_c}{2e}}\left(\sqrt{\frac{M}{m}}j_i - j_e\right) - 8\pi nT\left(1 - e^{-\frac{eV_c}{T}}\right) \qquad (2.3)$$

where M, m, and n refer to the ion mass, electron mass and plasma electron density at the sheath edge, respectively.

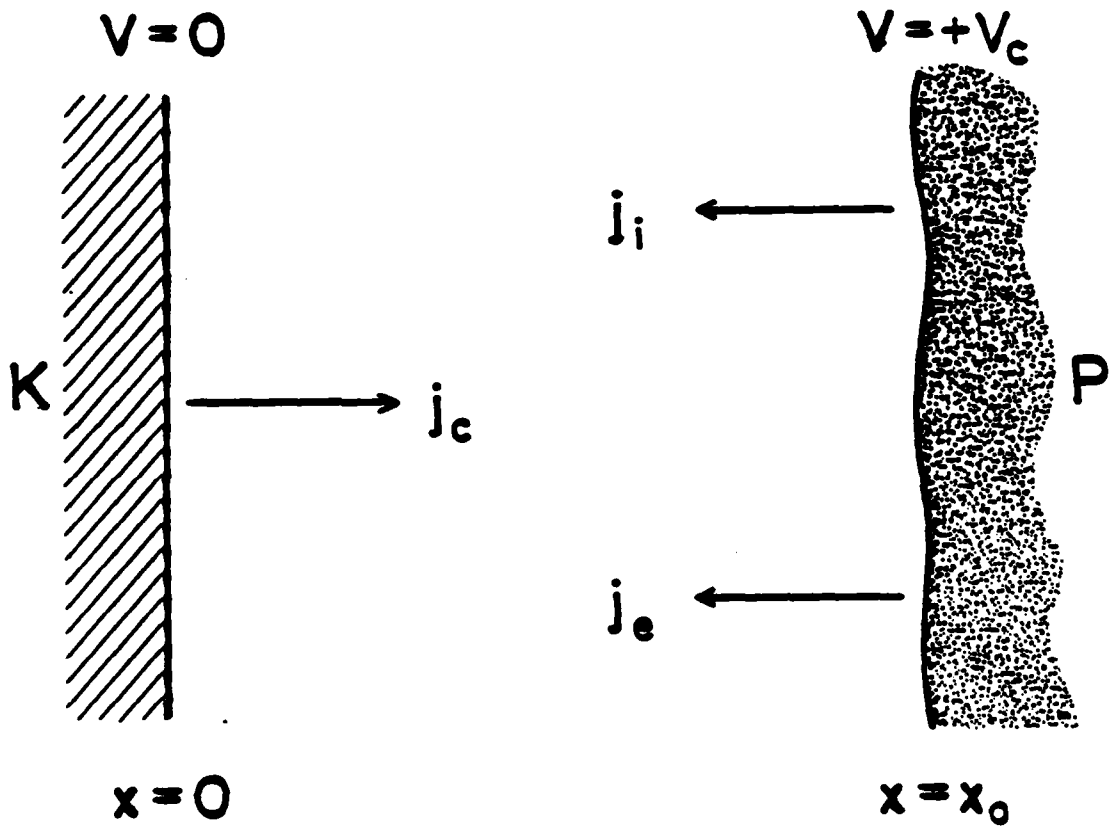

Fig. 2.4: Geometry of the cathode-cathode plasma sheath region.

If the sheath drop is large compared to the electron temperature, then the electron thermal current may be neglected. In this case the equation reduces to the Mackeown equation[76]

$$E^2 = 7.6 \times 10^5 \sqrt{V_c}\left(\sqrt{\frac{M}{m}} j_i - j_c\right) \tag{2.4}$$

where now the units are V/cm, V, and A/cm^2.

If there is no cathode current then this is just the Child-Langmuir equation for ion flow. If the ion current is determined by a condition analagous to the Bohm criterion[77]

$$j_i \simeq 0.5ne\sqrt{\frac{T_e}{M}} \tag{2.5}$$

then the cathode electric field E (in V/cm) and sheath thickness L (in cm) are given by

$$E = 1.6 \times 10^{-3} n^{1/2} (T_e V_c)^{1/4} \tag{2.6a}$$

$$L = 830 n^{-1/2} T^{-1/4} V_c^{3/4} \tag{2.6b}$$

where the units for n, T, and V_c are cm^{-3}, eV, and V.

As mentioned before, local fields exceeding 10^7 V/cm are necessary for intense field emission. In the case of vacuum breakdown, field enhancement reduces this requirement by a factor of 100–1000. However, if the sheath thickness is on the order of a micron or less, then the field enhancement drops to unity,[63] and the full field is required. For a sheath drop of tens of volts and electron temperature of a few eV, a density of about 10^{20} is required for intense field emission. (The authors of Ref. 42 state that in the region of such high density, immediately adjacent to the emission site, the interface actually has an ohmic character. Also, the very high local current densities will cause significant heating of the surface and can lead to thermionic emission.)

The point of this is that in order to draw current from the cathode, a high plasma density is required, such as exists immediateiy adjacent to the emission site. This means that current will flow into the plasma in localized regions.

2.5.2. Erosion Measurements

One of the primary tools used to investigate the physics of the cathode flare region has been electron microscopy of the cathode after breakdown. In Refs. 78–81, the Tomsk group investigated the erosion, of micron-sized tips, that occured as a result of explosive emission pulses of durations ranging from 5–100 ns. From these measurements, the velocity of the destruction of the emitter was inferred to be about 10^5 cm/sec, implying that the destruction was indeed of an explosive nature. Based on the comparison of measured erosion quantities with those predicted by theory led to the conclusion that for the first few tens of ns, all of the current passed through a narrow region at the end of the tip with a current density exceeding $10^8/cm^2$. For longer pulses, the rate of erosion dropped by an order of magnitude and this was attributed to the explosion of microscopic subtips under the plasma cloud on the sides of the original tip, resulting in an increased area of current transfer and hence reduced current density. Examination of the effect of multiple (short) pulses on erosion of tips showed that after a certain number of pulses, the erosion also dropped an order of magnitude, which was attributed to blunting of the tip and the formation of subtips. This occured when the tip radius was on the order of ten microns.

Similar results were reported by Fursei and coworkers,[82,83,84] who studied the erosion of micron sized tips in the stages of current growth indicated in Fig. 2.2 by using short voltage pulses. Most of the erosion was found to occur during the explosion of the tip (stage II). They also distinguished between the explosion of a single tip from the explosion of subtips on a large point, which, as above, was associated with lower erosion.

Microscopic examinations of graphite tips after breakdown inferred the existence of liquid graphite;[85] from this it was concluded that the pressure in the emission zone exceeds 10^{10} dynes/cm^2.

A picture of the field emission process emerged from these results. Initially a whisker explodes and forms an emission site, and current is drawn into the plasma by the sheath field. This field also causes subtips to explode under the plasma cloud. The intense heating causes the surface to liquify and the plasma

pressure acting on the liquid surface results in the formation of a micron sized crater. As the crater expands, (for a fixed current) the current density decreases and the loss mechanisms of conduction, convection, and radiation result in cooling. Meanwhile, the pressure has forced liquid up into ridges and droplets on the crater periphery, which can freeze into structures with high field enhancement (especially if the extended droplets break off, leaving sharp points). As the original emission site dies out, a new site can form at the edge of the old one. The period of this cycle is on the order of tens of ns.

The formation of new tips at the crater rim can explain why repeated pulses do not change the (average) breakdown characteristics of a surface. Whisker rejuvenation during a pulse has in fact been observed.[86]

If the voltage pulse is sufficiently short, then there will not be enough time for new tips to form and a polished surface may be produced. The dividing line between surface roughening and polishing is on the order of a few ns.[87,88]

Jüttner and coworkers at the Central Institute of Electron Physics in Berlin have also carried out extensive studies of cathode erosion, confirming this picture of tip destruction, crater formation, and tip formation at the crater rim (Refs. 89–90 and references therein).

2.5.3. Cathode Spots in Vacuum Arcs

Since a high plasma density is required for current transfer out of the cathode, it can be assumed that this tranfer takes place at localized regions. This has long been known to be the case in vacuum arcs, where the cathode surface is seen to be covered with a number of discrete points of light, called cathode spots. These micron sized spots are centers of high plasma and energy density, and this high energy density facilitates charge transfer. They are associated with erosion of the cathode and so it is assumed that they are also centers of transfer of material from the cathode into the plasma.

It has been observed that two different types of cathode spots exist — the so-called type I and type II spots. In the initial operation of a vacuum arc, all of the spots are of the first type. These are characterized by relatively rapid ($\sim 10^4$

cm/s) motion across the cathode surface, and relatively low erosion. With time, these spots are replaced by spots of the second type, which move more slowly ($\sim 10^2$ cm/s) and are associated with much greater erosion. The properties of the different spots are reviewed in Ref. 32.

Comparison of vacuum arc erosion studies with those of needle emitters suggests that emission sites in a diode are similar to cathode spots in a vacuum arc. Henceforth the term cathode spot will be used to refer to both.

2.5.4. Spot Currents

One of the features of arc spots is that the number of spots is on the average proportional to the total current, so that each spot carries a fixed average current. This spot current depends on the cathode material as well as other factors such as the rate of rise of the current and is ~100 A for type II spots and ~10 A for type I spots. There is a threshold current below which the spot will die out.

This fixed spot current is significant in that the spot properties will then be independent of the (macroscopic) current density.

The existence of a threshold current was also verified in a long pulse diode.[91] A decreasing stepped voltage pulse was applied to an 80 μm wire cathode. If the voltage on the second step was below that which would draw about 1 A, the current would die out. This threshold current was similar to that observed for arc spots.

2.5.5. New Cathode Spot Formation

If the number of spots is proportional to the current, then as the current rises new spots must be formed. Since these spots will be formed under the plasma cloud, it is necessary to examine spot formation under these conditions.

One possibility is that emission sites can form under the plasma cloud in exactly the same way they are formed in vacuum, but with the sheath field replacing the diode (vacuum) field. However, as mentioned in Sec. 2.5.1, a very high plasma density is required for sheath drops of tens of volts.

From both total arc voltage measurements and probe measurements, the potential drops in vacuum arcs are known to be about 10–30 V, as reviewed in

Ref. 32. Floating probe measurements of the potential drop in a diode plasma have been reported in Refs. 92 and 93. It was concluded that the drop was less than or on the order of 50 V, that is, similar to that in an arc. The plasma potential near the spot was seen to remain low even when the current rose rapidly. These measurements involved small needle cathodes with (presumably) one or a few spots.

There is another way in which the plasma can cause the formation of new explosive emission sites if there is a net ionic current to the cathode, as would be the case when the sheath voltage greatly exceeds the electron temperature. The ionic current deposited on nonconducting inclusions will build up a surface charge causing an internal electric field, which can lead to a bulk breakdown of the inclusion, as indicated in Fig. 2.5 b. If the dielectric is vaporized and ionized, then the resulting high density puff of plasma can cause field emission, and so turn on an emission site. This phenomena was originally studied in the context of the glow to arc transition (GAT) and is critically reviewed by Lutz.[94] To first order the inclusions may be treated as parallel plate capacitors (assuming an even distribution of ionic charge), in which case the internal electric field is determined solely by the surface charge:

$$E = \frac{4\pi\sigma}{\epsilon} \approx \frac{4\pi j_i t}{\epsilon} \tag{2.7}$$

where ϵ is the dielectric constant of the impurity. Actually, charge leakage places a minimum on the inclusion size (since leakage will be relatively more important for small inclusions) and a maximum limit on the size d is given by $E_b d < V_c$, where E_b is the breakdown field. In Ref. 61, it is stated that a calculated internal field of $\sim 3 \times 10^6$ V cm is necessary for inclusion breakdown to occur. Combining Eqs. 2.5 and 2.7, and assuming a dielectric constant of 3 results in the relation between charging time and plasma density:

$$t = \frac{1.4 \times 10^7}{n} \tag{2.8}$$

Thus, for a plasma density of 10^{16} cm^{-3} emission site formation by this method can occur in <1 ns. If the sheath drop is assumed to be about 30 V then in order for breakdown to occur, the dielectric thickness must be less than 1000 Å.

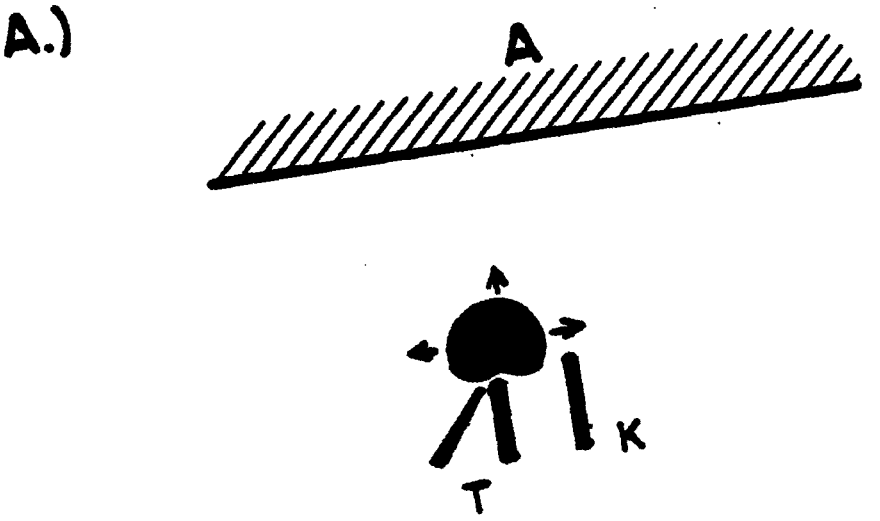

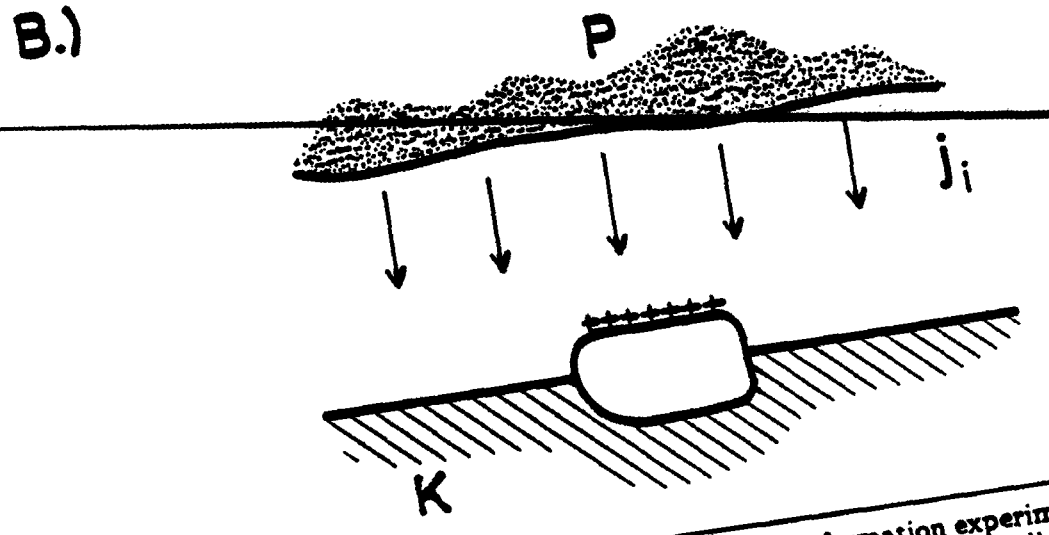

Fig. 2.5: (top) Schematic of plasma induced emission site formation experiments in Ref. 95–97. (bottom) Surface charging of nonconducting inclusions leading to breakdown.

The formation of new emission centers by the action of plasma was studied in a series of experiments by the Tomsk group.[95,96,97] The general experimental schematic is shown in Fig. 2.5 a. A constant voltage below that required for breakdown was applied across an anode-cathode gap. Plasma formation was induced on an external electrode by means of a nearby trigger electrode, and this plasma then expanded toward the cathode. It was observed that under certain conditions, emission from the cathode occurred when the plasma contacted it. These measurements were combined with floating probe measurements of the plasma potential and previous measurements of the plasma density. From this work it was concluded that the charging up and subsequent breakdown of dielectric inclusions was responsible for the formation of new emission sites at distances greater than tens of microns from the original site. This was strengthened by observations that breakdown did not occur if the cathode was clean, and was enhanced if the cathode was coated with an oxide layer.

2.5.6. Arcs on Clean and Contaminated Surfaces

Jüttner's group carried out extensive investigations of the effects of surface contamination on arc erosion tracks.[68,89,98] They were able to show that the type of arc spot was determined by the level of surface contamination. with spots of the first type occuring on contaminated surfaces. As the contaminations were cleaned off by the arc, spots of the second type were formed. It is important to note that they found the same results in studies of short (~1-10 ns) pulsed needle cathodes.

On contaminated surfaces. the erosion pattern consisted of many small (<1 μm) dispersed craters and tree-like patterns of branches about 0.1 μm deep. These branches were preferentially located along grain boundaries. which was attributed to the increased concentrations of impurities there. The erosion patterns on clean surfaces consisted of deeper (~10 μm). overlapping craters with no preference for grain boundaries.

The above observations give rise to a picture of spot motion under the plasma.[97] This apparent spot motion is actually a sequence of appearences and disappearences of (different) spots. On a contaminated surface during periods of increasing current (i.e.. in a diode). the formation of new spots is caused by the

plasma from existing spots and so spot propagation occurs at velocities equal to the plasma expansion veloscity, or about 2 cm/μs. Once the number of spots has reached equilibrium (as in the early stages of an arc), the formation of new spots will be determined by a random walk type process as old spots die out, and the apparent velocity of spot motion will be decreased to the 10^4 cm/sec observed for type I spots. On a clean surface, new spots can form only by the action of the sheath field, and as this requires a high plasma density, they may form only in the immediate vicinity of old spots, as discussed in Ref. 96. This gives rise to a much lower apparent velocity of ~100 cm/s. In the case of a clean surface, spot propagation is determined by the crater melting rather than the plasma cloud.

Since spots form more readily on a contaminated surface, there will in general be more spots and so the average spot current will be less, as is observed.

2.5.7. Spot Plasma Properties

There have been very few measurements of the plasma in the spot region. In Ref. 32, measurements are presented for a type I spot which suggest that the density is relatively constant at ~10^{17}–10^{18}/cm^3 from 5–50 μm from the spot. It is also claimed that the electron temperature in a type I spot is a few eV. Mesyats[40] has proposed a hydrodynamic model of plasma expansion from a single flare:

$$n_i = n_T \frac{1}{2\pi t^2} \frac{vt - r}{v^2 r^2} \tag{2.9}$$

where n_T is the total quantity of material, v is the plasma velocity and r is the distance from the spot. With a current of 20 A and a velocity of 2×10^6 cm/μs, this predicts a density of about 4×10^{17}/cm^3 at 25 μm away.

2.5.8. Theoretical Efforts

There have been a number of attempts at a global theoretical description of cathode plasma microprocesses (see Ref 32 and 99–101), but so far all of these have been directed toward type II (clean surface) spots, and many involve assumptions of steady state behavior, so that their relevance to pulsed, contaminated surface diodes is questionable. An effort is currently being directed toward the development of a global model of (broad area, contaminated) cathode/cathode plasma microprocesses by Bacon *et al.*[102]

2.6. Summary

This chapter summarizes the current knowledge regarding cathode plasma microprocesses. The central feature is the cathode spot, a region of high energy and plasma density (and thus, difficult to study) that facilitates both material and current transfer from the cathode into the cathode plasma. A key role is played by cathode surface contaminants. They are believed to enhance vacuum breakdown, although the exact mechanism(s) is (~~are~~) ~~not~~ presently known. They definitely dominate breakdown and spot formation under the plasma cloud (a distinction should be drawn between vacuum breakdown and breakdown under the plasma; for example, a thick uniform oxide coating is known to retard vacuum breakdown,[103] but to enhance breakdown under the plasma[96]).

2.6.1. Relevance to Diodes

Since electrode surfaces in a diode are in general contaminated, and since most of the vacuum arc studies to date involve long pulses with type II spots, the validity of these results to (broad area) diode plasmas must be questioned. A similar situation exists with the needle emitter measurements. For example, with a 50 μm cathode and 50 A current, and if it is assumed that one contaminant atom is removed for every three current electrons (see Ch. 7), then 10^{17} contaminant atoms/cm^2 will be removed in 3 ns (no re-contamination is to be expected on these timescales). In other words, the high current densities in these cases will rapidly clean the surfaces.

On the other hand, there are certain applications, such as repetitively pulsed diodes, where a clean surface would be expected, and for which the results of vacuum arc and needle cathode studies are more relevant.

In addition to its effect on initial breakdown, a contaminated surface is seen to be advantageous for the following reason. As will be discussed in Ch. 4, once an emission site has turned on, the electronic space charge drawn towards the anode will tend to reduce the (vacuum) electric field at locations adjacent to that site, and so retard neighboring emission site formation. This means that plasma induced emission site formation will play a role in the formation of a uniform

plasma layer, and this plasma induced turn-on is seen to be aided (strongly) by surface contaminants.

In fact, Buttram has observed that the performance of repetitively pulsed diodes (where a clean surface would normally be expected) is enhanced by the use of oil-impregnated brass cathodes.[104]

Finally, it should be pointed out that cathode spots are central to both clean and contaminated surfaces, so that many of the ideas developed regarding vacuum arcs and needle cathodes are still relevant to broad area contaminated cathodes, as will be discussed in later chapters.

Chapter 3

Nereus Accelerator

The accelerator, diode, and electrical monitors are described in this chapter.

3.1. Accelerator

The Nereus accelerator[105] consists of a Marx bank,[106] water dielectric pulse forming line, self breaking output switch, and diode. A schematic of the oil insulated Marx bank is shown in Fig. 3.1. The bank consists of twelve 0.25 μF capacitors arranged in a N=2, plus-minus charged configuration. The copper sulfate grounding and charging resistors were omitted in the figure for clarity. Six Physics International[107] T-670 spark gaps, pressured with 8–11 PSI of SF_6, are used to switch the Marx; these are triggered by three cables from a PI TG-70 pulse generator. The first two gaps are triggered by one cable each while the last four are triggered in parallel from the third cable. A charging voltage of 30 kV was used throughout this work, giving a stored Marx energy of 1350 J.

The Marx output is connected through an inductor to a 1.9 Ω water dielectric pulse forming line which has a one way transit time of 18 ns. The capacitance of the line is 8.2 nF, giving a ringing gain[2] of roughly 1.5 when charged by the 20 nF series capacitance of the Marx. A copper sulfate resistive divider is connected to the case of the last capacitor and a capacitive voltage monitor was installed at the far end of the pulse line. Typical Marx and pulse line waveforms are shown in Fig. 3.11. As can be seen, the line takes about 500 ns to charge. Distilled and then filtered water with a typical resistivity of 0.5–1 MΩ-cm (yielding a lumped line resistance of ~0.5–1 kΩ) was used in the line.

A self breaking output switch separates the pulse line from the diode as shown in Fig. 3.2. These switches consist of 3.2 mm thick low density polyethylene disks which were stabbed repeatedly to a depth of 0.9 mm. These stabs were confined to a 2.5 cm diameter circle in the center of each disk and there were about 1500 stabs per switch. If the switches were stabbed at larger radii then the breakdown path through the switch would be lengthened, increasing the switch inductance

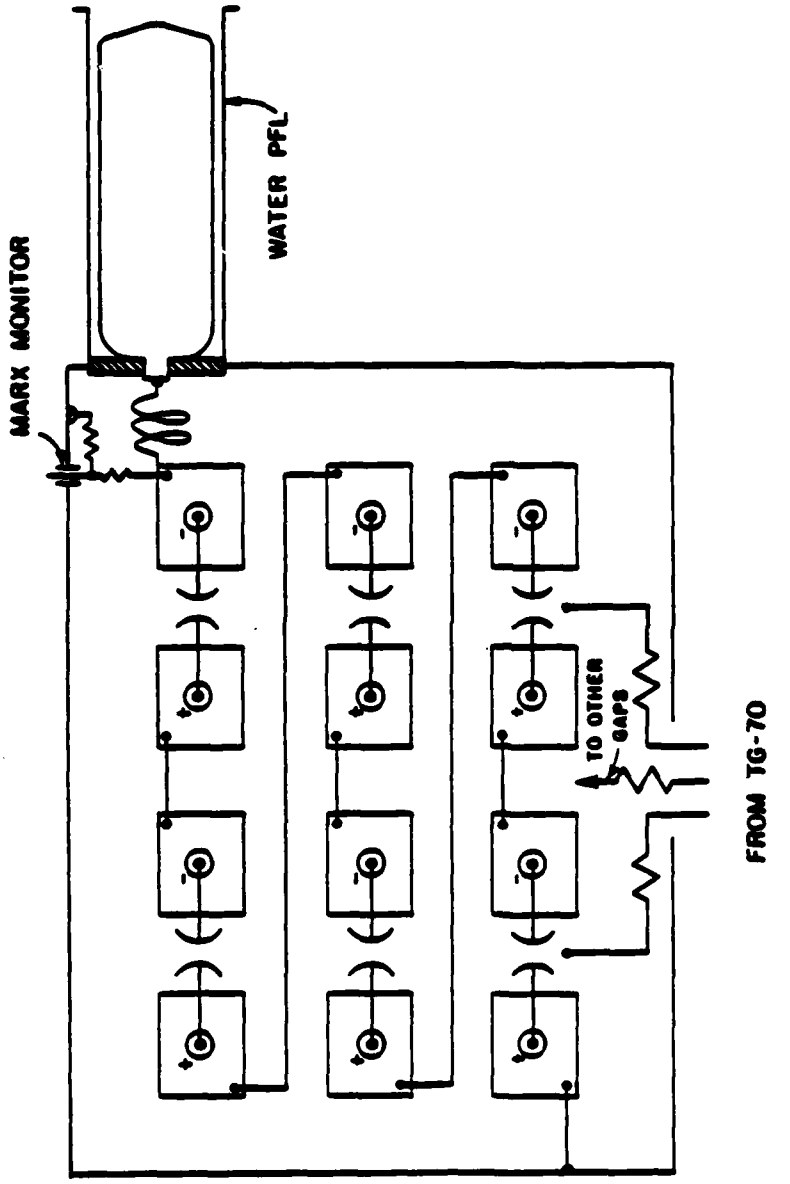

Fig. 3.1: Nereus Marx and pulse forming line. The indicated capacitor charging polarities are those for positive polarity output.

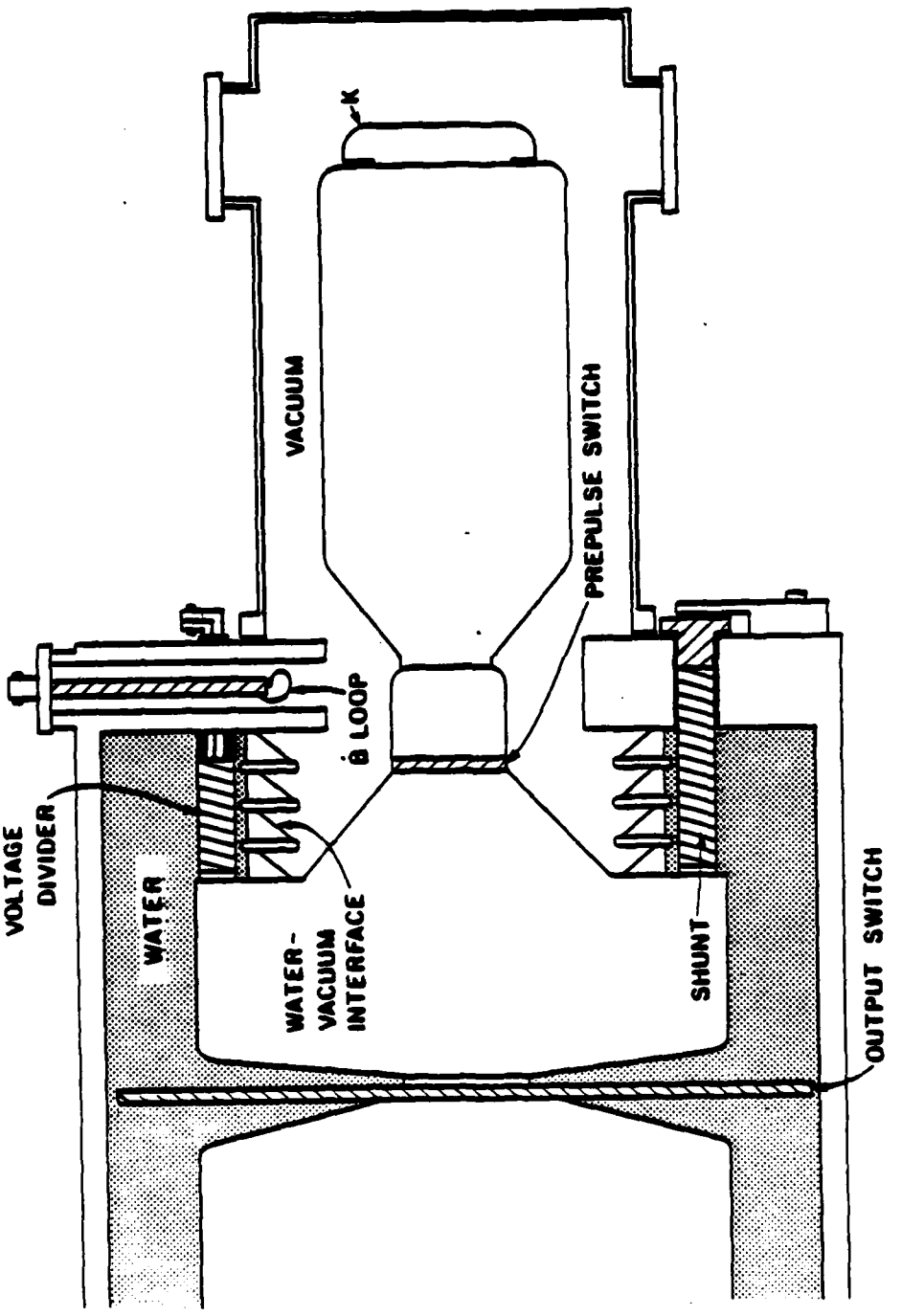

Fig. 3.2: The Nereus front end. The prepulse switch shown here was absent for most shots. Negative polarity operation is shown here — for positive polarity, the plexiglass rings in the water-vacuum interface were reversed and the cathode was attached to the other electrode (see Figs. 1.1. 3.3. and 3.4).

and the rise time of the diode voltage pulse. The switch inductance is quoted in Ref. 105 as being 11 nH. For a few shots, the switches were purposely stabbed off center to increase the switch inductance and reduce the rate of rise of the diode electric field. This rate could be varied by varying the distance from center to where the switches were stabbed.

A short (~3 ns) uncharged section of line joins the switch to the diode; as discussed in chapter 6, this short section has a significant effect on the diode voltage and current waveforms. In order to reduce the prepulse due to capacitive coupling across the output switch, a 40–50 Ω shunt consisting of a NaCl solution inside a nylon rod (see Fig. 3.2) connects the center conductor to ground. The resulting prepulse is about 8 kV; this could be reduced further with a nylon prepulse switch in the diode as mentioned in chapter 6.

The water-vacuum interface consists of a four stage graded axial insulator stack, with the lucite insulators beveled at 45 degrees to reduce flashover and coated with silicone pump oil to prevent damage in the event that flashover did occur. Debris from the anode was deposited on the stack after each shot; when metallic anodes were used the rings would flash over unless cleaned every 1–3 shots, but it was found that with a graphite anode 50–100 shots could be taken between cleaning the rings even though they quickly became coated with an oil-carbon sludge.

Occasionally it was necessary to chop the current pulse early in time and this was easily accomplished by causing the stack to flash over prematurely, either by inserting objects in between the grading rings or by positioning the lucite rings with the bevel in the wrong direction.

Besides cleaning the stack and replacing the water every few months, the only machine maintanance consisted of replacing an occasional faulty capacitor or switch in the Marx. The Marx switches were vented roughly every 20–30 shots. The only problem encountered with the accelerator was the jitter, which could be as high as 80 ns. This arose from jitter in the firing of the Marx switches and jitter in the breakdown of the polyethylene output switch, and caused difficulties in synchronizing the accelerator with the nitrogen laser.

3.2. Diode

The diode used in this work consisted of a parallel plate diode with the cathode in the shape of a bar. This shape was chosen in order to have a long path length in one direction to increase the sensitivity of interferometric measurements and a short path length in the other direction to improve spatial imaging for spectroscopy. Also, the rectangular shape eliminated the need for Abel inversion of the measured quantities. A parallel plate feed was used to insure uniformity of current flow along the length of the diode; this uniformity was confirmed as discussed below. The diode is shown in Figs. 3.3 and 3.4.

The gap in the feed region was set to 1.2 cm to confine plasma formation to the cathode. That the line did not emit significantly was verified by covering the cathode with 0.08 mm Mylar tape. Occasionally the tape was observed to have punched through with <1 mm holes at one or two places; however in these cases the electrical traces were identical with those in which the tape did not break through. The total diode inductance, as determined from short circuit shots, was 60 nH.

Some typical cathodes used are shown in the top half of Fig. 3.5. All cathodes were 7.5 cm in length. The current density was varied by changing the diode gap while varying the cathode width simultaneously to keep the same total current. Side views of the three cathodes used in most of this work are shown in Fig. 3.6. The cathode widths, diode gaps and peak current densities for these three were: 9.6 mm, 2.6 mm, 9 kA/cm^2; 6.4 mm, 2.2 mm, 13 kA/cm^2; 1.6 mm, 1.7 mm, 39 kA/cm^2. The 9.6 and 6.4 mm wide cathodes had radii of 1.6 mm machined along each edge while the 1.6 mm cathodes had a 1.6 mm diameter circular tip cross section. All of the cathodes of a given size were machined to the same dimensions to within 25 μm. The 9.6 and 1.6 mm wide cathodes were machined of aluminum while 6.4 mm wide cathodes of aluminum, brass, stainless steel, Poco graphite[10a] (a dense, fine grained, high purity graphite) and reactor grade graphite (machined from ordinary scraps of unknown origin) were used.

The diode could be set up for either polarity (polarity in this case refers to the center conductor of the pulse forming line and the bottom plate in Fig. 3.3;

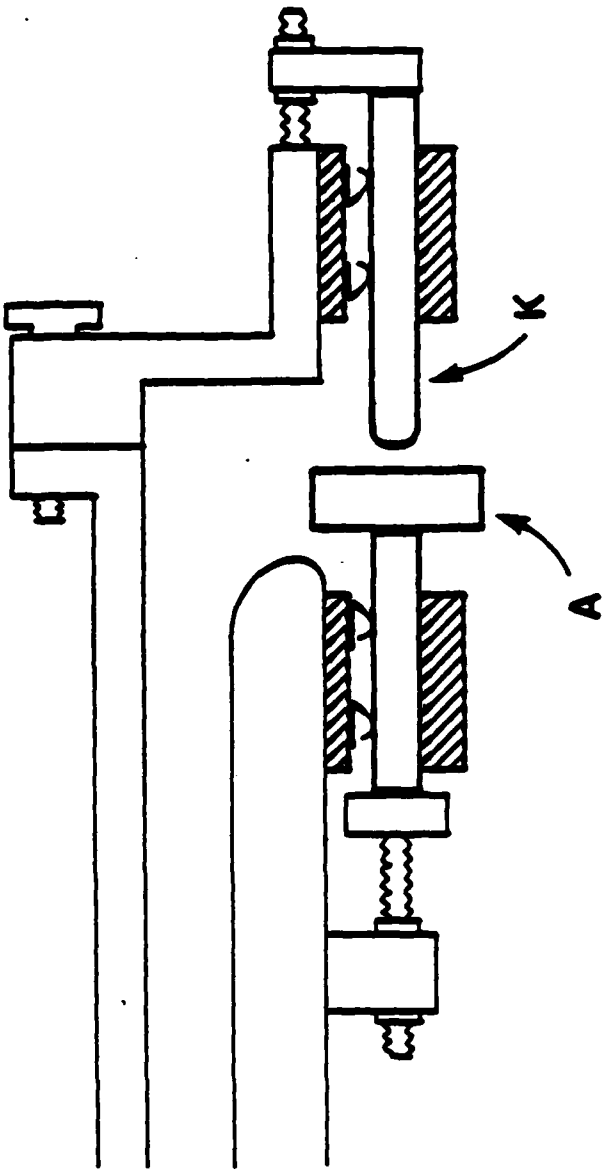

Fig. 3.3: The diode used in this experiment. Adjustable backstops positioned the removable electrodes: finger stock insured good electrical contact.

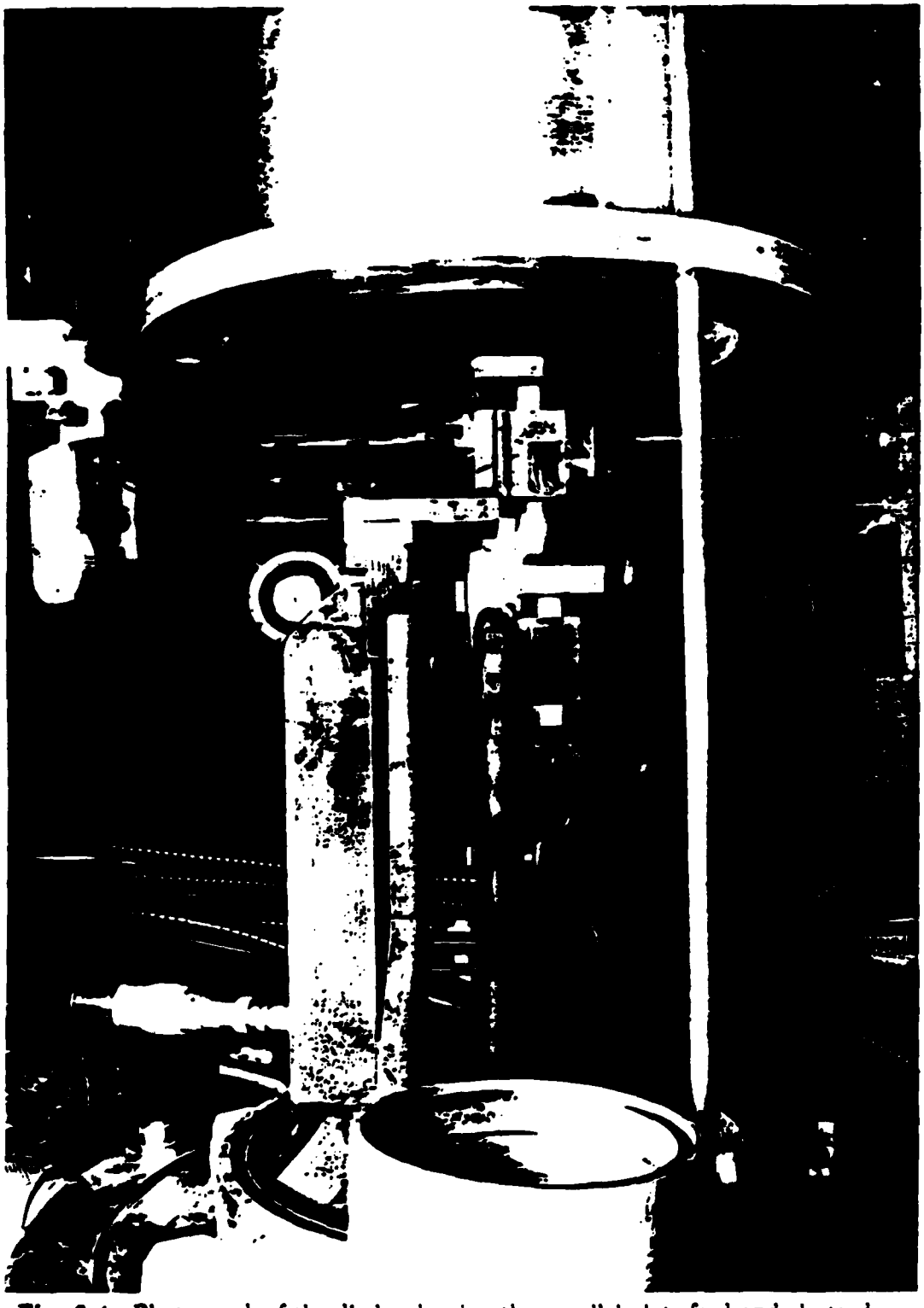

Fig. 3.4: Photograph of the diode, showing the parallel plate feed and electrode holders. The set-up here is for positive polarity.

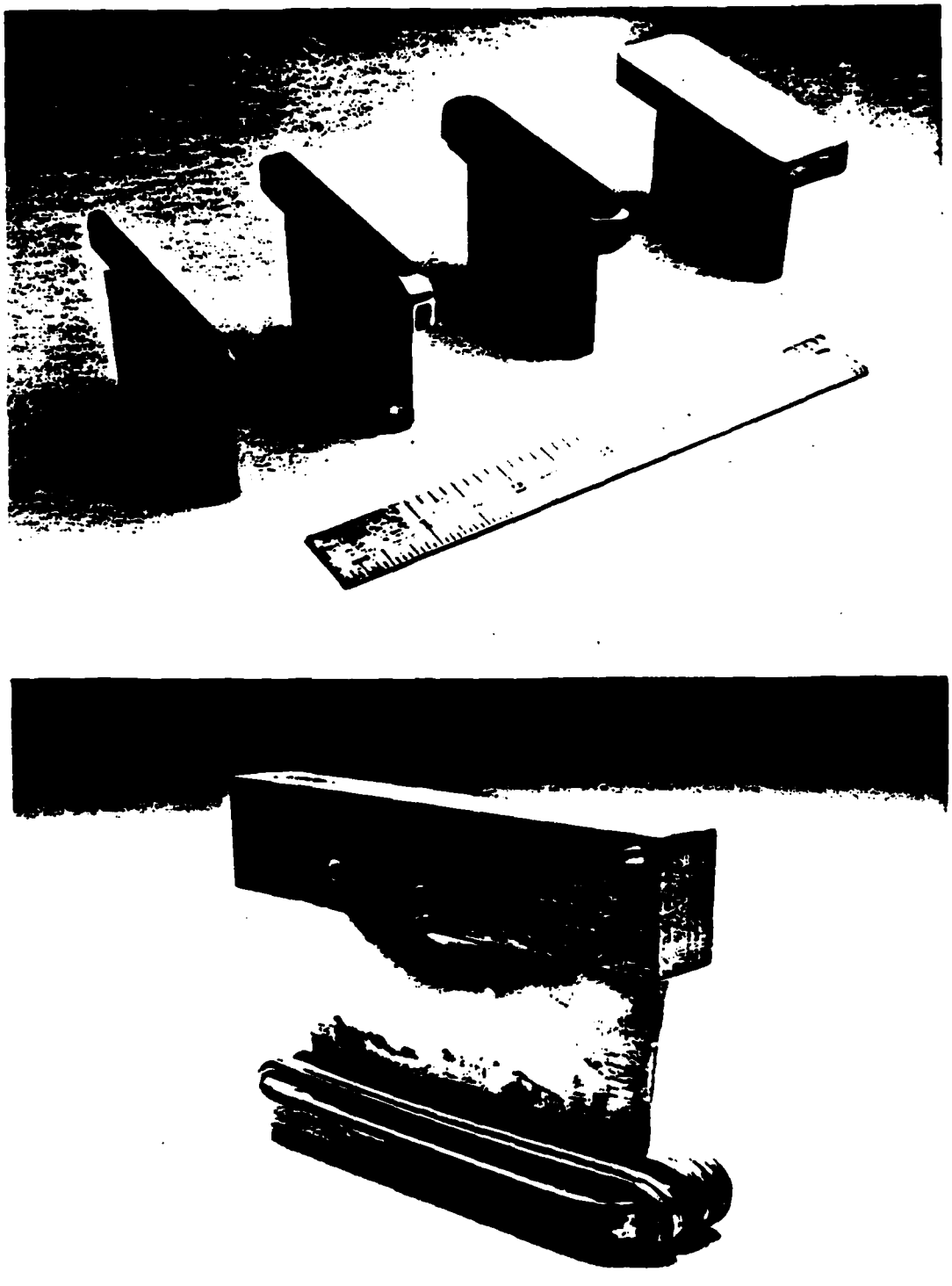

Fig. 3.5: (a) Photographs of some typical cathodes. (b) Stainless cathode which could be heated *in situ*.

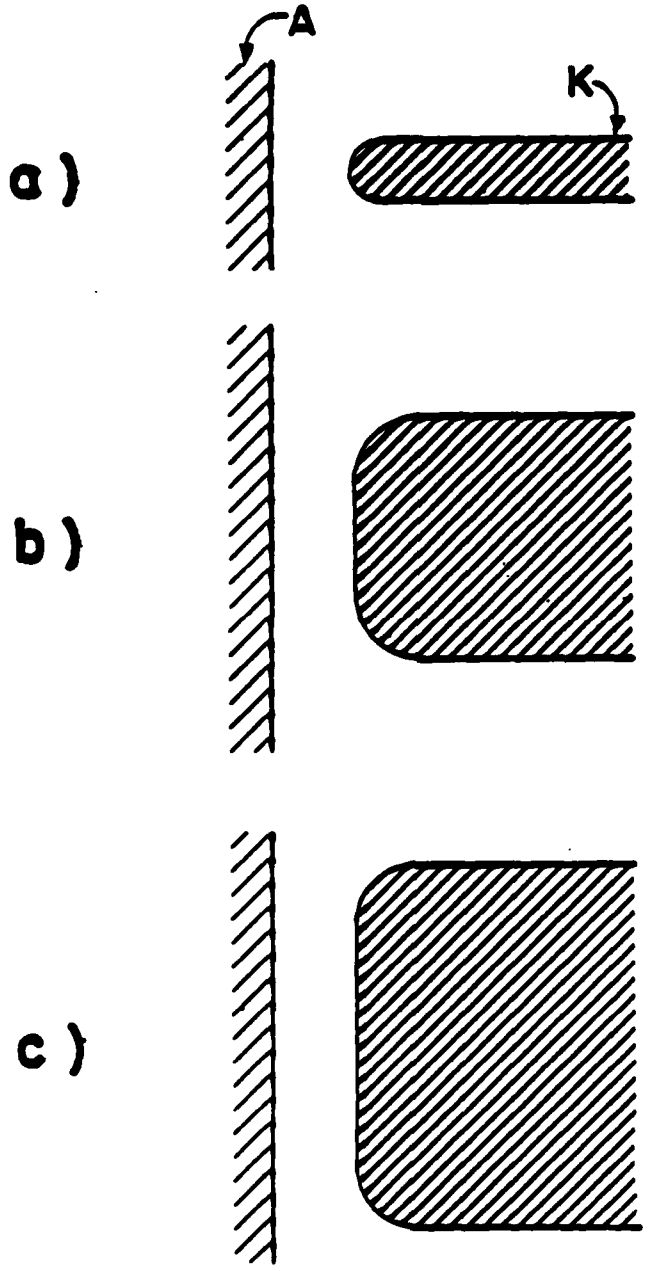

Fig. 3.6: Side views of the three cathodes most frequently used: (a) 9.6 mm wide cathode: (b) 6.4 mm wide cathode: (c) 1.6 mm wide cathode.

the positive polarity arrangement is shown in Figs. 3.3, 3.4 and 1.1, while that for negative polarity is shown in Fig. 3.2). Negative polarity operation was necessary with the dosimetry diagnostic (Ch. 4) while positive polarity was necessary when the hot cathode was used (described below). In general, the machine was operated in positive polarity. The cathodes (and anodes for positive polarity operation) were held in a slot against a backstop with finger stock to insure good electrical contact (see Fig. 3.3). These backstops were positioned to set the gap, and when set, electrodes could be easily replaced without remeasuring the gap (~30 seconds between opening and pumpdown). The anode and cathode faces were set parallel to within 25 μm.

The cathodes were cleaned after each shot by sandblasting with 90 grit aluminum oxide. Unfortunately, the only sandblaster available was in a machine shop and the purity and air pressure were not controlled so that the surface finish was not necessarily reproducible, as discussed in Ch. 4. The cathodes were either left blasted or smoothed with a fine abrasive wheel. In this case, "smooth" meant shiny to the eye — no attempt was made to remove any small pits or scratches. Following this they were ultrasonically cleaned in methanol for about one hour. The graphite cathodes were not sandblasted but were rubbed clean with a tissue after each shot. No special attempts were made to prepare the graphite surfaces. For some shots the cathodes were coated with a spray on graphite coating (Aerodag G[109]). In this case several light coats were applied and the underlying metal was not visible to the eye before or after the shot. In general, the cathodes were replaced after every shot.

A 6.4 mm wide stainless steel cathode, shown in the bottom half of Fig. 3.5, that could be heated *in situ* to over 700°C was also used. This cathode was heated by running up to 5 A through several turns of coaxial heater wire.[110] This wire consisted of a resistive inner conductor through which the current was passed, an insulating refractory material, and a stainless outer jacket which was brazed to the cathode.

The anodes consisted of slabs of reactor grade graphite which were heated (once) to ~1000°C to remove any machining oils and then were allowed to equilibrate with the ambient air. They were wiped clean after each shot; after a few shots they became appreciably eroded (with pits of depth >25 μm) by the electron beam and were replaced.

The vacuum chamber was an aluminum can with several observation ports. Pressure was maintained below 3×10^{-4} T with a standard oil diffusion pump and no effort was made to control the pressure beyond this or to study the effects of varying pressure.

The effect of glow discharge cleaning was examined on a few shots. For this, a water cooled copper electrode was inserted in the vacuum chamber and held at -500 VDC. The chamber was filled with Argon at a pressure of about 100–200 microns and the discharge was run for about 40 minutes, after which the chamber was pumped down to shot pressure. The purpose of this was not to clean the chamber as the few minutes between cleaning and the shot would completely undo any cleaning action that took place, but rather to see if the discharge in any way affected the cathode surface. A one hundered watt light bulb series resistance limited the current to 200 mA: with an estimated area of about 2400 cm^2, the time integrated surface bombardment was then roughly 200 mC/cm^2.

3.2.1. Diode Field Distribution

The field enhancement at the rounded cathode edges was determined with the aid of an electrostatic code developed by W. B. Herrmannsfeldt at SLAC, described in Ref. 111. This code, written to calculate electron trajectories in (relatively low current, compared to the present case) electron guns, solves the Poisson equation by finite difference equations. Either Dirichlet or Neumann boundary conditions may be used, the trajectory equations are fully relativistic, and (electric and B_θ) self field effects are included. The code has an optional Laplace mode where the vacuum potential distribution is calculated and which includes in its output the calculated values of the electric field at the boundaries — this mode was used to determine the field enhancement.

The diode was modeled by the geometry in Fig. 3.7. Because of the (vacuum) symmetry, the cathode centerplane could be replaced by a Neumann boundary. The model boundary was completed by plane K1 and the lower Neumann boundary (see Fig. 3.4 for comparison) — presumably the enhancement at the cathode edge is relatively insensitive to the exact nature of these boundaries. This was checked by: raising the bottom boundary by 2 mm, which tended to push the field lines away from the cathode edge; making plane K1 a Neumann boundary, which tended to pull the field lines closer to the cathode edge; and running the program with one fewer iteration. In all cases the calculated electric fields at the cathode edge changed by less than a few percent.

The code output for a 6.4 mm cathode with a 2.2 mm gap is shown in Fig. 3.8. The surface electric fields obtained from the code are shown in Fig. 3.9. Below each plot is a cross-section of the diode with the electrodes shaded. In the top half of Fig. 3.9, the electric field is shown on portions of the cathode surface facing the anode, that is, the anode is above the cathode (out of view) and parallel to the horizontal axis. The field is seen to be highest at the start of curvature, as would be expected (compared to that point, points closer to the diode center plane have less curvature and the same gap, while points around the curve have the same curvature and a greater gap). The maximum field enhancement factor is 1.3, and thus the (macroscopically enhanced) field will be 1.5 MV/cm with a 250 kV diode voltage.

Of more relevance to this experiment is the plot in the bottom of Fig. 3.9, which corresponds to a silhouette view (with the anode along the vertical axis and shown shaded at the left), as would be observed by the framing camera described in Ch. 4.

Similar results for the 1.6 mm cathode with a 1.7 mm gap, and the 9.6 mm cathode, with a 2.6 mm gap, are shown in Fig. 3.10. In the former case, the maximum field enhancement is 1.6, giving a field of 2.4 MV/cm for 250 kV and in the latter case the maximum enhancement is 1.3, giving a field of 1.3 kV/cm at 250 kV. Note that while the field decreases around the curve, it remains finite —

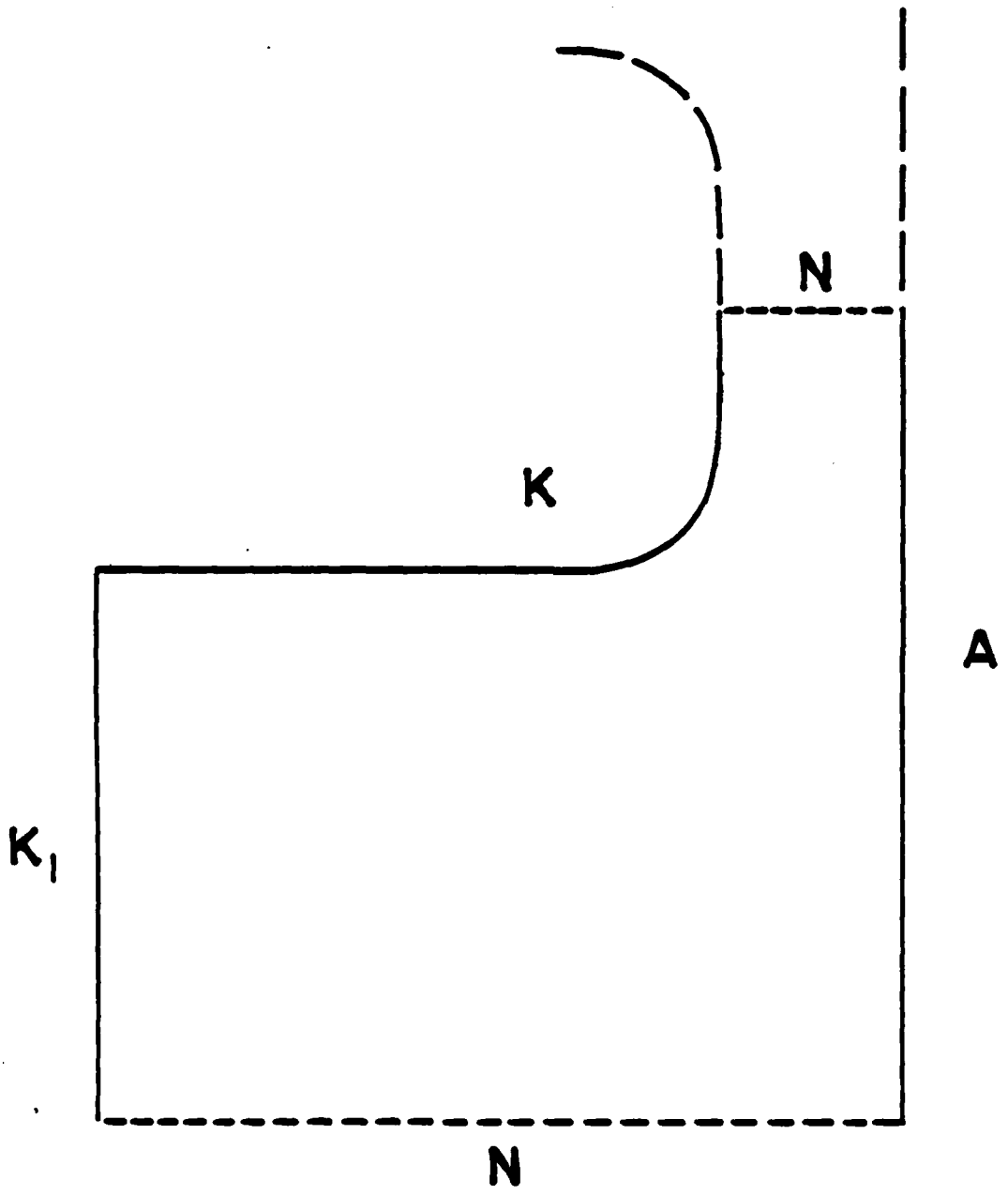

Fig. 3.7: The geometry used to model the diode with a 6.4 mm wide cathode. All diodes were modeled by the 1 cm^2 area enclosed by the anode (A), Neumann boundaries (N) and the cathode plane (K, K1).

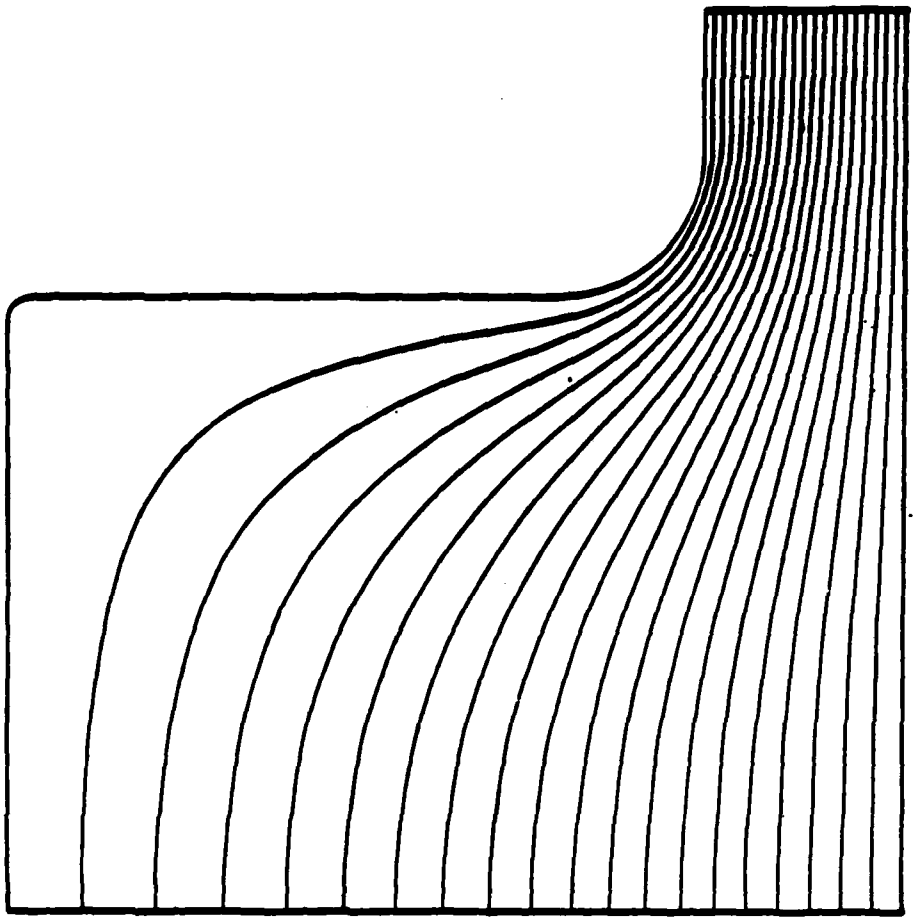

Fig. 3.8: Code output for the 6.4 mm cathode with a 2.2 mm gap.

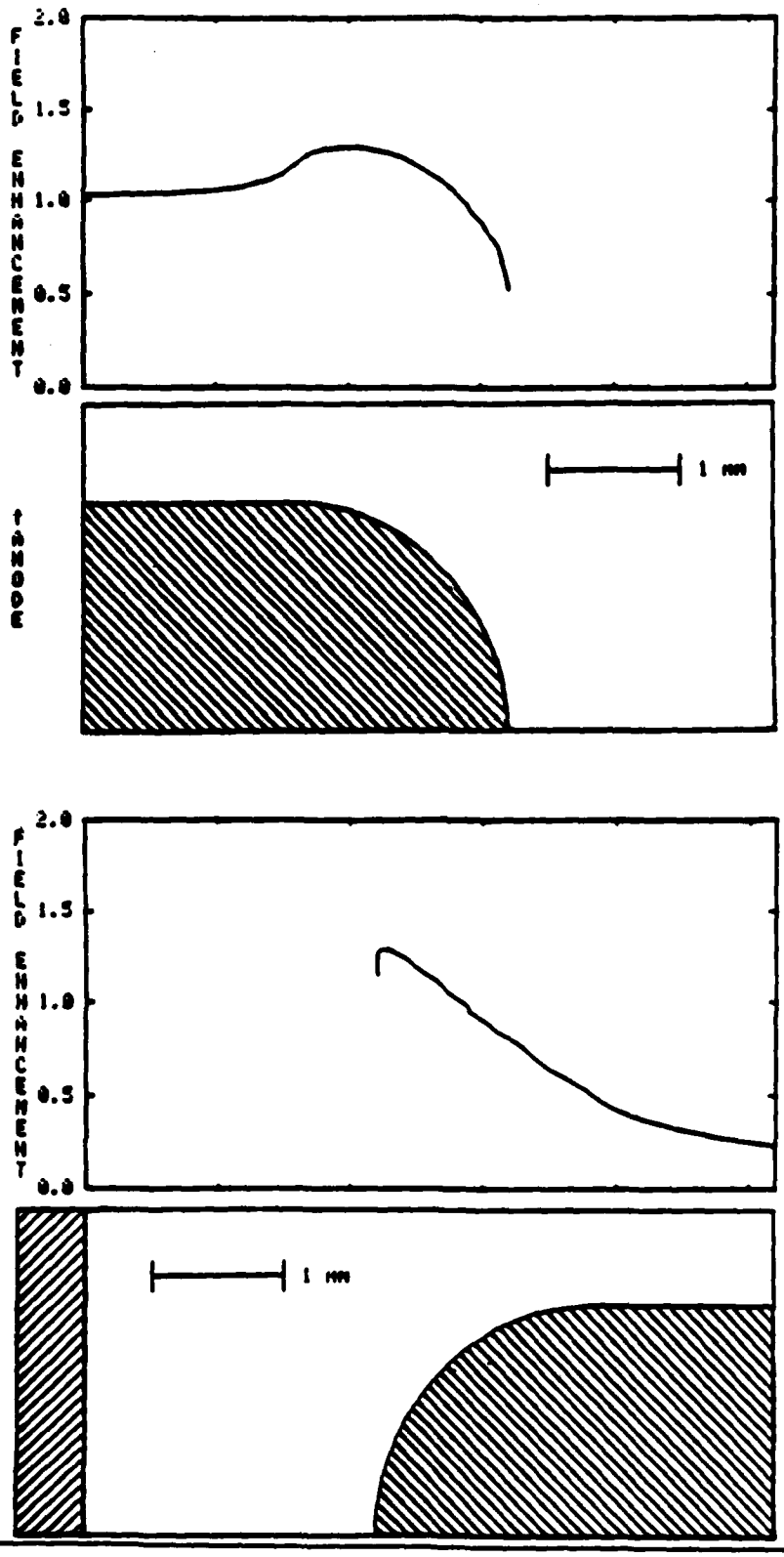

Fig. 3.9: Field enhancement factor at different locations for the 6.4 mm cathode.

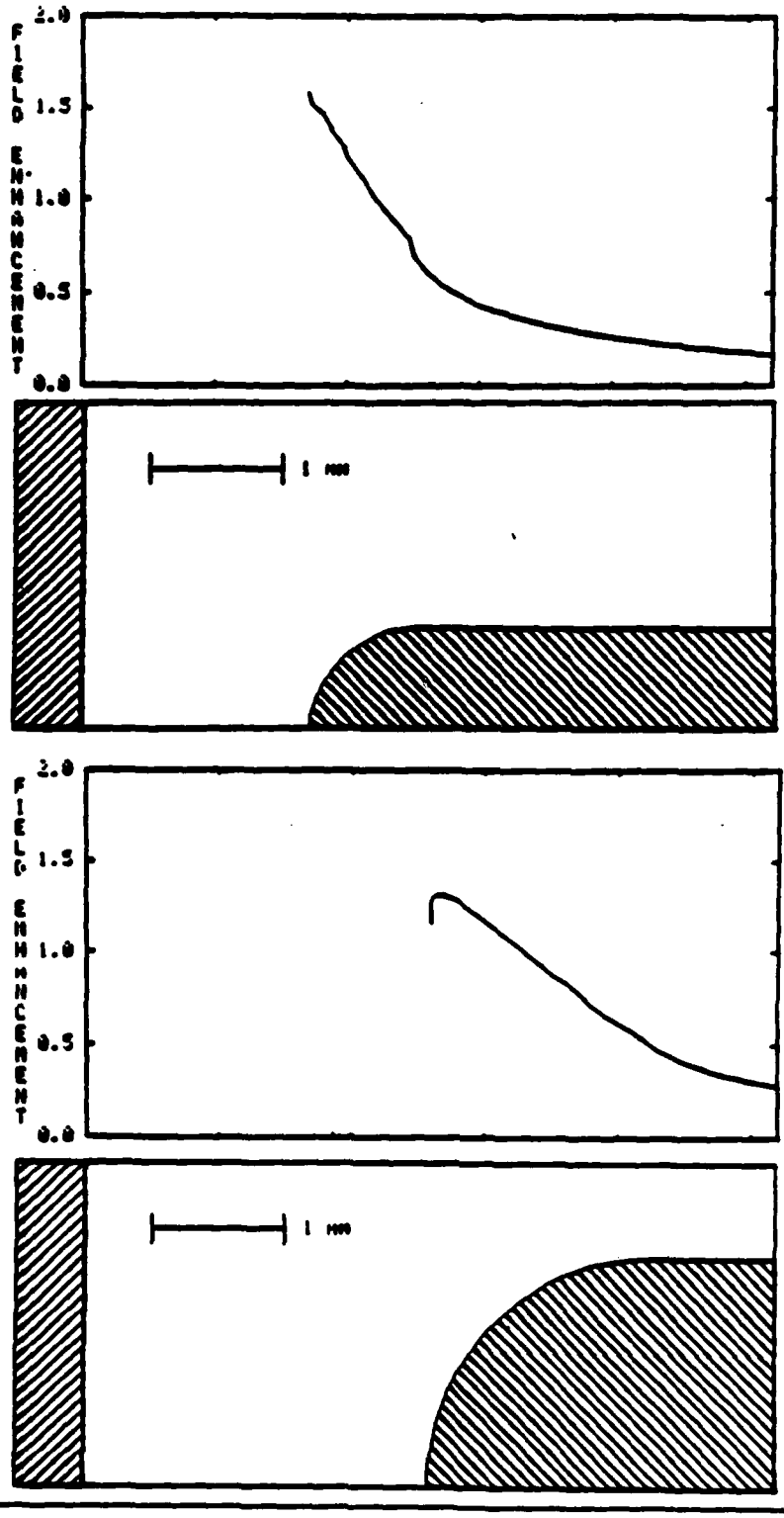

Fig. 3.10: Field enhancement factors for the 1.6 and 9.6 mm cathodes.

in particular for the 1.6 mm cathode it is still ~300 kV/cm at 3 mm back along the cathode.

3.3. Electrical Monitors

The electrical monitors — an externally integrated $\dot{B}$ loop for current and a resistive voltage divider — are shown in Fig. 3.2. The voltage divider consisted of a nylon tube filled with copper sulfate solution, with a resistance of roughly 1 kΩ. The brass cap at one end was connected to ground by eight parallel carbon resistors having a combined resistance of 1.2 Ω and a pickoff at this cap was connected to the center pin of a BNC connector which was soldered to the outside of the machine.

The monitors were both calibrated by feeding the output from a Pulsar Associates[112] Pulspak 10-A pulse generator to the Nereus center conductor just downstream of the output switch (via a switch with copper tape on it). This pulser supplied a 10 kV output pulse into 50 Ω with a rise time of 10 ns. The current monitor was calibrated by shorting the anode and cathode with a 1 cm diameter rod which passed through the center of a calibrated current transformer.[113] The voltage monitor was calibrated by placing a carbon resistive divider across the gap. This resistive divider consisted of five 2W carbon resistors in series to restrict the voltage drop across each resistor to 2 kV. A further check was made by connecting a 50 foot length of 51 Ω cable across the gap, which resulted in an exact 51 Ω resistor for 120 ns, and comparing the voltage monitor output with the measured current. Both of these calibrations agreed. The rise time of the pulses in these cases was ~20 ns. comparable to that during the shots. The calibration and monitor signals for both the voltage and current monitors overlaid well (~5%). The calibrations of both monitors remained essentially constant during this experiment.

All electrical signals were sent to the screen room via 1/2 in. Cablewave[114] foamflex cables which had the same transit time to within 0.5 ns. These cables (at the lengths used) had a frequency response better than the 100 MHz oscilliscopes used.

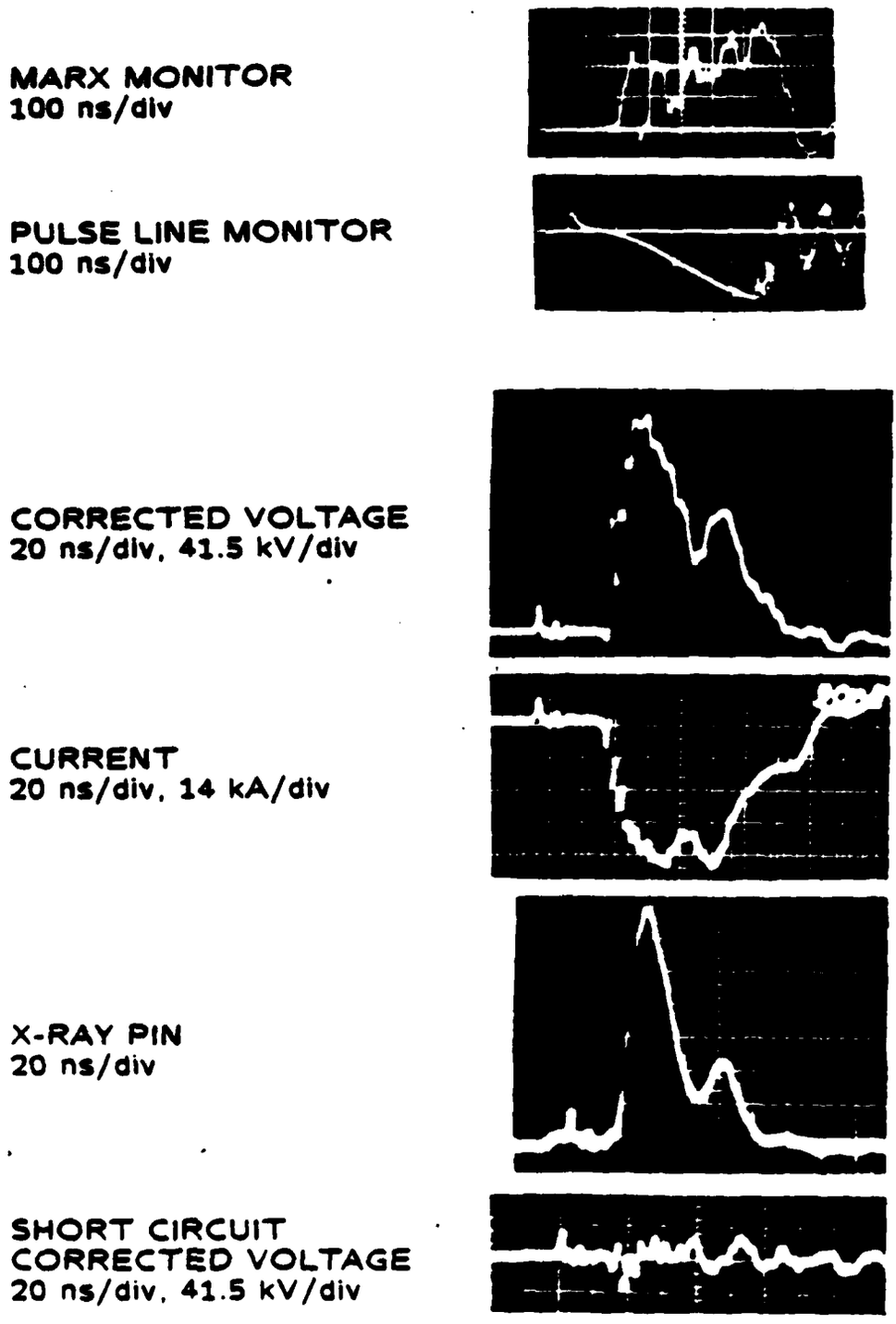

Fig. 3.11: Typical waveforms.

The voltage was inductively corrected in the usual way by subtracting the LdI/dt signal at the scope input and determining the proper attenuation by minimizing the corrected voltage on short circuit shots. Typical waveforms are shown in Fig. 3.11.

That the parallel plate feed caused a uniform current flow along the length of the cathode was confirmed by shorting the A-K gap, pulsing current through the line with the Pulspak, and measuring the local magnetic field with a small moveable magnetic probe as shown in Fig. 3.12. The field strength as a function of position along the cathode is shown in the figure. The field was uniform on the inside and very small on the outside of the line, that is, on the bottom edge of the cathode. It should be noted that there was thus a magnetic field assymetry between the two cathode edges so that, for instance, plasma on the top edge would be expanding against the self magnetic field while that on the bottom edge would (nominally) see no field. This point is discussed further in Ch. 7.

As a further check, the diode was shorted out at a single point as shown in Fig. 3.12. In this case the field became uniform at a distance back in the line roughly equal to half the line width, that is, as if the current flowed at 45 degrees. All discontinuities in the feed, such as slots in the top plate for viewing the plasma, were designed with this criterion in mind.

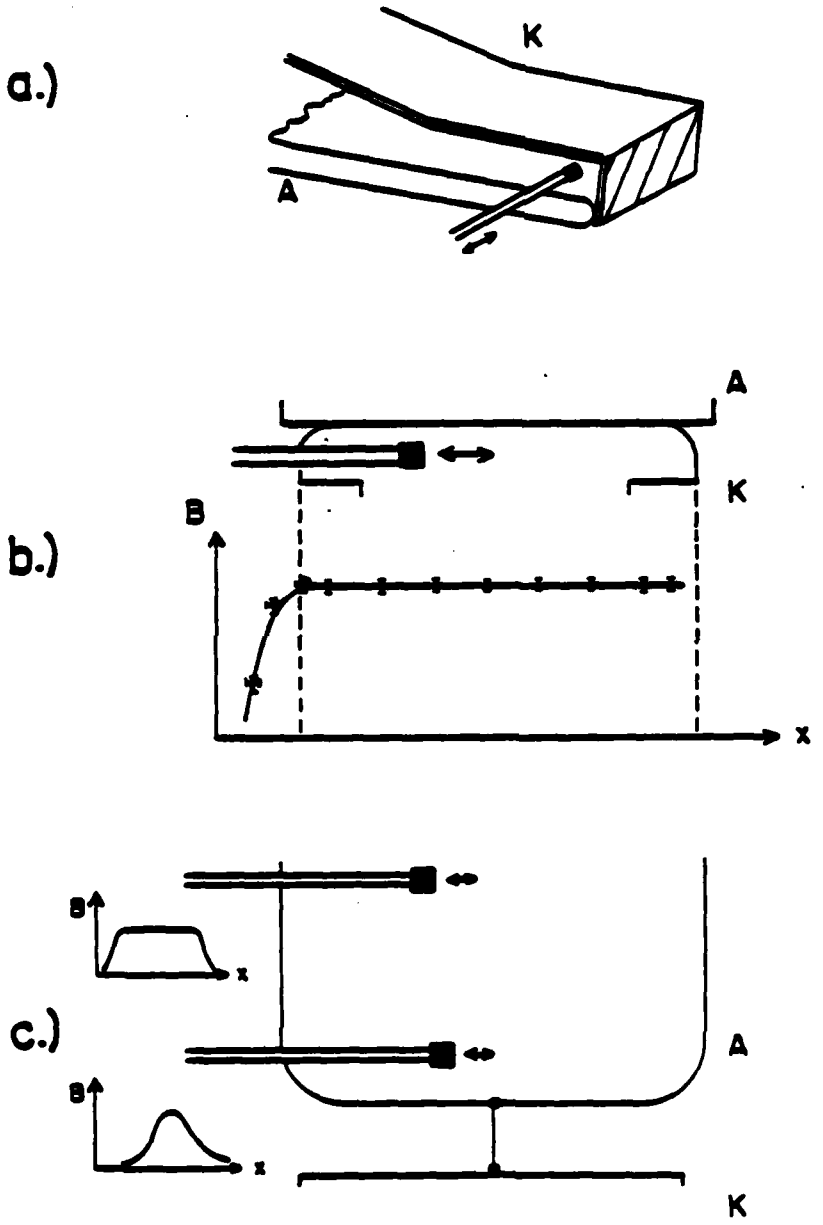

Fig. 3.12: Magnetic field mapping: (a) Arrangement; (b) current flow uniformity: (c) current flow downstream of perturbation.

Chapter 4

Uniformity

4.1. Introduction

The results from two uniformity diagnostics are discussed in this chapter. While these diagnostics are not particularly quantitative, they both provide a 'quick and dirty' uniformity measurement which permitted a variety of cathodes to be examined. A single frame framing camera was used to observe the plasma luminosity, and a dosimetric technique was used to obtain information on both the electron trajectories and on the electron source brightness uniformity. These diagnostics are complimentary in that the former measures plasma uniformity while the latter measures electron beam uniformity. It will be shown that the results from each are in agreement, indicating that electron beam nonuniformities are caused at least in part by plasma nonuniformities.

These two diagnostics are described, along with a review of previous related work, in Secs. 4.2 and 4.3. The effects of different cathode conditions are examined in Secs. 4.4–4.11, the time evolution of plasma luminosity is briefly examined in Sec. 4.12, and conclusions are given in Secs. 4.13 and 4.14.

4.2. Framing Photography

4.2.1. Diagnostic Description

The single shot framing camera system is shown in Fig. 4.1. This camera was nothing more than a gateable image intensifier (Varo model 5772[115]) coupled to a film back. Light from the cathode plasma was focussed onto the intensifier photocathode with an achromatic lens. While the tube had an extended red version of an S-20 photocathode which was sensitive to wavelengths from roughly 2000–8000 Å, the glass achromat blocked light below about 3000 Å and so this camera recorded primarily only visible light. The tube consisted of a photocathode, microchannel plate, and phosphor with a fiber optic output window to permit coupling to a film back.

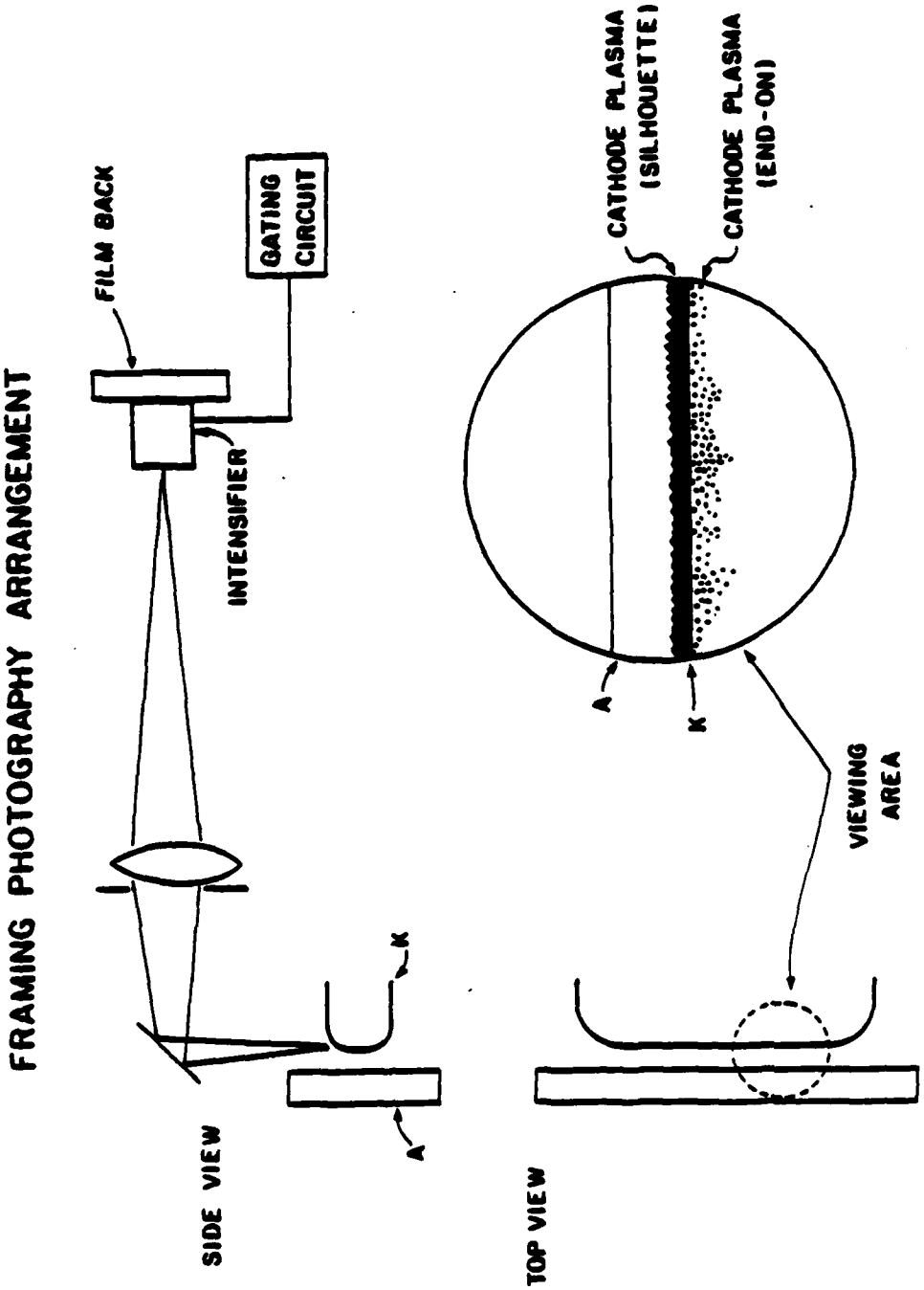

Fig. 4.1: Framing camera system.

The gating circuit is shown in Fig. 4.2. The tube had an internal power supply which furnished all necessary bias voltages except that between the photocathode and channel plate; the tube was turned on by applying −250 V across this gap. A DC reverse bias of +100 V was applied across this gap to turn back leakage electrons and to prevent electrical noise from turning on the tube. The gating pulse of −250 V was supplied by an avalanche transistor switched cable pulser (through blocking capacitors, as the channel plate floated at −850 V). The transistors were selected to avalanche at 220–230 V. The relatively short trigger delay of this circuit permitted it to be triggered from the diode voltage monitor (or current monitor for negative polarity shots), thus reducing the jitter in the timing of the camera relative to the shot to ~5 ns. This was important as the light intensity increased rapidly with time and even a slight difference in timing made a large difference in film exposure. In Fig. 4.3 the gating pulse and relative timing are shown.

While this tube had a stated gain of about 10^4, the gain in the pulsed mode was only about 100. The tube resolution was about 20 lp/mm and the focus was checked by backlighting the gap with a Xenon flashlamp synchronized with the gating pulse. Polaroid type 665 P/N film was used.

The field of view of this camera is shown in Fig. 4.1. Plasma formed on the front face of the cathode was observed in silhouette while plasma formed on the cathode upper edge was observed end-on. Since the electric field decreases at points further around the curve of the cathode edge (i.e., downward in the figure), the photograph from a single shot gives an idea of turn-on as a function of electric field.

4.2.2. Previous Work — Plasma Luminosity Imaging

Several fast electro-optical observations of cathode plasmas have been reported, but generally these involved streak photography, with the slit positioned across the gap to observe the motion of the electrode plasmas, and these are reviewed in Ch. 6. Few two dimensional observations of cathode plasma luminosity have been made.

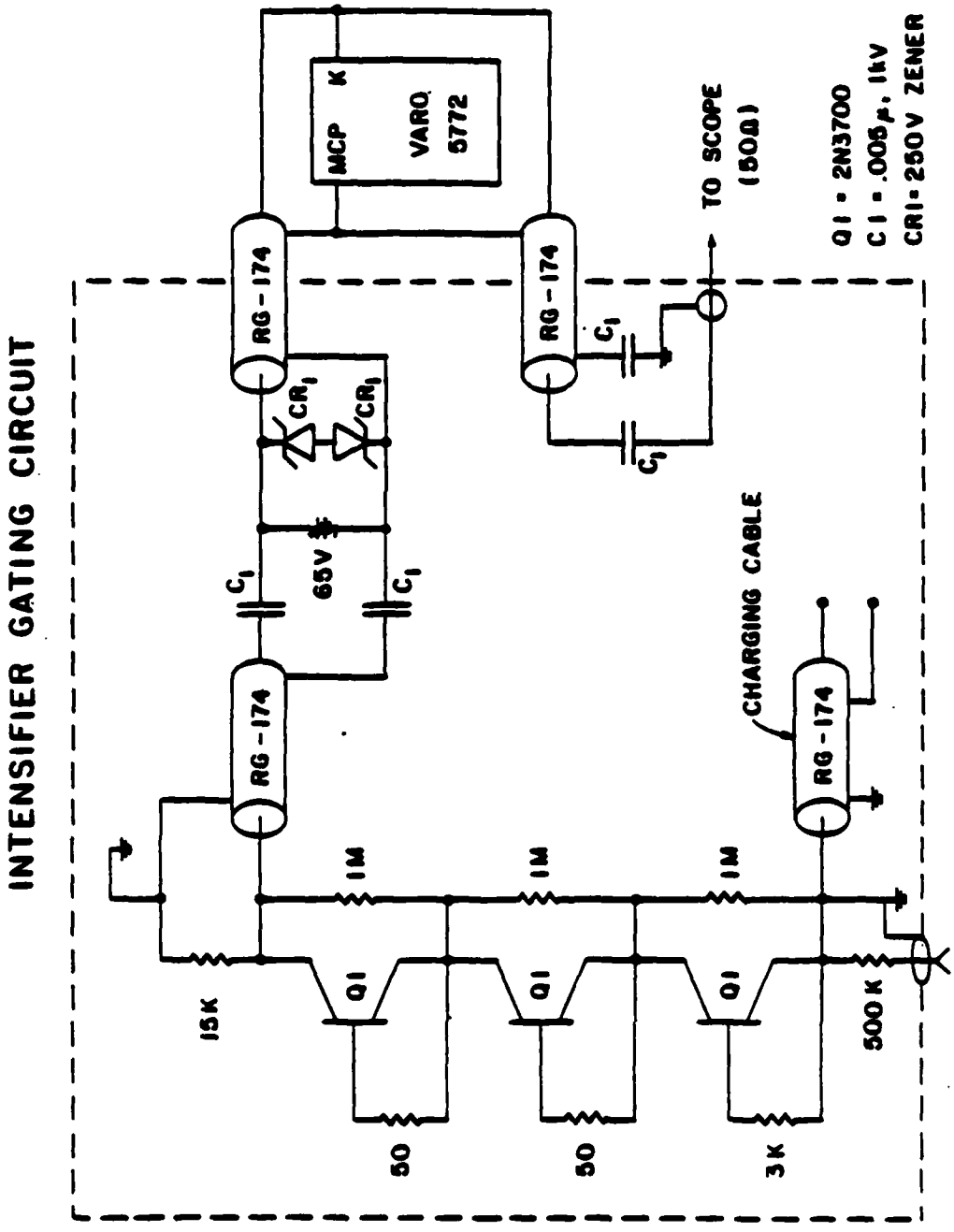

Fig. 4.2: Intensifier gating circuit. The cable was charged to −800 V which gave an output of ~−250 V.

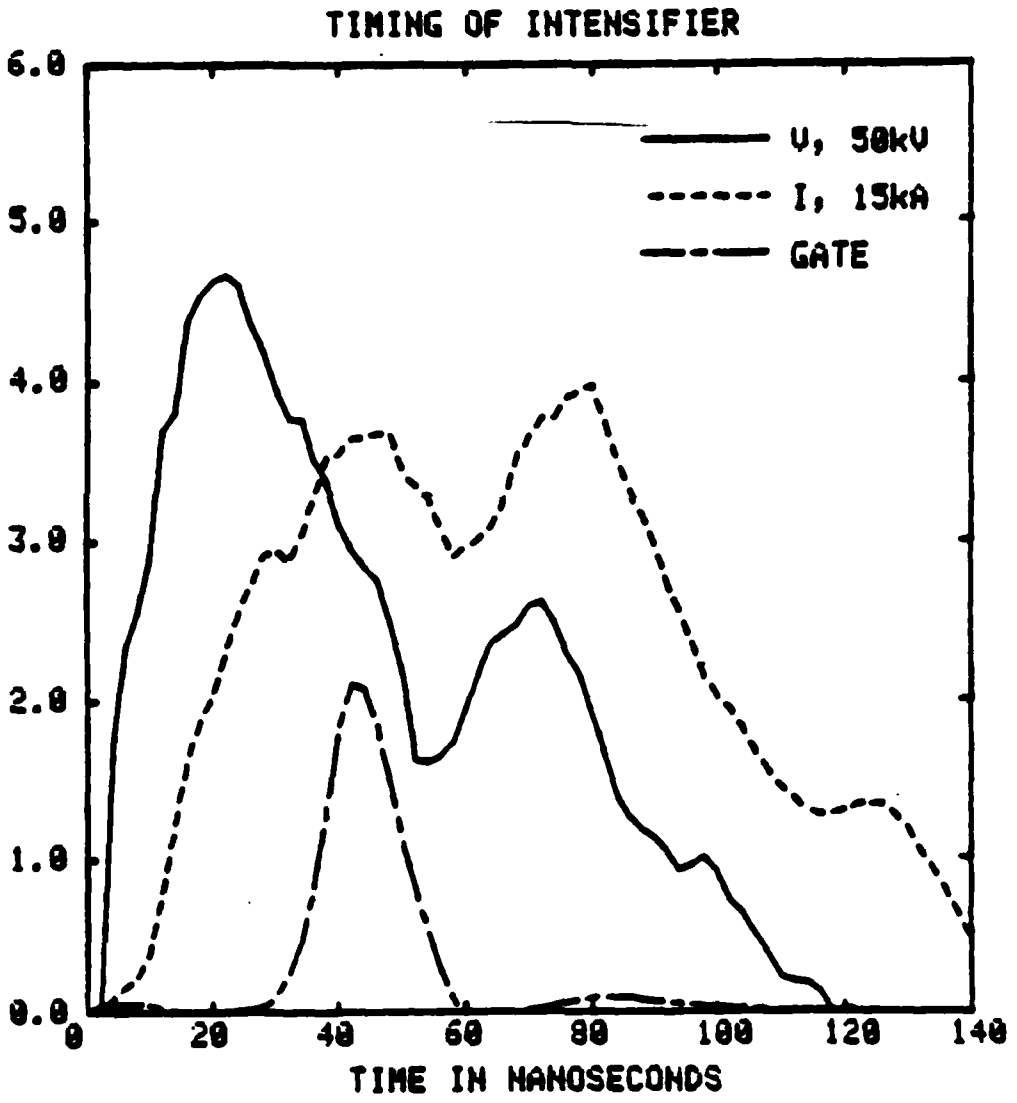

Fig. 4.3: Timing of intensifier gating pulse.

Bugaev *et al.*,[116] observed electrode plasmas in a diode consisting of 1 cm hemispherical electrodes separated by a 0.35 mm gap, with diode parameters of 35 kV, 230 kA, and 30 ns. Framing pictures (of a few ns duration) taken in the first few ns of the pulse showed isolated regions of luminosity, ~100 μm in size, on the cathode. In later frames, the luminosity expanded out into the gap. At the time of closure, the luminosity intensity was greatest in the middle of the gap.

Framing photography of a needle cathode is mentioned in Ref. 117; a spherical luminous region was observed at the cathode tip.

In other experiments, luminosity observations were made by the Tomsk group with open shutter photography, where time resolution was obtained by using diode pulse lengths of a few ns.[118,119,120] In these experiments, which involved cylindrical magnetically insulated diodes, discrete cathode flares were observed. Plasma was observed flowing from these flares in the $\vec{j} \times \vec{B}$ direction. In Ref. 120, a flare was produced, before the pulse, at a particular location on the diode circumference. Photography showed that plasma from this flare caused the formation of a chain of flares propagating around the circumference in the $\vec{j} \times \vec{B}$ direction, with an inferred velocity of propagation of about 2 cm/μs (cf Sec. 2.5.5).

4.2.3. Typical Data

The orientation of the framing photographs relative to the surface electric field is shown in Fig. 4.4. Typical framing pictures are shown in Fig. 4.5. To check the dynamic range of the system. half of the camera was covered with an ND 0.5 neutral density filter. This filter has a response which varied slightly with wavelength, ranging from about three to four times attenuation over the wavelengths involved. The framing picture so obtained is shown in Fig. 4.5 a. This difference in signal intensity can be seen to have a large effect on film exposure. which must be kept in mind when examining these pictures. The jitter in timing was only about 5 ns but since the total light output rose fairly rapidly this did cause variations in the exposure. The exposure also decreases toward the sides of the picture. presumably because of the properties of the optical system. Note that the luminosity appears less uniform where the exposure is less. For this reason

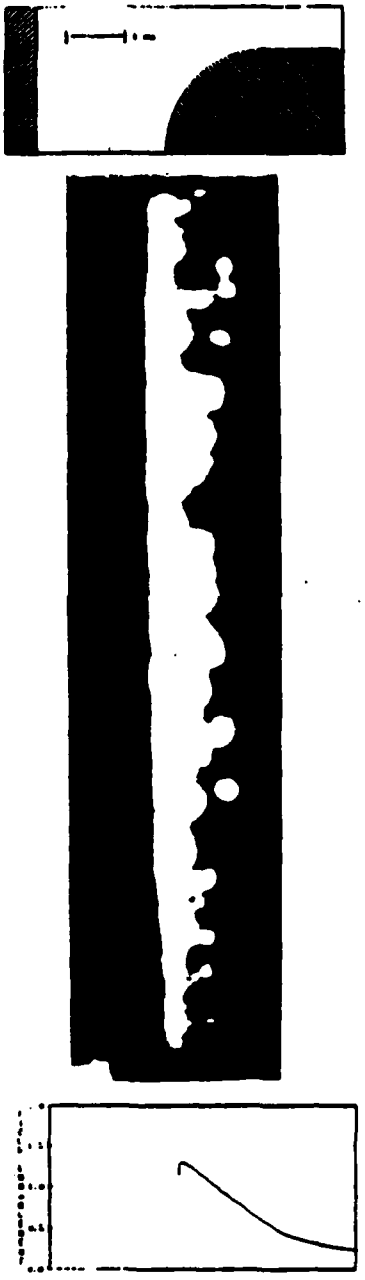

Fig. 4.4: Orientation of the framing pictures relative to the strength of the cathode surface electric field.

different pictures are compared by comparing areas which have roughly equivalent exposure.

On most of these pictures the location of the cathode front surface can be seen as a fairly distinct shadow, particularly off to the sides. The scale is noted in the figure and unless noted the gap was 2.2 mm. The downward direction in these pictures corresponds to the direction around the 1.6 mm cathode edge radius (see Figs. 4.1 and 4.4) and hence to lower electric field regions. Fig. 4.5 d is compared with the calculated surface electric field in Fig. 4.4. Spot formation is seen to be confined to regions where the electric field (in the absence of space charge) at peak voltage is >700 kV/cm. This seems high, and could be due to either shielding from the electronic space charge (discussed in Sec. 4.14) or the fact that spots formed at peak voltage have not grown bright enough to be visible at the time of the gating pulse (see Fig. 4.3).

Henceforth, the plasma on the cathode front surface (observed in silhouette) will be referred to as the front plasma while that on the edge (observed end-on) will be referred to as the edge plasma.

Figs. 4.5 b and c show examples of the observed extremes in luminosity uniformity. In Fig. 4.5 b the luminosity is relatively uniform. The edge plasma luminosity consists of very small spots. and the density of these spots decreases on the lower field strength regions of the cathode. In contrast, the picture in Fig. 4.5 c shows quite nonuniform luminosity. The front surface location can be clearly seen and above that line are silhouettes of discrete plasma flares. Very few edge plasma spots can be seen. The flares on top consist of bright centers with diffuse surrounding regions of (presumably) expanding plasma. The inferred plasma expansion appears roughly hemispherical. but assymetries are also present since plasma flares from several spots seem to be expanding preferentially to one side or the other. From the locations of the spot centers it appears that the spot density is highest right at the beginning of the cathode curvature where the field is highest. Faint luminous regions can be seen extending from the edge spots and the extensions of light seem to be preferentially in the direction of the anode. It should be noted that this corresponds to the direction of the $\vec{j} \times \vec{B}$ force.

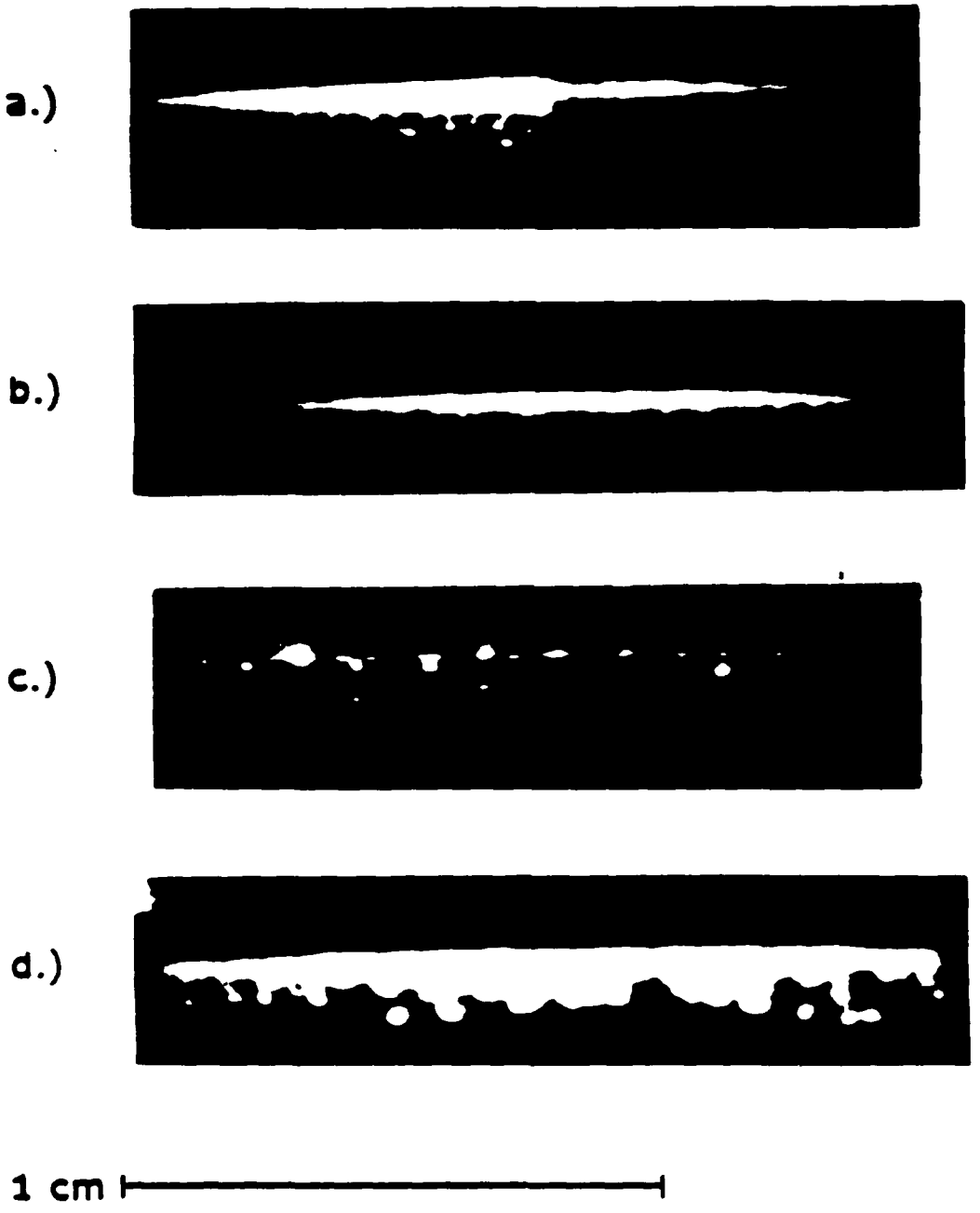

Fig. 4.5: Typical framing pictures: (a) the right half of the camera was covered with a ND 0.5 filter; (b) example of uniform luminosity; (c) example of nonuniform luminosity; (d) picture showing connected spots.

This picture is interesting because the spots are sufficiently isolated that they can be presumed relatively independent. In that case it is possible to observe the expansion from an individual flare.

Fig. 4.5 d shows a more typical picture with the uniformity being in between that of the two above cases. The structure of the edge spots is very interesting. Each spot has an area of luminosity extending out from it, in most cases in the forward direction. Sometimes, the direction changes. In particular, at the lower right, three spots are seen grouped in a 'dog leg' where the line of luminosity turns from parallel to the cathode edge to perpindicular to it (i.e., towards the anode). These spots clearly seem to be coupled.

This luminosity structure is reminiscent of the erosion patterns observed on dirty surface cathodes by Jüttner and coworkers,[87,98] where the erosion consisted of both small spots and branch-like structures. It is suggested that the luminosity and erosion structures are related: plasma expanding from a spot charges up and burns off surface impurities, preferentially in the $\vec{j} \times \vec{B}$ direction and preferentially along grain boundaries (because of higher impurity concentrations there). The propagation along grain boundaries explains the shifts in direction of the luminosity lines. At certain points where conditions are favorable, the plasma causes a new spot to form.

4.3. Dosimetry

4.3.1. Initial Observations

The electron beam uniformity was initially inferred from x-ray pinhole photographs and observation of the anode damage patterns. A pinhole photograph and photograph of the anode damage pattern are shown in Fig. 4.6. The 3 mm pinhole required by the low x-ray intensity severely limited the resolution of this diagnostic: the pinhole photographs only show that the beam is more or less uniform over a large scale length (the apparent fall-off of intensity at the edges is due to attenuation by the vacuum can). The anode damage patterns show a relatively sharp upper edge and a lower edge that consists of streaks projecting downward. The disadvantages to this measurement ware that the anode damage

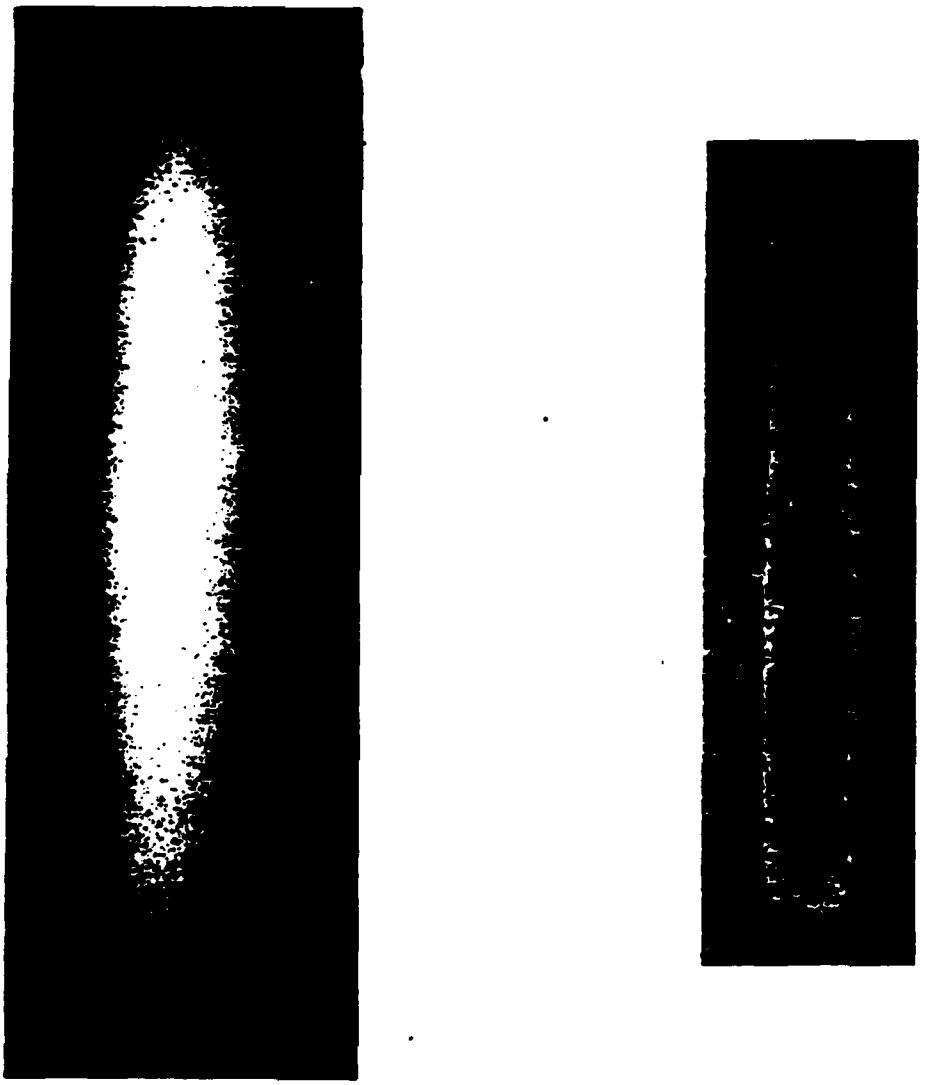

Fig. 4.6: (Top) X-ray pinhole photograph. (bottom) Photograph of the anode damage pattern.

is most sensitive to low energy, late time electrons. Because of these limitations. these diagnostics will not be discussed further, except to mention that the anode damage patterns are similar to those on the dosimetric films to be discussed next.

4.3.2. Diagnostic Description

A rather powerful dosimetric technique was used to diagnose the electron beam uniformity. A schematic of the arrangement, which was essentially the same as that used by Bradley,[121] is shown in Fig. 4.7. This diagnostic used as a recording medium 4-chlorostyrene,[122] a clear plastic which turns color upon energy deposition by electrons. It is insensitive to heat or x-rays but somewhat sensitive to soft UV and the linear dose range is about $1–10^4$ J/gm.

A 0.05 mm sheet was placed behind a 0.2 mm aluminum anode, and this sheet recorded the current density distribution at the anode plane of electrons with energies greater than about 250 kV. Several 0.4 mm diameter pinholes were drilled in the aluminum and styrene; electrons that passed through these were recorded on a second styrene sheet located 1.5 cm behind the anode plane and covered with a 0.15 mm aluminum sheet which stopped electrons having energies below 200 kV. The pattern on this styrene sheet consists of a spot (or spots) corresponding to each pinhole. The displacement of the spot(s) indicates the local electron bending angle, the area covered by the spot(s) indicates the electron beamlet divergance (emittance) and the uniformity of each pinhole image (i.e., whether it consists of one even spot or several separate spots) indicates the source uniformity.

The diode current was chopped for these shots (by operating in negative polarity with the insulator rings set for positive polarity) to reduce damage to the styrene.

Three effects which might complicate the interpretation of data from this diagnostic are the self magnetic and electric fields of the beamlet emerging from the pinhole. and electric field distortions caused by the pinhole edge. The latter was seen to be negligible by taking some shots where half of the front of the anode plate was covered by a sheet of 2 μm aluminized polycarbonate. No difference was observed between the pinhole images on the two halves.

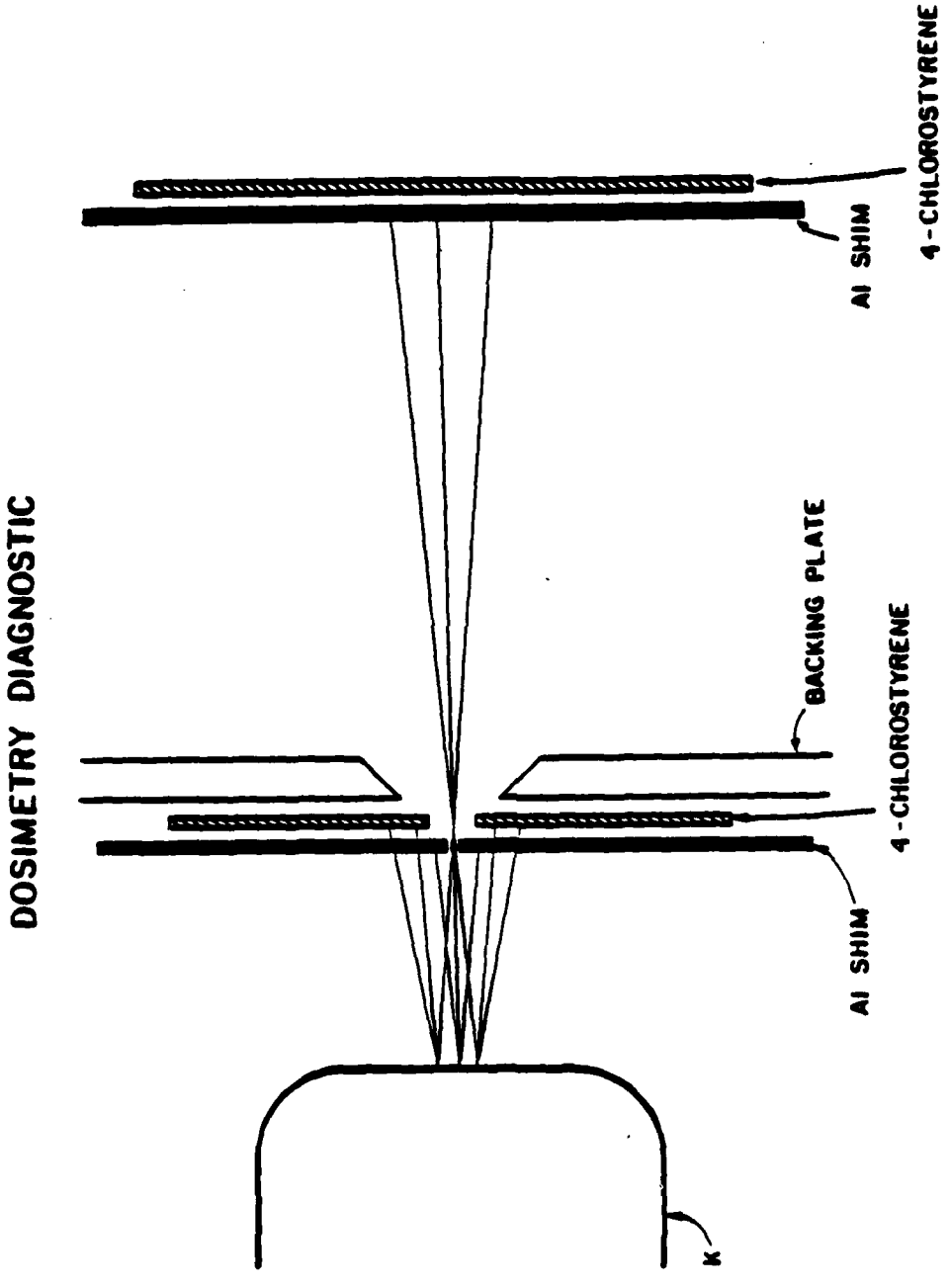

Fig. 4.7: Schematic of the dosimetry diagnostic. An aluminum shim anode was used on these shots.

Magnetic field effects can also be shown to be negligible. The field B (in kG) of a beamlet is given by

$$B = \frac{\pi j r}{5} \tag{4.1}$$

where j is the beamlet current density in kA/cm^2 and r is the beamlet radius in cm. The larmor radius r_l in cm is given by

$$r_l = 1.7 \frac{\sqrt{\gamma^2 - 1}}{B} \tag{4.2}$$

For j=10 kA/cm^2, V=250 kV, and r=0.2 mm, the Larmor radius is about 14 cm. As the beamlet spreads out, the field will decrease; once the beam has spread out to 0.8 mm in diameter, the field will have dropped by a factor of four, giving a Larmor radius of about 56 cm. The magnetic bending due to the beamlet self field during the 1.5 cm path length to the rear film is then roughly $1.5/r_l$, or about 2°, which is significantly less than the observed divergence angles.

The electric field effects are also calculated to be negligible; moreover, the conducting aluminum sheets at the pinhole and image planes will tend to short out the self radial electric field.

4.3.3. Previous Work

As far as the pinhole diagnostic goes, the only relevant paper is apparently Ref. 121, where a divergence angle of 3.5 degrees was quoted for a graphite cathode. Similar diagnostics have been used before, but in contexts unrelated to the present experiment.

The current density distribution at the anode plane (which is recorded on the first film in the present experiment) has been measured in previous experiments. Anode damage patterns from needle cathodes were investigated by Bazhenov, et al.[123] The diode consisted of two needles, 0.1-2 mm apart, with a (plane) anode-cathode gap of 0.2-1 mm. For inter-needle spacings of >0.8 mm, distinct damage spots were observed on the anode opposite each needle. For inter-needle spacings less than this, damage having the appearance of a 'brush stroke' was observed, in between the needles and perpindicular to the line joining them. This was attributed to the interaction between the beamlets from each needle.

Toepfer and Bradley observed similar striations in the anode damage (using 4-chlorostyrene film behind a thin anode) on shots with razor blade cathodes.[124] The spatial frequency of the striations depended on the edge geometry. Parker observed similar striations on shots with right circular cylinder cathodes if the edges were sharp enough ($\ll$1 mm).[43] These authors attributed the striations to a resistive tearing instability.[125] Similar conclusions were drawn in Ref. 126, although a thermal resistive instability[127] has also been suggested as the cause.

Milton[128] observed the exposure pattern on chlorostyrene film placed behind a thin anode, using a planar diode. The interesting feature of this experiment was the relatively low electric field (~200kV/cm) which resulted in incomplete turn-on of the cathode. The exposure pattern consisted of isolated circular spots. Analysis of these spots showed that the electron trajectories were roughly conical, with a (rather large) divergence angle of 75 degrees. When cathodes with epoxy filled holes were used, emission occured from the epoxy-metal boundaries.

4.3.4. Typical Data

Typical photographs of the exposed dosimetric films are shown in Fig. 4.8. Again, the two pairs shown depict roughly the extremes of observed uniformity. The upper photograph in each pair is of the film. henceforth refered to as the anode film, that was placed directly behind the anode and which measured the total current density profile at the anode plane. (The holes in the film were drilled beforehand and correspond to the locations of pinholes in the aluminum anode.)

There are several features to the anode films. The exposure has a relatively sharp boundary on the upper edge while it extends several mm below the cathode on the lower edge. The exposure has a cellular structure. Below the lower edge. the exposure consists of several 'brush strokes', spaced about 1 mm apart. Each brush stroke is seen to have a finer structure. being composed of several intertwined filaments. These brush strokes are similar to those observed in Ref. 123.

More anode films are shown in Fig. 4.9. The film in Fig. 4.9 a (from a shot with a 1.6 mm cathode) shows that brush strokes are also visible under the damage on the top edge. The film in Fig. 4.9 c shows that the strokes are continuations of the cellular structure (as if it 'unraveled'). Another interesting feature is seen

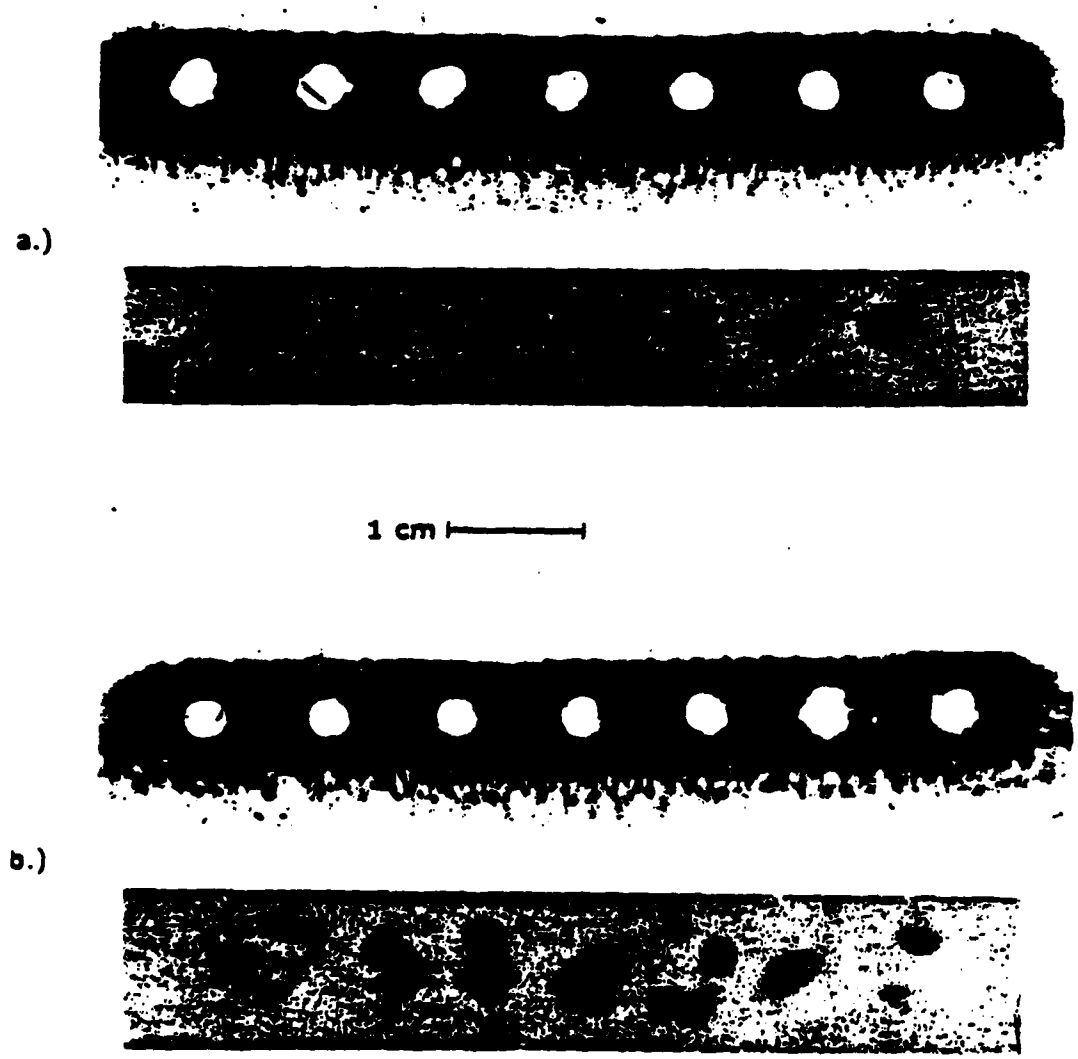

Fig. 4.8: Photographs of typical exposed dosimetric films. The top film in each pair is the anode film and the bottom is the target film. These are examples of (a) relatively uniform, and (b) relatively nonuniform exposure.

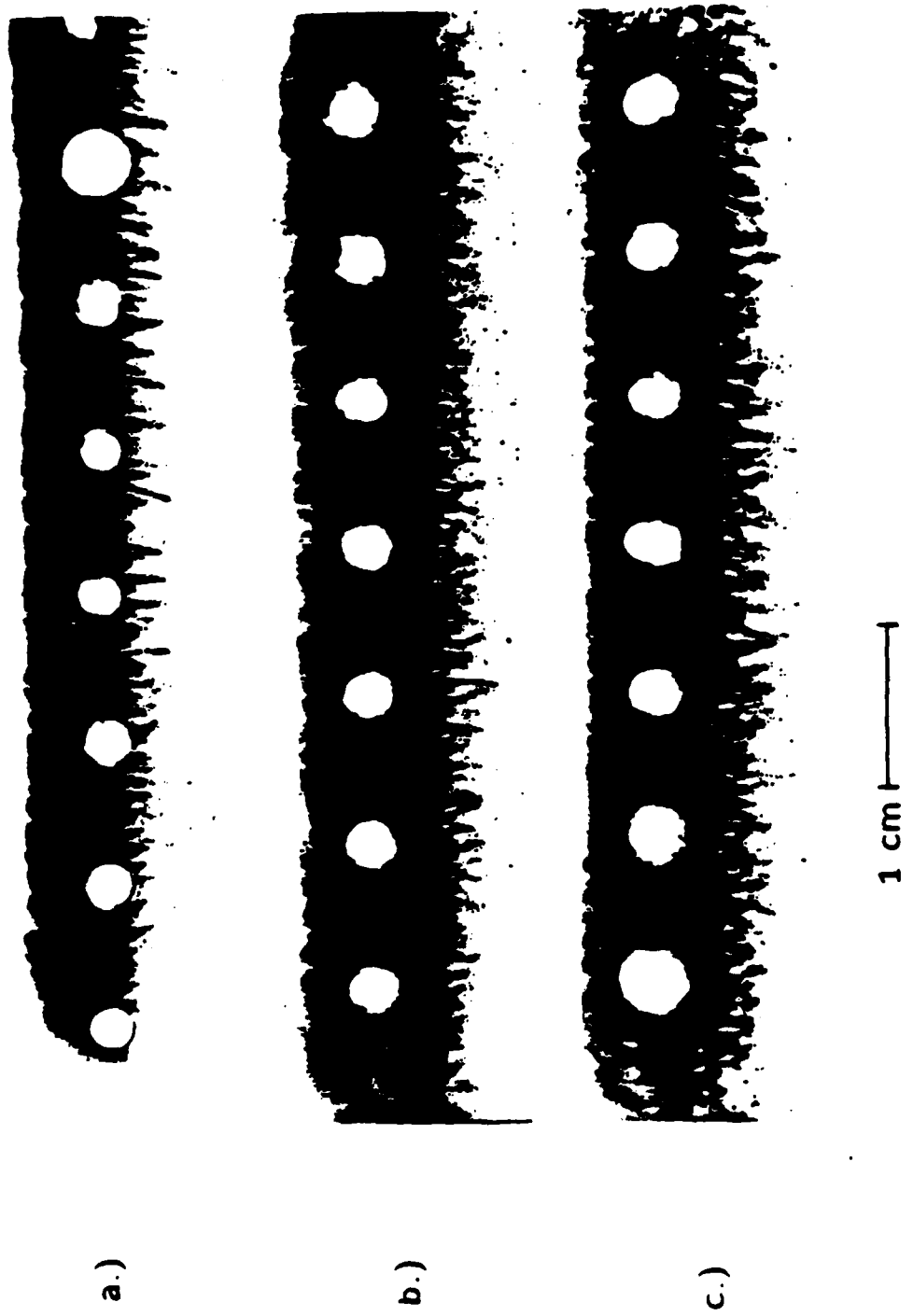

Fig. 4.9: Further photographs of anode films.

in Fig. 4.9 b, where a series of overlapping spots of relatively uniform exposure are seen at the top edge, similar to those reported in Ref. 128. These spots are about 2 mm in diameter and 1 mm apart.

The following explanation is proposed for the patterns on these films: the spots are exposure patterns from the initial emission sites (they presumably occur over the whole pattern but are obscured by later exposure everywhere but at the top). The spot diameters imply that the spread of electrons from the initial emission sites has a large included angle, similar to that observed in Ref. 128.

As time progresses, more sites are formed and the beamlets interact, forming the cellular patterns, as observed by Bostick.[129] It is believed that the patterns here are due to interaction of beamlets rather than a plasma instability since the edges on these diodes were not particularly sharp.

If the cellular pattern is due to interactions between beamlets, then the spacing should reflect the density of emission sites and be related to the luminosity uniformity. Indeed, this is the case. The cellular spacing is finer on the top anode film in Fig. 4.8 than on the bottom; this correlates with the fact that framing pictures for this case show the structure of luminous spots also to be on a finer scale. The spacing is about 200 μm, implying a site density of 10^3–10^4/cm^2 which is consistent with estimates of emission site density in Ref. 43. Because of the uncertainties in the interpretation of these films no more will be said about them other than to note that the fineness of cell spacing is always correlated with the uniformity of pinhole images on the films, henceforth referred to as target films, that were placed 1.5 cm behind the anode plane.

These target films are shown in the lower of each pair of photographs in the figure. The locations of pinhole images are not exactly matched to the pinhole locations, implying that there was some magnetic bending of the beamlets in the diode. The beamlets are seen to be bent inwards and down, as would be expected from the magnetic field structure in the diode. The bending angles are about 10–15°. Local electron beam divergence (emittance) is indicated by the area of each pinhole image. Some of the spots are elongated with longer dimensions along the direction of magnetic bending and this elongation is presumably caused by a

movement of the image with time; for this reason the spot dimensions transverse to the bending direction are considered the relevent dimensions for measuring divergence. The pinhole images on the upper film are relatively uniform and are about 2 mm or less in diameter. This implies a divergence half angle of about 4 degrees, similar to the value of 3.5 degrees quoted in Ref. 121.

The current density at the anode plane was about 10 kA/cm^2; with 0.4 mm pinholes and a spot size of 2 mm, the current density on the film was about 100 A/cm^2; with a typical rate of energy deposition of 5 MeV-cm^2/gm,[130] this implies a deposition in the film of 40 J/gm, which is within the 4-chlorostyrene linear range. The deposition in the anode film was about 1 kJ/gm, also within the linear range.

The target film for the bottom pair shows a striking difference in exposure uniformity. To begin with, the area over which each pinhole image is spread is larger, implying a divergence half angle of about 10 degrees. More important, each pinhole image is not solid but consists of several discrete spots. This implies that either the electron beam source brightness is highly nonuniform, with some areas not emitting at all, or that the local bending angle varies greatly, as if the magnetic field structure is chaotic.

Since chopping the current caused most of the energy to be reflected back to the Marx, a limited number of shots were taken with this diagnostic. In general, 2-4 shots were taken with each cathode condition.

4.3.5. Electron Flow

It was originally planned to use the Herrmannsfeldt code to predict the electron trajectories. However, the current density in these experiments was greater than the code was designed to handle, and the code failed to converge. A typical output is shown in Fig. 4.10. Note that because of the magnetic field assymetry (which was irrelevant as far as potential plotting is concerned), it was necessary to model the entire diode cross section. It is interesting to note that even though the code results did not converge quantitatively, the general qualitative nature of the current flow remained unchanged over the iterations of the program, and correctly reproduced the observed damage patterns: the confined flow at the top edge, with

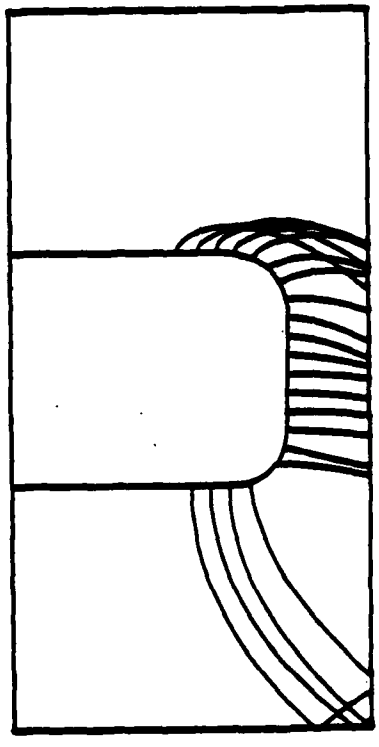

Fig. 4.10: Hermannsfeldt code output for a 6.4 mm cathode and 2.2 mm gap.

the upper limit of anode damage being opposite the cathode upper edge, and the diverging flow at the bottom edge with anode damage extending well below the cathode lower edge. Also, the degree of bending predicted by the code was similar to that inferred from the target films.

4.4. Effect of Prepulse

It is stated in Ch. 6 that the effect of prepulse can be neglected; that is supported here by framing pictures taken on shots with and without prepulse. As for those mentioned in Ch. 6, these shots involved Aerodag coated 1.6 mm cathodes, which had the highest prepulse electric fields (~70 kV/cm for several hundered ns). No difference is seen in framing pictures between the two cases, as shown in Fig. 4.11 (the difference between the two pictures in Fig. 4.11 is less than the shot-to-shot variation).

4.5. Dependence on Cathode Surface Preparation

In large machines, design considerations often mandate that the cathode(s) be made of aluminum because of its low weight and good machineability. In particular, this is the case for the Sandia PBFA-II accelerator mentioned in Ch. 1. Because of this a variety of surface preparations were examined for aluminum cathodes. Particular attention was given to the effect of an Aerodag coating. Such a coating has long been assumed to be beneficial, but its use on extended area cathodes causes a problem due to outgassing. In addition there is the need to periodically recoat the surface which can be an expensive and time consuming procedure requiring extensive disassembly.

Framing pictures of cathodes with different surface preparations are shown in Fig. 4.12. The effect of surface roughness is examined in the first two pictures — the cathode in Fig. 4.12 a was sandblasted, while that in Fig. 4.12 b was smoothed on an abrasive wheel to a relatively shiny finish. The uniformity is clearly enhanced when the cathode was sandblasted — in the smooth case the luminosity boundary facing the anode is less even and there are fewer edge spots.

Similar pictures of sandblasted and smooth Aerodag cathodes are shown in Figs. 4.12 c and d. It should be pointed out that there are shot-to-shot variations

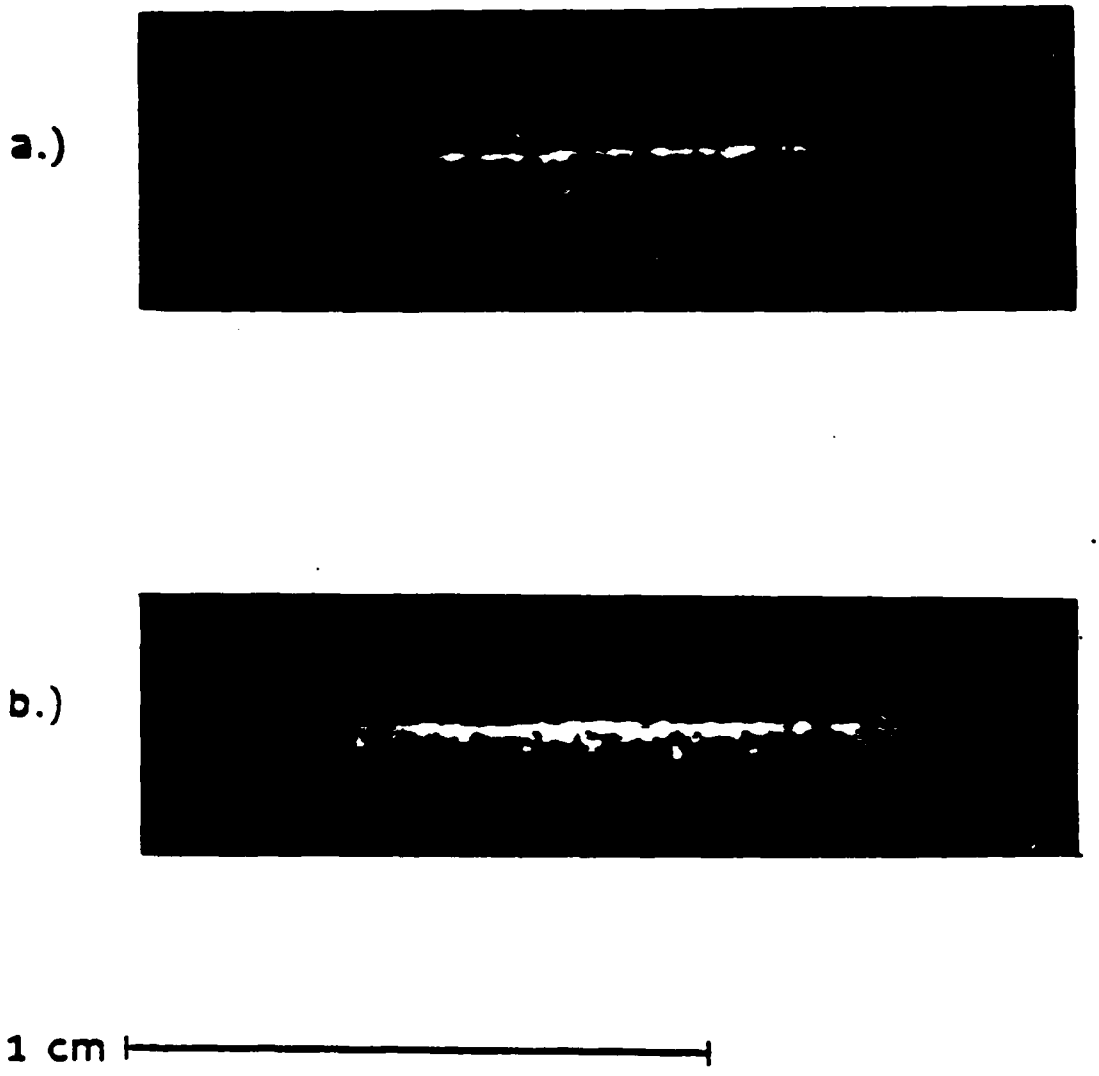

Fig. 4.11: Framing pictures taken on shots (a) with and (b) without prepulse.

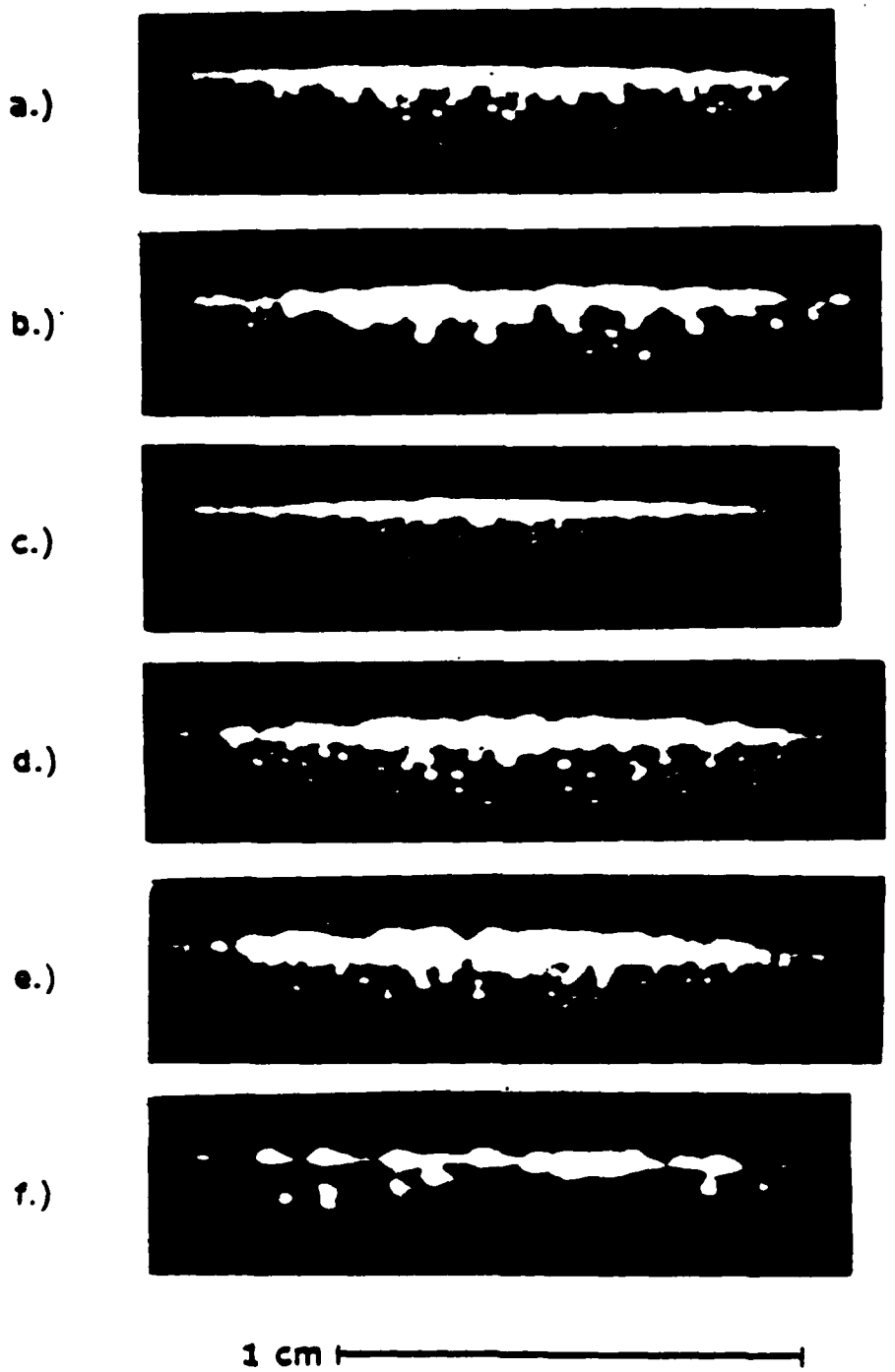

Fig. 4.12: The effects of surface preparation: (a) sandblasted; (b) smooth: (c) Aerodagged blasted; (d) Aerodagged smooth; (e) polished Aerodag; (f) oiled smooth.

in framing pictures taken with similar cathodes. In general, the beneficial effect of sandblasting is also observed with Aerodagged cathodes but the difference is on the average less striking than with aluminum cathodes.

Aerodagging is seen to have a decidedly beneficial effect when smooth cathodes are used. When sandblasted cathodes are used, however, the effect is less, being almost lost in the 'noise' of shot-to-shot variation.

Fig. 4.12 e is a picture of a smooth Aerodagged cathode. Now, normally the Aerodag was applied in three light coats with no subsequent preparation. In this case the Aerodag was polished with a cloth to a shiny finish. The uniformity is seen to be worse than that of the unpolished Aerodagged smooth cathode in the picture above it.

Finally, the cathode in Fig. 4.12 e had a smooth surface and was coated with a thin layer of silicone pump oil (DC 704). In this case a small drop of oil was applied and then rubbed off with a clean cloth; the resulting surface had a glossy appearance but did not have any visible 'puddles' of oil. The uniformity is severely degraded in this case, which is not too surprising since oil is often used to suppress emission. The effects of coating sandblasted surfaces with both silicone and hydrocarbon oil were also examined. Here the uniformity degradation was slight, if at all, and perhaps this is because the roughened edges poked through the oil.

The tree-like luminosity structure can also be observed in these pictures. In particular, in Fig. 4.12 d there are several 'dog legs' connected by fine strands ($\sim$100 μm wide) of luminosity.

Target films for different surface preparations are shown in Fig. 4.13. Again, Figs. 4.13 a. b. c. and d correspond to sandblasted and smooth aluminum. and sandblasted and smooth Aerodag cathodes. respectively. Here the improvement in uniformity when (bare) aluminum cathodes are sandblasted is even more apparent than in the framing pictures — several of the pinhole images for the smooth case consist of many spots spread out all over the place. With Aerodagged cathodes, again the effect of sandblasting is less pronounced. Only two shots were taken

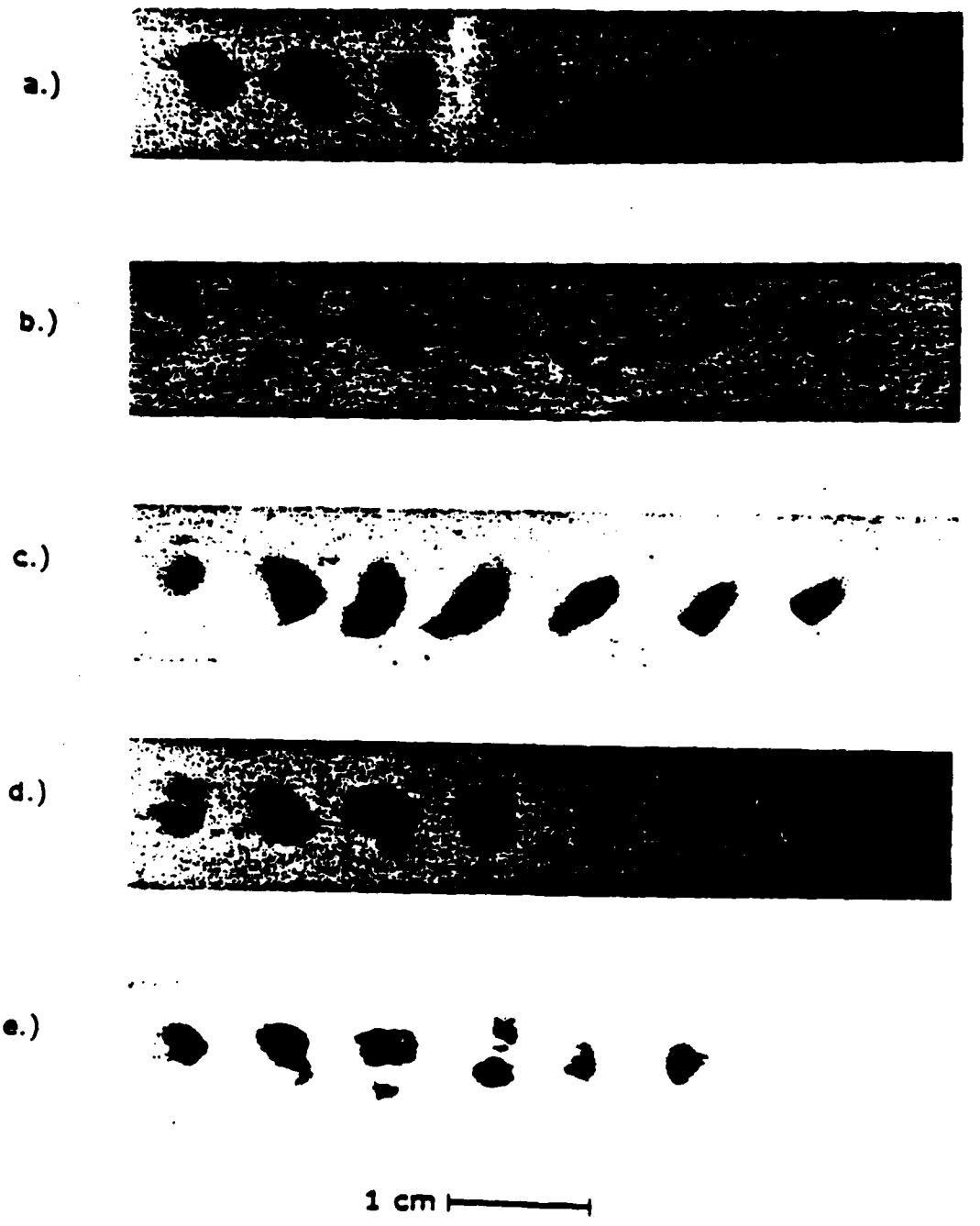

Fig. 4.13: Target films for different surface preparations: (a) sandblasted: (b) smooth: (c) Aerodagged sandblasted: (d) Aerodagged smooth; (e) bead blasted.

with sandblasted Aerodagged cathodes and the target film exposure uniformity was about the same as when sandblasted aluminum cathodes were used.

It has been suggested[131] that glass bead blasting produces a 'better' surface and so two shots were taken with cathodes that had been glass bead blasted. In this case the surface appeared less shiny than with the usual sandblasting, having almost a matte finish. A target film is shown in Fig. 4.13 e and as can be seen the uniformity is worse than that with the sandblasted cathodes.

4.6. Effect of Conditioning

Since a serious drawback to Aerodagged surfaces is the need to recoat them, it is desirable to determine whether a sandblasted aluminum surface will hold up or whether it will become smooth with repeated shots and need to be re-blasted. In general, the effect of conditioning could not be examined in this experiment as blow-back of anode material after the shot covered the cathode and dominated any effects due to electron emission. For a few shots, however, decreased resistivity in the PFL resulted in a roughly 20% reduction in the diode current and voltage. This 40% reduction in energy virtually eliminated damage to the anode and resulted in cathodes that appeared unaffected after the shot. On the assumption that post-pulse anode effects were negligible, seven shots with the same cathode were taken in series. Framing pictures for this case are shown in Fig. 4.14. In this case the integrated charge transfer was about 1 mC/cm^2 per shot. While there are shot to shot variations, caused partly by variations in the current (the generally low current can explain why these look fainter than those with the blasted aluminum cathode in Fig. 4.6), there is no observable steady degradation in uniformity. If anything, the later pictures look better than the first. So it can be concluded that a total charge transfer of 6 $mC\ cm^2$ does not blunt or otherwise render ineffective a sandblasted surface. This is not surprising since explosive emission pulses longer than a few ns are known to roughen a surface, as discussed in Ch. 2. Also, the roughness due to sandblasting is on a much larger scale than the micron scale associated with melting of metallic protrusions.

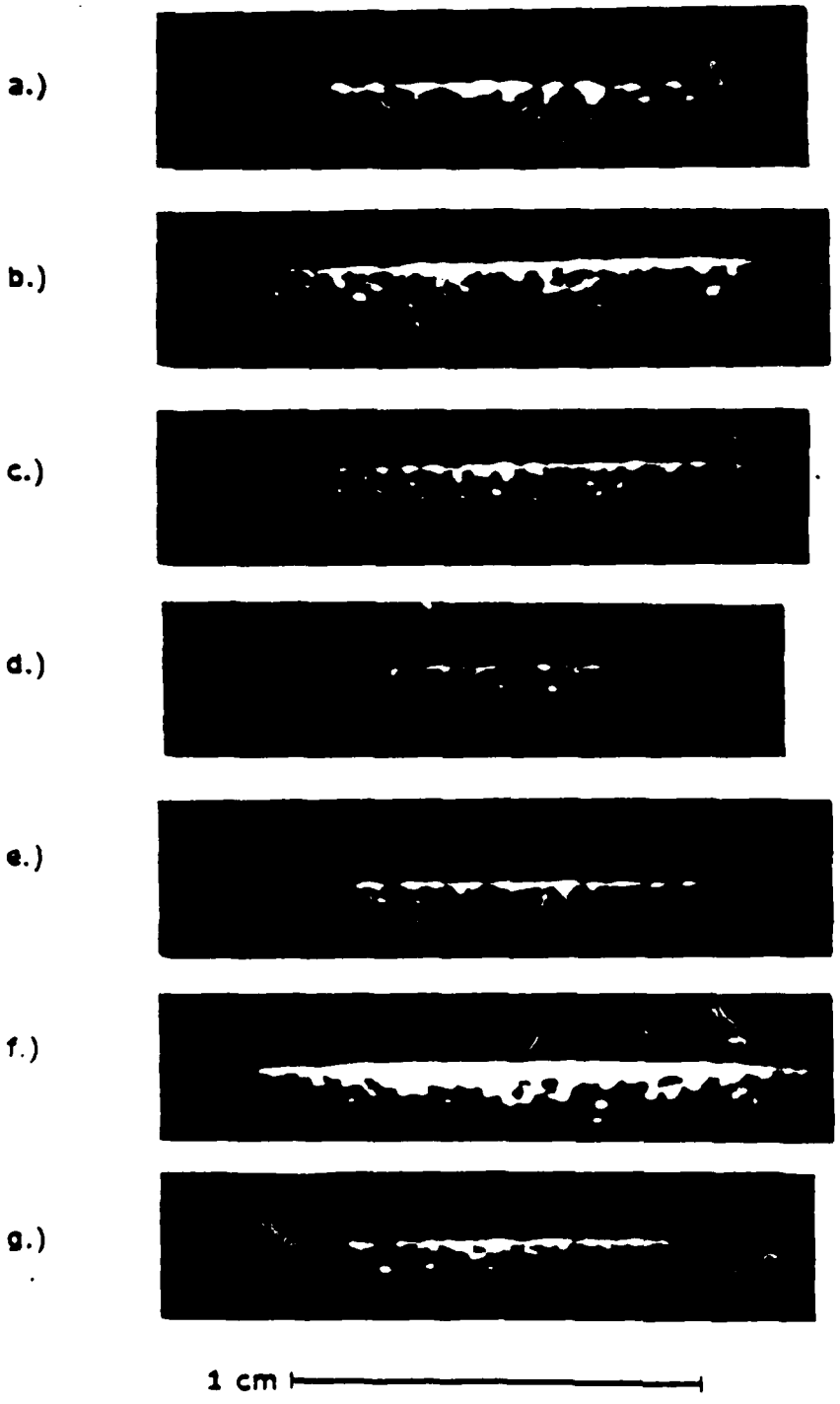

Fig. 4.14: Framing pictures taken on successive shots with the same cathode.

AD-A147 917 PLASMA STUDIES IN ION DIODES(U) MASSACHUSETTS INST OF TECH CAMBRIDGE RESEARCH LAB OF ELECTRONICS G BEKEFI SEP 84 N00014-83-K-2024 2/4

UNCLASSIFIED F/G 20/9 NL

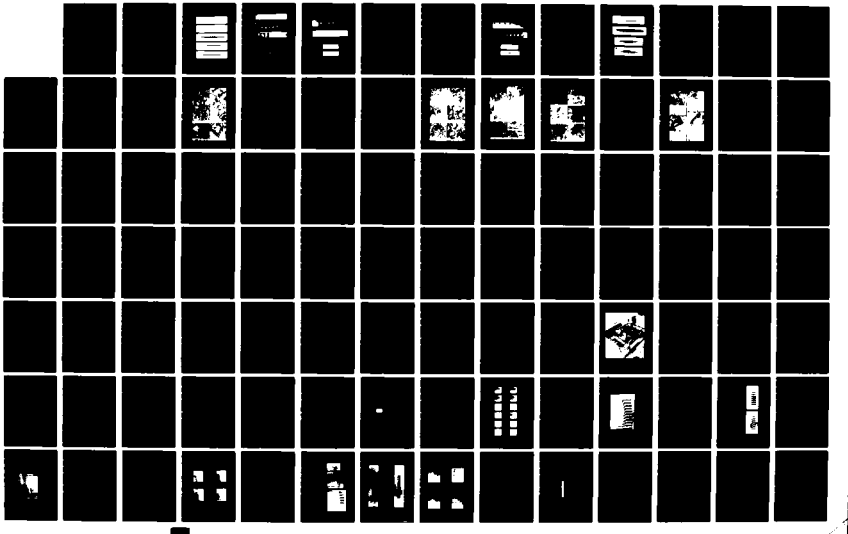

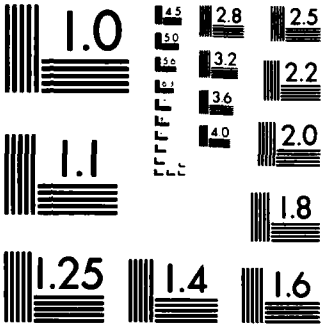

4.7. Effect of Different Materials

Framing pictures of cathodes of different materials are shown in Fig. 4.15. Poco graphite (Fig. 4.15 a) is definitely associated with the most uniform luminosity. Reactor grade graphite (Fig. 4.15 b), which is cheaper than the higher quality Poco, is seen to have almost as much luminosity uniformity as Poco graphite. Figs. 4.15 c, d, and e are of aluminum, brass, and stainless cathodes, respectively. In general, any differences in luminosity uniformity between different metals are only slightly, if at all, greater than shot-to-shot variations for a single metal. It appears that brass produces slightly higher uniformity than aluminum while stainless cathodes have slightly less luminosity uniformity.

Target films for different materials are shown in Fig. 4.16. As with the framing pictures, the graphite cathodes produces the most uniform exposure. With dosimetry, brass appears superior to aluminum with stainless slightly worse.

4.8. Effect of Electric Field Rise Time

The one factor that has the greatest effect on uniformity is the electric field rate of rise dE/dt, as shown in Fig. 4.17. This rate of rise was varied by punching the PFL output switches off center as described in Ch. 3. Poco graphite cathodes were used for the shots in the figure, although similar results were observed when aluminum cathodes were used. Framing pictures for values of dE/dt that differ by a factor of four are shown in Figs. 4.17 c and d. Voltage and current traces, along with the intensifier gating pulses, for the reduced dE/dt shots are shown in Fig. 4.18. The value of dE/dt prior to turn-on was 2×10^{14} V cm·sec on normal shots and 5×10^{13} V cm·sec for for the reduced dE/dt shots. The value of dE/dt decreased by about a factor of three after the initial turn on in both cases.

Target films are shown in Fig. 4.10 a and b. In this case there was a limit on how slow the field could rise because the diode voltage had to be high enough for electrons to penetrate the aluminum that covered the target film, so that the slow field rise in Fig. 4.18 b was only a factor of two less, that is, 1×10^{14} V cm·sec. Even the 'best' emitter, Poco graphite, has seriously degraded uniformity when the field rise time is slowed.

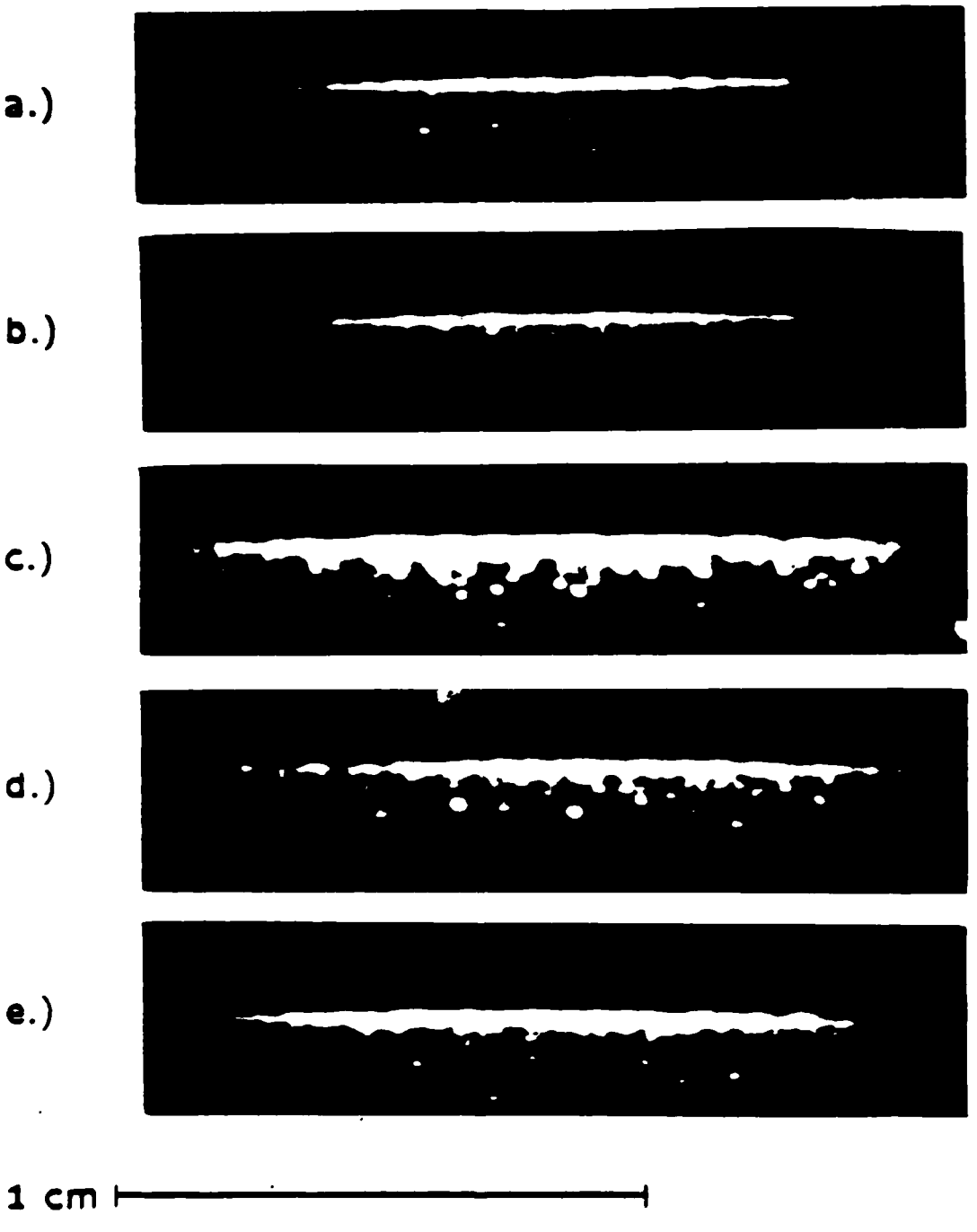

Fig. 4.15: Framing pictures for different materials: (a) Poco graphite: (b) reactor graphite: (c) aluminum (type 2024); (d) brass: (e) stainless steel (type 304).

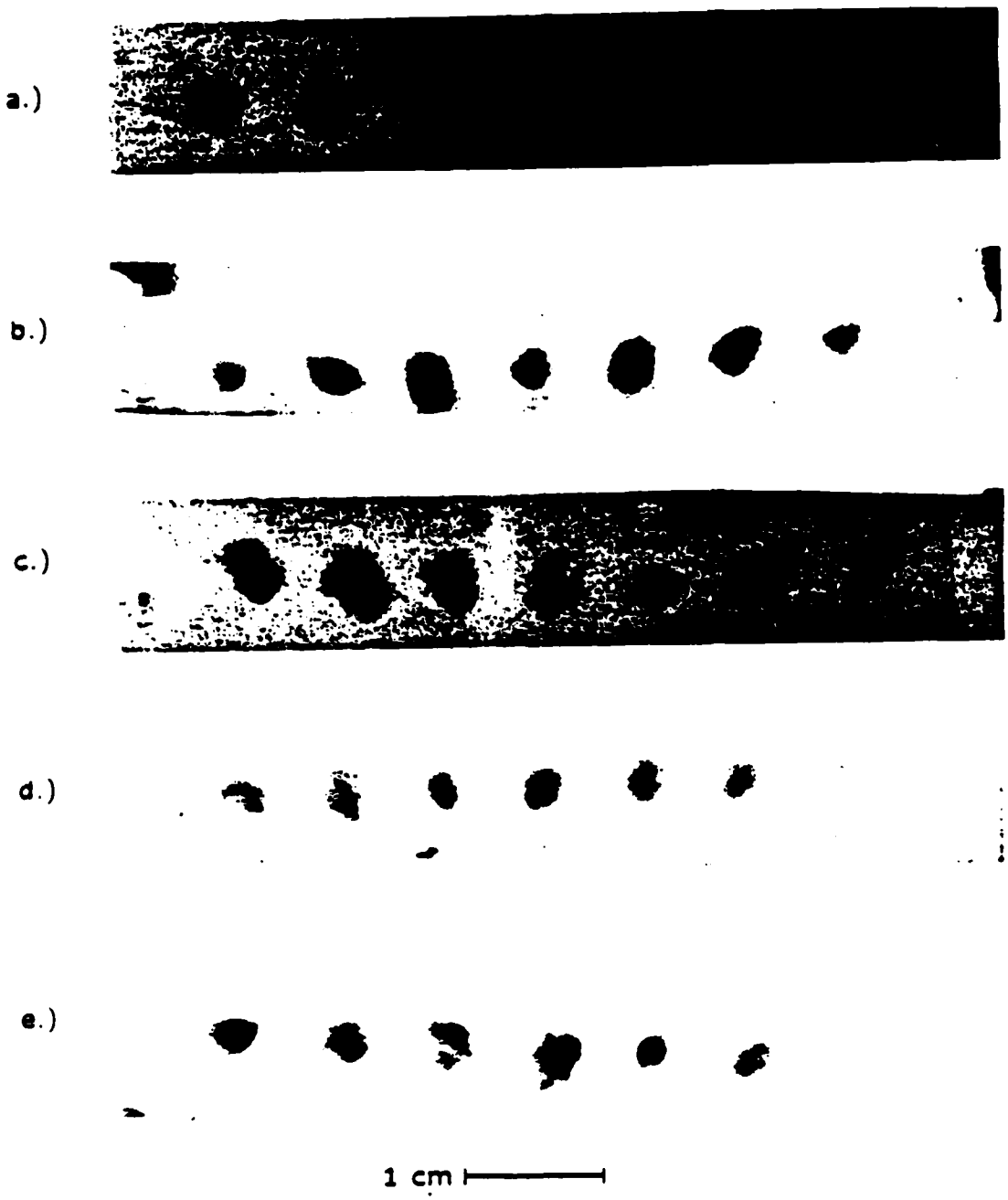

Fig. 4.16: *Target films for different materials:* (a) Poco graphite: (b) reactor graphite: (c) aluminum: (d) brass: (e) stainless steel.

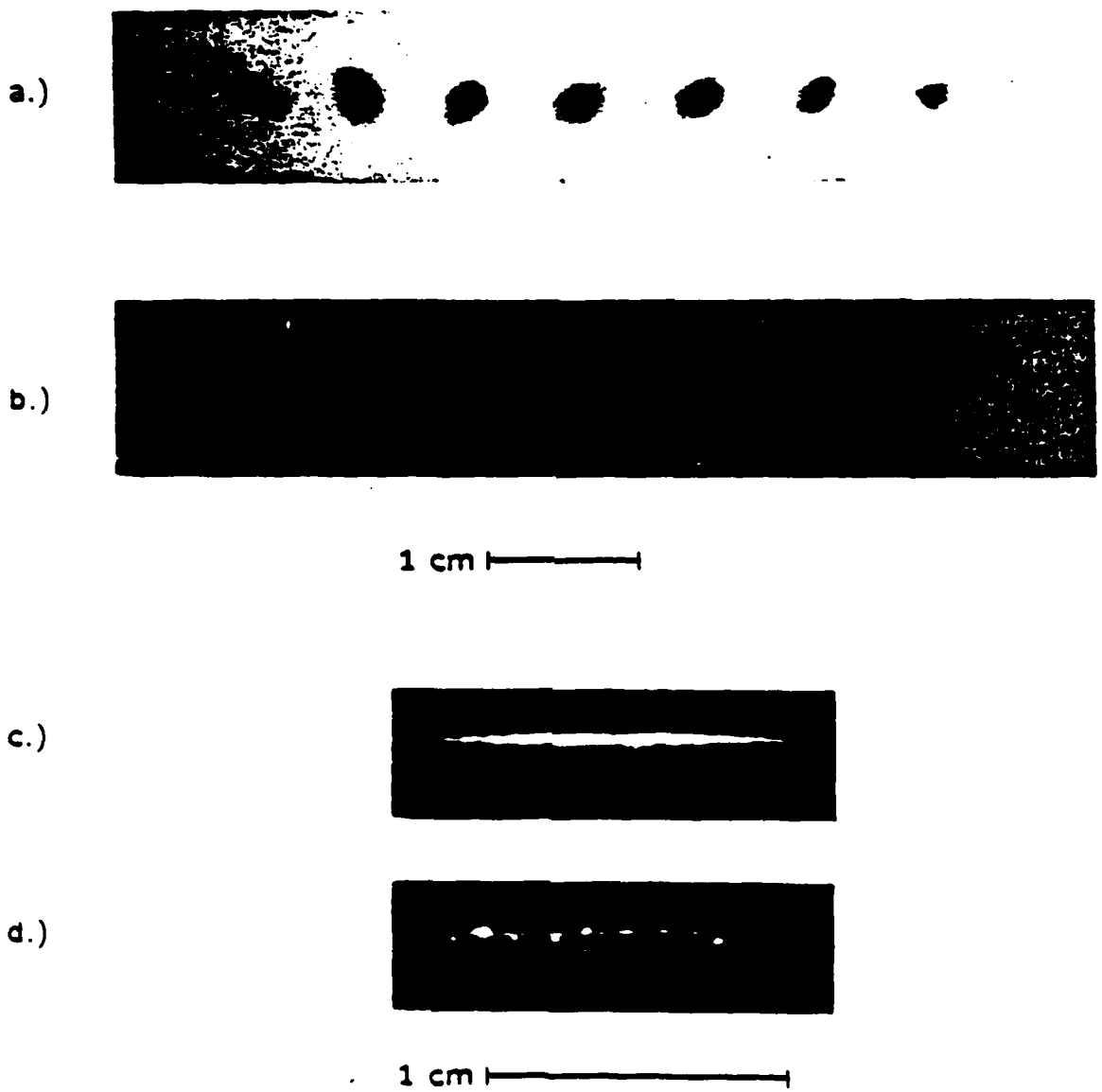

Fig. 4.17: The effect of dE/dt on uniformity with Poco cathodes. dE/dt was 2×10^{14} V cm·sec (prior to turn-on) in (a) and (c). 1×10^{14} V cm·sec in (b), and 5×10^{13} V cm·sec in (d).

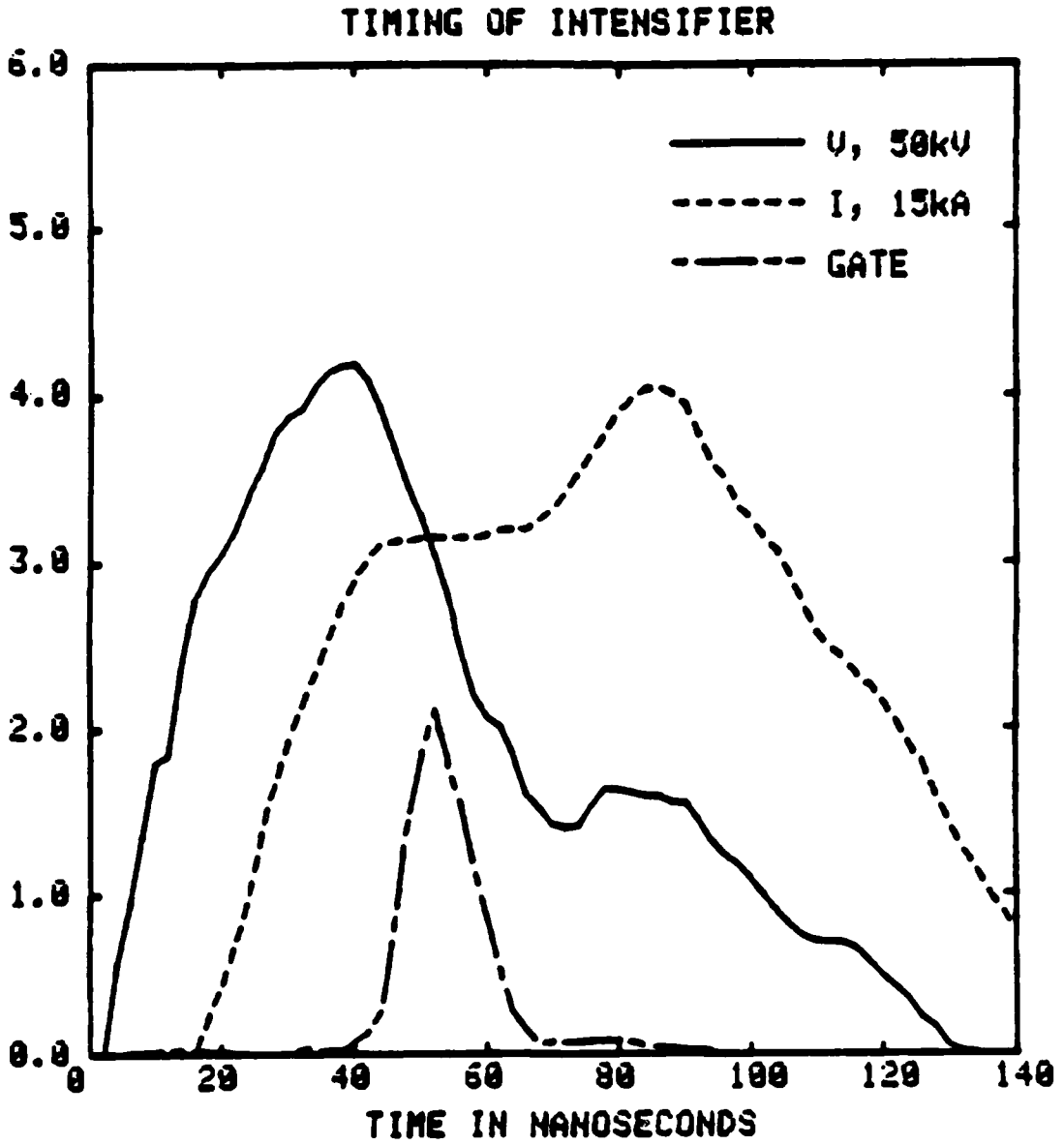

Fig. 4.18: Electrical characteristics and gating pulse for the reduced $dE\ dt$ shots.

It could be argued that this degradation in uniformity is only due to the plasma formation time being longer for the lower dE/dt and that with time these cathodes would show uniform luminosity. However, framing pictures taken 20 ns later show that the nonuniform nature of the luminosity persisted.

4.9. Epoxy-Metal Coatings

A few shots were taken with cathodes that were coated with a mixture of copper dust and liquid epoxy. It was hoped that either the field enhancement due to all of the dielectric metal junctions or enhanced breakdown of epoxy caused by ionic charging under the plasma cloud would improve uniformity. It should be stressed that little attempt was made to investigate or optimize the coating technique and the coating was often somewhat uneven, causing variations in the gap. It should also be pointed out that this epoxy-metal coating was a distributed mixture, that is, different than previous epoxy metal cathodes that consisted of epoxy filled grooves in metal. Plasma formation on the earlier cathodes was dominated by flashover of the epoxy. In the present case, the small size of each epoxied area (tens of microns or so versus mm) prevented flashover as such. Also, the coating looked like a conductor to an ohmmeter. Target films and framing pictures are shown in Fig. 4.19. In Figs. 4.19 a and d, the cathode was simply coated with the mixture, while in Figs. 4.19 b, c, and e a light coating of copper dust was sprinkled on afterwards (the coating was only partial; epoxy was still visible underneath). Clearly, in the first case uniformity is degraded. However, in the latter case the uniformity is about as good as sandblasted aluminum, and perhaps it would be possible to improve the coating to where it was superior to aluminum. Of course, such a coating would cause even more outgassing problems than Aerodag.

4.10. Effect of Current Density

It is important to determine the scaling of uniformity with current density. However, it is not possible in the present experiment to differentiate between effects due to variations in curent density and those due to the corresponding variations in the electric field. In this experiment very little difference was noted

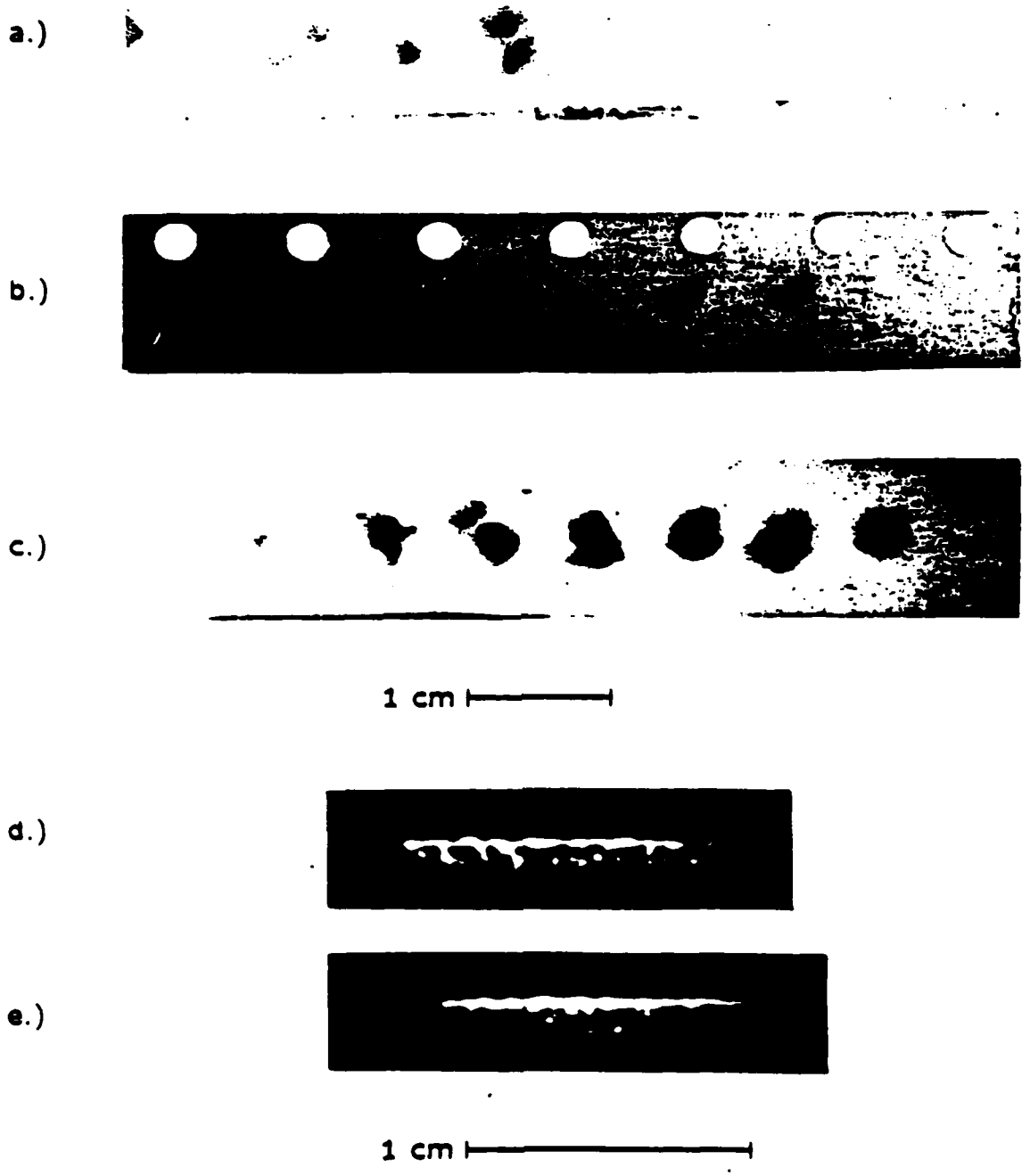

Fig. 4.19: The effect of a copper-epoxy coating.

between the three current densities used (8, 13, and 39 kA/cm^2, peak), with perhaps slightly greater uniformity at the higher current densities. In this case the peak electric fields varied as (0.8:1:1.5). At first this would seem to contradict the aforementioned strong effect of dE/dt. Now, the lowest dE/dt in this case was about 85% of the dE/dt for the 'good' case previously mentioned, and so one reason for the seeming independence of uniformity on electric field in this case might be that there is a threshold dE/dt, below which uniformity is degraded but above which there is little improvement with increasing dE/dt.

If so, then the threshold value of dE/dt is about 2×10^{14} V/cm·s. It would also seem from the framing pictures for different current density cathodes that a fivefold increase in current density has no effect.

4.11. Other Effects

For some shots, Aerodagged stainless steel cathodes were heated *in situ* to 500°C and no difference was observed with framing photography. Likewise, no effect of discharge cleaning for 40 minutes in 200 mT of argon (with sandblasted aluminum cathodes) was noted.

4.12. Framing Pictures Later in Time

A few shots were taken with the framing camera gating pulse delayed to look at the plasma later in time, as shown in Fig. 4.20. Fig. 4.20 a is a standard picture, while that in Fig. 4.20 b was taken 40 ns later. Fig. 4.20 c 70 ns later and Fig. 4.20 d 90 ns later. The gating pulses in this case are indicated in Fig. 4.21. The bottom two pictures were taken with an ND 0.5 filter. At 40 ns delay the plasma is seen to have expanded with no obvious change in profile. At the later times an interesting feature is observed: the plasma is seen to be brightest at about 1 mm from the cathode surface with a darker layer closer to the cathode. On the latest picture some anode plasma can be seen (it can be seen very faintly on the previous picture) and an arc is visible off to the left. In general the division into bright and dark bands occurs at this time, that is, at the end of the voltage pulse. This is similar to that observed in Ref. 116.

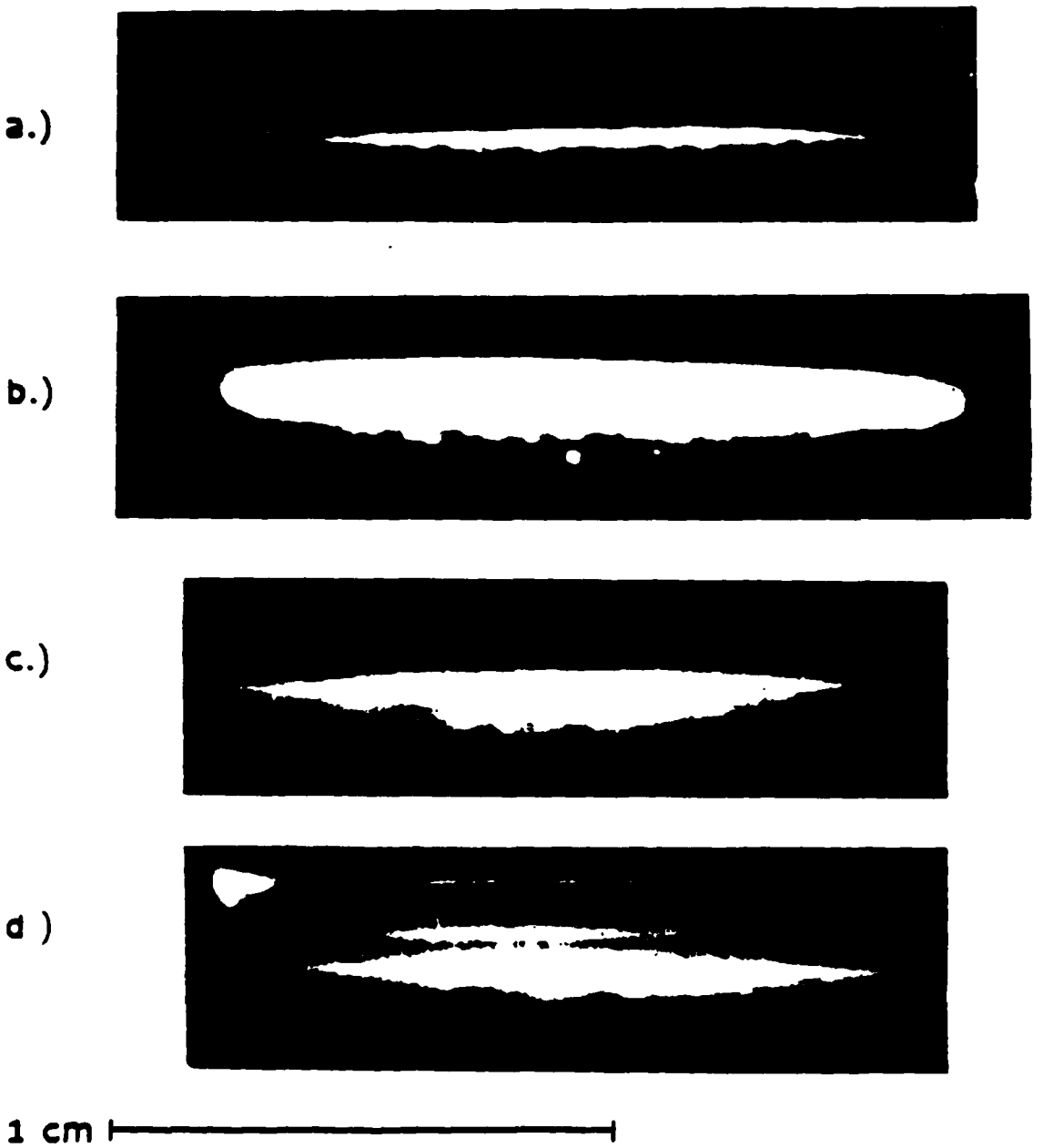

Fig. 4.20: Framing pictures taken later in time (see Fig. 4.21): (a) usual timing; (b) 40 ns delay; (c) [redacted] ns delay; (d) [redacted] ns delay.

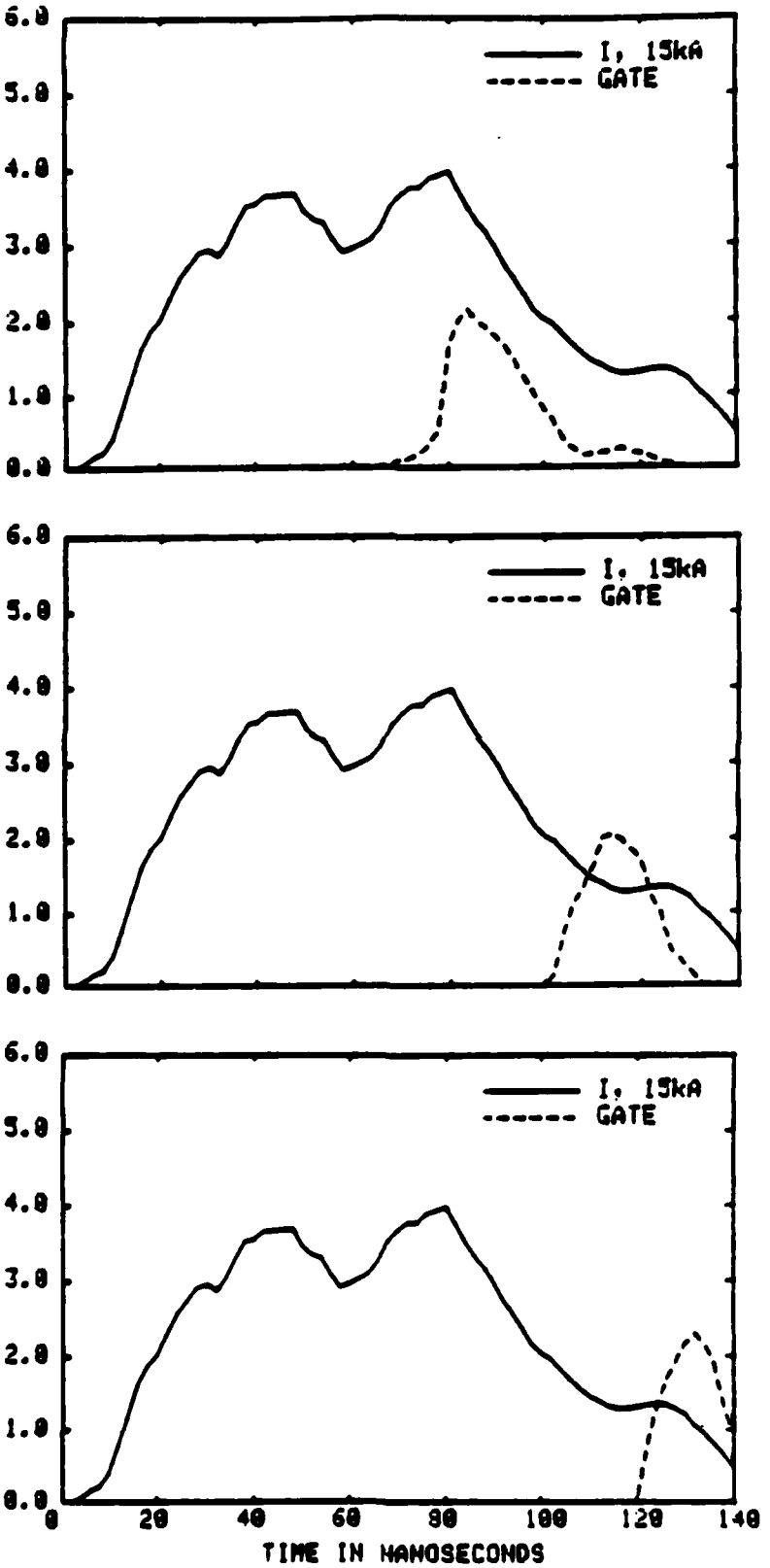

Fig. 4.21: Timing of the gating pulses in the previous figure.

4.13. Conclusions — Technology

This chapter summarizes measurements of plasma luminosity and diode electron beam trajectories which are used to infer the uniformity of plasma formation. Although both are qualitative, it is encouraging that the luminosity uniformity, evenness of exposure patterns on the anode film, average divergence (emittance) angles, and electron source brightness uniformity (the latter two inferred from the target films) are all correlated with one another. From this several conclusions can be drawn.

Sadly, graphite is indeed the best material from which to fashion a cathode (sadly, because it was hoped that a more practical surface would be found). The cheaper reactor grade graphite works about as well as Poco graphite. There is little difference in the performance of the metals examined, with brass being slightly better and stainless slightly worse than aluminum. The apparent slight increase in uniformity with brass cathodes and decease with stainless cathodes could be due to the hardness of the metals — brass would be expected to be more, and stainless less, affected by the sandblasting than aluminum.

With aluminum cathodes, performance is enhanced either by coating with Aerodag or by sandblasting the surface (or better yet, by doing both). The difference in performance between sandblasted and Aerodagged cathodes is sufficiently slight for sandblasting to be an acceptable alternative where Aerodagging is undesirable. Sandblasting is superior to the glass bead blasting tried; whether this is due to the coarser finish from sandblasting or the different abrasive materials used is unknown. It is suggested that the optimum sandblasting technique is that which produces the roughest, or most 'sparkly' appearance. The effect of sandblasting is not diminished by successive shots with integrated charge transfers of 1 mC cm^{-2}. Uniformity is degraded when the cathode is coated with oil.

Aerodag surfaces do not behave similarly to solid graphite surfaces. In particular, the Aerodag surface that (visually) most resembles solid Poco is the smooth polished coating, which performs the worst. If Aerodag is used it should be simply sprayed on and left as is.

The single most important factor in determining uniformity is the diode dE/dt. There is some evidence that there is a threshold dE/dt needed for optimum uniformity. This value of dE/dt is about 2×10^{14} V/cm·sec for the few ns prior to initial turn-on and about 7×10^{13} V/cm·sec after that.

No effect of heating, glow discharge cleaning, or fivefold variations in current density is noted.

A few shots taken with an epoxy-copper coating showed promising results and perhaps an improved surface could be developed using this technique, although it may not be worth the effort involved in preparing such a surface.

4.14. Conclusions — Physics

The beneficial effects of roughness and the harmful effects of an oil coating are both consistent with the beneficial effects of a high dE/dt, since the first will provide a locally enhanced field and the second will reduce the field. The importance of a high dE/dt is believed to be related to the shielding effect pointed out in Ref. 119: electrons emitted from an emission site will tend to shield neighboring sites from the diode field. From the anode films in this experiment and the results of Ref. 128, distances on the order of the diode gap from an emission site will be shielded, so that the effect can be significant.

When a rising electric field is applied to the cathode, some initial emission sites will turn on as soon as the field reaches a critical value. The shielding effect of the electron current from these sites will increase with time as each plasma flare expands and allows more current to be drawn from its surface. Thus, the local electric field at a potential emission site, adjacent to one that has turned on, will be influenced by the diode (average) $dE\ dt$ (which tends to increase the field with time), and by the shielding effect (which grows stronger with time). The net effect is then determined by the magnitude of $dE\ dt$. The improvement with increased $dE\ dt$ is analagous to the behavior of a multichannel gas switch.

Similar conclusions were drawn in Ref. 132, which involved a study of emission from multi-tip cathodes.

The expanding plasma from a smaller number of early emission sites will give rise to a bumpier surface, and local electric fields at the plasma surface can increase the electron transverse velocities.

Several interesting phenomena have also been observed. The framing pictures show that the edge spot luminosity consists of discrete spots connected by fine strands. It is believed that the strands are related to plasma formation along grain boundaries, and the spots are evidence of plasma induced emission site formation.

The cellular structure on the anode films is believed to be due to the interaction of individual beamlets, and this interaction is evidently a contributing factor to the electron beam emittance.

The nonmonotonic variation in luminosity intensity with distance from the cathode front surface observed late in time is also interesting. This could be due to an enhanced heating of the lower density plasma further from the cathode surface, or to a flow of colder material from the cathode late in time, and will be discussed further in Chs. 7 and 8.

Chapter 5

Cathode Surface Analysis

5.1. Introduction

This chapter describes surface analysis of the cathodes, both before and after shots, using scanning electron microscopy (SEM) and energy dispersive x-ray analysis (EDAX). The purpose of this work was not to carry out a comprehensive investigation of the cathode surface microstructure, but rather to answer a few specific questions.

If the energy deposition in the anode is sufficient to form an anode plasma, then an ion current will flow in the diode. The presence of ions, as shown in later chapters, would complicate analysis of data from several diagnostics. It will be shown that the results of cathode surface analysis place a limit on the ionic energy deposition at the cathode, and hence on the ion current in the diode.

In the previous chapter, different cathode materials and surface coatings were associated with variations in inferred plasma uniformity. This was presumed to be due to variations in the local dE/dt due to different surface roughnesses. SEM was used here to see whether plasma uniformity is correlated with any obvious differences in cathode microrelief.

As mentioned in Ch. 2, there is a growing body of evidence that implicates dielectric inclusions in breakdown initiation. In particular, one possible reason for the beneficial effect of sandblasting, in addition to the increased surface roughness that results, would be that the abrasive particles become lodged in the surface and become potential emission sites. The cathodes were examined to see if there was a significant presence of abrasive particles on sandblasted cathodes. In addition to this the cathodes were examined to characterize the (higher atomic number) impurity constituents.

5.2. Before/After Comparisons

Micrographs of 6.4 mm sandblasted aluminum cathodes before and after shots are shown in Fig. 5.1. Magnifications of 120× and 1000× are shown (the scales are indicated at the bottom of each picture). Those in the top row were taken of a cathode before the shot. The surface is very rough on a tens of microns scale. This roughness consists of a complex "chewed up" pattern with twisted peaks, valleys, and ridges. A white (which indicates that it is nonconducting) particle can be seen in the center of the 1000× picture, and several can be seen at the lower magnification.

After the shots, portions of the cathode surface were seen to be darkened. These darkened areas consisted of spots a few mm in radius. For higher current densities the entire cathode was darkened while for lower current densities only a small part of the cathode area was darkened, and no darkening was seen if the pulse was prematurely terminated because of flashover. It is believed that the dark areas are caused by carbonization of surface oils, and because of the above observations it is reasonable to assume that this is due to ions. It is certainly true that these dark areas represent areas of maximum cathode surface change by the shot. In the middle row in Fig. 5.1 are shown micrographs of a dark area from a cathode after one shot. There is no obvious difference in the surface structure between these and the pictures above. Visible micrographs of the surface were consistent with the assumption that the darkness consisted of carbonized oils.

There is clearly no evidence of melting in these micrographs. Because of the complex structure, if the layer where melting occured was sufficiently thin, it would not have been noticed. From these pictures a reasonable upper limit on the thickness of any molten layer can be placed at a few microns.

From the absence of melting, a limit on the diode ion current can be obtained. Protons with energies between 50 kV and the peak diode voltage have a specific energy deposition rate of about 1.1×10^9 eV/cm in aluminum.[133] The range of 200 kV protons in aluminum is about 2 μm. The range of energy deposition will be increased somewhat because of heat conduction: as described in Ch. 10, the heat conduction length in aluminum is about 1.5 μm in 40 ns. The resulting range

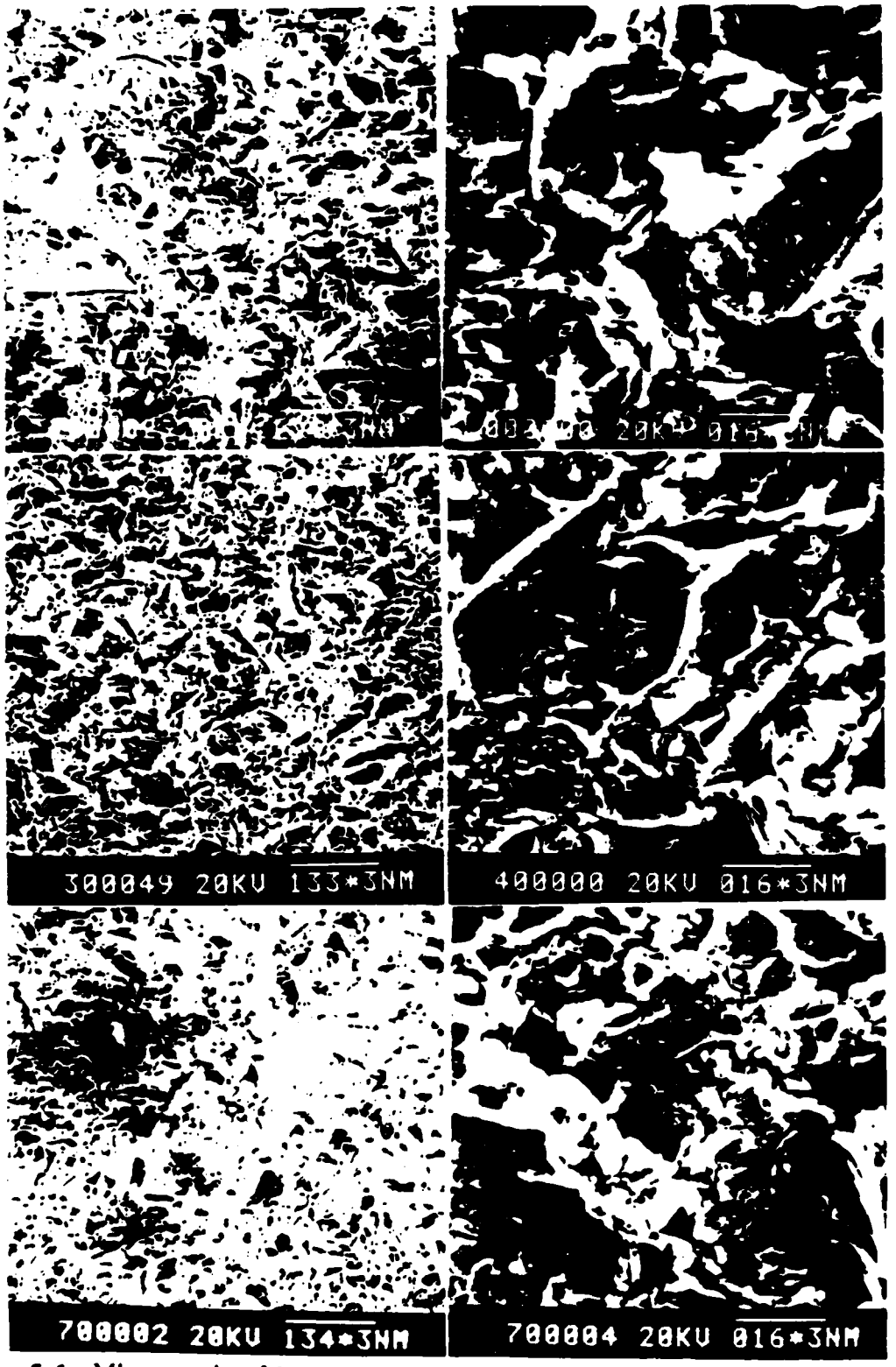

Fig. 5.1: Micrographs of 6.4 mm sandblasted aluminum cathodes, at 120× magnification (left) and 1000× magnification (right). (top row) Before the shot; (middle row) a dark damage area after one shot; (bottom row) a cathode which was used for five succesive shots at reduced energy.

of 3 μm or so is sufficient for melting to have been visible. An energy deposition of 1.1 kJ/gm, or 2.9 kJ/cm^3, is required to melt aluminum.[134] In the absence of heat conduction, from the energy deposition rate above this gives a required dose of 2.6 μC/cm^2 of ions for melting. Heat conduction will increase the range by less than a factor of two, giving an energy of about 5 μC/cm^2, or 3×10^{13} protons/cm^2.

In order to obtain a limit on the time of ion current onset, it is necessary to relate the ion current to the electron current. In a planar diode with bipolar flow, the electron and ion currents are related by[135]

$$j_i/j_e = (m/M_i)^{1/2} \tag{5.1}$$

so that the proton current would be about 2% of the total current. The effect of pinching will be to increase the ion current, so that the 2% value may be taken as a lower limit. Thus, the total charge transfer in the diode during the time when ion current is present is at most 50 times the maximum ion charge deposition, or 2.5×10^{-4} C/cm^2.

The charge transfer density (i.e., the time integral of the current density) in the diode is shown in Fig. 5.2. Since at most 2.5×10^{-4} C/cm^2 could have been transfered during the time of ion current, the earliest possible time of ion current onset is that for which the subsequent charge tranfer density equals 2.5×10^{-4} C/cm^2. From the graph, this time is 70–80 ns.

Electrons at the diode energy have a specific energy deposition rate of about 2×10^6 eV cm in aluminum.[130] From Fig. 5.2, at 70 ns the energy deposited in the anode by the electron beam is then 3.4 kJ gm. In Ref. 136, ion current was observed from carbon anodes when about 2 kJ gm was deposited in the anode, although the rapidly rising value of the energy deposition with time gave rise to some uncertainty in this number. Considering this, the 2 kJ gm number here is reasonable.

It can be assumed that ion current can be neglected when larger cathodes were used, since the energy deposition density in the anode was less because of the reduced current density. The area of the anode damage pattern when 1.6 mm

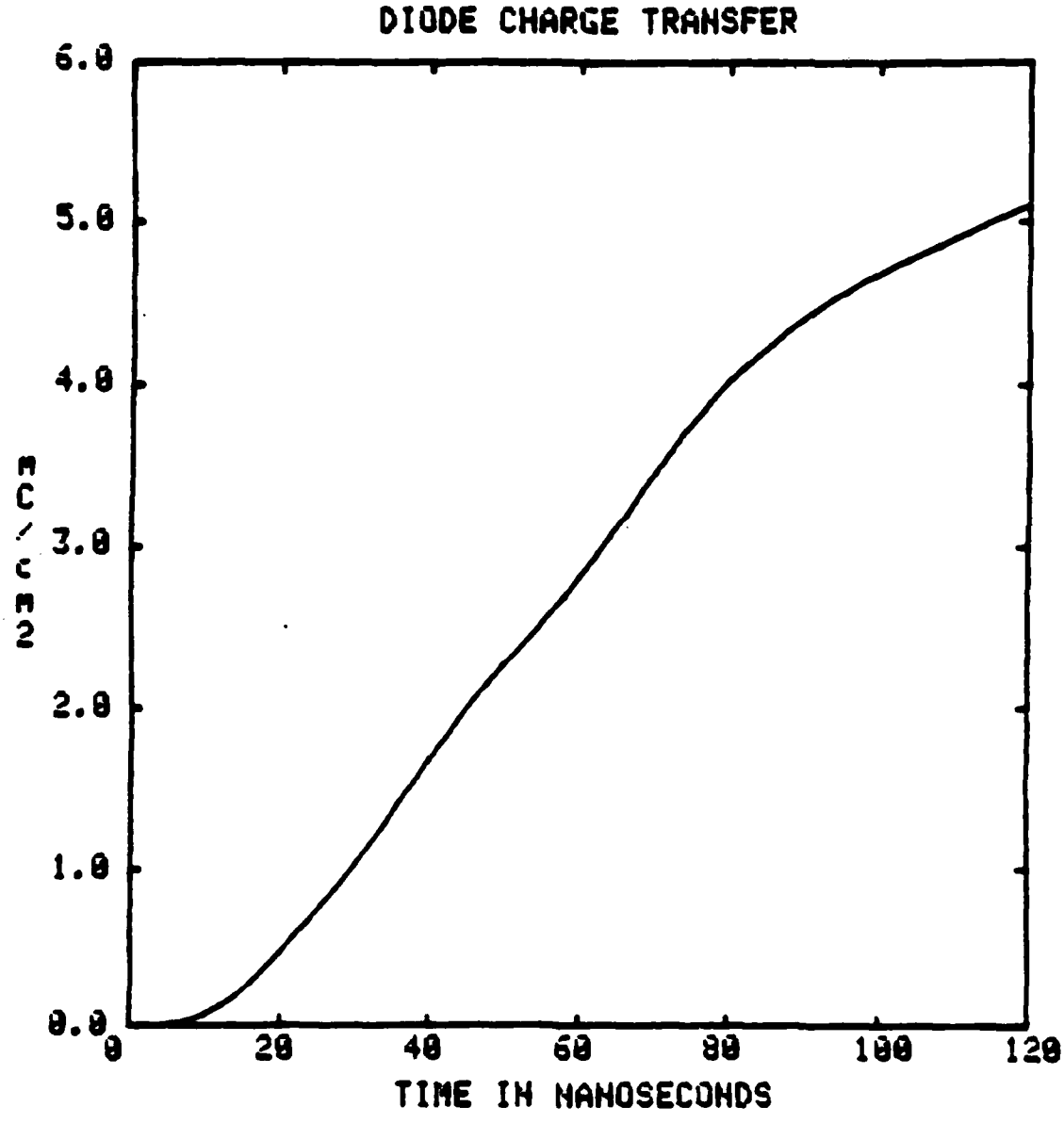

Fig. 5.2: Charge transfer in mC for the 6.4 mm cathode. The cathode has an area of 4.2 cm^2, so that the charge transfer density is $2.4 \times 10^{-4} C\ cm^2$ per division.

cathodes were used is about 0.6 of that when 6.4 mm cathodes were used. In this case 3.4 kJ/gm would have been deposited in the anode after 40–50 ns.

The lower micrographs in Fig. 5.1 are of a cathode after five shots were taken, under the conditions of reduced current mentioned in the previous chapter where the ion current was assumed zero and so any damage observed would be indicative solely of the effects of current transfer from the cathode. There is no obvious effect of the five shots. This is probably because the roughness induced by sandblasting dominates any effects of the shot, which is consistent with the fact that the inferred uniformity showed no obvious change when several sucessive shots were taken with the same cathode. From Ch. 2, the typical size of emission centers (and hence, presumably any resulting erosion) is on the order of microns.

5.3. Different Cathode Materials

Micrographs of aluminum, stainless, and brass cathodes (before the shot) are shown in Fig. 5.3, at magnifications of 50× and 1000×. The surface structures of each are relatively similar and appear equally rough, although the brass and stainless roughness seems to be on a somewhat finer scale. This similarity is consistent with the fact that cathodes of all three metals give rise to similar inferred uniformity of plasma production.

Micrographs of an Aerodagged sandblasted cathode. Aerodagged smooth cathode, and a smooth aluminum cathode are shown in Fig. 5.4. The Aerodagged sandblasted cathode appears very similar to the sandblasted aluminum cathode in Fig. 5.1. The smooth cathodes are both very smooth, even on a scale of a few microns.

One of the interesting results in Ch. 4 was that a great difference in inferred uniformity exists between Poco and smooth Aerodag cathodes, even though the two appear similar to the eye. Micrographs of a Poco cathode are shown in the top row of Fig. 5.5, and the difference between Poco and smooth Aerodag is now apparent as the Poco surface, while smooth on a 10 μm scale, consists of a collection of flakes that cause great roughness on a submicron scale. The 5000 · micrograph of a Poco cathode in the middle left of Fig. 5.5 shows this more clearly.

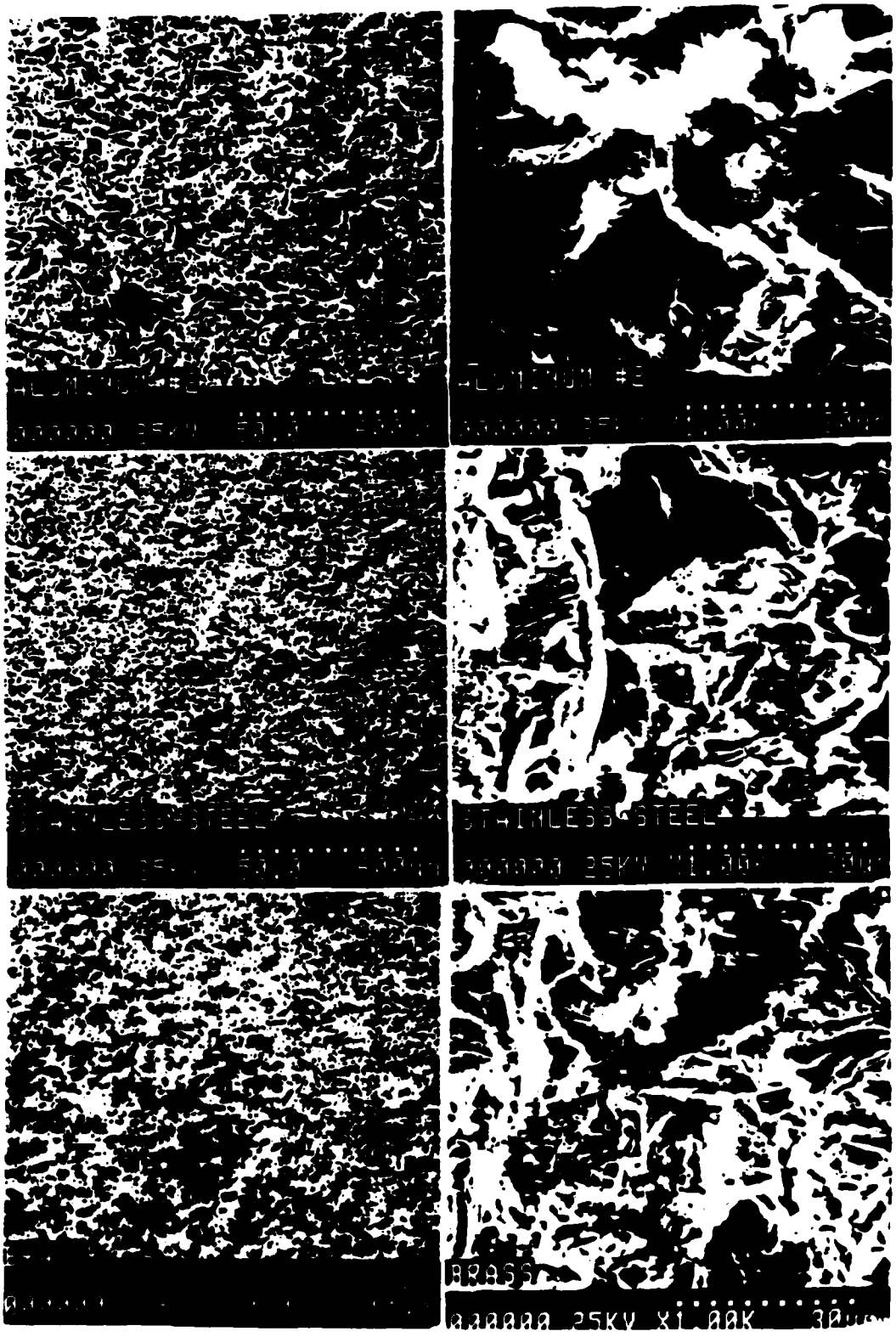

Fig. 5.3: Micrographs of aluminum (top), stainless (middle), and brass (bottom) cathodes, taken before the shot. Magnifications are indicated.

Fig. 5.4: Micrographs of an Aerodagged sandblasted cathode (top). Aerodagged smooth cathode (middle), and bare smooth cathode (bottom). Magnifications are 120× (right) and 1000× (left).

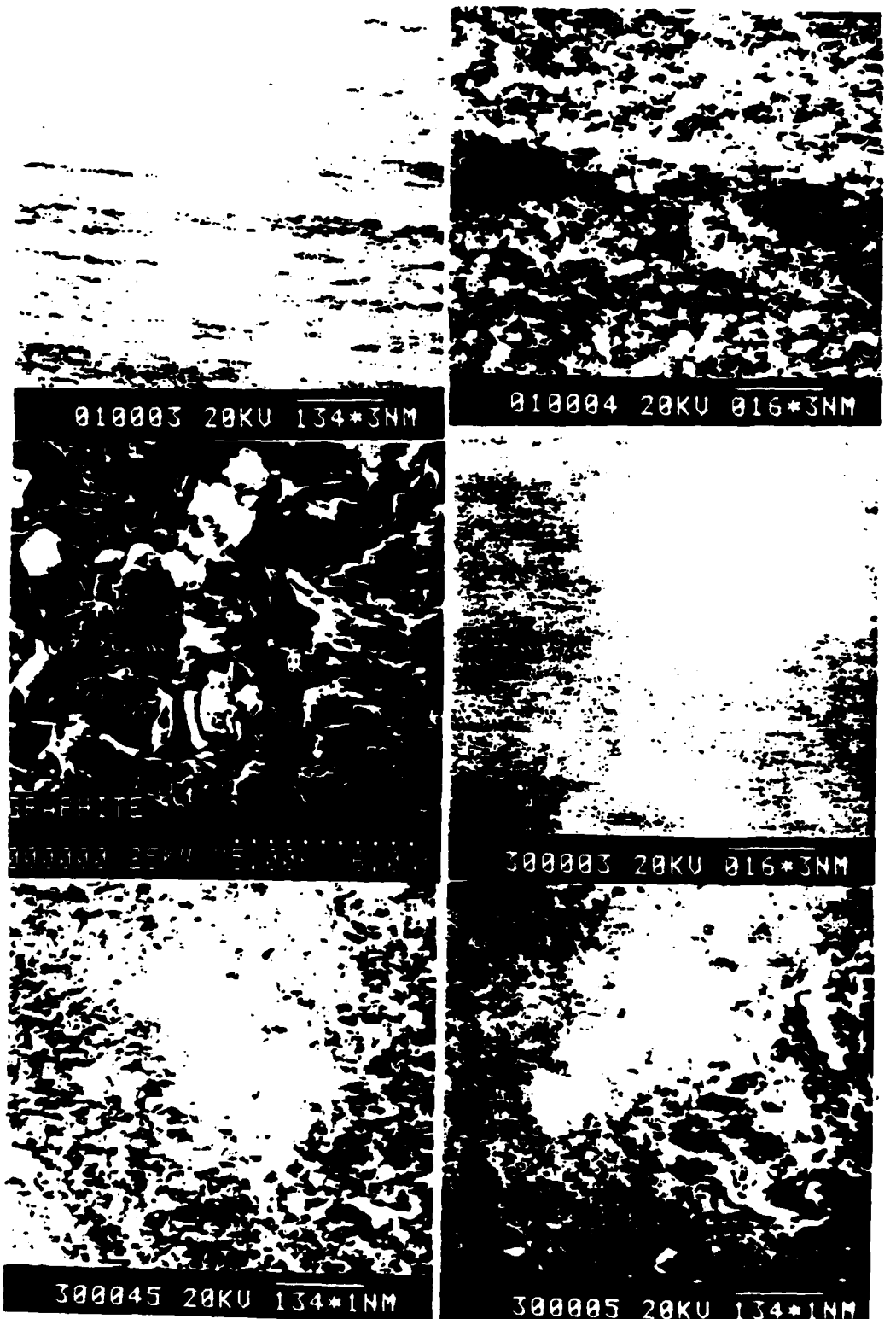

Fig. 5.5: Micrographs of different graphite surfaces: (top and middle left) Poco: (middle right and lower right) polished Aerodag on smooth aluminum: (bottom left) Aerodag on smooth aluminum. Magnifications on the bottom traces are 12000×.

The flakes are about a micron in width with apparent thicknesses of only a few hundered Å.

Particularly poor uniformity was seen in Ch. 4 when the Aerodag surface was polished. A micrograph of such a surface, at 1000× magnification, is shown in the middle right of Fig. 5.5 and the surface is seen to be extremely smooth. In the bottom row of Fig. 5.5 are shown micrographs, at 12000×, of Aerodagged and polished Aerodagged smooth cathodes. Both surfaces are again shown to be very smooth, particularly the polished surface.

Actually, all of the graphite surfaces appear to consist of the thin 1 μm flakes. The difference is that the flakes are randomly ordered on the Poco cathode and so the sharp edges of vertically oriented flakes can provide field enhancement, while on the other cathodes, particularly the polished surface, the flakes are lying flat. The Aerodagged sandblasted cathode looks like the bare sandblasted cathode with a layer of flakes conforming to the sandblasted surface.

5.4. Composition

The cathode compositions were examined with EDAX. This technique is sensitive to the presence of all elements of atomic number greater than sodium that are present within a few microns of the cathode surface. Aluminum was seen in scans of all graphite cathodes. This can explain the fact, mentioned in Ch. 8, that aluminum line emission was observed when Aerodagged cathodes were used.

EDAX showed the presence of 15 foreign elements in all, with several seen even on the graphite cathodes. Several forms of nonconducting impurities were observed. Sometimes the impurities appeared to lie on the surface like dust, as in the Poco micrograph in the middle right of Fig. 5.5, where the impurity contained silicon, or the upper right hand micrograph in Fig. 5.3, where only aluminum was observed and so the material was presumably aluminum oxide. Embedded inclusions were also observed, such the lead containing inclusion in stainless, and the aluminum and silicon containing inclusions in aluminum, in Fig. 5.6. The latter was a cathode that had been blasted with glass beads. Also shown in the figure is what appears to be molten iron on an aluminum cathode.

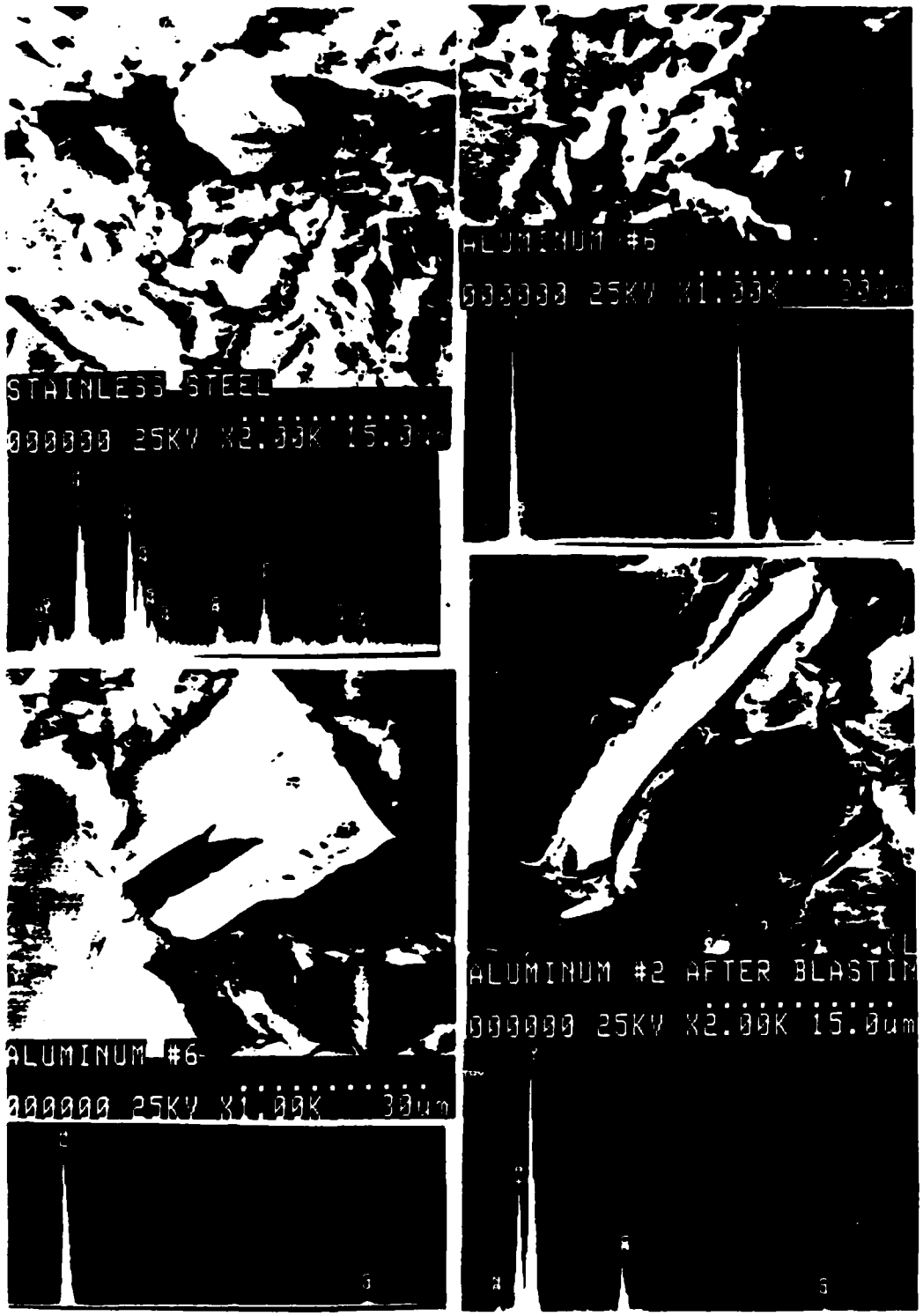

Fig. 5.6: Micrographs of cathodes showing impurities. The aluminum cathode pictured in the lower right was blasted with glass beads. The elements detected by EDAX are indicated in the spectral scans below each micrograph.

No aluminum containing inclusions were observed in the brass or stainless cathodes. However, "caves" were observed that were correlated with concentrations of aluminum, as shown in fig. 5.3. Similar caves were also observed on sandblasted aluminum surfaces. It appears that the abrasive particles either burrowed in very far or were dislodged by the ultrasonic cleaning.

5.5. Conclusions

As stated at the beginning, the surface analysis was neither detailed nor comprehensive, but the results do lead to several conclusions. A good case can be made that ion current is negligible for the first 40–50 ns on shots with a 1.6 mm cathode and the first 70–80 ns on shots with other cathodes.

Variations in observed surface roughness among different cathodes are consistent with the variations in inferred plasma uniformity described in Ch. 4. Thus, it can be concluded that differences in plasma uniformity among different cathodes are caused by variations in the local dE/dt due to differences in surface roughness.

Graphite is seen to consist of very thin ($\sim$300 μm) flakes; the flakes on a Poco surface stick up while on Aerodagged surfaces they lie flat, and this is presumably why plasmas on Poco cathodes have significantly greater inferred uniformity.

The surface roughness due to sandblasting dominates any effects of current flow during the shot.

There are many impurities on these cathodes. Nonconducting inclusions are observed, but they do not appear to be correlated with sandblasting, and there is no evidence to suggest that the beneficial effects of sandblasting arise because bits of abrasive material are implanted in the surface.

Chapter 6

Electrical Behavior

6.1. Introduction

This chapter is concerned with analysis of the diode electrical characteristics. It is possible in principle to infer the cathode initial turn-on time, the time required for uniform plasma formation (i.e., the time required to fill in the plasma layer), and the plasma expansion velocity from the time dependence of the diode voltage and current. Because of the rather high dE/dt in this experiment, however, both turn-on and plasma formation occured very rapidly, and it was not possible to measure the turn on and formation times with enough accuracy to determine how they were affected by variations in the cathode parameters. The bulk of this chapter is devoted to calculations of the plasma front expansion velocity based on the diode electrical behavior. This analysis is seen to be complicated by several effects which give rise to an uncertainty in the determination of an absolute gap closure velocity. However, the relative effect of cathode material, surface coating, electric field rise time and cathode temperature on expansion velocity can be determined by comparing shots with the same diode geometry. The relative effect of current density on expansion velocity can also be examined, although some uncertainty remains because of the change in diode geometry with current density.

In Sec. 6.2 the general nature of the voltage and current traces is discussed, and the effect of prepulse is examined in Sec. 6.3. Previous studies of plasma expansion in diodes is reviewed in Sec. 6.4. Sec. 6.5 describes the model used to calculate the plasma expansion, and the experimental results are described in Secs. 6.6 and 6.7. Discussion and conclusions are given in Secs. 6.8 and 6.9.

6.2. Voltage and Current Traces

Typical inductively corrected voltage and current traces for a shot with a 6.4 mm Poco cathode are shown in Fig. 3.11. For comparison, the corrected voltage trace for a short circuit shot is also shown in the figure, and the correction

is seen to be good, especially for the first 50 ns of the shot. Even though the voltage and current monitors are at locations in the diode 1–2 ns apart, the best correction was obtained with equal cable lengths for each monitor, as is often the case.[137] Actually, as the voltage monitor is spread out over about 3 ns of the line (Fig. 3.2), the whole concept of a standing wave voltage measurement is meaningless for timescales shorter than this.

The voltage is seen to rise very rapidly during the first few nanoseconds, with a corresponding dE/dt of about $2\text{–}3\times10^{14}$ V/cm·sec (not including macroscopic field enhancement), depending on the cathode size. Within a few ns the voltage drops sharply — this drop is due to the inductive correction as the current turns on (the spike on the voltage trace is not due to breakdown of a prepulse switch, as claimed in Ref. 136, since no such switch was used on these shots). In principle, the turn on time and voltage could be determined for different cathodes; however, turn-on occured sooner than the aforementioned 3 ns response time of the voltage monitor.

Typical digitized voltage and current traces and calculated power and impedance traces are shown in Figs. 6.1 and 6.2. The double hump in the voltage and current traces is due to the properties of the accelerator; analysis with a transmission line code[138] showed that it is due to the presence of the 3 ns long initially uncharged section of 2 Ω line beyond the switch. This section of line also causes the (6 ns period) oscillations on the voltage and current traces.

6.3. Prepulse

As mentioned earlier, no prepulse switch was used for these shots. The calculated and measured prepulse was about 8 kV and was present for a few hundered ns before the shot. For the smallest gap, this gave a field (including macroscopic field enhancement) of about 75 kV/cm. Since this field is on for a long time, it might be expected to have some effect. The significance of prepulse was checked in the following manner: for a few shots, a nylon prepulse isolator was put in the line (see Fig. 3.2). (The presence of the prepulse isolator caused difficulties in alignment, so that it was generally not used.) With the diode shorted, the prepulse was still observed on the voltage trace, verifying that the switch was indeed holding

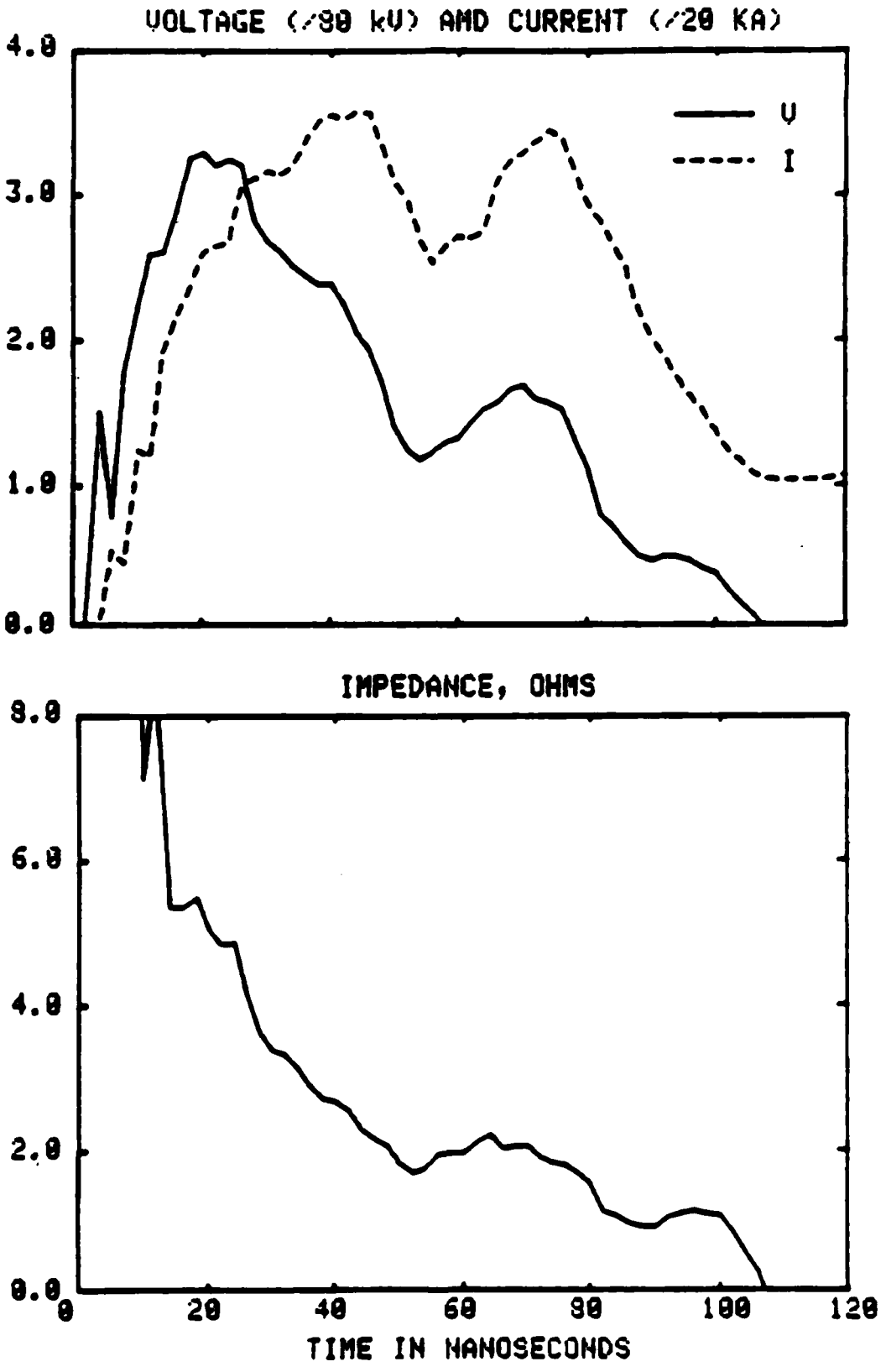

Fig. 6.1: (top) Typical voltage and current traces. A 6.4 mm Poco cathode was used on this shot. (bottom) The calculated impedance for this shot.

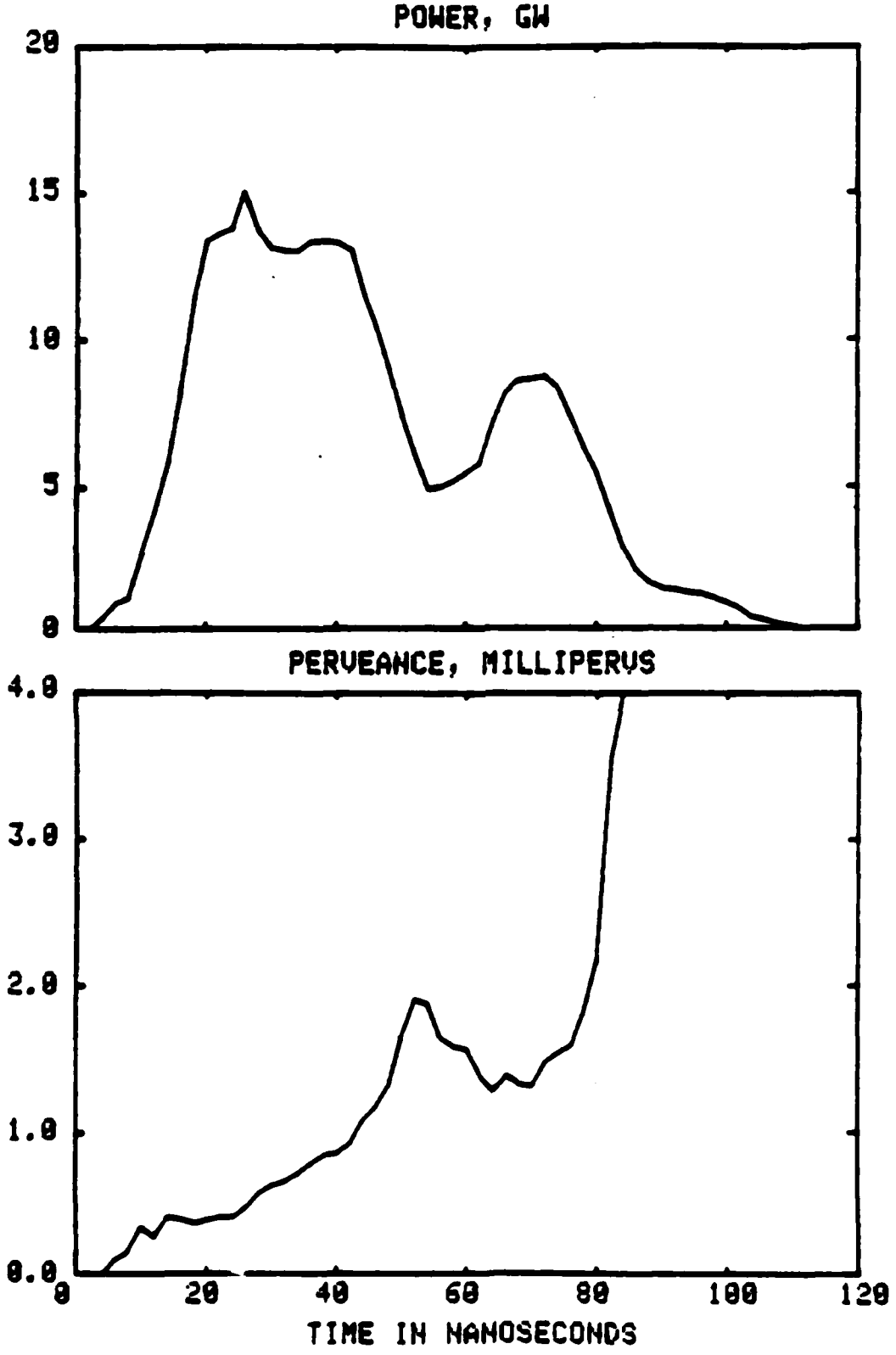

Fig. 6.2: The calculated power (top) and perveance (bottom) for the shot in Fig. 6.1.

off the prepulse. Then, shots were taken with the switch in, with the cathode which had the highest surface electric field. No difference was observed in either the electrical traces or in framing pictures of the cathode plasma (as described in Ch. 4). Of all dignostics used in this work, the electrical characteristics would be the most sensitive to the presence of a plasma formed by the prepulse, since the emission layer density (see Sec. 6.6) is less than that observable by spectroscopy or interferometry. It can thus be concluded that prepulse had no effect on the measurements reported in this work.

6.4. Previous Expansion Measurements

The expansion of the cathode plasma, and of different components thereof, has been deduced from the results of three types of measurements: the time dependence of the diode electrical behavior, observations of the propagation of (total) luminosity from the cathode surface, and direct measurements of the expansion of specific ions using spectroscopy and charge collectors. Previous measurements of the first two are reviewed here; measurements of the expansion of particular species are reviewed in Ch. 8.

The simplest way to infer the plasma expansion velocity from electrical measurements is to assume a constant velocity, in which case the velocity is simply given by the diode gap divided by the time required for the diode to short out.

It can be shown that if the diode electron flow is everywhere along the electric field lines and limited only by space charge, then the diode current will be proportional to the three halves power of the diode voltage:

$$I = kV^{3/2} \tag{6.1}$$

where k, termed the diode perveance, is determined by the diode geometry. The change in perveance with time will be solely due to changes in the diode geometry caused by plasma motion. If the plasma expansion is assumed to be expressed in terms of a single parameter (e.g., the cathode plasma-anode gap in a planar diode) and the perveance is known as a function of this parameter, then the plasma expansion can be determined from the measured perveance. (Of course, even if

the perveance is not a useful quantity, as is the case in a pinched beam diode, the gap closure can still be calculated if the diode current can be modeled.)

Plasma expansion from needle cathodes has been studied in several experiments by the Tomsk group. Perveance measurements for diodes with 1–10 μm radius needle cathodes and plane anodes were reported in Ref. 117. Cathodes of W, Mo, and Cu were used and the current density was about 10^7 A/cm^2. The plasma flare was presumed to consist of an expanding sphere at the needle tip. The perveance of that geometry was calculated using a method similar to the method of equation of capacitances described in Ref. 139. The measured perveance agreed with that calculated assuming a plasma expansion velocity of 2 cm/μs. The velocity was seen to be independent of voltage (over a range of ten), roughly constant and independent of cathode material. Framing pictures were consistent with spherical expansion at this velocity.

The breakdown of gaps involving single emitter cathodes was studied in Ref. 140. In this case the tip radius was about 10^{-5} cm and the current was about 15 A. The velocity was estimated by measuring the time required for a cathode-grid gap to short out. This velocity ranged from 2–2.5 cm/μs, with a 3.5 cm/μs velocity reported for very high values of dE/dt of about 10^{18} V·cm·s.

The electrical behavior of diodes involving 1 mm wire cathodes, with current densities exceeding 10^5 A/cm^2, was examined in Ref. 141. The time required for the diode to close was recorded, using a collector behind an anode grid. The average expansion velocity was 2.3 $\pm$ 0.1 cm/sec, independent of diode voltage (over a range of 1.7) and cathode material (Al, Mo, Cu).

The electrical behavior of 1 cm radius electrodes separated by submillimeter gaps was studied in Ref. 142. The current was about 200 A, and the expansion velocities inferred from closure times ranged from 2–2.5 cm/μs. No dependence on pressure was observed in the range of 10^{-6}–10^{-2} T.

Many authors have inferred plasma expansion velocities in broad area diodes from the electrical behavior. The most detailed (as well as among the earliest) measurements of this type were those carried out by Parker and co-workers.[43] The diodes consisted of right circular cylindrical graphite cathodes and planar

anodes. The cathode diameters ranged from 2.5–5 cm and the gaps ranged from 3–6 mm. Peak current densities ranged from about 2–15 kA/cm^2. The perveance model used consisted of two terms, describing current flow from both the cathode face and the circumferential edge. The flow from the face was assumed to be planar while the flow from the edge was modeled by a 45 degree segment of the flow between concentric cylinders. (This model is discussed more fully and the appropriate equations are given in Sec. 6.5.)

Several stages of the diode operation could be identified from the perveance measurements. For the first few ns after voltage was applied, no current could be measured, indicating that breakdown had not occured. Once the current flow began, there was a period of about 15 ns where the perveance was below the calculated value, and from this it was inferred that during this time the plasma layer had not completely formed. Further examination resolved this formation time into a period of a few ns where emission occured only from the cathode edge, followed by a gradual filling in of the cathode face. Once the plasma layer formation was complete, the measured perveance agreed with that calculated assuming planar plasma expansion with a (constant) velocity.

The delay before the onset of current flow was found to be consistent with the single emitter results of the Tomsk group when both microscopic and macroscopic (due to the cathode edge) field enhancement were taken into account. That the edge turned on first could be explained by the higher local field there. It was concluded that with a graphite cathode, an (average macroscopic) electric field of $4 \cdot 10^5$ V cm was required for turn-on.

The calculated plasma expansion velocities ranged from 1.8–2.8 cm μs. On some shots, the measured perveance diverged from the calculated values and this was attributed to a change in the nature of the electron flow or to anode plasma formation, both of which are discussed further in Sec. 6.5. A weak correlation was seen between the expansion velocity and the rise time of the applied electric field, similar to the findings of the Tomsk group with single emitters. No correlation between expansion velocity and current density was observed. In general, the results of this experiment established the relevance of the single and needle emitter

experiments to broad area diodes, and established the significance of the cathode plasma layer in diode performance.

The electrical characteristics of diodes with cylindrical razor blade cathodes and planar anodes were examined by Phelps *et al.*[143] In this case the current density can be estimated at about 3 kA/cm^2. The electrical behavior agreed well with that predicted from an empirical model of the diode perveance, assuming a constant plasma velocity which ranged from 1.9–2.1 cm/μs for various gaps. The velocity was seen to be relatively constant over a factor of five range in the applied electric field and is stated as being constant to within 25% for different materials and geometries. The presence of an axial magnetic field was seen to increase the expansion velocity, for example with one cathode the velocity increased from 2 to 2.5 cm/μs when an axial field of 18 kG was present.

Plasma expansion in low current density, microsecond pulse length diodes was inferred from electrical behavior by Ramirez and Cook.[144] Two cathodes were used — a long blade cathode and a cathode consisting of an 18 by 23 cm array of carbon fiber bundles. A gap closure velocity of about 3 cm/μs was calculated for the former, although there was some uncertainty about the perveance model used. For the fiber array, a velocity of 1.5 cm/μs was calculated.

A similar study involving planar graphite electrodes and microsecond pulses was reported by Lebedev *et al.*,[145] and the expansion velocity determined from perveance measurements was quoted as being between 1.5-2 cm μs.

Most of the remaining studies of diode electrical behavior involve diodes where an anode plasma, and hence ion current, are present. The presence of the ions greatly changes the nature of electron flow and increases the uncertainty in the calculation of the diode gap. Also, it is difficult to distinguish between the effects of anode and cathode plasma expansion, and the two are often treated together. In general, cathode plasma velocities around 1.5-5 cm μs are quoted.

6.4.1. Luminosity Measurements

Plasma expansion has been inferred from the expansion of plasma luminosity, which is in turn measured by fast streak or framing photography. In a sense this

method is more direct and less model-dependent than perveance measurements, but it suffers from the fact that it is difficult to determine what plasma density the observed luminosity corresponds to, and how that relates to the emission layer.

In Ref. 146, a photomultiplier tube-slit combination was used to measure the rate of luminosity advance for cathodes of Al, Cu, Mo, and Pb. No description of the diode geometry was given. Luminosity velocities were quoted as being 3.4 cm/μs for Al, 2.6 cm/μs for Cu, 2.0 cm/μs for Mo, and 1.1 cm/μs for Pb. Luminosity measurements in Refs. 116 and 142 gave velocities of about 2 cm/μs.

Luminosity expansion was measured with streak photography in Refs. 43 and 136. In the former, the velocities were consistent with the 2–3 cm/μs velocities determined from the perveance measurements, and in the latter, a velocity of 3.8 cm/μs was inferred.

6.5. Perveance Analysis

The perveance measurements described in this chapter were obtained for shots with the three cathodes shown in Fig. 3.6. In addition to these, a 25 mm wide cathode with a 3.3 mm gap was used on a few shots. This cathode was also 7 cm in length with 1.6 mm radius edges. The peak current densities for the four cathodes were 39, 13, 8, and 3 kA/cm^2, respectively.

The perveance of an ideal planar diode is given by the Child-Langmuir equation[147,148]

$$\frac{I}{V^{3/2}} = 2.3 \times 10^{-6} \frac{A}{d^2} \tag{6.2}$$

where A is the diode area, d is the diode gap, and the units are A, V, cm^2, and cm. Edge effects must be taken into account for a real diode. One would expect the importance of edge effects to be related to the ratio of gap size to cathode length (or width). As the 7 cm diode length was much greater than the gap, edge effects due to the cathode ends will be neglected. The long cathode edges (i.e., those in

the cross sections in Fig. 3.6) would be expected to have an effect, especially for the 1.6 mm cathode which is nothing but edges.

Edge effects may be taken into account in several ways, as indicated in Fig. 6.3. In Ref. 43, the flow at the edges was approximated by a segment of the flow between concentric cylinders (Fig. 6.3 b), as described by the Langmuir-Compton equation[149]:

$$I = (\frac{\theta}{2\pi})I_{LC} = (\frac{\theta}{2\pi})2.3 \times 10^{-6}\frac{2\pi}{r(d/r)\alpha^2} \tag{6.3a}$$

$$\alpha \equiv ln(d/r) - .4ln^2(d/r) + .09ln^3(d/r) + \ldots \tag{6.3b}$$

$$d = d_0 + r_0 \tag{6.3c}$$

$$r = d_0 + r_0 - x \tag{6.3d}$$

where r_0 and d_0 are the edge radius and initial gap and x is the distance the cathode plasma has expanded. In Ref. 43, θ was taken as $\pi/4$.

The edge perveance may also be calculated by noting that the electron flow from an edge is the same as that in one half of a cylinder-plane gap (Fig. 6.3 c). The perveance of a cylinder-plane gap, in turn, has has been calculated using the method of equal specific capacitances.[139] This method involves a transformation of the cylinder-plane gap to a system of concentric cylinders; the essential assumption is that the presence of space charge alters the value, but not the shape, of the equipotential surfaces, which is equivalent to the assumption that the flow is everywhere parallel to the electric field lines (if this is not true then the perveance is not a useful quantity anyway). The resulting perveance (of one edge) is the same as that given by Eq. (6.2), with

$$d/r \rightarrow d/r - \sqrt{(d/r)^2 - 1} \tag{6.4a}$$

$$\theta = (1/2)(2\pi) \tag{6.4b}$$

A simpler, phenomenological approach is to use the planar equation with an effective area somewhat larger than the cathode area to take into account the edge flow (Fig. 6.3 d). The motivation for this comes from experimental studies of the perveance of a blade cathode-planar anode gap (which is the extreme case of a

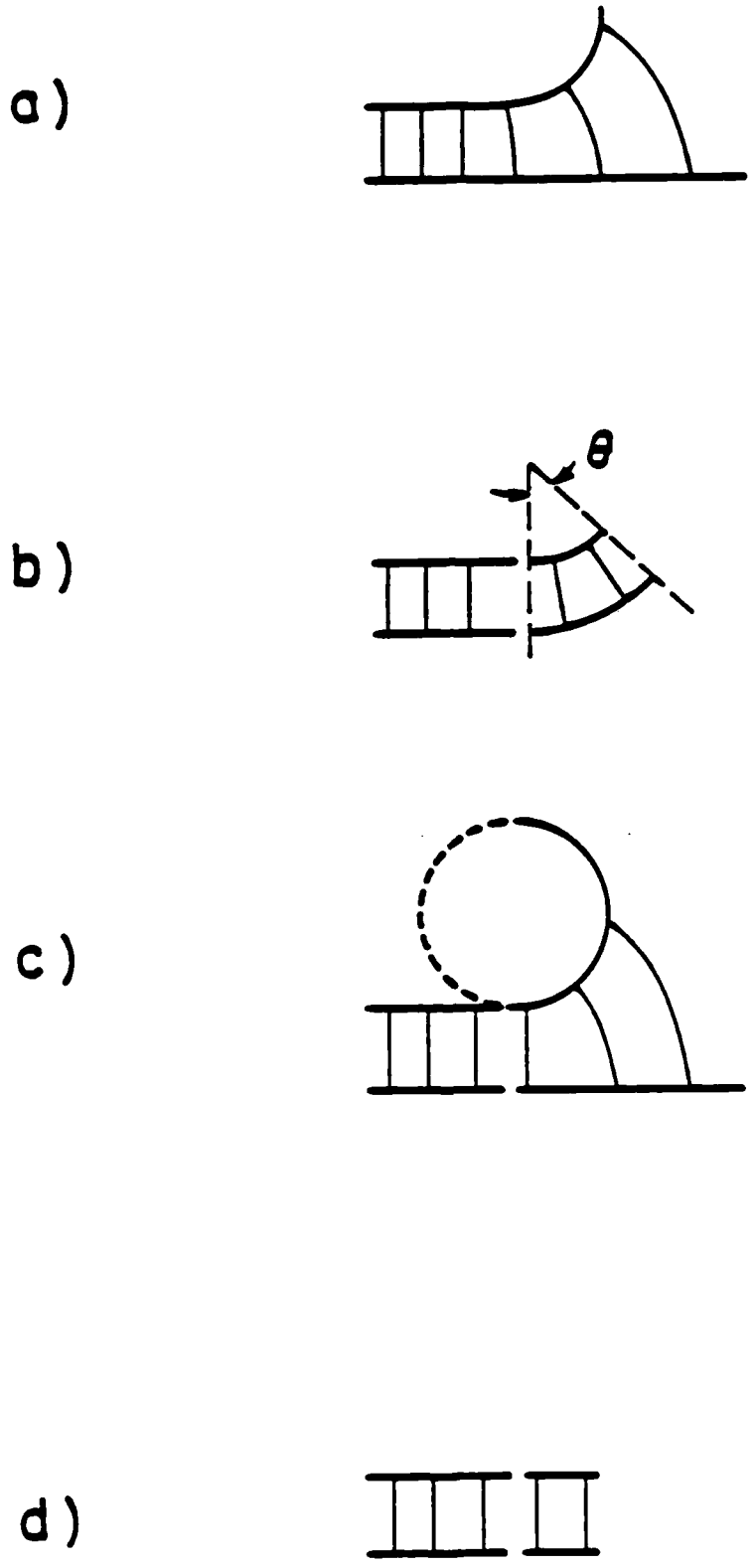

Fig. 6.3: Modeling of edge effects: (a) actual geometry: (b) cylindrical segment: (c) cylinder-plane: (d) effective area.

thin cathode). In this case the perveance is given by Eq. (4.1), with the area being the beam area on the anode.[144] The thickness of this area is approximately equal to twice the gap.

The situation is further complicated by the fact that current may be drawn from the cathode sides; for example, the potential plots presented in Ch. 3 showed that electric fields in excess of 0.5 MV/cm would be reached at peak voltage on parts of the side surfaces of the 1.6 mm cathode.

The key assumption in all of this is that the flow is along electric field lines. This is a good approximation if the field line curvature and self magnetic field are not too large (the two effects generally act in opposite directions). As the current density increases, the self magnetic force (the conducting electrodes are assumed to short out the radial electric field due to the beam space charge) will cause the electrons to pinch in, with a component of their velocity along equipotential surfaces. In this case the perveance is described by the focussed flow model of Ref. 150. In Ref. 43, magnetic effects are claimed to be significant in a planar diode when the Larmor radius of electrons emitted at the cathode edge becomes less than the diode gap.

6.5.1. Electron Flow

Originally, it was planned to use the Hermannsfeldt code to predict the electron trajectories and the diode perveance, at least for early times before significant plasma expansion occured. However, as mentioned in Ch. 4, the current density was higher than the code was designed to handle and the code failed to converge. For what it is worth, it is interesting to note that according to the code, electrons emitted from the cathode front surface are not greatly bent.

The fact that the damage pattern extends downward from the cathode location implies that some magnetic bending occured. If strong pinching occured, the damage would be concentrated at or below the lower cathode edge (because of the single sided feed). Since this is not observed, it is concluded that strong pinching did not occur.

6.5.2. Perveance Model

Two models were used for the perveance in this analysis. In what will be referred to as the planar model, Eq. (6.2) was used with the area given by 7cm × (the width of the anode damage pattern). In what will be referred to as the 'exact' model, the perveance is given by two terms: Eq. (6.2), with the area being that of the flat cathode face, and Eq. (6.4).

There are several factors which complicate the interpretation of perveance measurements, as shown in Fig. 6.4. In the figure, the dashed lines represent an assumed actual gap between the plasma front and the anode; the solid lines represent sketches of the gaps which would be calculated under these conditions. The ideal case is shown in Fig. 6.4 a, where the plasma expands so that the shape of the diode remains constant. During the plasma formation time, the calculated gap will be larger than the geometric gap, as illustrated in Fig. 6.4 b. The effects of magnetic bending and uneven expansion are illustrated schematically in Fig. 6.4 c. Both effects will cause a reduction in perveance, and hence an increase in the calculated gap. However, the calculated gap must decrease to zero as the diode closes.

If an anode plasma is formed, the perveance can be affected in several ways. The resulting ion current in a (nonrelativistic) planar diode will increase the perveance by a factor of 1.86,[135] resulting in a decrease in the calculated gap, as shown in Fig. 6.4 d. The enhancement in other geometries is presumably similar. This change would be easy to spot if the entire anode turned on at once. However, if the anode turns on gradually, the reduction in calculated gap will be gradual. Another effect of the ions is to enhance the pinching of the beam.[151,152] Thus, the perveance due to electron flow will decrease, and this may also mask the effects of the ion current.

None of the above effects change the diode shorting time. If the anode plasma also expands, however, that time will be reduced as shown in Fig. 6.4 e.

From the results of the previous chapter, ions may be neglected for the first 70–80 ns on shots with a 6.4 mm cathode, and thus presumably at lower current densities as well, and for the first 40–50 ns on shots with the 1.6 mm cathode.

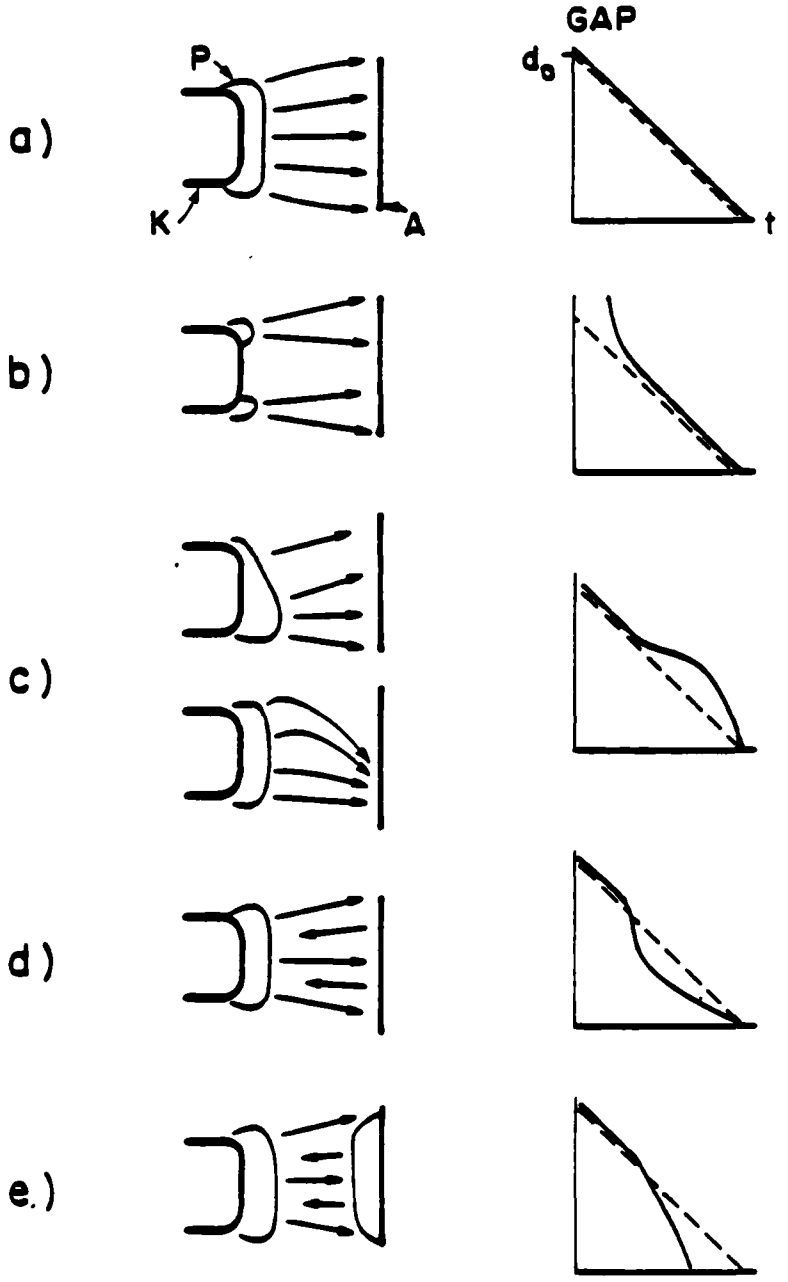

Fig. 6.4: Factors complicating the interpretation of perveance measurements: (a) ideal case: (b) turn-on delay: (c) magnetic bending and uneven expansion: (d) ion flow: (e) anode plasma motion.

It can be seen that the average closure velocity, that is, the gap width divided by the length of the voltage pulse, can be determined without the above uncertainties. However, in this experiment, for all but the smallest gap, the voltage and current fell at about the same time so that only an upper limit to the average velocity could be obtained.

6.6. Perveance Measurements

The calculated perveance for a typical shot is also shown in Fig. 6.2. For the first 50 ns the perveance increases as would be expected, but then the perveance drops rather suddenly before increasing again. The calculated diode gap based on the two perveance models is given as a function of time in Fig. 6.5.

The two calculations are in reasonable agreement, with the exact model predicting a somewhat smaller gap. This agreement suggests that the derived gap is not too sensitive to the specific model. After about 10 ns, the calculated gap falls below the geometric gap of 2.2 mm, implying that the entire cathode surface is emitting. The early time perveance places a constraint on the perveance model used. If the perveance model predicted a significantly greater perveance than the models here, the calculated gap would be larger and the time required for the calculated gap to equal the geometric gap would be inconsistent with the results of Ref. 43 (especially since the electric fields are higher in this experiment).

The gap is seen to close at a roughly constant velocity of 3 cm μs. for a period of 60 ns. After that point, the calculated gap opens somewhat before closing again. This opening occurs at the same time as the rise of the second hump on the current trace. The *average* closure velocity is at most 2 cm μs.

To verify that this apparent opening is not just an artifact of a timing error between the current and voltage traces, the gap was calculated with the current shifted by $\pm$ 3 ns (the maximum conceivable error) and as shown in Fig. 6.6 a, this caused little change in the calculated gap.

It would seem at first that the apparent opening could be due to either a transition to pinched flow or to an uneven expansion. The Larmor radius for electrons at the cathode top edge (where the magnetic field is greatest) is shown

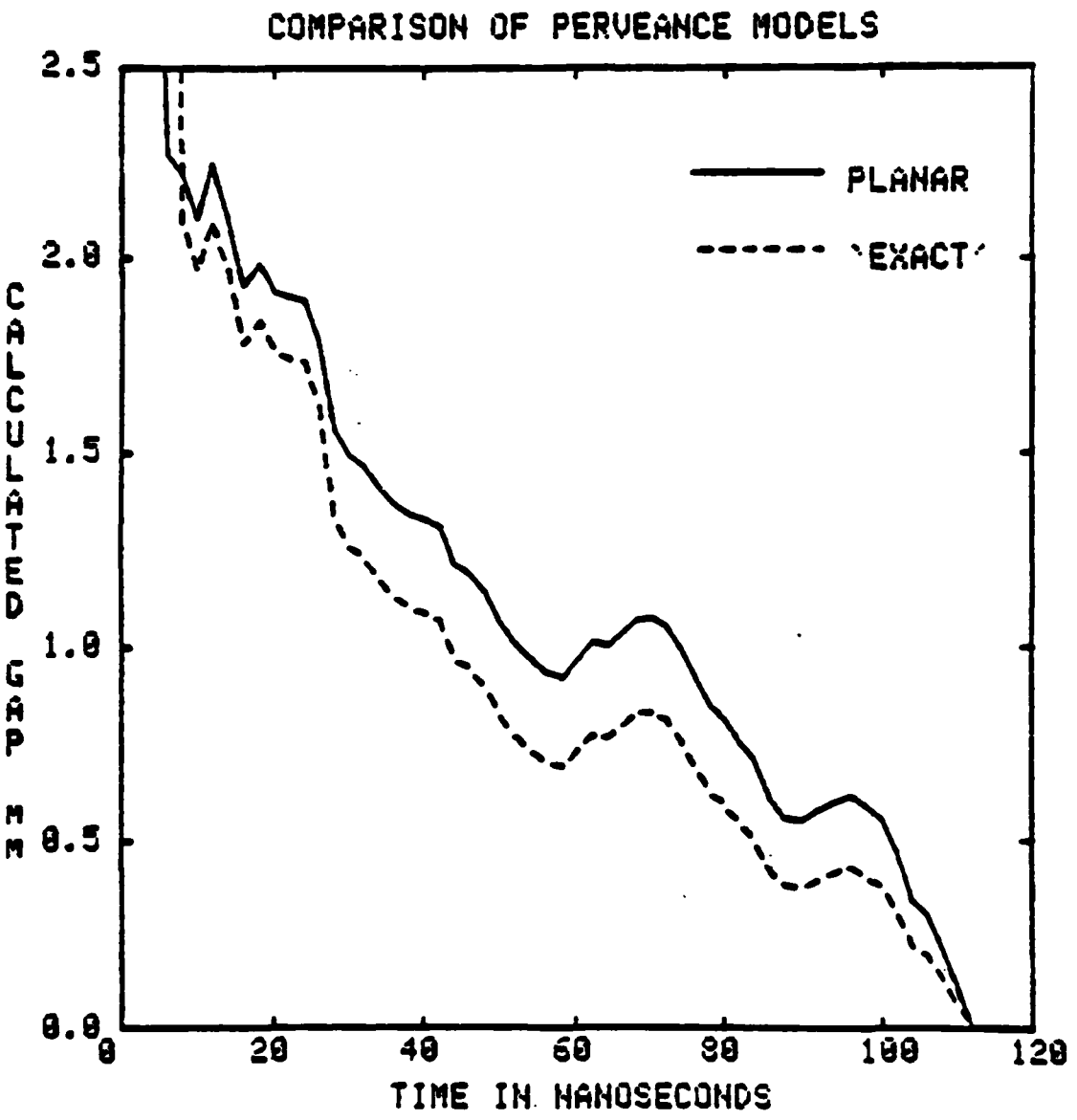

Fig. 6.5: The calculated gap, based on the two perveance models, for the shot in Figs. 6.1 and 6.2.

along with the calculated gap in Fig. 6.6 b, and is seen to exceed the gap (although not by much) at all times, especially when the apparent opening occurs. Also, it should be noted that, in contrast to Fig. 6.5 c, *the closure time is later than that predicted from an extrapolation of the early linear part of the curve.* This would imply that there is indeed a temporary halt to the motion of the plasma front.

Since this apparent opening coincides with the second rise in the current, it could be suggested that the plasma is held back by the increase in magnetic pressure that accompanies the current rise. The effect of magnetic pressure is determined by the ratio between magnetic and kinetic pressure gradients, where the magnetic pressure gradient is determined by the degree of diffusion of the field into the plasma. This effect is calculated and shown to be plausible, and actually observed interferometrically, in Ch. 7. However, magnetic pressure cannot alone explain the opening in this case because the magnetic field decreases along the cathode height, becoming zero at the cathode bottom edge. Magnetic pressure would be expected (and is indeed seen to) produce a plasma profile like that in Fig. 6.5 c, but to have no effect on the plasma at the bottom edge. In other words, magnetic pressure can explain the apparent opening at first, but cannot explain the late closure time.

The gap could have been opened by electric pressure, however. The plasma density at the emission layer n_{el} is determined by equating the plasma thermal current with the space charge limited current drawn from the plasma:

$$j = \frac{1}{4} n_{el} v_{the} \tag{6.5}$$

If $n \geq n_{el}$, the current will no longer be space charge limited and the resulting electric field will draw electrons from the plasma, expose the ions and push them back to the point where $n = n_{el}$.

The magnitude of this pressure can be calculated. For currents below the space charge limited value j_{cl}, the electric field at the cathode surface E is determined from[153]

$$\frac{16}{27}\left[\frac{j}{j_{cl}} - \left(\frac{j}{j_{cl}}\right)^2\right] = \left(\frac{E}{E_0}\right)^2 - \left(\frac{E}{E_0}\right)^3 \tag{6.6a}$$

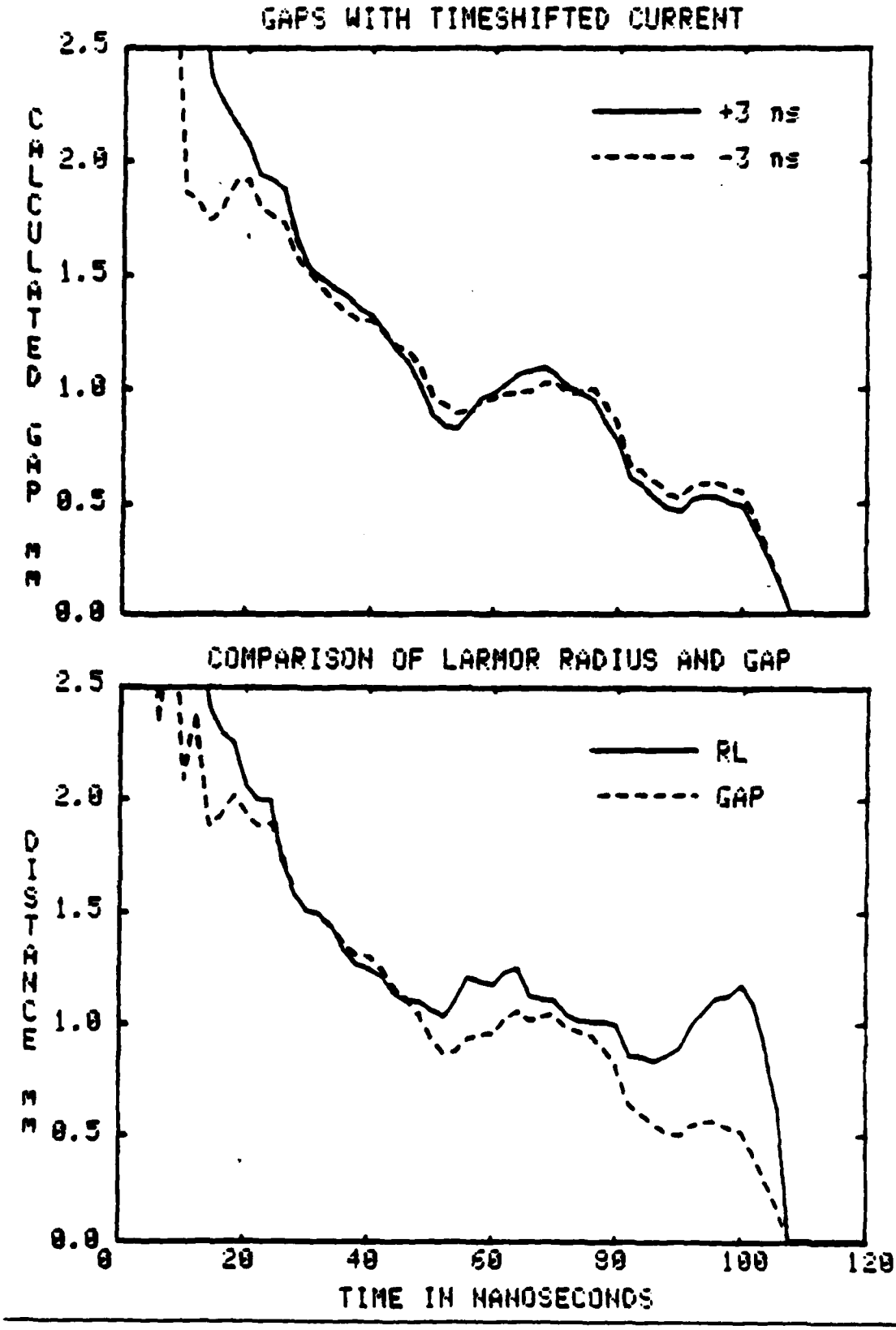

Fig. 6.6: (top) Effect of a ± 3 ns timeshift of the current relative to the voltage on the calculated gap: (bottom) The Larmor radius at the location of peak self magnetic field.

where E_0 is the average diode field. For $j \approx j_{cl}$, this reduces to

$$\frac{E^2}{8\pi} = \frac{E_0^2}{8\pi}\left[\frac{16}{27}(1 - \frac{j}{j_{cl}})\right] \qquad (6.6b)$$

The ratio of electric to kinetic pressure is given by

$$\frac{P_{elec}}{P_{kin}} = \frac{E^2}{4.0 \times 10^{-11} nT} \qquad (6.7)$$

With an average field of 1 MV/cm, temperature of 4 eV, and density of $3\times10^{15}/cm^3$ (the typical emission layer density in this experiment), this ratio exceeds unity when j_{cl} exceeds j by 7%.

Since n_{el} depends on j, emission layer movement occurs both as a result of plasma expansion and as a result of a change in current density. If the plasma density gradient is steep, then as the current changes the emission layer location will change little, and the plasma may be considered to have a well defined edge. If the density gradient is shallow, then an increase in current will cause the emission layer to move back into the plasma. The density gradient will tend to steepen during periods of rising current (due to the electric pressure) and flatten during periods of falling current (because the relaxed requirements for n_{el} will allow free expansion). In this experiment, it could be that when the current falls from the first peak, the plasma density gradient flattens, so that when the current rises again, a noticeable movement of the layer occurs. It is suggested that the key factor in this case is the fact that the current first falls, then rises again. Thus, the significance of electric pressure is related not only to the plasma and current densities, but also *to the shape of the current pulse*. The calculated gap opening corresponds to a plasma density profile that has a 25% increase in density over 0.2 mm.

6.6.1. Previous Observations of Electric Pressure Effects

The effect of electric pressure was observed in Refs. 154 and 155, although in those experiments the effect was apparently triggered by the dimensionality of the expansion. Those experiments involved needle cathodes, and the 3-D expansion resulted in a density fall-off as the plasma expanded, so that even with a constant current, electric pressure effects would arise with time.

Electric pressure is discussed in Ref. 156, and three regimes are distinguished. Under steady conditions, Eq. (6.5) holds. If the current suddenly drops (or the density rises) so that $j > j_{cl}$, the thermal electrons will tend to move out beyond the ions, forming a double layer which then accelerates the ions (this effect discussed in many references, for example Refs. 157 and 158). This acceleration will increase the plasma expansion until the density drops to where Eq. (6.5) is once again satisfied. If the current suddenly increases (or the density falls), then the resulting electric pressure will retard the expansion, piling up plasma (and also decreasing j_{cl} as the gap opens) until $j = j_{cl}$.

Thus, as the current changes, electric pressure and ion acceleration act to maintain Eq. (6.5).

Electric pressure effects also come into play in long pulse diodes, as discussed in several Soviet papers, but in these cases the effect is controled by yet another factor — the supply of material into the cathode plasma. Discussion of this will be postponed until Ch. 10.

6.7. Comparisons of Different Cathodes

6.7.1. Effects of Cathode Material and Surface Preparation

While the determination of absolute closure velocity is subject to uncertainty, the relative effect of cathode material and surface preparation on plasma expansion can be determined by comparing cathodes of the same shape. Calculated gaps for 6.4 mm wide cathodes of different materials and surfaces coatings (using the planar model) are shown in Fig. 6.7. Calculated gaps for 1.6 mm and 9.6 mm aluminum cathodes, with and without Aerodag coatings, are shown in Fig. 6.8. Each trace is the average of calculated gaps for 5–16 shots, except those in the bottom of Fig. 6.7, which are from single shots. With the exception of an Aerodag coating, the plasma expansion velocity is seen to be independent of cathode material or surface coating. Only at the highest current density does Aerodag have any noticeable effect, and even in that case the difference is barely statistically significant. If the Aerodag coating does indeed cause a different perveance behavior, it is important to determine whether this is because the cathode turns on sooner

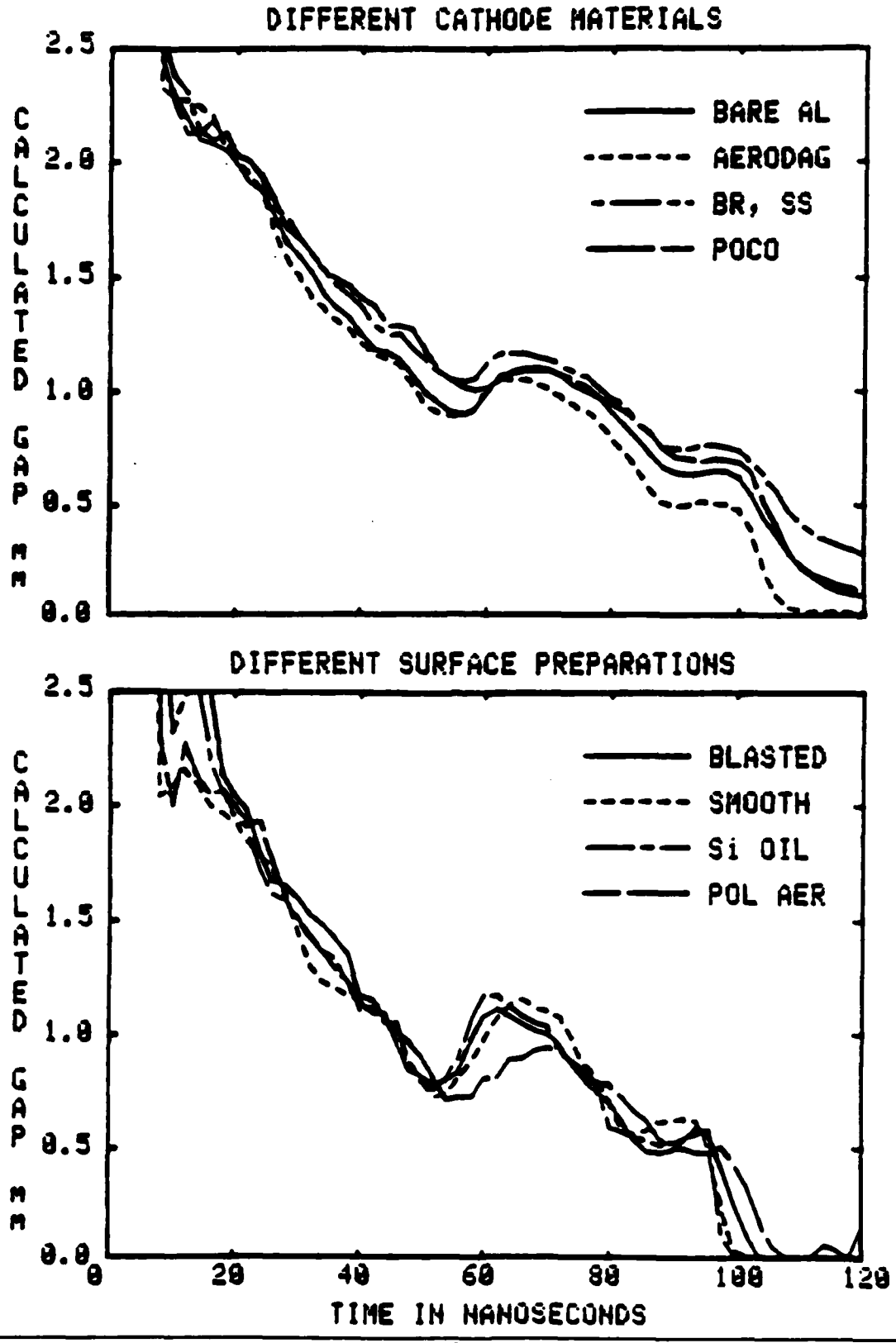

Fig. 6.7: (top) Calculated gaps for different materials: (bottom) calculated gaps for different surface coatings.

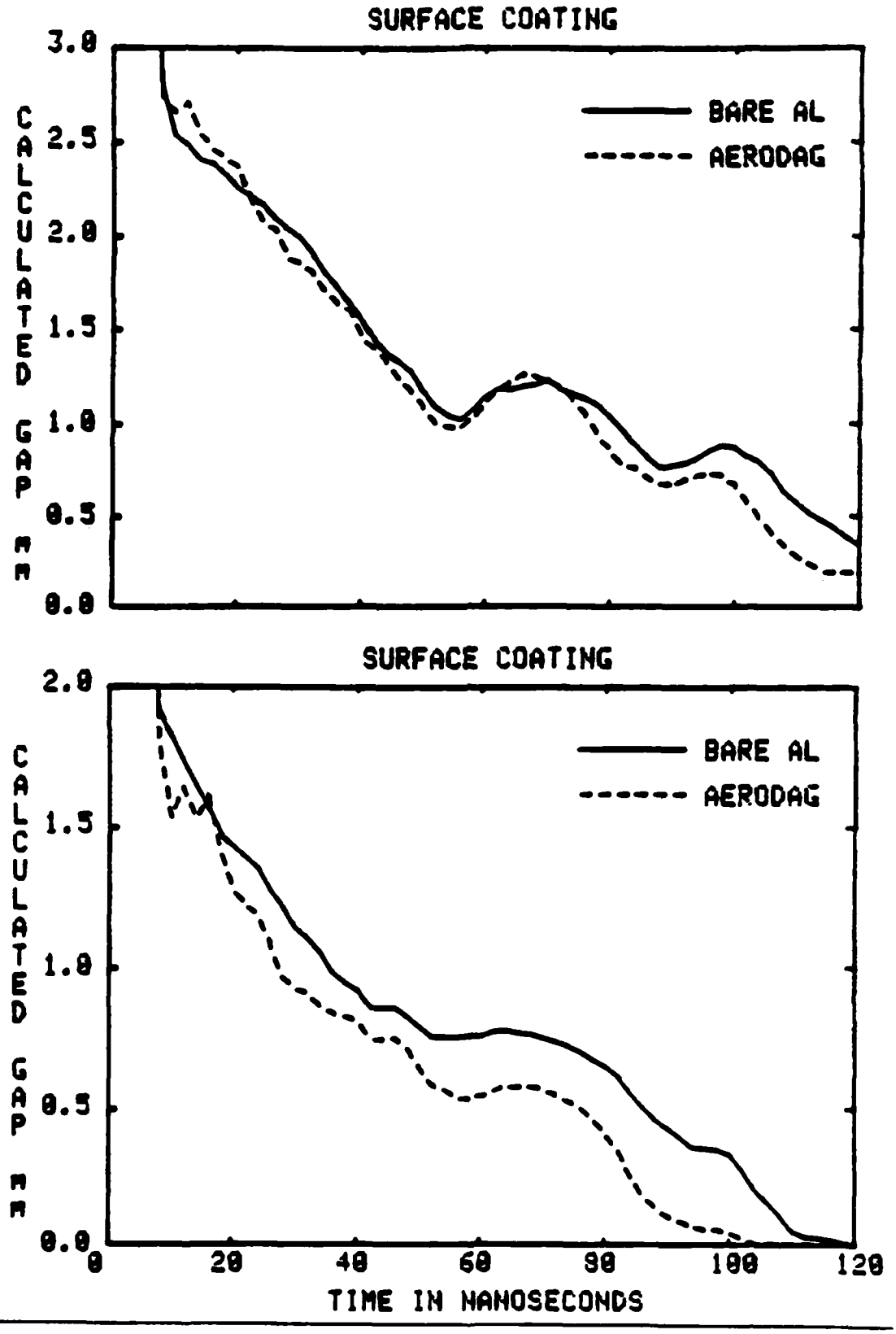

Fig. 6.8: The effect of Aerodag coating (on blasted aluminum) for the 9.6 mm (top) and 1.6 mm (bottom) cathodes.

(which would be beneficial) or because the plasma expands more rapidly (which would be undesirable). The difference in calculated gap is so slight, however, that it is not possible to resolve between these two possible causes.

If plasma expansion is dominated by protons from surface impurities (because of their smaller mass) then gap closure would be inhibited by cleaning the cathode surface. To test this, the heatable cathode described in Ch. 3 was used. Calculated gaps for stainless and gold plated cathodes, at room temperature and 700°C, are shown in Fig. 6.9. The plasma expansion is not affected by heating. Of course, from Ref. 68, in the dirty vacuum of this experiment a surface coating of several monolayers (containing more than enough protons to close the gap) is still expected at these temperatures. Thus, the observation of unchanged perveance behavior with heating does not allow any conclusions to be drawn regarding the mechanism of plasma expansion. This observation is however of empirical value in diode design. Similar results were reported in Ref. 118, where the cathode of a cylindrical magnetically insulated diode was heated to 1400°C with no effect on the closure time.

6.7.2. Effects of Electric Field Rise Time

In Ref. 140 the expansion velocity of single emitter plasmas was seen to depend on the rate of rise of the diode electric field. In Ref. 43 similar results were observed with broad area graphite cathodes. However, in the latter case the change in dE/dt was accompanied by a change in the diode geometry. In this experiment, the ability to vary the inductance of the polyethelyne output switch allowed dE/dt to be varied while the geometry was kept constant. Voltage traces for shots with values of dE/dt that differ by a factor of ten before turn-on and six after turn-on are shown in Fig. 6.10 a. The dashed voltage trace was obtained by punching the dielectric switch 10 cm off center, as described in the Ch. 3. Calculated gaps for these two shots are shown in Fig. 6.10 b. The gaps have been timeshifted relative to one another so that the times of current initiation coincide. Calculated gaps for other shots with reduced dE/dt are shown in Fig. 6.11. All four calculated gaps show the same 3 cm μs initial velocity, showing that a factor of six variation in dE/dt *per se* has no effect on the expansion velocity (the values of dE/dt in

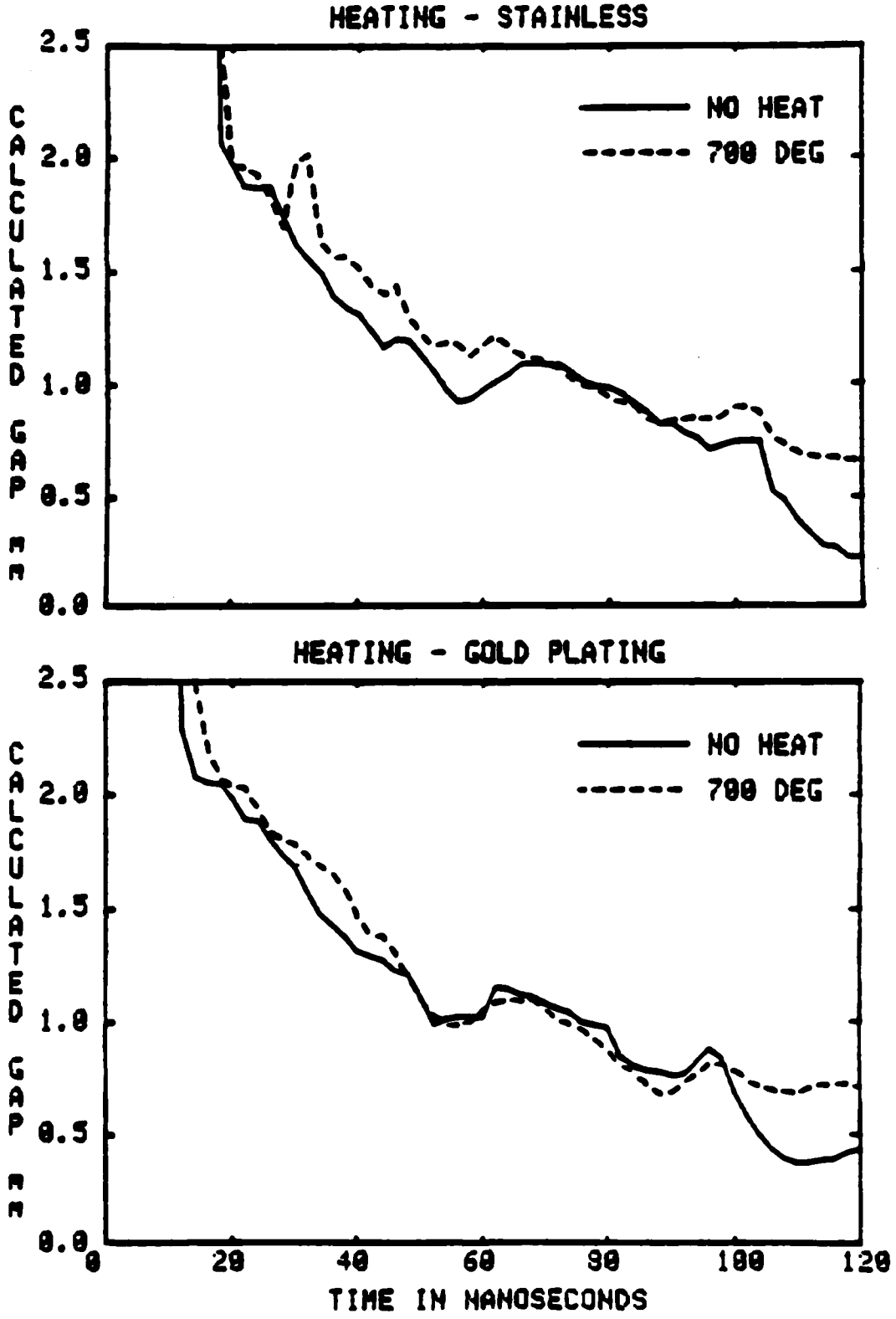

Fig. 6.9: The effect of heating the cathode *in situ* to 700°C on the calculated gap: (top) stainless steel cathode: (bottom) gold plated cathode.

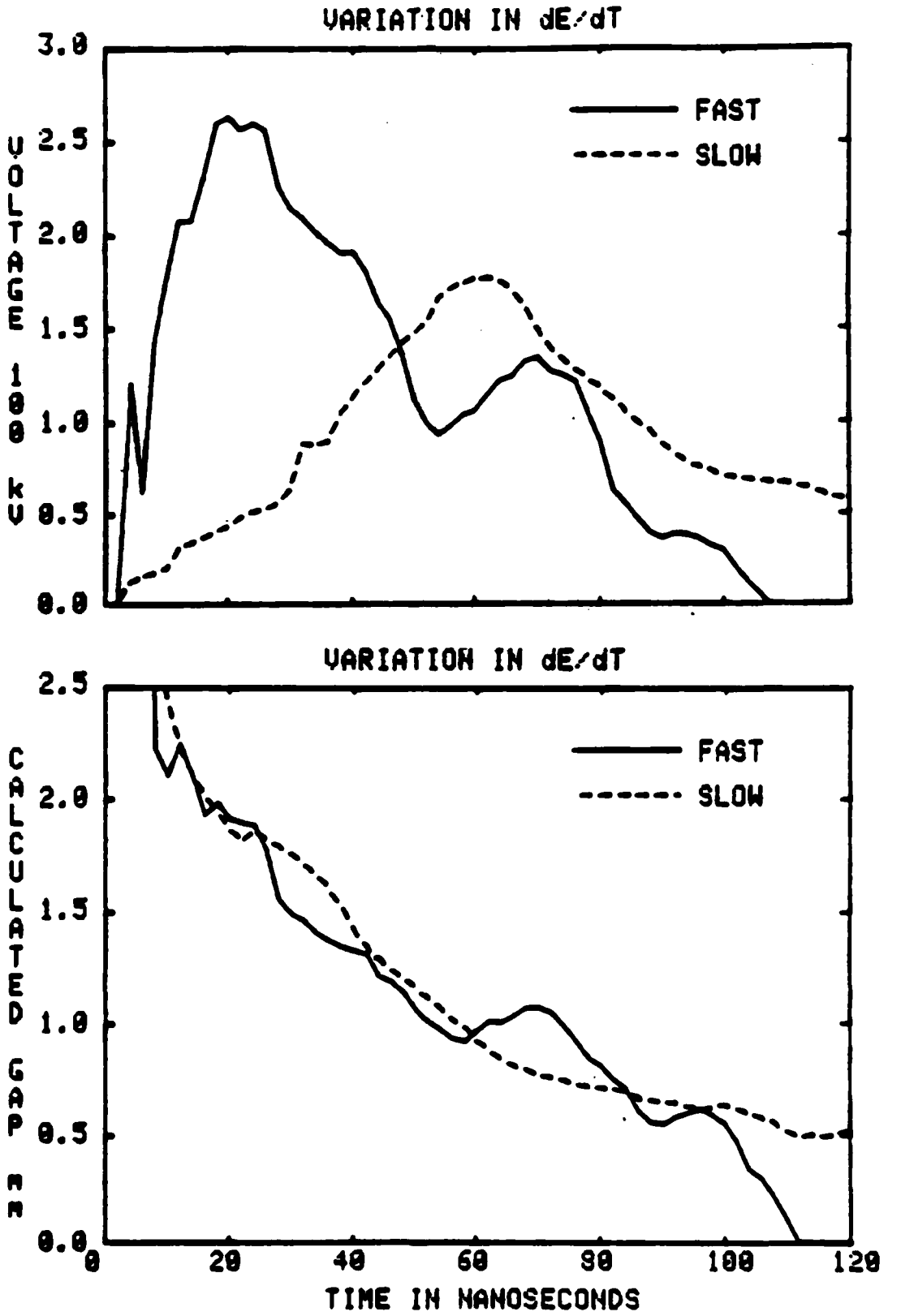

Fig. 6.10: (top) Voltage traces for shots with different $dE\ dt$: (bottom) calculated gaps for these shots.

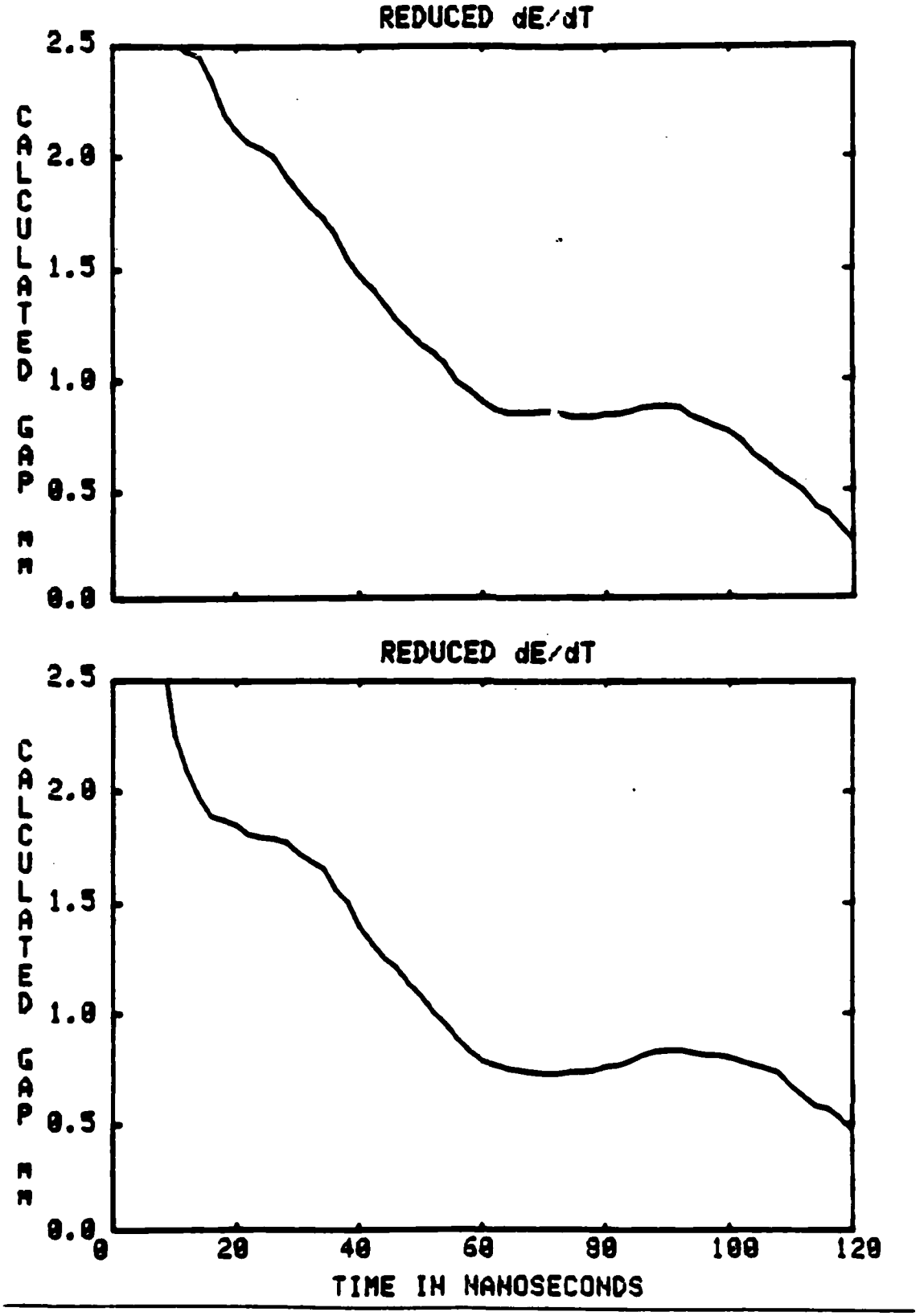

Fig. 6.11: Calculated gaps for other shots with reduced $dE\ dt$.

this case were similar to those in Ref. 43). The details of the gap behaviors differ later in time, with the reduced dE/dt shots showing a slowdown rather than an opening and a constant gap for about 40 ns. The difference in calculated gap behavior at this time is consistent with the claim that electric pressure effects are influenced by the shape of the current trace, since that shape was different on the reduced dE/dt shots.

There is an important point to be noted here. From the results of Ch. 4, the two shots in Fig. 6.10 (normal dE/dt with a Poco cathode, and reduced dE/dt) represent extremes of inferred plasma uniformity. In particular, reduced dE/dt is seen to cause highly nonuniform plasma formation. However, the calculated gaps (during early times) are similar for the two cases. From this it can be concluded that agreement of the measured perveance with that calculated for a uniform emission surface does not necessarily imply that the surface is indeed uniform.

In fact, the nonuniform luminosity for these shots observed in Ch. 4 suggests that the electric pressure effect may be enhanced by the dimensional effects of the expansion of plasma bumps (as opposed to that of a plane layer).

6.7.3. Effects of Current Density

The planar and 'exact' gap calculations are compared for the 1.6 mm and 9.6 mm cathodes in Fig. 6.12. For the wider cathode the two are in good agreement while there is a significant difference between the two for the narrower cathode. This is as expected since edge effects will be more important in that case. The gap for the 1.6 mm cathode was sufficiently small so that the closure time could be clearly identified; this gave a maximum *average* closure velocity of 1.7 cm/μs.

Calculated expansion curves are shown for the four diodes and for both models in Figs. 6.13 and 6.14 (these curves are just the gaps turned upside down — the distance plotted is that between the plasma front and the cathode, rather than the anode surface). For both models, the calculated expansion curves for different cathodes are fairly similar, consisting of a constant expansion velocity of about 3 cm/μs, followed by an apparent opening. For both models the opening is greater for the higher current density cathode. There is an inherent uncertainty in any determination of relative closure velocities at different current densities, because

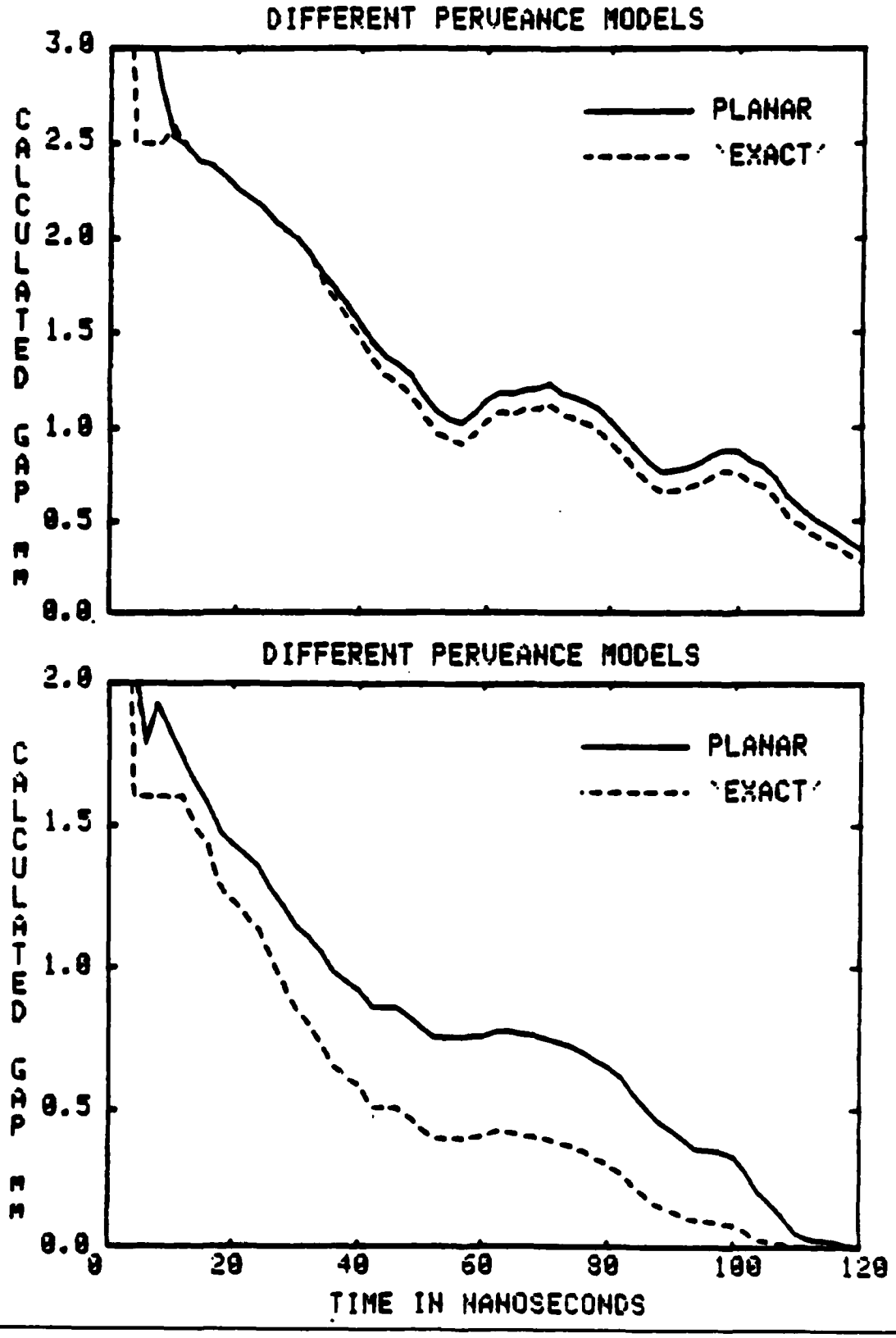

Fig. 6.12: Comparison of perveance models for the 9.6 mm cathode (top) and 1.6 mm cathode (bottom).

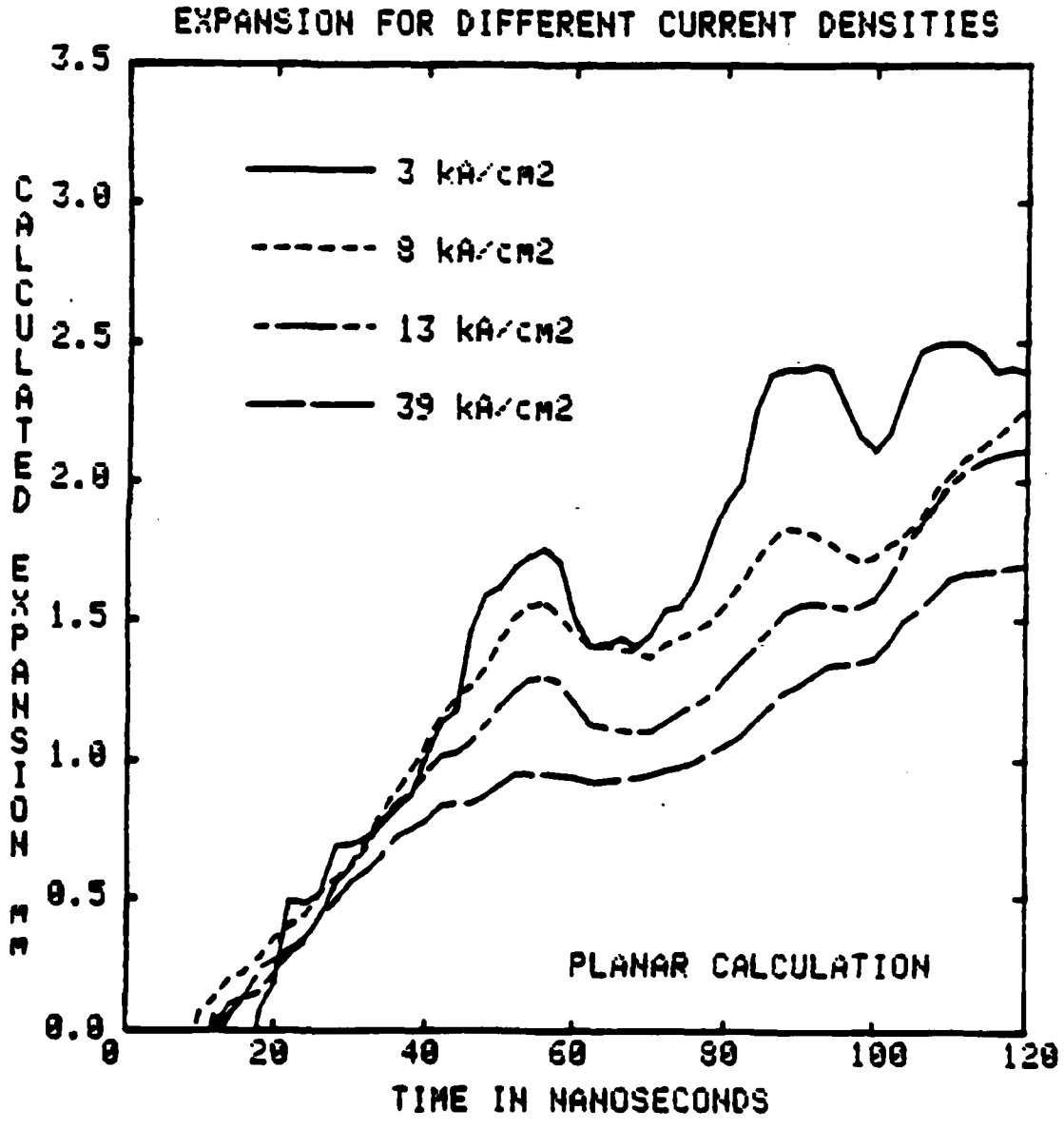

Fig. 6.13: Calculated gaps based on the planar model for different current densities.

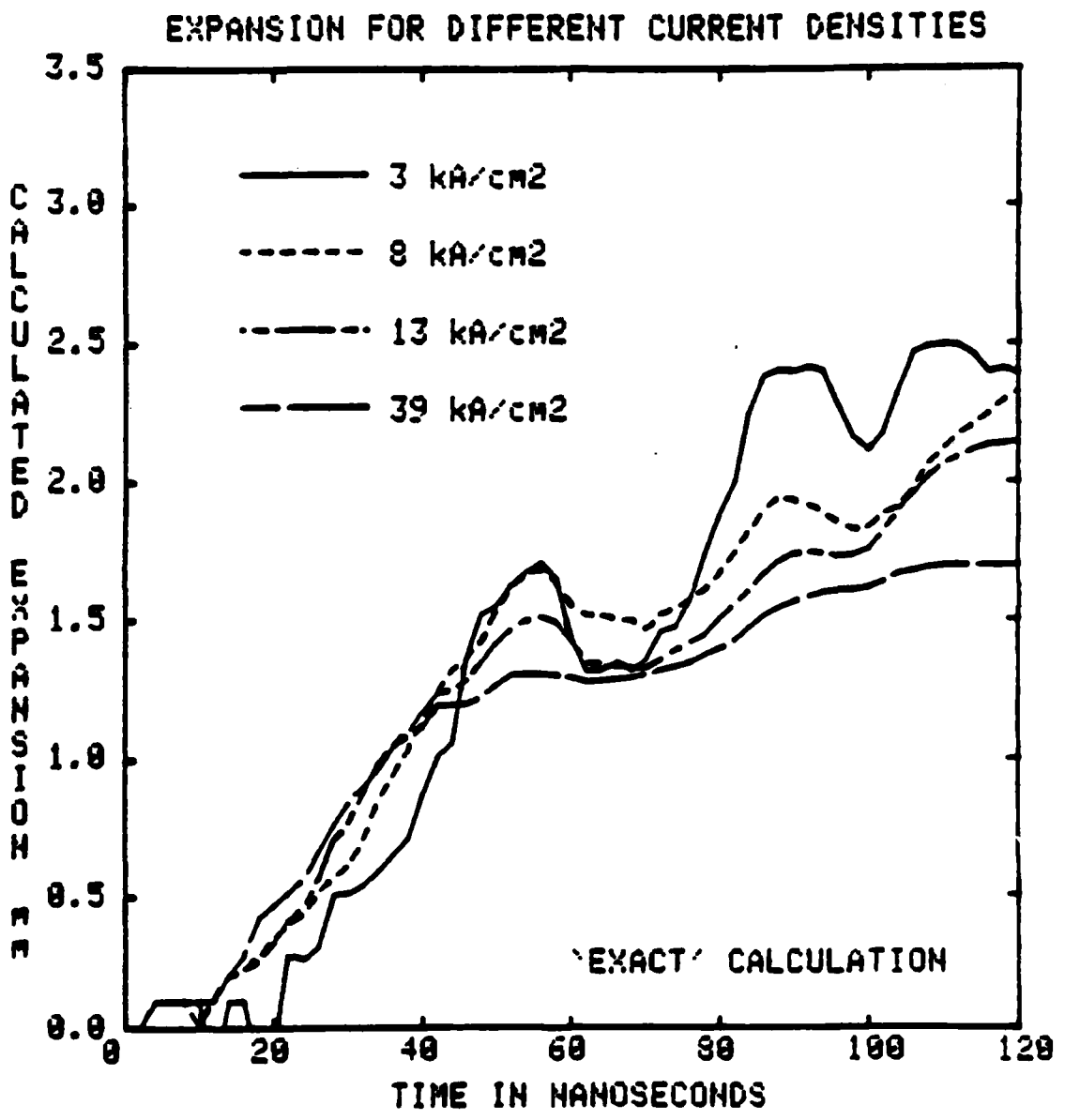

Fig. 6.14: Calculated gaps based on the 'exact' model for different current densities.

of the different geometries involved, but it can certainly be stated that there is no observed increase in closure velocity with current density.

6.8. Discussion

From these measurements it can be concluded that the cathode material, surface coating, dE/dt, and temperature (up to at least 700°C) have no effect on the plasma expansion velocity, and the current density (over a factor of 13) apparently has no effect. This is in agreement with the findings in Ref. 143, where the inferred velocity was relatively independent of geometry and cathode material. Further indication of an independence of velocity on current density comes from the results of Ref. 144, where an expansion velocity of 1.5 cm/μs was inferred for a long pulse diode at an average current density of a few A/cm^2; this is to be compared with the maximum *average* velocity of 1.7 cm/μs inferred in this experiment for a current density of 39 kA/cm^2.

The ratio of plasma density to current density will affect plasma motion to the extent that such motion is influenced by electric pressure. Since diodes with current densities differing by a factor of 10^4 are seen to have similar closure velocities, it is tempting to conclude that the cathode plasma density is in some sense proportional to the current density. To the extent that plasma motion is influenced by thermal expansion, it it also tempting to conclude that the plasma temperature is independent of current density. Both of these points will be discussed in later chapters.

On the other hand, velocities reported in the literature range from 1.5–5 cm/μs, and it is to be wondered what factor causes differences in expansion velocity, since so many of them have been eliminated here. It is suggested here that the differences in reported velocities are due more to the ambiguities mentioned in this chapter than to actual differences in velocity. An example to illustrate this is taken from Ref. 43, which is the most careful study to date. In Fig. 6.15, the calculated gap is given for the voltage and current traces in Fig. 12 of that reference, using the same pervence model as the authors. An expansion velocity of 1.8 cm μs was quoted for this shot, and this velocity is indicated by one of the

dashed lines in Fig. 6.16. The deviation between calculated and measured perveances that occured at 50 ns was taken as evidence of anode plasma formation. However, as shown by the other (steeper) dashed line the figure, a velocity of 3 cm/μs, with a 10 ns delay, fits the data equally well. Most of the other references involve less detailed analysis, and many involve diodes strongly influenced by anode plasma and ion current effects, so that the plasma velocities quoted in those references are even more subject to uncertainty.

6.9. Conclusions

The machine prepulse had no effect in this experiment.

The motion of the plasma emission layer has been calculated, based on perveance models and the diode electrical characteristics, and the effects of several parameters have been investigated. The cathode material, surface coating, temperature (up to 700°C), and dE/dt (over a factor of six) are seen to have no effect on the plasma velocity. The current density (over a factor of 13) also has no apparent effect.

By comparing these measurements with those of luminosity uniformity in Ch. 4, it is concluded that the agreement of the measured perveance with that calculated for a plane layer is not sufficient evidence that such a layer exists.

The calculated expansion velocity is between 1.7 and 3 cm/μs, depending on whether the average or instantaneous velocity is used. These velocities are consistent with those quoted in the literature, considering the uncertainties and ambiguities involved in the determination of absolute velocities.

According to these calculations, the plasma emission layer is seen to move with a constant velocity for about 60 ns. After this the motion is seen to change and it is suggested that this change is produced by the (falling, then rising) shape of the current trace through electric pressure effects.

Tentative conclusions regarding the dependence of plasma density, and the independence of temperature, on current density have been advanced; these ideas will be addressed in later chapters.

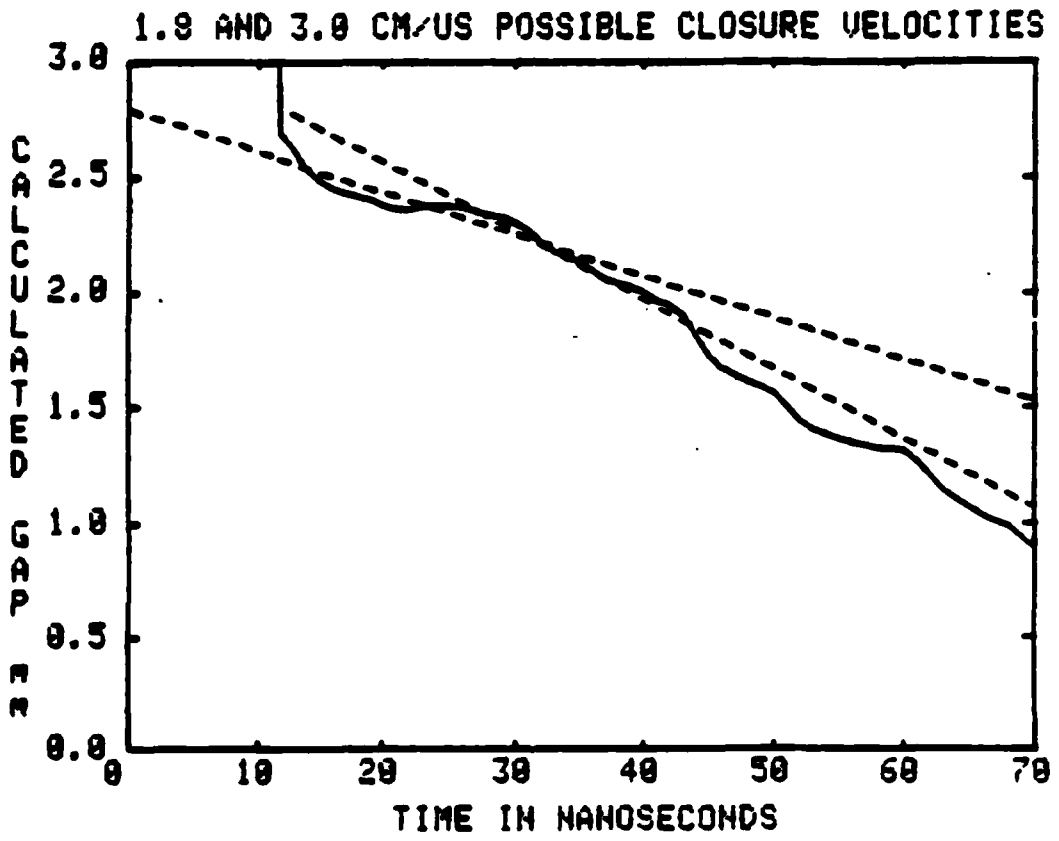

Fig. 6.15: Possible expansion velocities for the traces given in Fig. 12 of Ref. 43. using the perveance model of the authors.

As far as the physics is concerned, it is seen that the motion of the plasma emission layer is a complicated process which depends on both the hydrodynamics of the expanding plasma, which is apparently similar for all diodes. and the 'demands placed on that plasma' by the external electric circuit. The emission layer motion depends not only on the plasma density and current density, but also on the plasma density gradient, the dimensionality of expansion, and the shape of the current pulse.

As far as diode design is concerned, cathode plasma expansion cannot apparently be reduced by some magic choice of cathode properties such as surface coating or current density. It is conceivable that plasma expansion could be reduced by a clever combination of the external driving circuit and the diode geometry. In particular, the influence of the shape of the current pulse has significant ramifications for diode design, as will be discussed further in Ch. 11.

Chapter 7

Electron Density

7.1. Introduction

This chapter describes electron density measurements obtained from interferometry. A two frame Mach-Zehnder interferometer,[159] using a double pulse nitrogen laser as a light source, was used to measure the plasma electron density. After a brief discussion of interferometry, the interferometer system, including the laser, interferometer optics, and the alignment procedure, is described. Sec. 7.3 consists of a review of previous density measurements obtained both from interferometry and erosion measurements. The data is presented in Secs. 7.4 and 7.5. The former consists of a general descripton of the features of the interferograms and the latter consists of a quantitative analysis of the interferograms and a comparison of interferograms from shots with different cathodes and current densities. Comparisons with previous work and conclusions are given in Secs. 7.6 and 7.7.

7.1.1. Mach-Zehnder Interferometer

The arrangement of this system is shown in Fig. 7.1. In the following, the z-axis is taken to be along the direction of laser beam propagation, with the x-y plane then transverse to the beam.

In its simplest form, the interferometer consists of two beamsplitters and two mirrors: The input light is split into two beams which travel along opposite legs of a rectangle to be recombined at the output beam splitter. Photographic film is used to record the intensity distribution in the x-y plane of the resulting output beam.

For a uniform input beam, this intensity distribution is determined by the difference in optical path length (at each point in the x-y plane) between the two legs of the interferometer, and is a maximum for

$$\Delta(\xi dl) = N\lambda \qquad (7.1a)$$

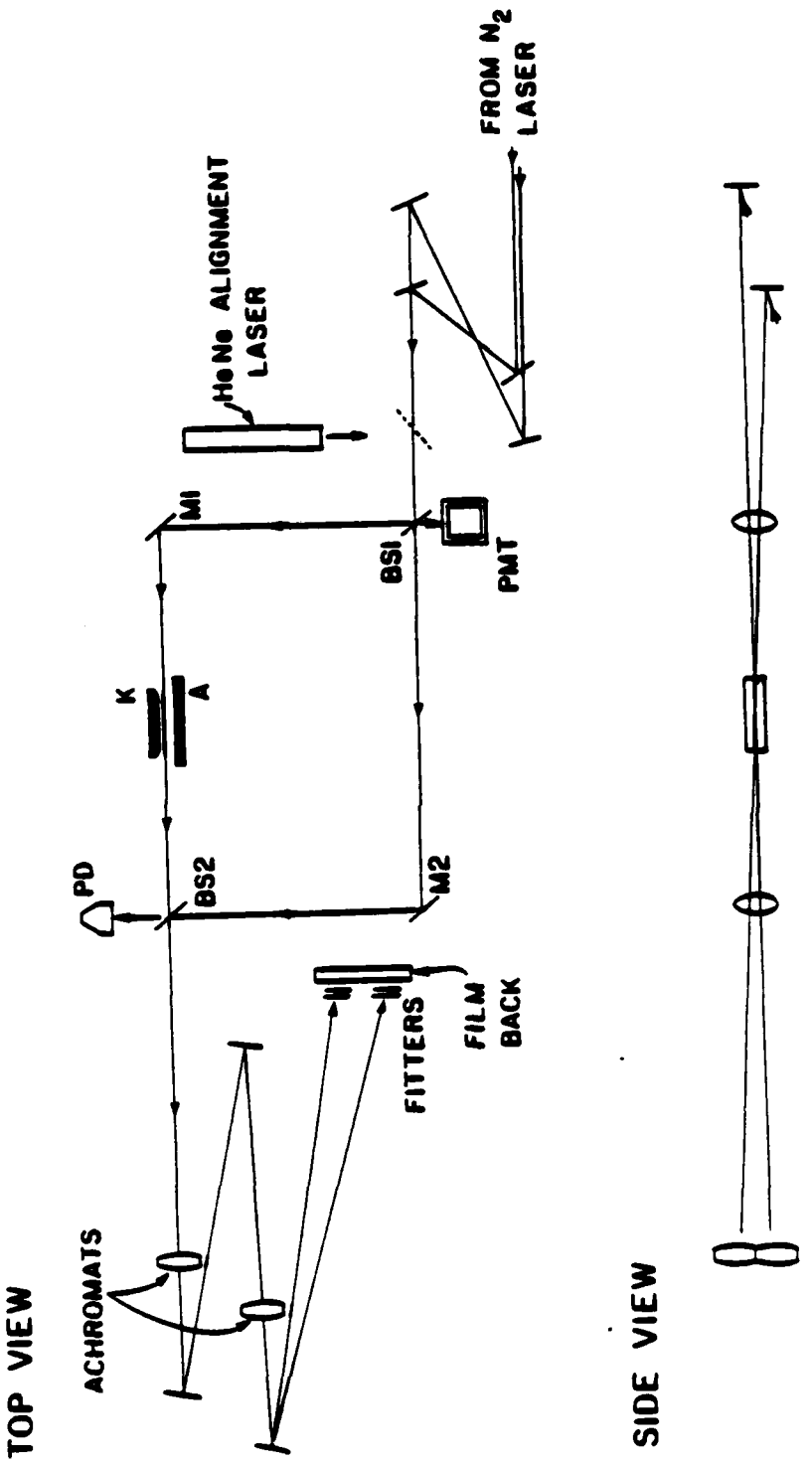

Fig. 7.1: Arrangement of the Mach-Zehnder interferometer.

and minimum for

$$\Delta(\xi dl) = (N + 1/2)\lambda \tag{7.1b}$$

where λ is the laser wavelength, ξ the (phase) refractive index (this symbol is used to distinguish the index of refraction from the density), l the path length, and $N = 0, 1, 2...$ If the planes of the four optical elements are all parallel then the phase difference will be constant across the x-y plane and the film exposure will be uniform. If one of the elements is then tilted around (for instance) a horizontal axis, the phase difference will vary linearly in the vertical direction, causing a series of horizontal stripes, or fringes, on the film. Now, if the refractive index differs from unity along part of one leg (e.g., in the A-K gap) in a local region of the x-y plane, the fringes will be bent. The local bending of the fringes is given by

$$\delta N = \frac{L(\xi - 1)}{\lambda} \tag{7.2}$$

where L=the path length of the disturbance and δN is the shift expressed in the number of fringes. Thus, the interferometer will record, at a given instant in time, the local line averaged refractive index at each point in the A-K gap.

7.1.2. Index of Refraction

The dielectric constant $\epsilon = \xi^2$ of a material is given by[160]

$$\frac{\epsilon - 1}{\epsilon - 2} = 1 - \sum_{\alpha} \frac{4\pi n_\alpha e^2}{3m} \sum_{j} \frac{f_j}{\omega_j^2 - \omega^2 - i\omega\gamma_j} \tag{7.3}$$

where n_α is the density of electrons in level α, f_j is the oscillator strength for transitions from that level to level j, ω_j is the frequency of the transition, γ_j the linewidth. and ω is the frequency of the probing light. The effect of free electrons $n_\alpha = n_e$ is taken into account formally by replacing the sum over transitions with a single term for which $f_j = 1$ and $\omega_j = \gamma_j = 0$. If the density is sufficiently low so that $\epsilon - 1 \ll 1$ and the probing frequency is not close to any transition frequencies ($\omega - \omega_j \gg \gamma_j$), then ϵ is purely real and

$$\epsilon \approx 1 - \frac{\omega_{pe}^2}{\omega^2} - \sum_{\alpha} \frac{4\pi n_\alpha e^2}{m} \sum_{j} \frac{f_j}{\omega_j^2 - \omega^2} \tag{7.4}$$

where ω_{pe} is the electron plasma frequency. The first term gives the contribution from free electrons and the second term gives that from bound electrons.

The free electron term is modified by the presence of a magnetic field and/or by collisions; these effects are negligible if the probing frequency is significantly greater than the electron cyclotron frequency and collision frequency, respectively. That condition is satisfied by several orders of magnitude in this experiment. (The ions also contribute to the dielectric constant, but that effect is down from the electron effect by a factor of the electron-ion mass ratio).

For $\epsilon \approx 1$, the index of refraction is then given by

$$\xi - 1 \approx -\frac{n}{2n_c} + \sum_{\alpha} \frac{n_\alpha}{2n_c} \sum_j f_j \frac{\lambda_j^2}{\lambda^2 - \lambda_j^2} \tag{7.5a}$$

$$n_c = \frac{mc^2}{e^2\lambda^2} \tag{7.5b}$$

Where now the probing light and the transitions are given in terms of wavelength and n_c is the density of free electrons at which cutoff occurs (in the absence of bound electrons). For the 3371 Å laser line, $n_c = 9.7 \times 10^{21}$ cm^{-3}.

It can be seen that the index of refraction, and hence the fringe shift, is proportional to the density. For the 7 cm path length of this experiment, a shift of one full fringe will occur at an electron (neglecting bound electrons) density of about 10^{17} cm^3.

The contribution from the bound electrons can be of either sign, depending on the sign of $\lambda - \lambda_j$. If the material is cold, then all of the atomic species will be in their ground states. Since most transitions out of the ground state of an atom or ion have frequencies in the UV, the effect of cold material is generally to increase the index of refraction and act in the opposite direction as the free electrons. This may not always be true; for example, the ground state of neutral aluminum has resonance lines at 3944 and 3961 Å, and if the probing wavelength is slightly below these lines then neutral aluminum will tend to decrease the index of refraction. In any event, if appreciable numbers of atoms or ions are in excited states, then all bets are off and the determination of the effect of bound electrons

becomes a complicated calculation, requiring a knowledge of the populations of all levels of all species.

Fortunately, in this experiment the effect of bound electrons may be neglected, as will be shown. The numbers of bound electrons and free electrons may be assumed to be roughly equal (the spectroscopy described in Ch. 9 shows that the plasma consists mainly of multiply ionized species. Each ion contributes 1–3 free electrons, and each ion has generally 1–3 valence electrons. Inner shell electrons will not contribute to the index of refraction at these frequencies). It is also shown in Ch. 9 that most of the ions are expected to be in their ground states, with typical transition wavelengths of 1000 Å. With a typical oscillator strength of 0.5, the bound electron contribution is seen to be less than that of the free electrons by about a factor of twenty.

This is all assuming that there are no lines close to the laser wavelength. None of the lines listed in Ref. 161 (including all those observed in this experiment) are close to the laser line. Any possible unknown impurity with a line close to the laser line would presumably occur in such small concentration that there would be little effect on ξ. Further discusion of influence of bound electrons on ξ can be found in Ref. 162.

7.2. Experimental Description

7.2.1. Description of the Laser

The double pulse nitrogen laser which was constructed for the interferometer is shown in Fig. 7.2. with a schematic diagram and equivalent circuit shown in Fig. 7.3. This consists of two atmospheric pressure TEA lasers, closely based on designs given in Refs. 163 and 164, in a single box with a common gas feed, trigger input and charging voltage input. Each laser produces a pulse of <3 ns duration at 3371 Å. The output power has not been measured but powers of several hundered kilowatts are quoted for similar lasers in the literature. The beam divergence was fairly large, as is typical for nitrogen lasers, being about 15 mr.

There are several advantages to using a nitrogen laser as a light source for the interferometer. The short pulse allows excellent time resolution and, as the

Fig. 7.2: Photograph of the double pulse nitrogen laser.

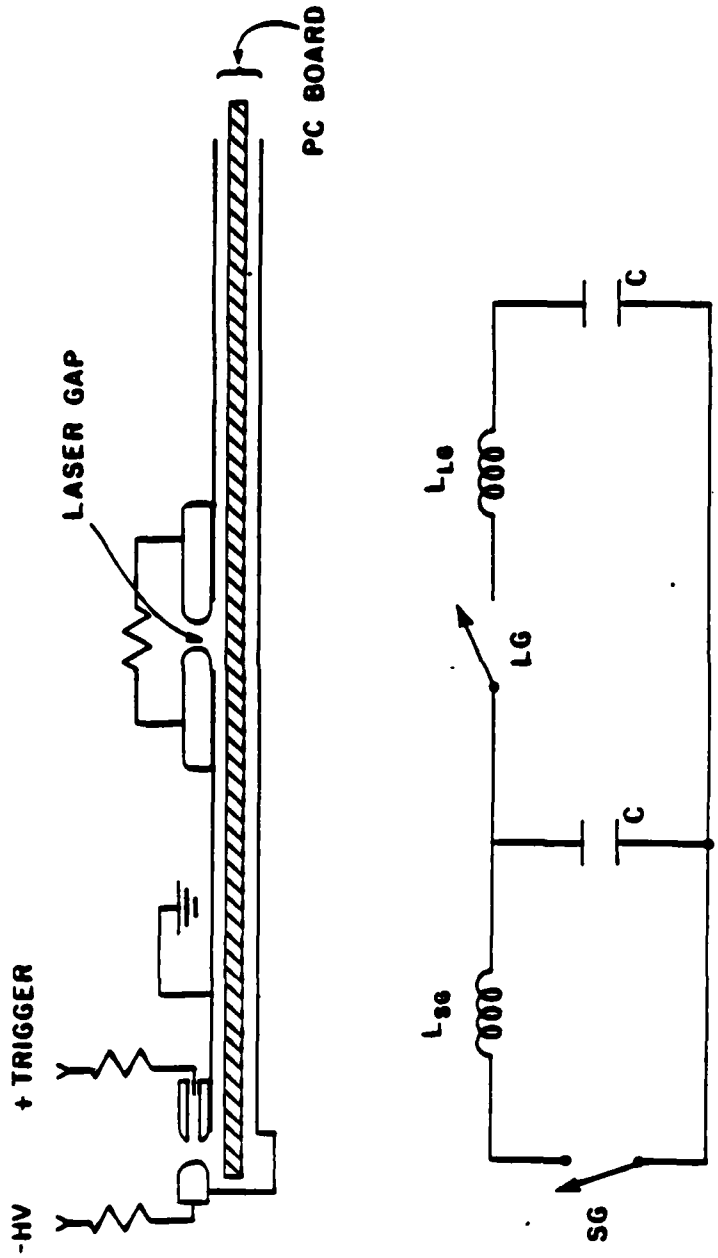

Fig. 7.3: (top) Laser schematic; (bottom) equivalent circuit diagram.

laser may be pulsed at 5–10 Hz, it is essentially CW for alignment purposes. While the wavelength is too short to observe electron densities below $10^{16}/\text{cm}^3$ (in this experiment) it offers the convenience of working in the near visible (exposed Polaroid film scintallates very brightly, so that the beam pattern may be easily viewed) and the beam may be recorded using Polaroid film. Finally, this is the simplest (and cheapest) laser to build, as the atmospheric pressure eliminates the need for a sealed tube and the large gain of the medium eliminates the need for output mirrors.

The laser channel consists of two 30 cm long by 6 mm high aluminum electrodes, set about 4 mm apart and resting on a sheet of 0.035 mm copper clad fiberglass epoxy printed circuit board (see Fig. 7.3). The printed circuit board is etched to form an LC inversion circuit[165] which impresses a pulsed voltage of ~20 kV, with a 30 ns risetime, across the laser gap. This circuit works in the following way: when the spark gap closes, the capacitor C_1 discharges through the switch inductance L_1, and as the voltage across C_1 goes through zero and swings negative, a voltage approaching twice the initial charging voltage appears across the laser gap, causing it to break down. Once this occurs, the spark gap may subsequently be regarded as an open circuit (since $L_1 \gg L_2$, the laser channel inductance) and the two capacitors discharge in series through L_2 to pump the laser. For proper operation the electrodes are spaced slightly closer at the back end to initiate breakdown there so that a traveling wave is launched toward the output end. Single pass lasing (i.e., a superradiant oscillator) is possible but the presence of a mirror at the back end increases to output power several times. Nitrogen is flowed at slight overpressure through the spark gaps and laser channels.

The spark gaps consist of homemade trigatron type switches. The Pulsepak 10-A is used to trigger the gaps in parallel and a cable delay between the two gaps controls the interpulse timing. When the gaps are properly adjusted (by varying the gap length and trigger pin placement) so that the trigger pin breaks down first to the opposite electrode. the spark gap jitter is <1 ns and the laser jitter is <3 ns.

Tuning up the laser consists of first adjusting the spark gaps, and then adjusting the spacing and angle between the laser electrodes and the orientation of the rear mirror to optimize the brightness of the output beam. Trigger pin and laser gap voltage monitors were built in to aid in spark gap adjustment. The laser performance is relatively insensitive to the gas flow rate, which was about 2 lpm.

Once tuned up, the laser worked quite reliably for several months at a time before routine maintainance (polishing the laser and spark gap electrodes) was necessary. Occasionally the printed circuit board dielectric would break through at the etched copper edges; in this case the copper was scraped away in the area of the hole, which was then sealed.

7.2.2. Interferometer Optics

The interferometer optical arrangement is shown in Fig. 7.1. In the previous discussion of fringe shifts it was assumed that rays of light passing through the diode are not strongly bent. Bending of the rays can occur due to two effects: a gradient in the index of refraction and grazing incidence reflection from the electrodes. In the first case, the bending is given by

$$\tan\theta = l\frac{d\xi}{dx} \tag{7.6}$$

The largest observed density gradients in this experiment were about $4\times10^{18}/\mathrm{cm}^4$ which implies a bending angle of $\sim$1 mrad. The observed bending due to reflections was of this order also. To reduce these effects the electrode plane was conjugated with the film plane by an achromatic lens. An achromat was necessary as the spherical aberration caused by a normal lens was observed to severely distort the fringes. With a lens, the residual resolution limitations due to bending are due to the finite depth of field of the electrodes: for an angle of 1.3 mrad (with 1:1 magnification) and electrode half length of 3.5 cm, the resolution is about 0.05 mm.

In the drawing, a second set of lenses, which magnify the image 4x, are shown. This arrangement aided in real time data analysis and was used for many of the shots but suffered from the fact that the depth of field in the image plane was increased by 16 times (for a system of magnification M, the depth of field in the

image plane is M^2 times that in the object plane) with a resulting resolution of ~0.8 mm on the film, or 0.2 mm actual size.

The two laser beams were aligned with four steering mirrors to run parallel to the electrode surfaces and cross in a vertical plane. The eight degrees of freedom given by the mirrors (two axis tilt for each mirror) were used to: position the beams in the x-y plane to pass through the diode gap (4 degrees of freedom); position each beam to pass as parallel as possible to the electrode surfaces (2 degrees); adjust the crossing angle to the minimum required to allow each beam to pass through a separate achromat; and adjust the angles (in the vertical plane) to be approximately equal for each beam.

All optical surfaces were flat to one tenth wave or better, the beamsplitters were coated with antireflection coatings on the rear side to minimize ghost images, and aluminum coated mirrors, which reflect well at 3371 Å, were used. Fused silica beamsplitters were used while the achromats were a flint glass/crown glass combination which did not absorb too strongly at this wavelength. Interference filters with 30 Å bandwidth[166] were placed in front of the recording film (Polaroid 667) to reject plasma and room light (no shutter was necessary if the room light was dim) and Kodak ND filters were also used.

The fringes in the x-y plane at the recording film occur due to a coherent superposition of the two beams in the interferometer. In order for this superposition to be coherent there are two requirements which must be met. The laser has a finite bandwidth which gives rise to a finite longitudinal coherence length of the beam and the path difference between the two legs must be less than this length. In addition, the laser beam has a finite coherence length in the transverse direction and the relative displacement between the two beams in the x-y plane (produced by imperfect interferometer alignment) must be less than this lateral coherence length. The longitudinal coherence length of this laser is of the order of mm while the lateral coherence length is much less.

7.2.3. Alignment Procedure

Since the Mach-Zehnder interferometer has the desirable property that the fringe pattern is independent of the input beam angle, the interferometer optics and steering optics could be aligned independently. The interferometer was aligned first using a set of alignment fixtures which were located by holes in the interferometer baseplate and which defined a rectangle in the horizontal plane. A helium-neon laser beam was sent through the interferometer, and the entrance beamsplitter and two mirrors were adjusted to send the two resulting beams around this rectangle, to recombine at the output beamsplitter, which was then adjusted so that the output beams overlapped. By aligning the beams to form a rectangle the path lengths were set equal.

These adjustments were sufficient to produce fringes with the HeNe laser. Then, the N_2 laser was sent through the interferometer and only a small amount of adjustment was necessary to get fringes with it. The spacing and angle of the fringes could be varied by adjusting mirror 2.

The vacuum windows were 3 mm quartz plates.[167] The index of refraction of the quartz added to the index of refraction of one leg and that was often enough to degrade the fringe quality. In that case, compensating quartz plates were added to the other leg.

Once fringes were obtained, the steering optics were adjusted. The most critical point here was the need to have the beams parallel to the electrode surfaces — this was checked by measuring the apparent gap on a film exposure; the decrease in apparent gap from the actual gap is indicative of the angle of misalignment. In general, the resolution of the interferometer as limited by misalignment and finite depth of field was about 0.1–0.2 mm.

Finally, the exit optics alignment was straightforward.

7.2.4. Operation

The operation of the interferometer consisted of taking a reference exposure before the shot and a separate exposure during the shot. Interpretation of the interferograms depends on the fact that those taken during the shot have undisturbed fringes in some section of the x-y plane.

Once aligned, the interferometer was quite stable, requiring only minor adjustment (if any) of M2 from shot to shot. The total alignment procedure only needed to be carried out every few months or so. The windows got dirty after a few shots and were cleaned with NaOH solution (to remove carbon and aluminum) or HNO_3 solution (to remove other metals), depending on the anodes used.

In general, while tuning up the laser and interferometer from scratch was a rather lengthy procedure (requiring about one day), the subsequent operation of this dignostic was very straightforward and required little effort.

7.3. Review of Previous Work

The quantity of material in the cathode plasma was first deduced, in the case of vacuum arcs and needle cathode experiments, by the the cathode erosion measurements discussed in Ch. 2. Subsequently, interferometric (in vacuum arc, needle cathode, and broad area cathode experiments) and electrostatic probe (in vacuum arcs) techniques have been employed to measure the plasma density directly, and with temporal and spatial resolution. The erosion measurements will be reviewed first.

7.3.1. Erosion Measurements

The erosion measurements determined the total (metallic) mass removed from the cathode. Since the mass removal was observed to increase with increasing charge transfer, the results of erosion measurements are generally quoted in terms of the electron transport coefficient, defined as the ratio of mass removed to charge supplied by the cathode. On clean surface vacuum arcs, this quantity is typically about 10^{-4} g C, as reviewed in Ref. 32, or about 0.3 ions (or atoms) for every (current) electron transfered. The erosion measurements of needle cathodes gave a similar result.

Investigations with various collectors have shown that this erosion consists of directed ion flows[168] (to be discussed further in the next chapter) at a rate of about 0.1 ion per electron, with the remainder consisting of fine (~100 Å–1 μm) liquid droplets.[169] These droplets move with velocities from 10^3–10^5 cm/μs,[170] with higher velocities for smaller droplets. Droplets have also been observed in a 50 ns pulsed diode[171] (again, due to the current density the surface is presumed clean) although in that experiment the droplet fraction was estimated at being smaller than the ionic fraction.

The metallic erosion of dirty surfaces is much less, being typically about 10^{-7} g/C.[32] However, a large quantity of material is supplied in this case by cathode surface layers. In Ref. 89 micrographs are shown of the erosion of hydrocarbon and oxide layers with no visible erosion of the underlying metal; according to Jüttner, the total erosion can be greater than with clean cathodes. Also, in Ref. 172, it is concluded that erosion of dirty cathode surfaces is mostly erosion of the oxide layer.

7.3.2. Interferometric Measurements

Interferometric and electrostatic probe measurements of vacuum arc plasma densities are reviewed in Ref. 34. The plasma densities increase with increasing current density and are consistent with the electron transport coefficients measured in the erosion studies.

Cathode plasma density measurements have been made in several experiments, using the techniques of (holographic) interferometry and Stark broadening.

Bugaev *et al.* reported on interferometric measurements of plasmas in a diode involving a needle cathode, with a diameter of roughly 100 microns, and a 0.7 mm gap.[173] Electron densities of about 10^{19} cm^{-3} were observed and plasma jetting from the gap was also observed after gap closure. The electron transport coefficient was calculated to be about 5×10^{-5} g/C.

Mix *et al.*[174] observed cathode and anode plasmas with ruby laser holographic interferometry. The cathode consisted of an approximately 1 mm diameter needle, with a planar anode and 1.6 mm gap. The electrical parameters were not given

but the diode was driven by a Nereus accelerator. Electron densities ranging from 2×10^{18} to $10^{19}/cm^3$ were observed. Kelly and Mix reported on interferometric observations of a diode involving a glass rod cathode.[175] The holograms obtained were of rather high (~50 μm) resolution. Early in time (the time was not given), a bumpy plasma surface could be seen on the cathode, with the bumps separated by about 100 μm, and it was suggested that these bumps might be plasma flares from individual emission sites. The densities observed ranged from about 10^{18} to $10^{19}/cm^3$. Close to the cathode the plasma is seen to be opaque — this opacity was attributed to refraction. After the plasmas shorted, plasma jets were seen from the colliding plasmas. In the above experiments, the current densities were high ($>10^6 A/cm^2$).

Swain *et al.* carried out interferometric observations of diode plasmas in a diode with a few cm^2 area, also pulsed by a Nereus accelerator.[136] Plasma densities of about 8×10^{16}–$3\times10^{17}/cm^3$ were observed.

Electron densities based on time integrated Stark broadening of hydrogen and carbon lines were measured by Bekefi *et al.*[176] This experiment involved a cylindrical diode immersed in an axial magnetic field, with a Poco graphite cathode. In order to maximize the line intensity, the diode was filled with hydrogen for some time before each shot with the purpose of permeating the electrodes with hydrogen. They found densities of about 2×10^{17} cm^3 when no magnetic field was applied and about 1–2×10^{16} cm^3 when a strongly insulating field (about 1.6 times the cutoff field) was applied.

Interferometric and Stark broadening measurements were mentioned by Baksht *et al.*[118] in a study of the cathode plasma in a cylindrical magnetically insulated diode, at a current density of about 10^2 A/cm^2. An upper limit to the density of 10^{15} cm^3 was given.

Other density measurements were reported in Refs. 177 and 178, but these experiments involved ion beam diodes where the uncertain effects of ion bombardment of the cathode limit the applicability of the results to the present case.

In the above experiments, the observed plasma densities increase with increasing current density. The densities are seen be greatest at the cathode and decrease out into the gap.

7.4. Qualitative Measurements

The area observed by the interferometer is shown in Fig. 7.4. As mentioned in Ch. 3, the one sided feed caused a magnetic field assymetry, in that the field was large on the upper cathode edge and decreased to zero on the lower edge. The electrode positions in the drawing correspond to negative polarity operation. In the subsequent interferograms, the cathode will either be on the right or left side of the picture depending on the machine polarity.

A typical sequence of interferograms is shown in Fig. 7.6. The timing of these interferograms is indicated in Fig. 7.5. In these interferograms the cathode is on the right side. In all of the interferograms, a fringe shift in the downward direction corresponds to a decrease in the index of refraction (i.e., as caused by free electrons) while a shift in the upward direction corresponds to an increase in the index of refraction (due to bound electrons). The dependence of direction of fringe shift on refractive index was determined by observing the fringe pattern caused by a drop of methanol on the quartz window. Aerodagged 6.4 mm cathodes were used in these shots.

A slight fringe shifting at the cathode can just be seen in the first interferogram. By 40 ns (second interferogram) the fringe shift is quite noticeable. As time progresses, the fringe displacement at the cathode increases and the point where a bending of the fringes can first be observed moves out from the cathode. On the last interferograms an opaque region can be seen coming off of the anode. By the end of the shot the maximum fringe shift is about one fringe, implying an electron density of $10^{17}/cm^3$. The point of first noticeable fringe displacement, which will henceforth be referred to as the bend point (see Fig. 7.15), has moved about 0.7 mm from the cathode by the end of the shot. Assuming that this point corresponds to a bending of 0.1 fringe implies that this corresponds to a density of 10^{16} cm^3. The fringe shift decreases roughly linearly from the cathode

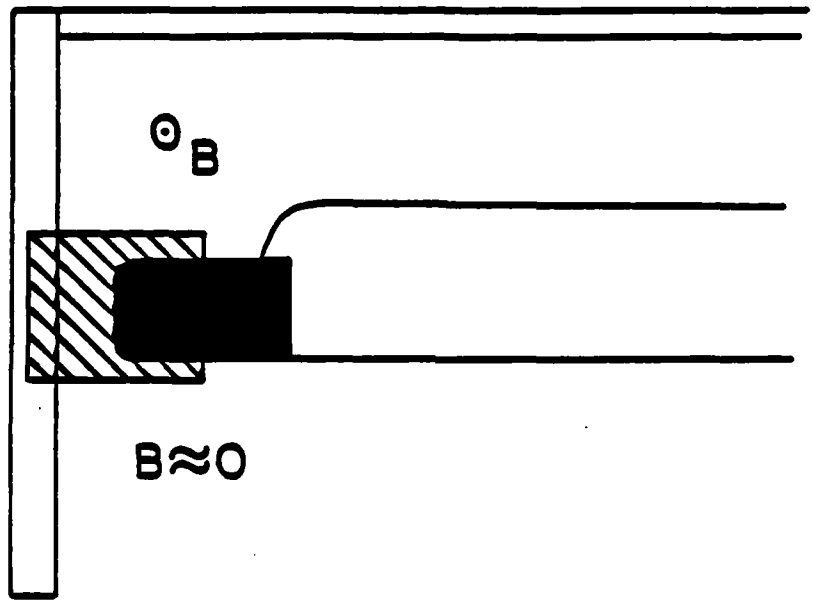

Fig. 7.4: The area viewed by the interferometer is shaded. Note the magnetic field assymetry.

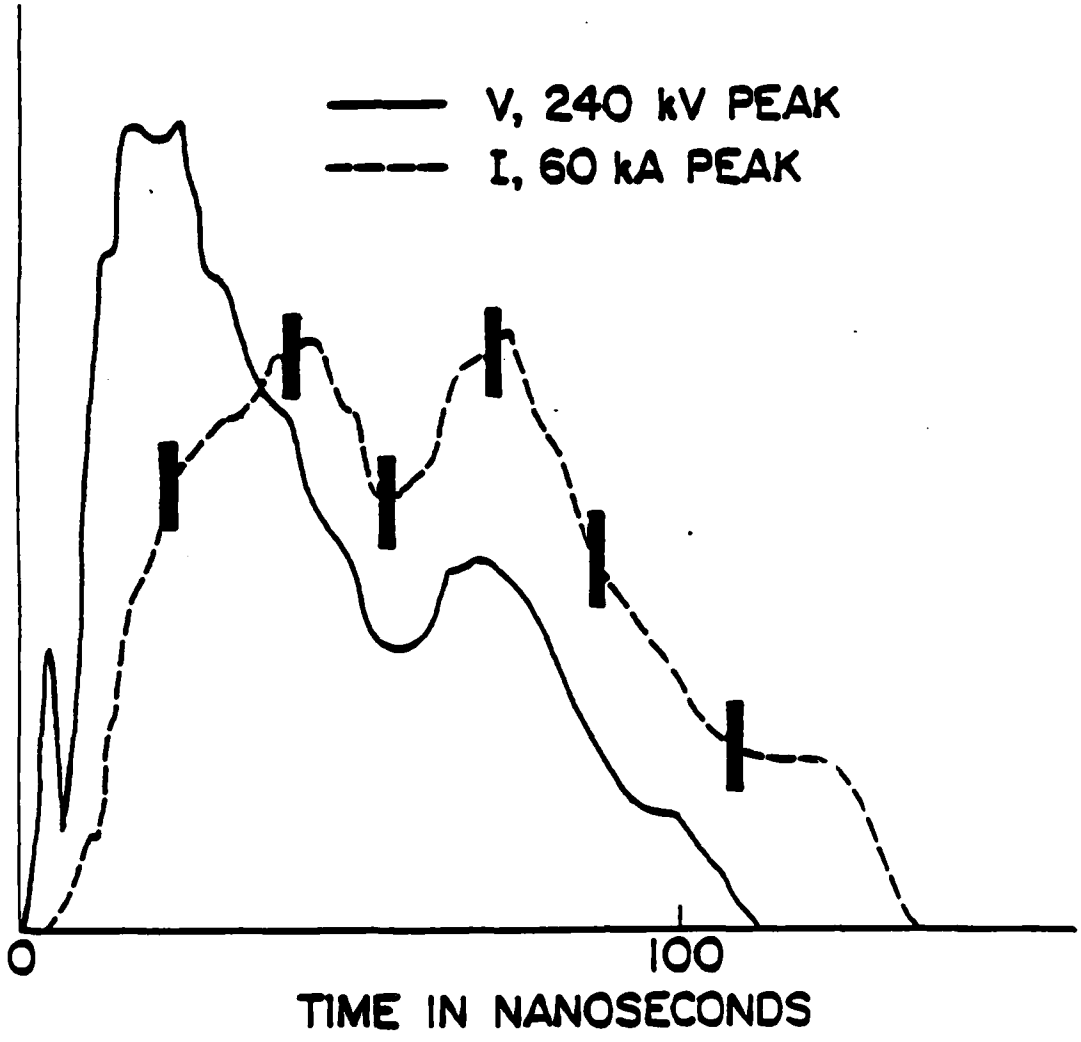

Fig. 7.5: Timing of the interferograms in Fig. 7.6.

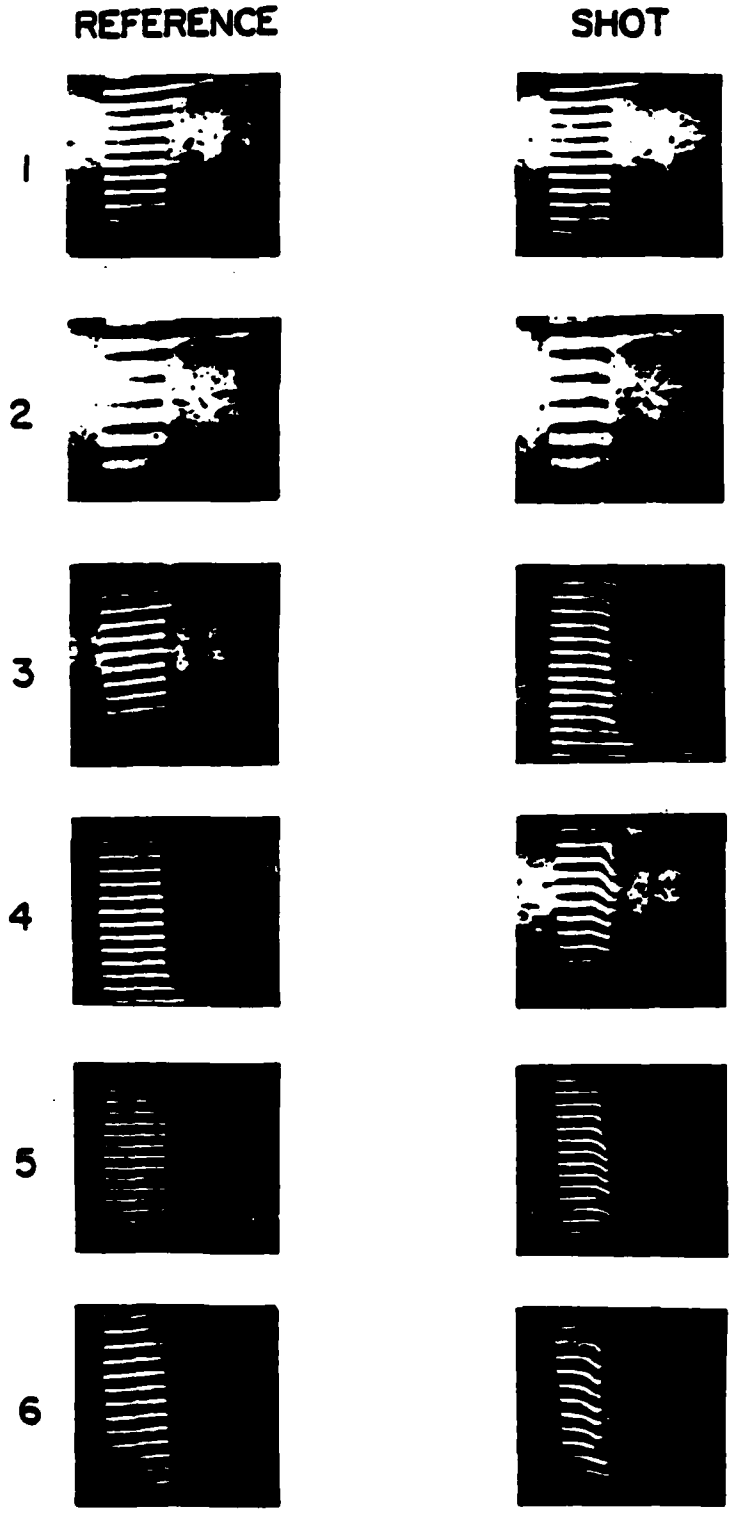

Fig. 7.6: Sequence of interferograms for 6.4 mm Aerodagged cathodes. The timing of the interferograms is shown in Fig. 7.5.

surface to the bend point. There are several other interesting features to these interferograms which will be discussed next.

7.4.1. Magnetic Field Effects

The fringe displacement depends on the fringe location along the cathode height, with those at the top having a greater displacement. This is seen most clearly in the fourth interferogram in the sequence, and is shown even more clearly in Fig. 7.7. That interferogram was taken 90 ns into a shot where a 6.4 mm blasted aluminum cathode was used. From Fig. 7.7, it can be seen that while the fringe shift at the cathode surface is higher at the top edge, the bend point is farther from the cathode surface at the bottom edge, with a gradual variation in these quantities between the edges. In particular, the locus of bend points is approximately a straight line that is tilted toward the cathode at the top. Within the resolution of the interferogram it appears that the total plasma inventory, in electrons/cm^2, (i.e., the 'area' under each fringe, roughly given by the shift at the cathode $\times$ the distance of the bend point from the cathode) is the same for each fringe.

In other words, the plasma expansion is apparently being retarded at points near the top edge and this expansion inhibition results in a pile-up of plasma, with steeper density gradients, at the top edge. It is claimed that this is due to the pressure of the self magnetic field, which, as mentioned above, is greatest at the top and decreases smoothly to zero at the bottom. The effect of this field will now be calculated.

The magnetic field of a parallel plate line is given by

$$B = \frac{4\pi I}{lc} \tag{7.7}$$

with $l = 7$ cm the field is then 0.18 G A, giving a field of 7.2 kG at 40 kA. The ratio of magnetic pressure to kinetic pressure is given by

$$\frac{P_{mag}}{P_{kin}} = \frac{B^2}{4.0 \cdot 10^{-11} nT} \tag{7.8}$$

With a temperature of 4 eV and a density of $2 \cdot 10^{16}$ cm^3, this ratio is 16. The magnetic field in this case is that at the top edge; at the midpoint the field will be

Fig. 7.7: Fringe shift assymetry which is assumed due to magnetic pressure effects.

one half that and the pressure ratio one fourth that, or 4. At peak current, the ratios at the top and middle of the diode are about 32 and 8, respectively.

This pressure ratio would be expected to virtually stop the plasma completely if the field did not penetrate the plasma at all. The skin depth L for field penetration is given by[160,195]

$$L = \sqrt{\frac{c^2 \tau \eta}{2\pi}} \tag{7.9a}$$

$$\eta = \frac{10^{-14} Z \ln \Lambda}{T^{3/2}} \tag{7.9b}$$

where τ is the timescale over which the field is changing, η is the plasma resistivity (see Ch. 10), and T and Z are the electron temperature and average ionic charge. With $\ln \Lambda$=6, Z=2, T=4 eV, and a time constant of 10 ns, the field diffusion length is 1.4 mm, which is slightly greater than the thickness of the observed plasma. The field reduction at 0.3 mm would then be $\exp(-.3/1.3)$, or 20%, resulting in a pressure ratio of about 1 at the cathode midpoint. Thus, a magnetic pressure gradient due to incomplete field penetration can explain the observed inhibition of plasma expansion along the top edge of the cathode. While the effect of a magnetic field on cathode plasma expansion has been observed previously,[176] these interferograms provide a particularly graphic display of this phenomenon.

7.4.2. Opacity

On the later interferograms in the sequence, the fringes do not terminate at the location of the cathode surface, but rather at an opaque layer that has moved out from the cathode. This is seen more clearly in Fig. 7.8. A 9.6 mm Aerodagged cathode was used in this shot.

What is so interesting about this opacity is that its front surface is very smooth. Any unevenness to the surface must be on a scale length of less than 40 μm. The opaque region is always observed to have such a smooth, even edge. The boundary is sharp, with total opacity on one side and no observed light attenuation on the other. There is also no variation in opacity expansion along the cathode height.

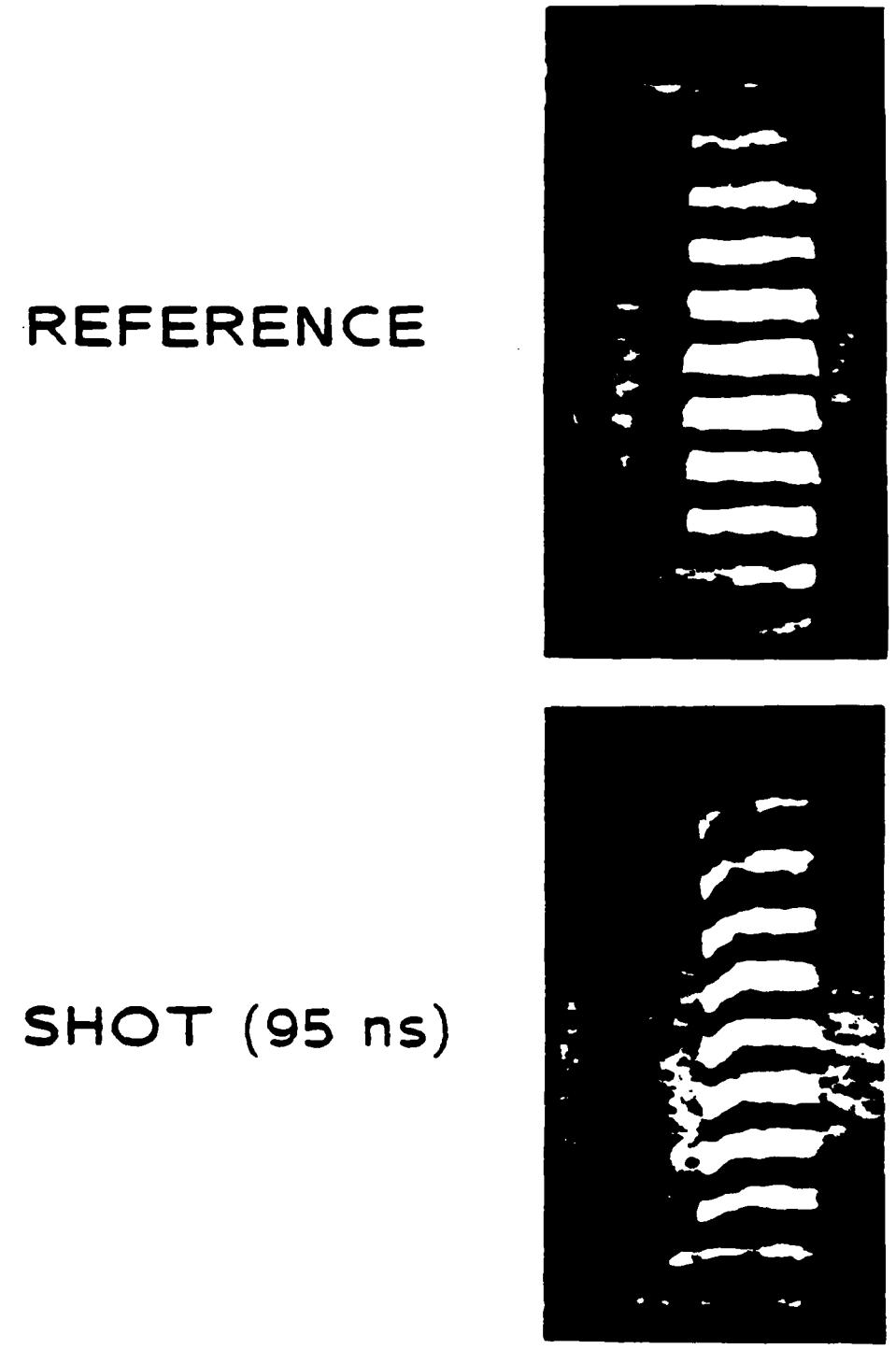

Fig. 7.8: Interferogram showing the opacity near the cathode.

It is difficult to account for this opacity. In order for the plasma to be opaque to the nitrogen laser light, a density of $10^{22}/cm^3$, or 1/6 solid density, is required, which cannot be the case (if that much material was removed, it would have been noticed after the shot). In general, plasma opacity on interferograms is caused by steep density gradients which refract the light out of the optical system. In the present experiment, a deflection of over 10 mrad is necessary for this. From Eqs. (7.5) and (7.6), this corresponds to a density gradient of $3\times10^{19}/cm^4$. While this cannot be ruled out, it would imply that the gradient itself has a large discontinuity, as the gradient is roughly constant outside the opaque region, ranging from $10^{18}/cm^4$ (in the photo) to $4\times10^{18}/cm^4$ on shots with the highest current densities.

If the opacity is due to a large $\nabla\xi$, then there is either a large electron density, or a very cold, dense region (with a high concentration of bound electrons), near the cathode. Spectroscopic measurements presented in Ch. 9 are not consistent with the latter, and comparisons of line intensities inside and outside of the opaque region are inconsistent with a large change in ion density. One possible explanation would be that there is a high electron density (without a correspondingly high density of atomic ions) due to molecular ionization. Molecules would not be expected in the plasma in equilibrium because of their relativly low dissociation energies (see Chs. 8 and 9), but examination of the dissociative ionization cross sections in Ref. 179 suggests that ionization times may be long enough for molecules to be present during the shot.

7.4.3. Neutrals

On the last interferogram in Fig. 7.6, the direction of fringe shift is seen to reverse at the cathode. This is shown more clearly in Fig. 7.9, which was taken at the end of a shot where a 6.4 mm Aerodagged cathode was used. By starting in the middle of the gap and 'counting fringes' in the vertical direction, it can be seen that this reversal of fringe shift direction is actually due to the presence of material with $\xi > 1$ and not just to a decrease in the plasma density. It was shown in Sec. 7.1.2 that the effect of bound electrons on the refractive index is small compared to that of the free electrons. Thus it can be concluded that

Fig. 7.9: Interferogram taken at the end of a shot showing fringe reversal due to bound electrons.

at the end of the shot that there are few free electrons, that is, the material is predominantly neutral.

A relatively high neutral density is implied by the fringe shift. If it is assumed that the neutrals are mostly in the ground states, then, from Ref. 180, a hydrogen density of $2\times10^{18}/cm^3$, or a carbon density of $10^{18}/cm^3$ is required for a fringe shift of one fringe. As shown in Ch. 9, the presence of neutrals cannot be due to recombination on this timescale, so that the neutral material must have come off the cathode at the end of the shot.

7.4.4. Time Dependence of Plasma Supply

From these interferograms, the plasma density is seen to increase with time. It is not immediately clear whether this increase is due to a continual production of plasma, or to the expansion (out into the field of view) of some dense initial layer formed at the cathode surface. In an attempt to resolve this ambiguity, shots were taken with a chopped current pulse, as described in Ch. 3. The chopped current pulse is compared with the normal pulse in Fig. 7.10, and interferograms for the two cases are shown in Fig. 7.11. The interferograms show that even by the time of the first laser pulse, and certainly by the time of the second pulse, there is a significant difference in plasma density between the two cases, with no plasma being seen on the shot with a chopped current pulse.

There are three possible explanations for this: an initial plasma layer is formed in both cases and the current in some way causes plasma expansion on the normal pulse, while no such expansion occurs on the chopped pulse: the drop in current on the chopped pulse results in rapid cooling and the plasma recombines; plasma production does indeed occur throughout the pulse. From the interferograms, it can be seen that if there is any plasma on the shot with chopped current, then it must be within about 50 μm of the surface at 50 ns, which implies an unreasonably low expansion velocity of 0.1 cm μs. Again, recombination times are far too long to explain the difference. It should be noted that both the electric and magnetic pressure effects mentioned in the last chapter would tend to cause expansion during the falling current pulse. From this it can be concluded that plasma production is a continual process.

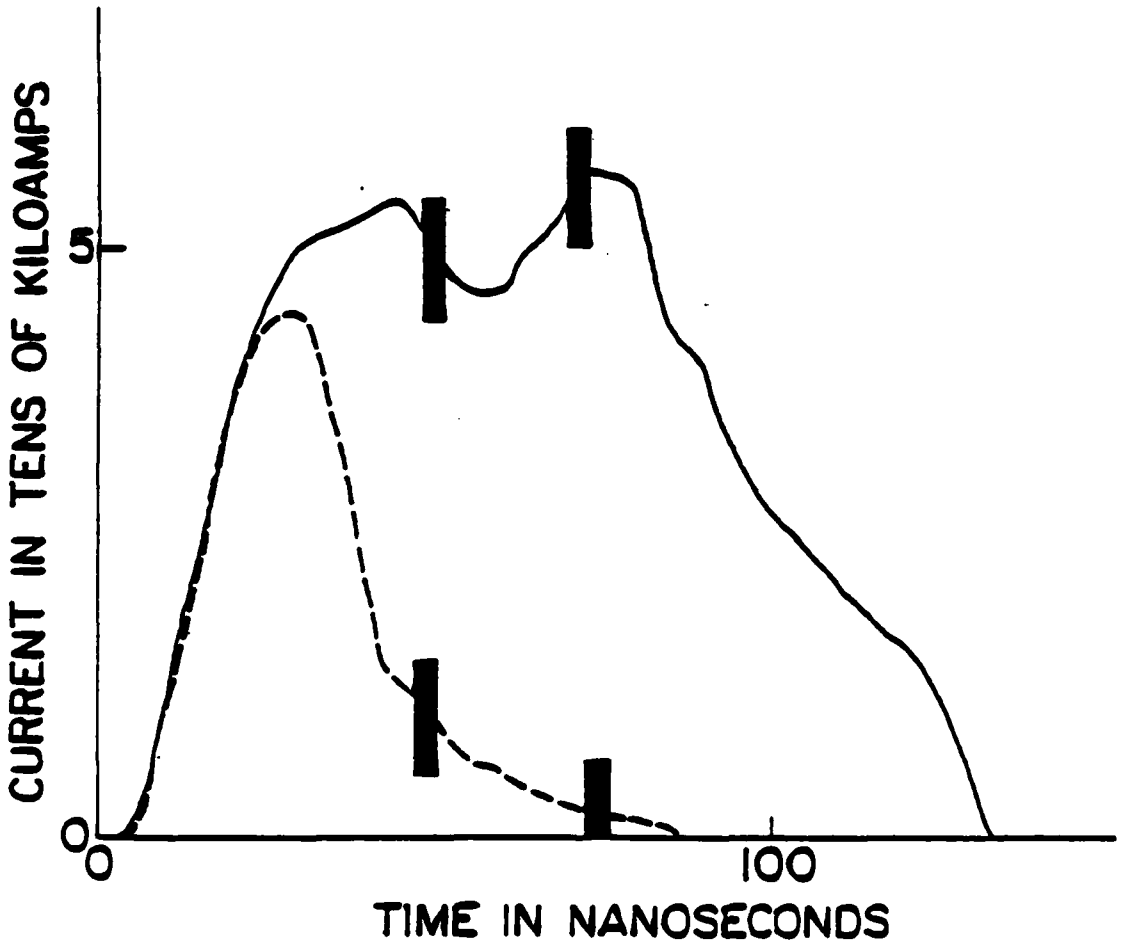

Fig. 7.10: Current traces for a normal and chopped shot, showing the times of the interferograms in Fig. 7.11.

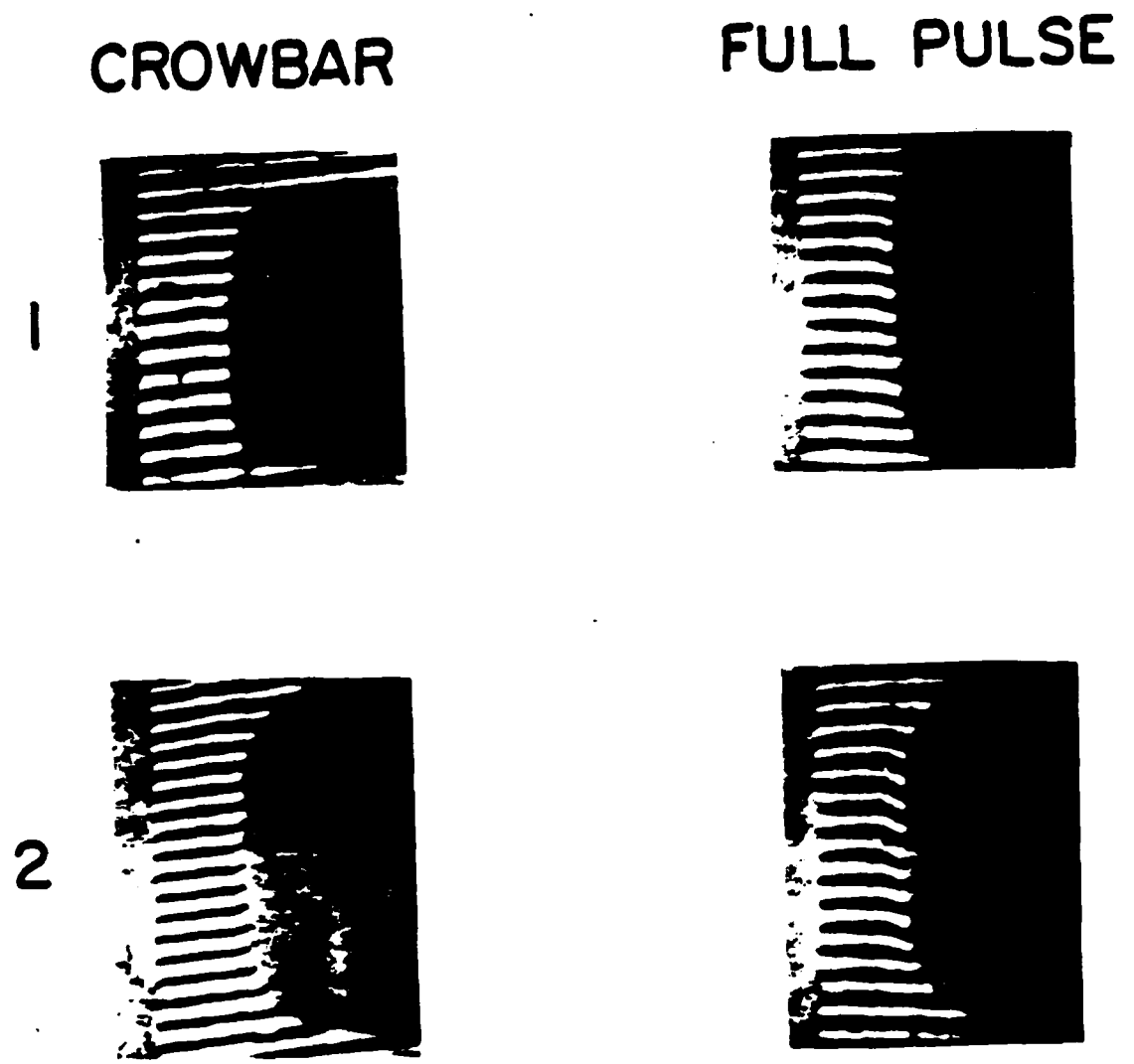

Fig. 7.11: Comparison of interferograms taken on normal and chopped current shots: the times are indicated in Fig. 7.10.

7.4.5. Current Density Effects

Plasma density is seen to be dependent on current density. In Fig. 7.12, interferograms taken at similar times for three different current densities are shown. To first order, the location of the bend point is the same on all pictures, but the fringe shift at the cathode surface is much greater for the higher current density. Interferograms taken at the same time as those in Fig. 7.12, and at the end of the shot, for a 3 kA/cm^2 cathode are shown in Fig. 7.13. In this case, no plasma at all is visible during the shot, and neutrals can be seen coming off the cathode after the pulse.

7.4.6. Late Time Behavior

A limit on the interpulse spacing of repetitively pulsed diodes is given by the time required for all of the material removed from the electrodes during the shot to clear the gap. Interferograms were taken at late times to investigate this. Interferograms taken between 1 and 100 μs after the shot are shown in Fig. 7.14. A 1.6 mm Aerodagged cathode was used for these shots. At 1 μs, the gap is completely closed by opaque material and a rather well collimated stream of material is seen coming off the cathode. This jet is very similar to those observed in Refs. 173 and 175. The direction of fringe shift indicates that the material is dominated by neutrals. This opacity continues for several tens of μs and the gap takes on the order of 100 μs to clear completely.

An interesting feature is that at the later times fringes can be seen through the partial opacity, and they appear undisturbed. This would indicate that the opacity (at least at these late times) is not caused by refraction but by attenuation. This attenuation could be due to molecular absorption (since there are no known atomic lines near the laser line; also, if the laser line was in the middle of a band, contributions to the refractive index from lines above and below the laser line would tend to cancel). Another possibility is that the attenuation is caused by scattering by small microparticles. Either of these possibilities may also explain the opacity observed during the shot.

The gap is observed to clear more quickly when the 1.6 mm cathode is used than when a 25 mm cathode is used (in that case the gap is still opaque at 100

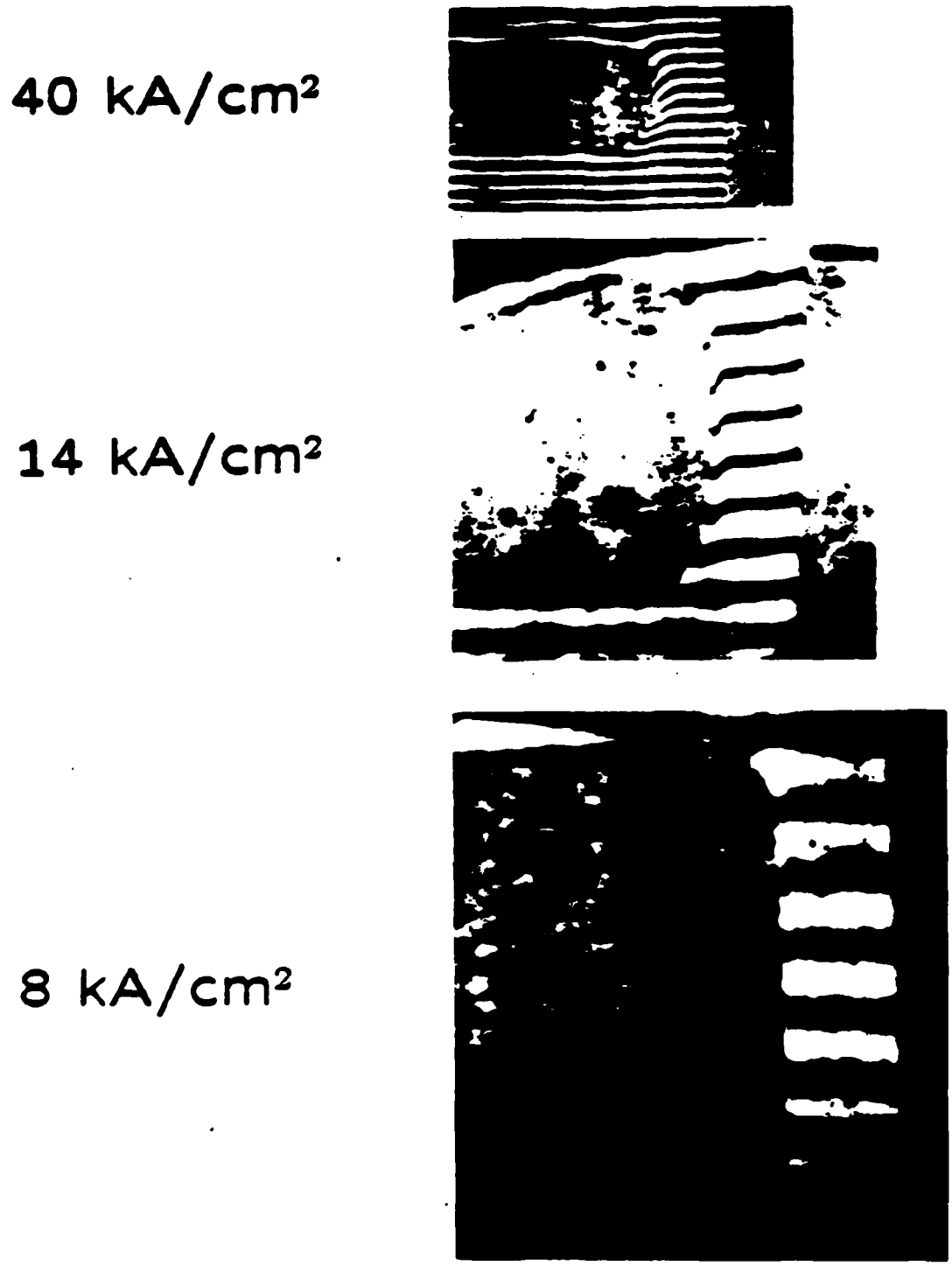

Fig. 7.12: Interferograms taken at the same times for different current densities: (a) 1.6 mm cathode, 39 kA/cm^2; (b) 6.4 mm cathode, 13 kA/cm^2; (c) 9.6 mm cathode, 8 kA/cm^2. The cathodes were Aerodagged.

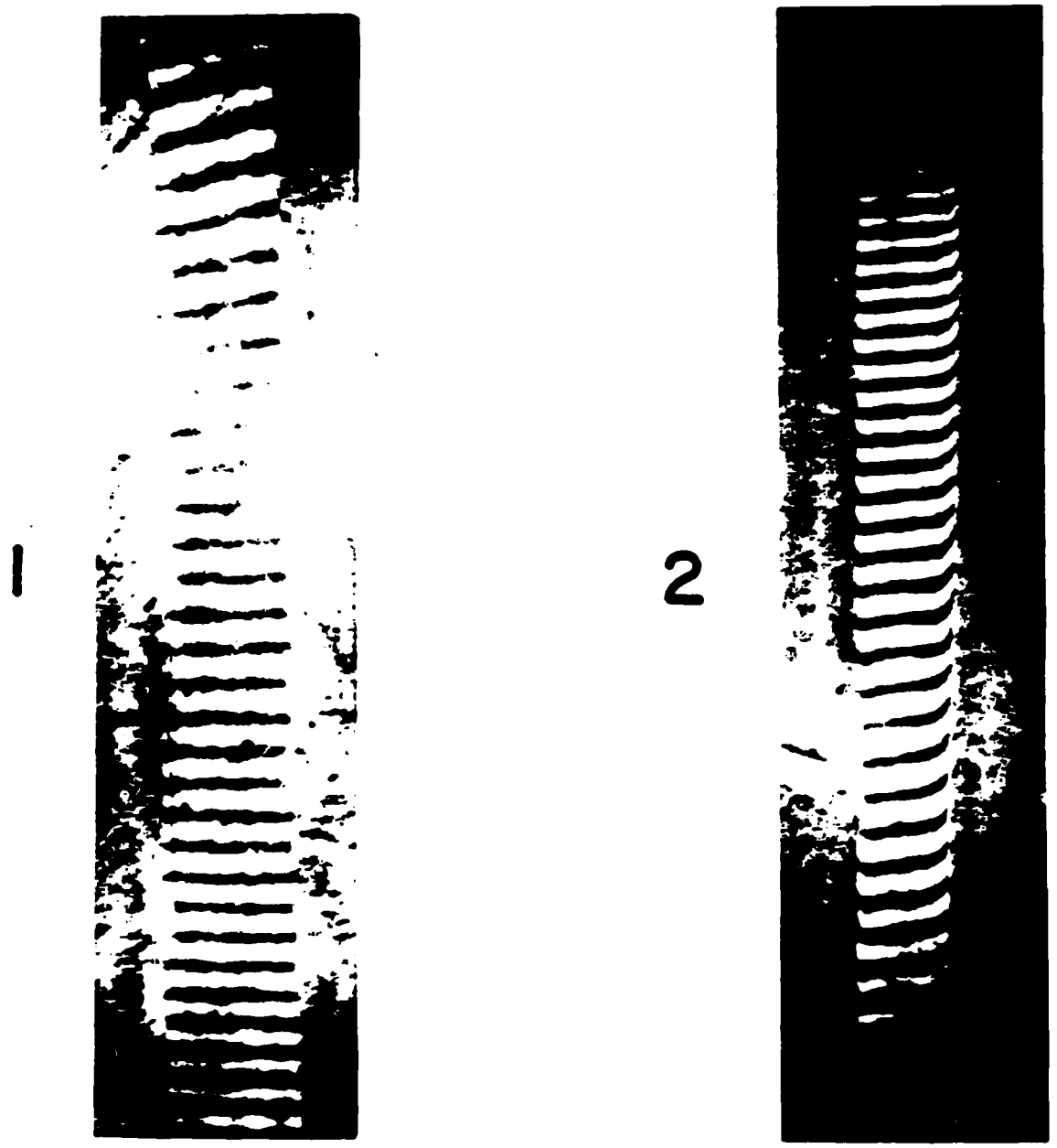

Fig. 7.13: Interferograms for a 25 mm cathode at 3 kA/cm^2: (a) taken at the same time as those in Fig. 7.12; (b) taken at the end of the shot.

1 μs

10 μs

50 μs

100 μs

Fig. 7.14: Interferograms taken at late times.

μs). This difference can be attributed to geometrical factors. With the 1.6 mm cathode, where the gap exceeds the cathode width, it is relatively easy for material to diffuse out of the gap. With the 25 mm cathode, which is much wider than the gap, material will tend to be trapped in the gap, bouncing off the electrodes (and/or dislodging more material from them) before leaving the gap.

Late time plasma behavior in a double pulse diode was studied in Ref. 181. The presence of material from the first pulse was inferred from the impedance behavior of the second. In that experiment the time required for the gap to clear was also on the order of 100 μs, and removal of material was attributed to diffusion and recombination.

Interferograms were also taken at late times for the 6.4 mm cathode with a chopped current pulse, and no opacity was seen. In this case the charge transfer density (in C/cm^2) was comparable to that when the 25 mm cathode was used in a normal pulse.

7.5. Quantitative Measurements

Quantitative analysis involved digitization of several quantities from each interferogram, as indicated in the schematic interferogram shown in Fig. 7.15. The thickness of the opaque layer is denoted by O_k. Toward the end of the shot, opacity was also seen coming off of the anode: this thickness is denoted by O_a. In addition to these quantities, the distance B of the bend point from the cathode surface, and the deflection F of the fringe at the beginning of the opaque layer, were recorded. As mentioned before and indicated in the picture, the pattern varied along the height of the cathode, so that the above mentioned quantities were recorded at the middle of the cathode.

7.5.1. Bend Point Motion

The location of the bend point is shown as a function of time for shots with 6.4 mm aluminum cathodes in the top of Fig. 7.16. Also shown in the figure are the calculated gap (using the planar model) and a least-squares linear fit to the data. The error bars indicated include the effects of interferogram spatial resolution as well as uncertainties involved in determining the bend point location.

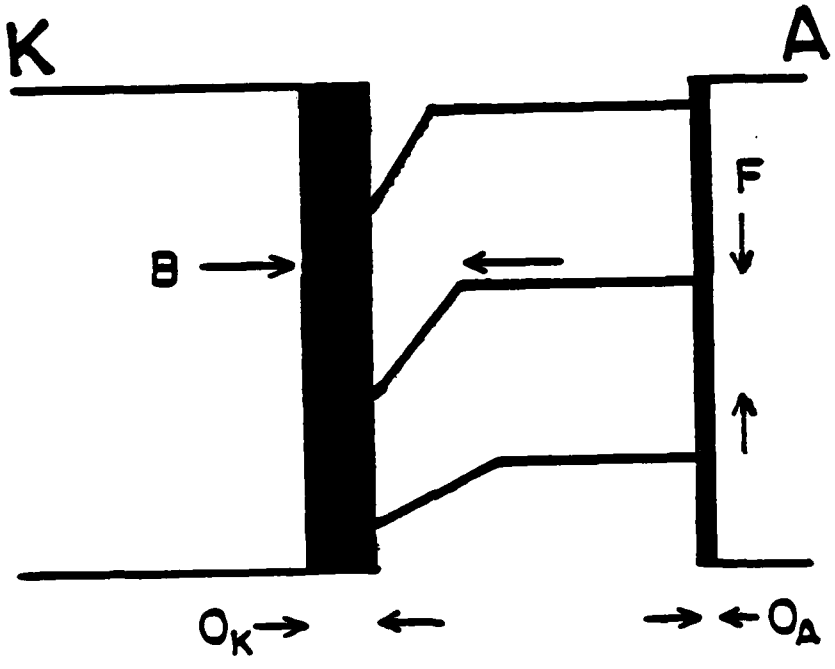

Fig. 7.15: Schematic interferogram illustrating the quantities which were recorded for each interferogram.

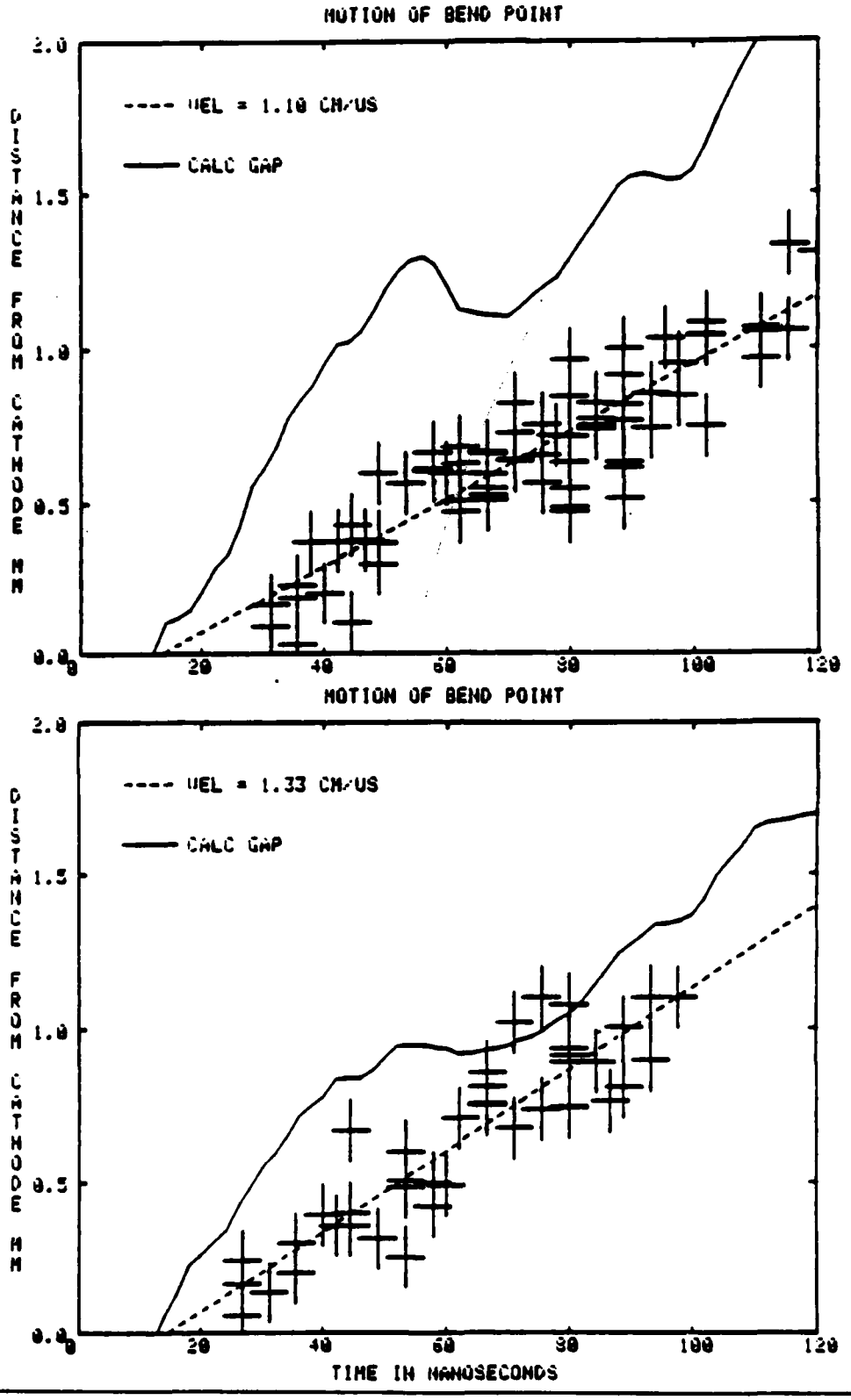

Fig. 7.16: Location of the bend point as a function of time for shots with aluminum cathodes. The dashed line is a least-squares linear fit to the data. The emission layer location calculated in Ch. 6 is also shown. (top) 6.4 mm cathodes: (bottom) 1.6 mm cathodes.

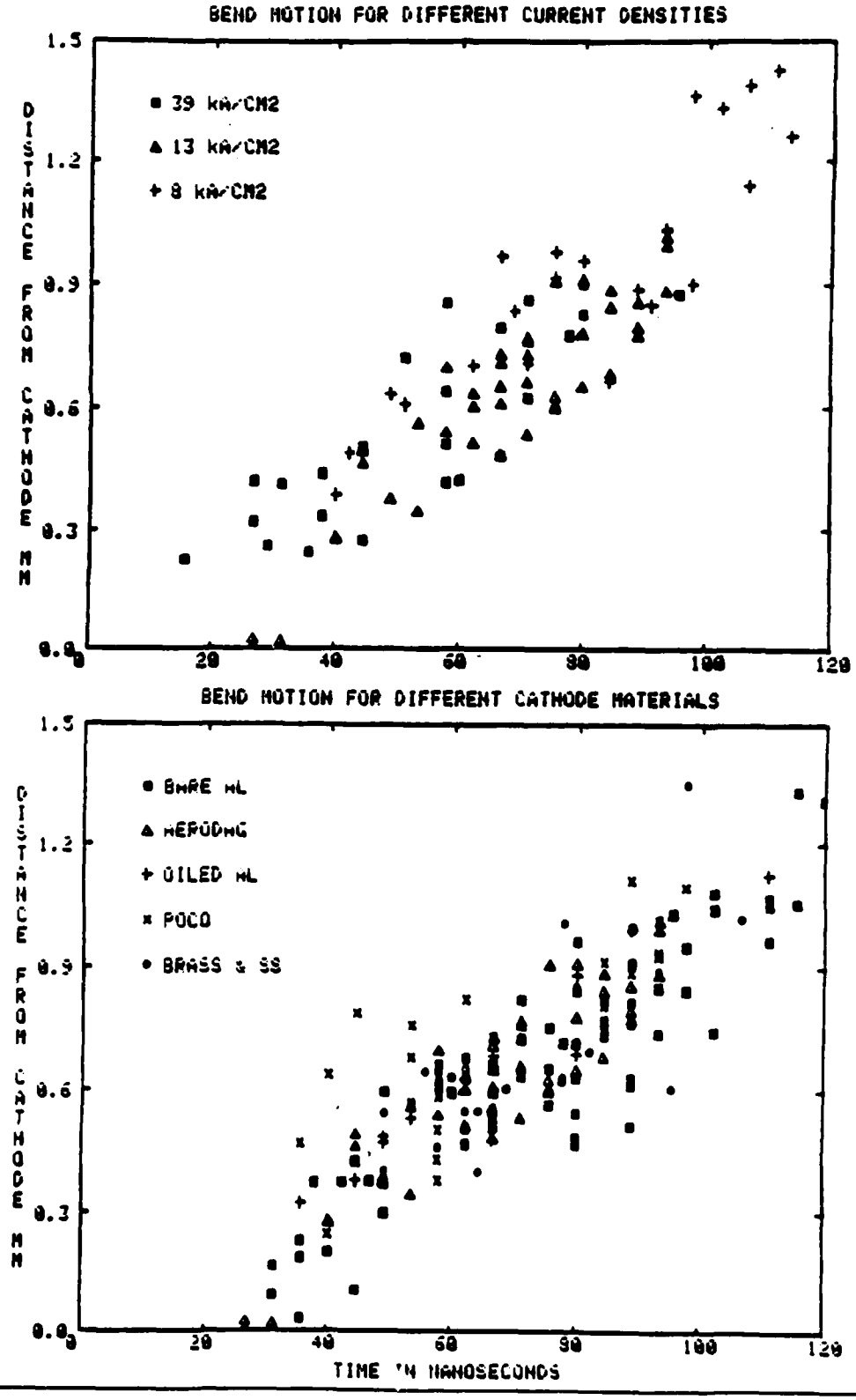

Fig. 7.17: Bend point motion for different current densities (top) and cathode materials (bottom).

As mentioned before, fringe shifts of 0.1–0.2 fringes could be observed, so that the bend point corresponds to a density of $1\text{–}2\times10^{16}/\text{cm}^3$. With an assumed electron temperature of a few eV, the density at the emission layer is about $2\text{–}3\times10^{15}/\text{cm}^3$, so that the bend point corresponds to a density of a 3–10 times the emission layer density.

The points lie reasonably close to a straight line with velocity of 1.1 cm/μs and a delay from the start of the shot of 10 ns. The distance from the bend point to the calculated emission layer location varies from about 0.3–0.8 mm. From Ch. 6, the assumption of an electric pressure effect in opening the gap at 55 ns implies a density gradient at the emission layer such that the density changes by a factor of 1.25 in 0.2 mm. At that time the average gradient inferred from Fig. 7.16, from the emission layer to the bend point location, is about a factor of 3 in 0.8 mm, which is close to the value assumed in Ch. 6. The reduction in the calculated gap at 60 ns can almost be resolved in the bend point plot, but this is not considered to be statistically significant.

A similar plot for shots with a 1.6 mm aluminum cathode is shown in the bottom half of the figure. In this case the least-squares velocity is somewhat higher, however, a straight line fit is rather arbitrary and the difference is not considered to be significant. The points lie closer to the calculated gap as would be expected, since in this case the emission layer density is greater, being within (at peak current) a factor of two of that observable interferometrically. (However, it should be restated that there is an uncertainty in the calculated gap, particularly for the 1.6 mm cathode).

In general, the bend point motion is the same for all cathodes used, within the given error bars. Plots for different current densities (with Aerodagged cathodes) and different materials/surface coatings are shown in Fig. 7.17. Error bars have been omitted in these plots for clarity.

7.5.2. Opaque Layer Motion

Plots of the motion of the opaque layer are shown in Fig. 7.18, for the same conditions as those in Fig. 7.16. The opaque layer velocities are about 0.5–0.8 cm/μs. As with the bend point motion, there is no observable dependence on current density or cathode surface, as indicated in the figure. It is suggested in Sec. 7.4.6 that this opacity is due to either molecular absorption or to scattering from microparticles. There is no reported data concerning the motion of molecules from the cathode. The velocity of motion of the opaque layer here is about 8 times higher than reported microparticle velocities, but would not be out of the question (in view of the inverse dependence of velocity on particle mass[171]) for small (~100 Å) microparticles.

7.5.3. Plasma Density Profile

The plasma electron density increases from the bend point back to the opaque layer. In Fig. 7.19, the density at 0.5 mm from the cathode surface (and thus outside the opaque layer) is shown as a function of time for shots with a 6.4 mm Aerodagged cathode. This density is relatively independent of cathode material, as shown in the lower plot in the figure. The oiled cathodes appear to have somewhat higher plasma densities, and the metallic cathodes somewhat lower densities, than the carbon cathodes.

As mentioned in Sec. 7.4.5, the density increases with increasing current density. Densities at 0.5 mm out are shown for three current densities in Fig. 7.20. To within the resolution of the measurements, the density at this point is proportional to the diode current density. The expansion of the layer corresponding to a density of $3 \cdot 10^{14}$ cm^{-3} is shown for two current densities in Fig. 7.20 b. This layer is farther out for the higher current density, in contrast with the behavior of the $1 \cdot 10^{14}$ cm^{-3} layer, the motion of which did not depend on the current density. These plots suggest that the (normalized) shape of the density profile is independent of, and the amplitude depends on, the current density.

By comparing the bend point motion with that of the emission layer calculated in Ch. 6, it can be seen that the density profile has a tail with reduced density

AD-A147 917 PLASMA STUDIES IN ION DIODES(U) MASSACHUSETTS INST OF TECH CAMBRIDGE RESEARCH LAB OF ELECTRONICS G BEKEFI SEP 84 N00014-83-K-2024 3/4

UNCLASSIFIED F/G 20/9 NL

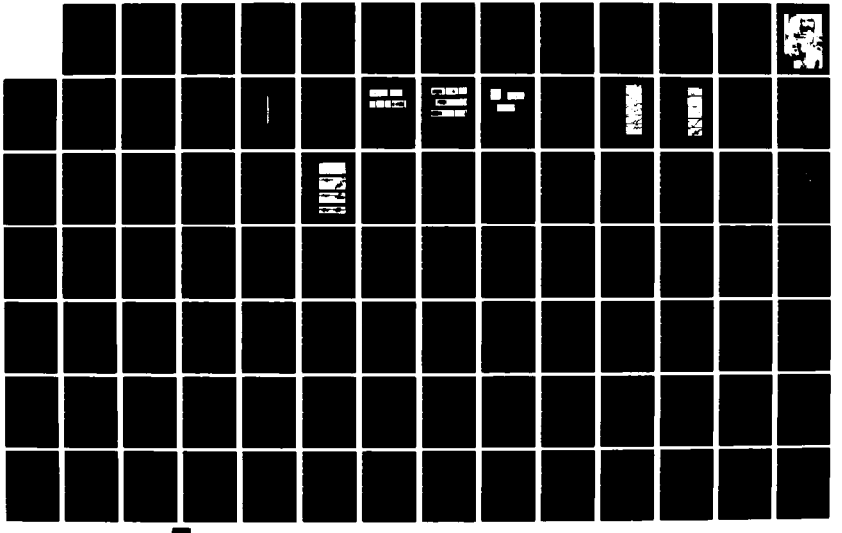

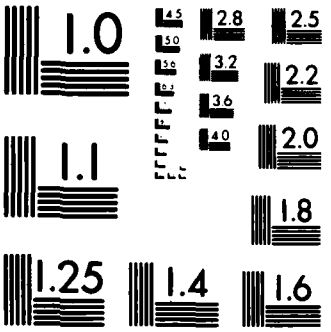

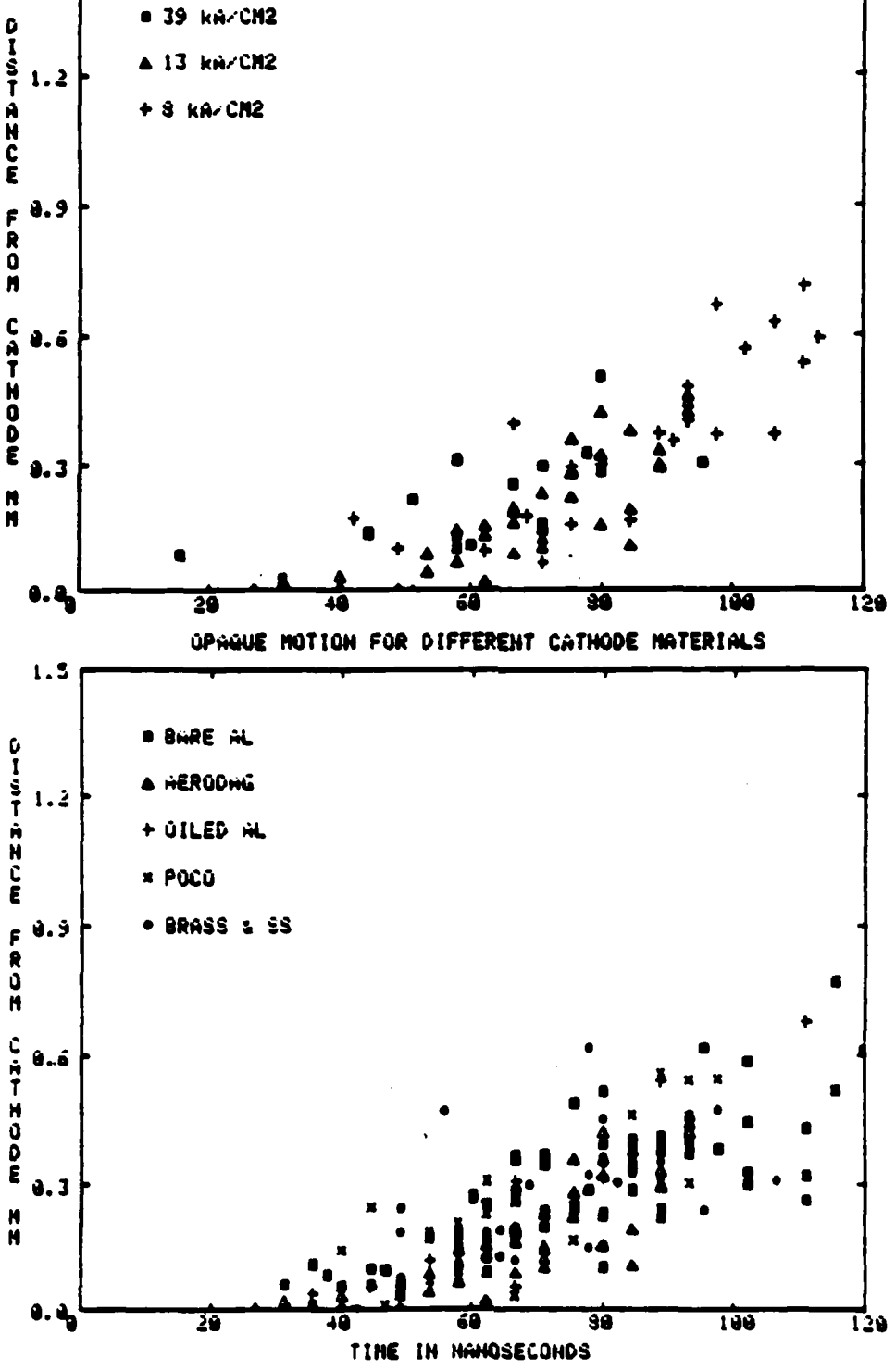

Fig. 7.18: The location of the opaque edge as a function of time, for different current densities (top, Aerodagged cathodes) and cathode materials (bottom).

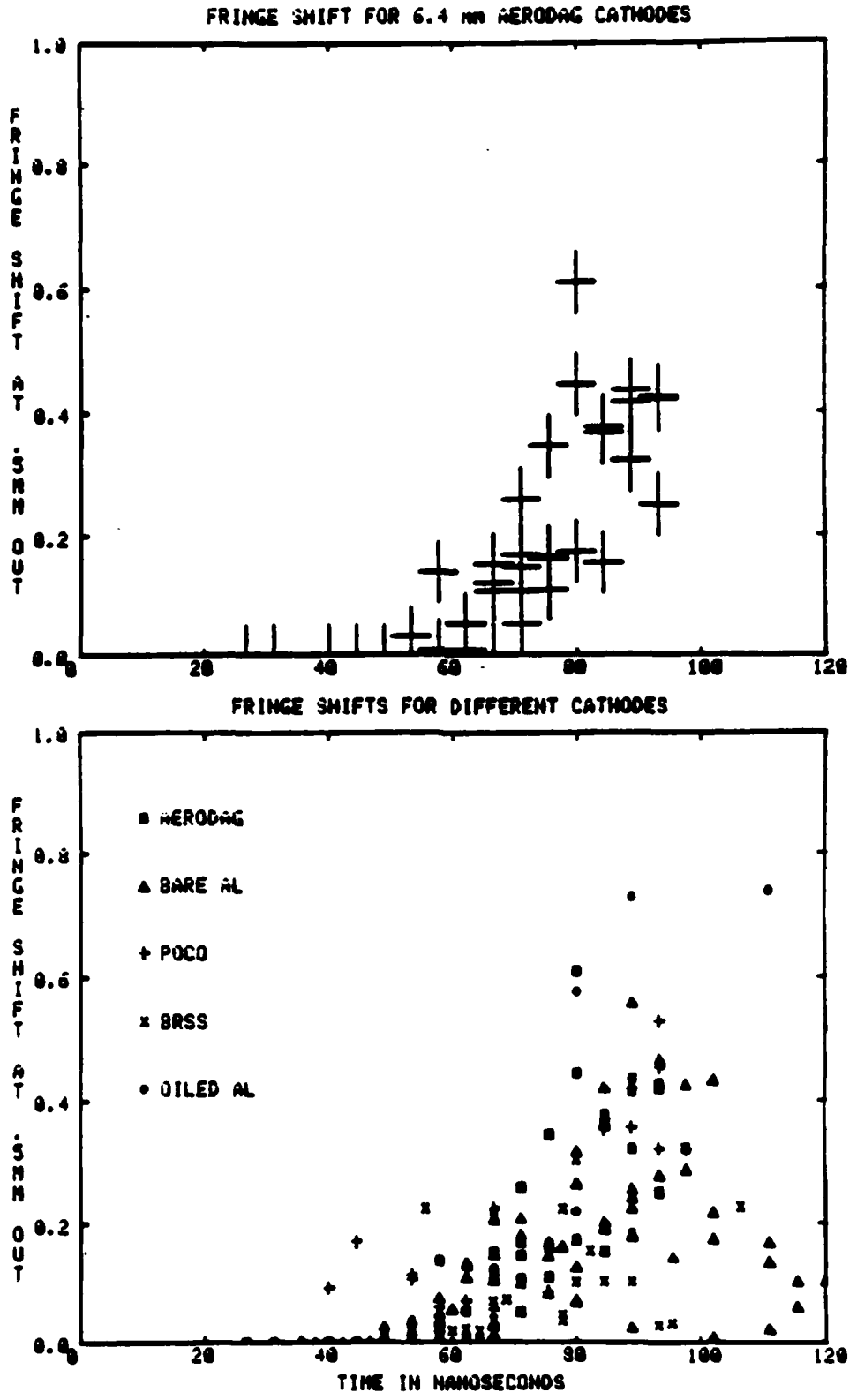

Fig. 7.19: Plasma density at 0.5 mm from the cathode surface, for shots with a 6.4 mm Aerodagged cathode (top) and different cathode materials (bottom).

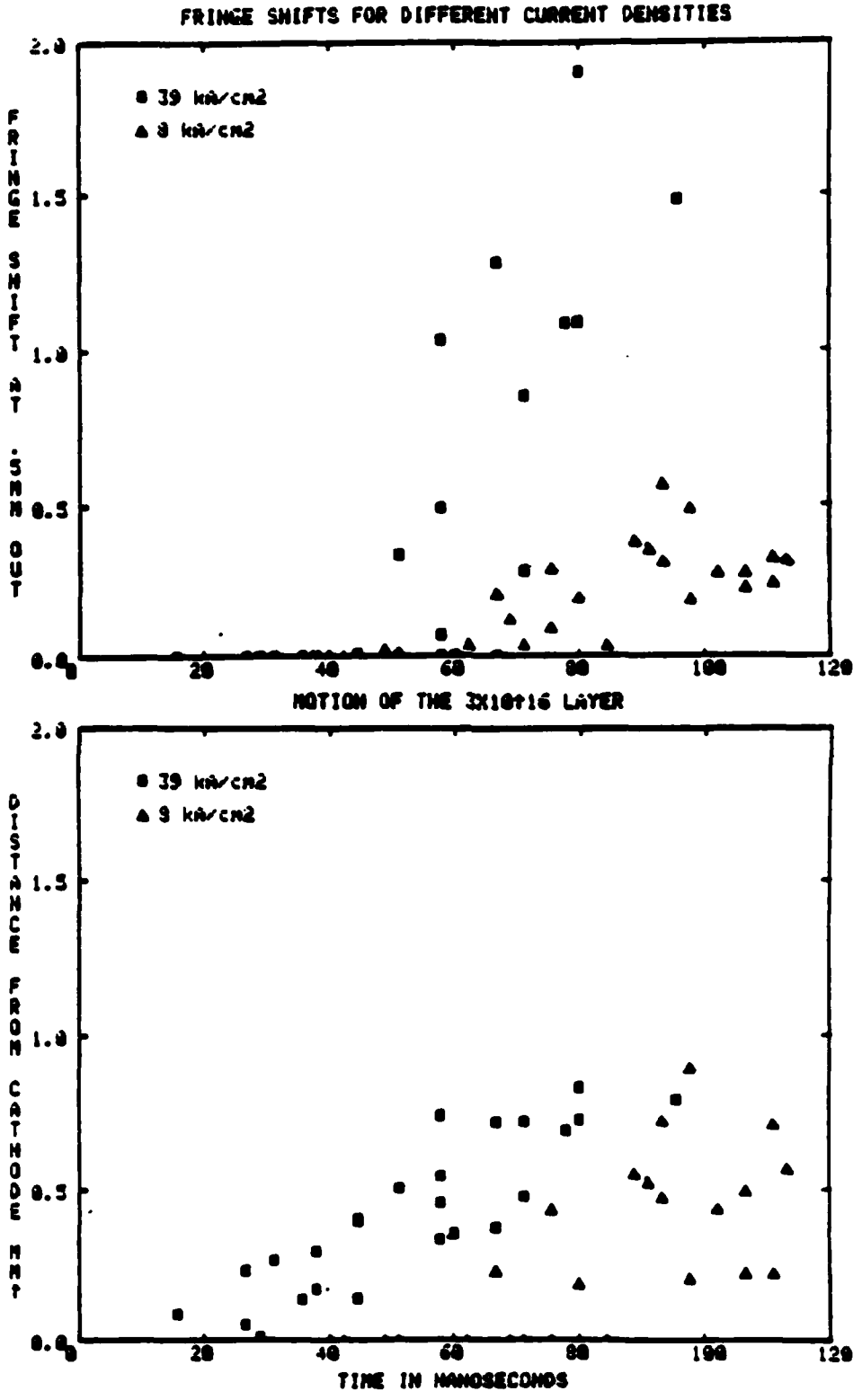

Fig. 7.20: (top) Plasma density at 0.5 mm from the cathode surface for different current densities. (bottom) Movement of the point of 3×10^{16} cm^3 plasma density. for different current densities.

gradient between the two (if the gradient was constant, the bend point would be much closer to the emission layer).

The emission layer motion calculated in Ch. 6 is independent of current density (at least during the early part of the pulse). Since the emission layer density goes up with the current density (from Eq. (6.5)), this suggests that the low density tail also has a shape which in independent of, and amplitude that is proportional to, the current density. In other words, on shots with a higher current density, the plasma density is proportionally higher so that the emission layer motion is the same.

This picture of the plasma density profile is summarized in Fig. 7.21. The solid lines indicate the density either measured from interferometry or calculated from the perveance behavior. The (visually inferred) locations of the bend points are also indicated in the figure. This type of profile is suggested by the interferometric and perveance measurements — the shape is independent of current density, the amplitude is proportional to the current density, and the bend point location is (to the accuracy of the measurement) independent of current density.

7.5.4. Plasma Inventory

This section is concerned with the rate of supply of material into the gap. The plasma inventory (in cm^{-2}), that is, the integral of density along the gap, or the area under each fringe, is a useful quantity in that it removes the spatial dependence of the density profile.

The existence of the opaque region causes difficulty in any attempt to quantify the inventory, however, since the density profile is not known in that region. In particular, it is entirely possible (depending on the cause of the opacity) that most of the material in the gap is in the opaque region.

The behavior of the opaque layer differs from that of the observed plasma in several ways. Whereas the motion of higher density plasma layers depends on the current density (as in Fig. 7.19), the motion of the opaque layer does not. The location of the opacity edge also does not show the up-down assymetry seen in the fringe shifts. Further differences are implied by the late time measurements

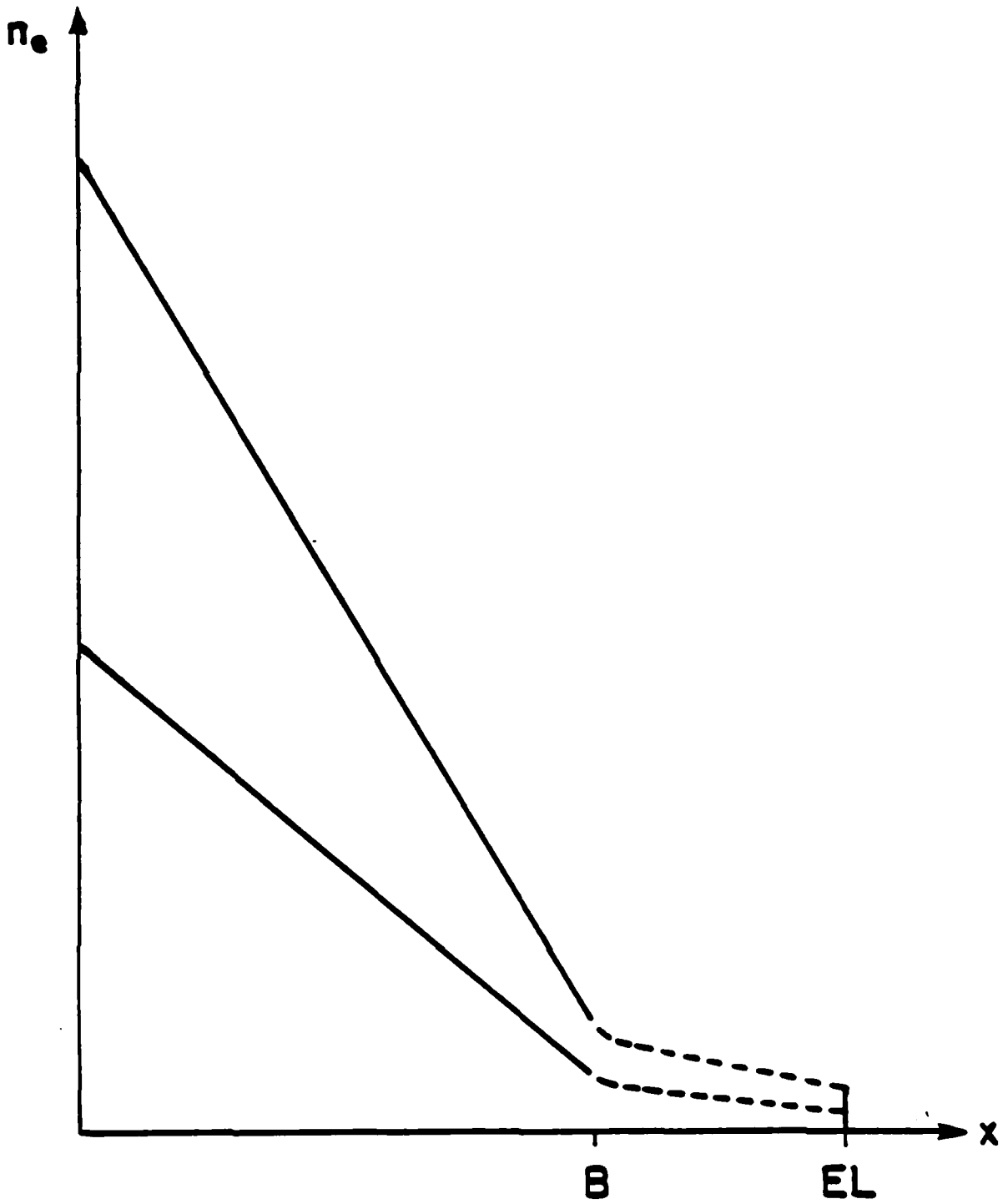

Fig. 7.21: Possible plasma density profiles for different current densities. The (visually inferrred) bend point locations are indicated.

described in Sec. 7.4.6. Comparisons of shots with low current density with those with higher current density but reduced pulselength (and thus roughly equivalent charge transfer) indicate that the opacity comes off the cathode at a rate that is less dependent on current density than that of the observed plasma.

All of these observations suggest that the material responsible for the opacity arises from a different mechanism than that which produces the observed plasma. In other words, the material in the gap consists of plasma which extends from the cathode surface to the emission layer as well as some other material of unknown type (plasma, microparticles, molecules, etc.) which extends out to the opacity edge.

By continuing this line of reasoning, and making an additional assumption concerning the plasma density in the opaque region (i.e., an extrapolation of the fringes back to the cathode) it is then possible to calculate the inventory of plasma produced by whatever mechanism is responsible for the observed plasma (i.e., the opacity is assumed to be due to a different process and will simply be ignored).

Calculated inventories are shown in Fig. 7.22 for two assumptions about the plasma density in the opaque layer. In the top plot, the fringe shift has been linearly extrapolated back to the cathode, that is, in terms of the bend point B, shift F, and opaque point O_k (see Fig. 7.15), the inventory I is given by

$$I = \frac{1}{2} B (F \frac{B}{B - O_k}) \qquad (7.10a)$$

while on the bottom trace only the observed inventory has been plotted

$$I = \frac{1}{2} BF \qquad (7.10b)$$

(Again, the spectroscopic results are consistent with a roughly constant density in the opaque region, i.e., in between these two cases.)

The integrated charge transfer density (i.e., $\int I dt$, in C cm^{-2}) is also shown on the plots, in units normalized to fit the calculated plasma inventories: 0.5 plasma electrons / current electron on the top, and 0.25 plasma electrons / current electrons on the bottom.

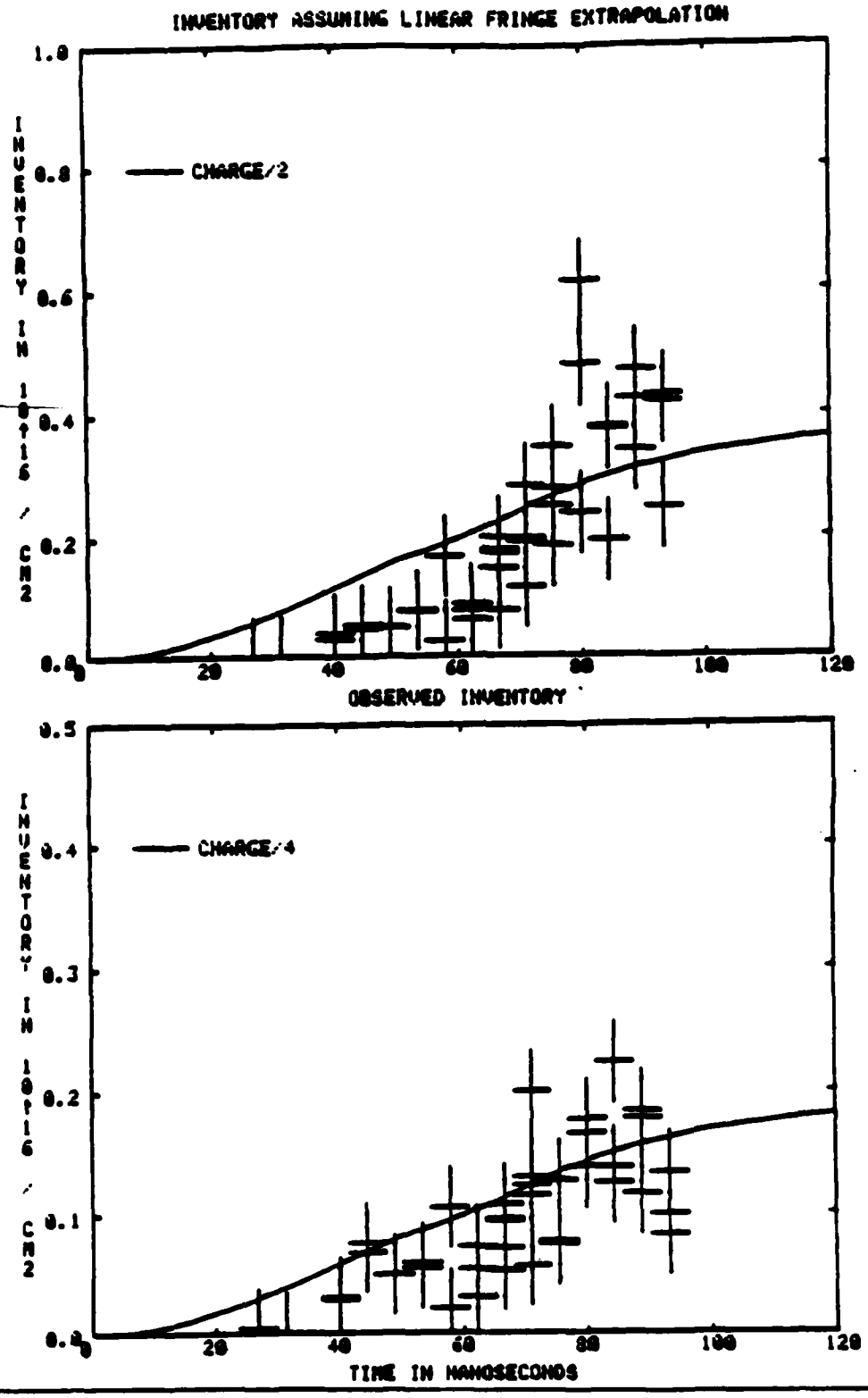

Fig. 7.22: Calculated plasma inventory as a function of time, for two assumptions concerning the plasma density in the opaque region: (top) linear extrapolation: (bottom) only the observed density. The charge transfer is also shown normalized to the inventory. These points are taken from shots with 6.4 mm graphite cathodes.

In vacuum arcs, the plasma inventory is proportional to the charge transfer, as mentioned in Ch. 2. If a similar relationship holds for diode plasmas, then the inventory should increase with time (on a particular shot) proportionally to the charge transfer, and the inventory at a given time (on different shots) should be proportional to the current density. As shown in Fig. 7.22, the first condition is approximately true. However, the uncertainties in the measurement do not allow this conclusion to be stated definitely. In particular, the plasma inventory seems to increase more rapidly with time than the charge transfer.

Comparison of inventories on shots with different current densities shows that, as stated in Sec. 7.5.3, the plasma inventory (at a given time) is roughly proportional to the current density. Agian, however, the uncertainties in the measurement do not allow this to be stated definitely.

7.5.5. Anode Plasma Behavior

Late in time, a *region of opacity* is also observed at the anode, as indicated in Fig. 7.15. This opacity appears at about 80 ns, which is consistent with the minimum inferred time of anode plasma formation calculated in Ch. 5. This opacity never extends out further than 0.2 mm from the anode surface, and it is not possible to quantify any aspects of the anode plasma, such as expansion velocity or density.

7.6. Comparison With Previous Work

The densities and density profiles measured here are consistent with the previous interferometric measurements of diode plasmas discussed in Sec. 7.3.2. The dependence of density on charge transfer, in particular, can explain the results of Bekefi *et al.*, who observed that plasma densities in a cylindrical diode were less with an insulating magnetic field: this can be explained by the reduced charge transfer in that case.

From the calculated inventories, the electron transport coefficient is about 0.1–0.5 plasma electrons/current electron, which is similar (within an order of magnitude) to the results in vacuum arc and needle cathode studies. A direct comparison is not justified since the latter cases involved clean surfaces. In Ref. 89,

however, it is suggested that total erosion rates for clean and dirty surfaces are similar.

7.7. Conclusions

The results of interferometric measurements are consistent with the following picture of plasma production: plasma is produced continually throughout the pulse, roughly in proportion to the charge transfer out of the cathode surface, at a rate of roughly 1–5 plasma electrons for every current electron. The rate of plasma production depends weakly on the cathode material, being slightly greater for oil covered cathodes, and less for metallic cathodes, than for carbon cathodes.

In addition to this plasma production, there appears to be an additional process of material supply to the gap that comes into play later in the pulse and shows less dependence on current density.

The density profile decreases from the plasma to the emission layer, and the profile shape is independent of, while the amplitude is roughly proportional to, the current density. A retarding effect of magnetic pressure on the plasma expansion has been observed.

After the shot, copious quantities of neutrals come off of the cathode, and remain in the gap for times on the order of 100 μs.

As suggested in the previous chapter, it is because of this proportionality of plasma density to current density that gap closure is relatively independent of current density: on shots with a higher current density, the increased electric pressure effects would limit plasma expansion if the plasma density did not also increase (i.e., both sides of Eq. (6.5) increase proportionally).

Chapter 8

Qualitative Spectroscopy

8.1. Introduction

Spectroscopic investigations of the cathode plasma are described in this chapter and the next. Qualitative measurements, that is, those which do not involve measurements of line intensities (other than relative comparisons of the same line with different cathodes) are described in this chapter. These measurements consist of line identification, where the species that compose the cathode plasma are identified, general observations of the line intensity time dependences, comparisons of the intensities of given lines on shots with different cathodes, and spatially and temporally resolved comparisons of line intensities at different distances from the cathode surface. The latter measurements provide information (for the first time in broad area diodes) concerning the expansion of different species. These measurements confirm that the interesting and not completely understood directed ion flows observed in vacuum arcs also exist in pulsed diodes.

Previous relevant spectroscopic studies are reviewed in the next section. The experimental set-up is described in Sec. 8.3. Sec. 8.4 describes line identification measurements and Sec. 8.5 describes the general characteristics of the observed spectral lines. Previous species-resolved expansion measurements in vacuum arcs and needle cathode diodes are reviewed in Sec. 8.6. The expansion measurements are presented in Sec. 8.7. and discussion and conclusions are given in Secs. 8.8 and 8.9.

8.2. Previous Spectroscopic Studies

A spectroscopic study of a needle cathode plasma was reported by Baksht *et al.* in Ref. 182. The cathode was aluminum and the current density was not stated. Lines of singly and doubly ionized aluminum were observed, with no neutral aluminum or impurity consitituents observed. A similar investigation of

a short pulse (~75 ns) arc was reported in Ref. 183; in this case ions and neutrals from both the electrode metals (Al, Cu) and surface impuritites were observed.

Vacuum arc plasmas, as mentioned in Ch. 2, consist of atoms and ions (mostly singly and doubly ionized) from the electrode material. Some arc spectroscopic studies are reviewed in the context of temperature measurements in the next chapter.

Few spectroscopic measurements of plasmas in broad area diodes have been reported previously. Two of these involved diodes on Nereus accelerators. Bekefi *et al.*[176] observed plasmas in (externally) magnetically insulated diodes with time integrated spectroscopy. Shots were taken with and without an external field and the current density was a few kA/cm^2. The H_α line and C II lines at 6578 Å and 6583 Å were observed as were other weak hydrogen and carbon lines. Swain *et al.* observed plasmas in a planar diode with time integrated and time resolved (using a streak camera coupled to a spectrograph) spectroscopy.[136] The current density was about 10 kA/cm^2, similar to that in this experiment. Strong continuum light was observed early in the pulse which obscured the lines. The H_α absorption line was observed after 30 ns and neutrals from the electrode materials were observed after 60 ns.

The experiment in Ref. 118 involved time integrated spectroscopy of the cathode plasma in a (externally) magnetically insulated diode. Cathodes of copper, aluminum, and graphite were used and the current density was apparently about 100 A/cm^2. Lines of Al I, II, and III, or Cu I and II (depending on the cathode material) were observed as well as lines from H, C I, C II, and bands from C_2 (the Swan bands) and CH. The intensities of metal lines were weaker than those of impurity lines and the H line intensities were the same for all cathodes.

8.3. Experimental Description

The plasma was viewed with a 0.5 meter spectrograph, 0.3 meter monochromator and 0.1 meter monochromator as well as the total light recording PMT previously mentioned. The optical arrangement is shown in Figs. 8.1 and 8.2. Spectral lines were initially identified with a Jarrel Ash 0.5 M Ebert spectrograph

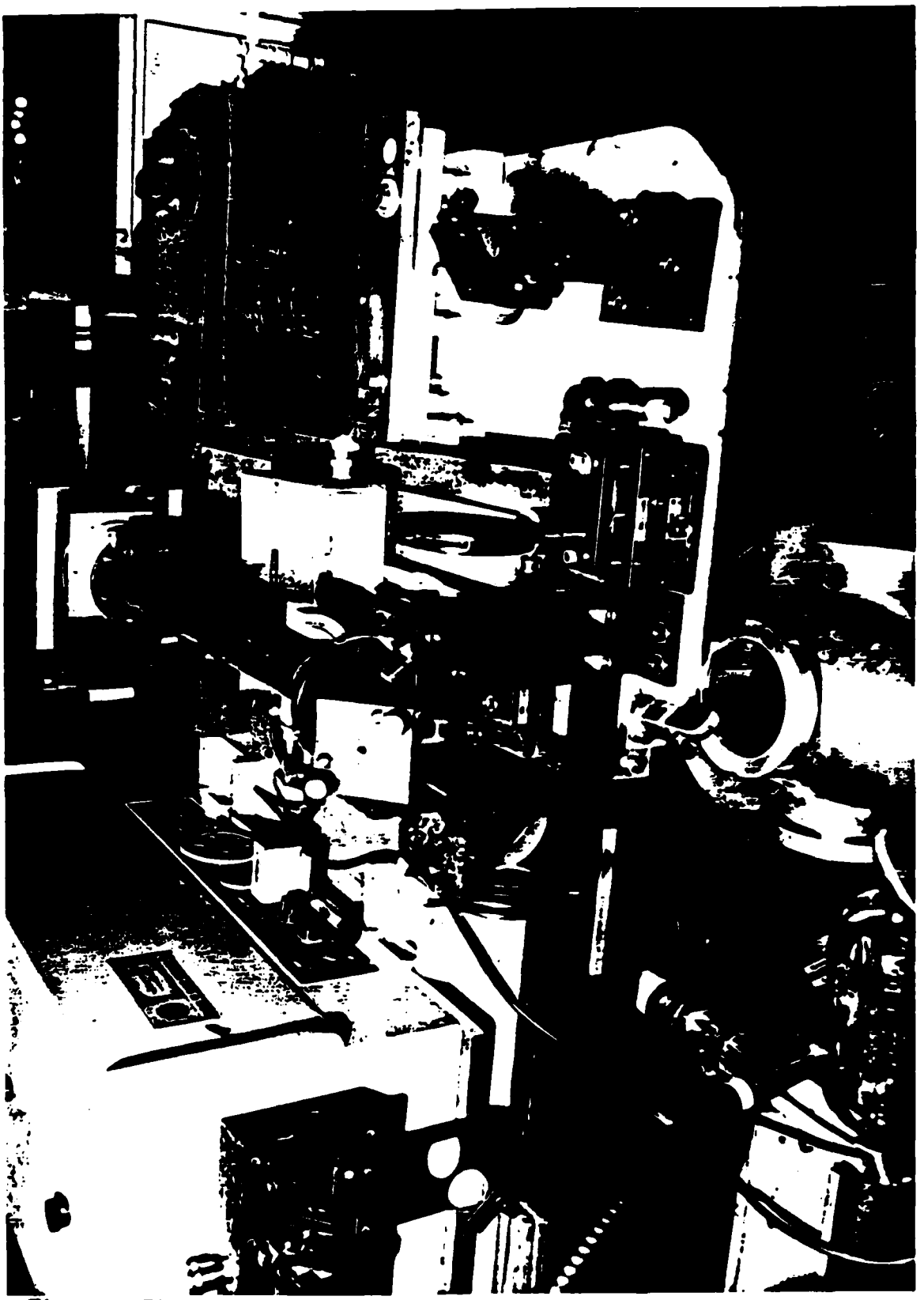

Fig. 8.1: Photograph of the spectroscopic optical system.

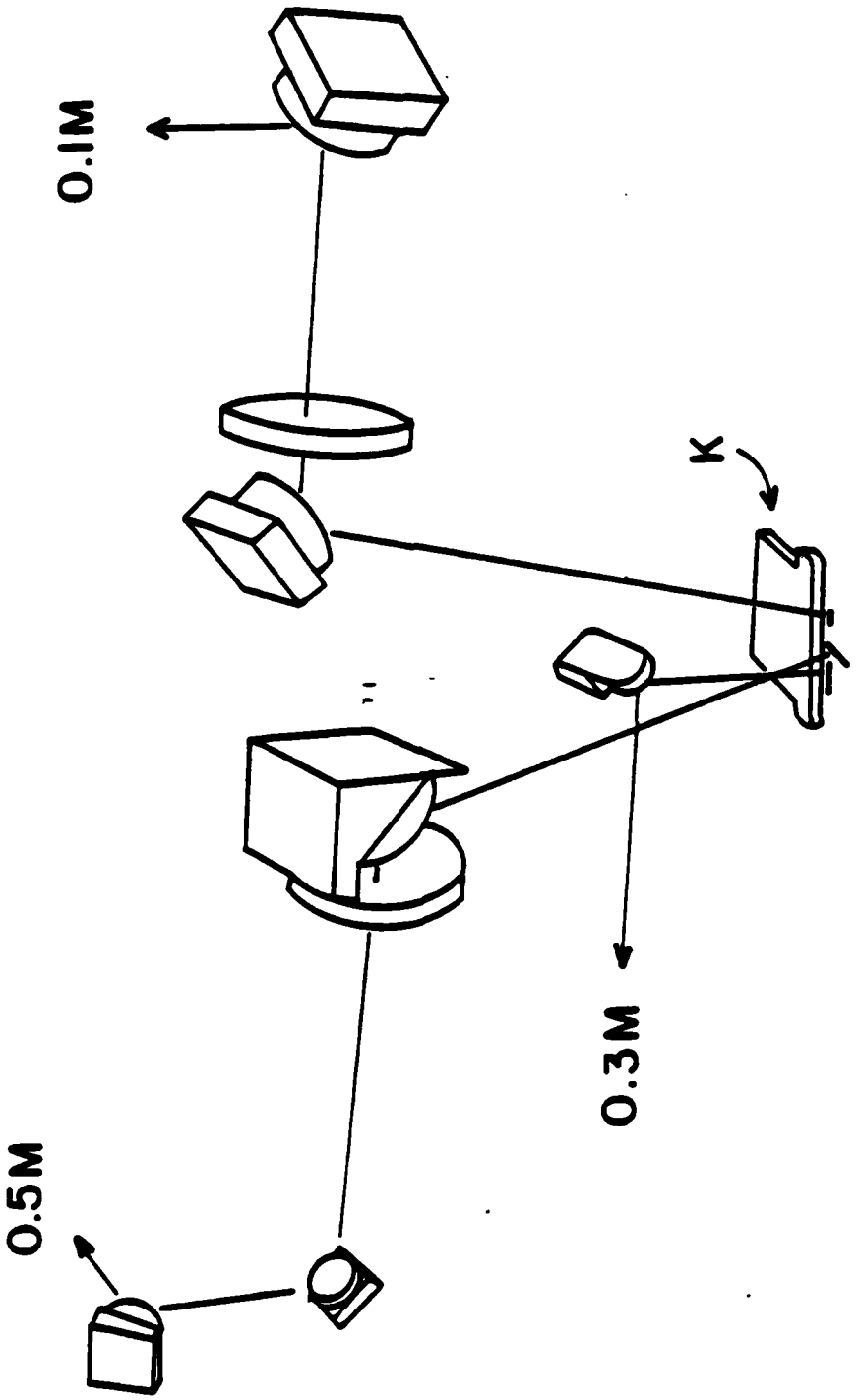

Fig. 8.2: Schematic of the spectroscopic optical system.

which was used with film to give time integrated information over a range of wavelengths. The entrance slit image was positioned across the gap with a lens and three mirrors as shown in figure 8.2, and the spectrometer was mounted on sliding rails to permit focussing at different wavelengths. It was found, however, that line emission during the shot was dominated by line and continuum emission after the shot. To obtain partial time resolution the spectrograph was coupled to the film back via the intensifier. In this case the gating pulse was set to about 50 ns to record light emitted during the bulk of the shot. The intensifier diameter permitted about 250 Å to be viewed on each shot. Polaroid type 667 film was used.

The principal spectroscopic diagnostic in this experiment was the 0.3 M monochromator system shown in Fig. 8.3. This involved a 0.3 M GCA/McPherson Czerny-Turner grating spectrometer with a linear dispersion of 26.5 Å/mm. The output light was monitored with an EMI 9781R photomultiplier tube, which had a response from 2000–6700 Å and a rise-time of 2 ns. The tube was operated at 700–1000 V and placed in a RF shielded enclosure. This enclosure was placed in a 16 mm thick cast lead housing to shield the tube from the diode x-rays. The linear operating region of the tube was determined beforehand and the fiducials on PMT traces were delayed at the scopes to compensate for the ~22 ns transit time delay of the PMT.

Two lenses and two mirrors imaged the diode gap onto the plane of the entrance slit. As shown in Figs. 8.2 and 8.3, the slit image was aligned parallel to the electrodes to yield spatial resolution in the direction across the gap. The slit image was swept across the gap by moving one of the lenses, mounted on a precision translation stage, transverse to its optic axis. Chromatic aberration of the singlet lenses used required the system to be refocussed for each spectral line. This was done by mounting the other lens on a precision sliding rail.

Since the gaps were only a few mm, a fairly high resolution was necessary. In order to justify the conclusions drawn later in this chapter concerning the expansion of various species, it is also necessary to verify such resolution. Factors limiting resolution include the finite depth of field due to the cathode width, lens

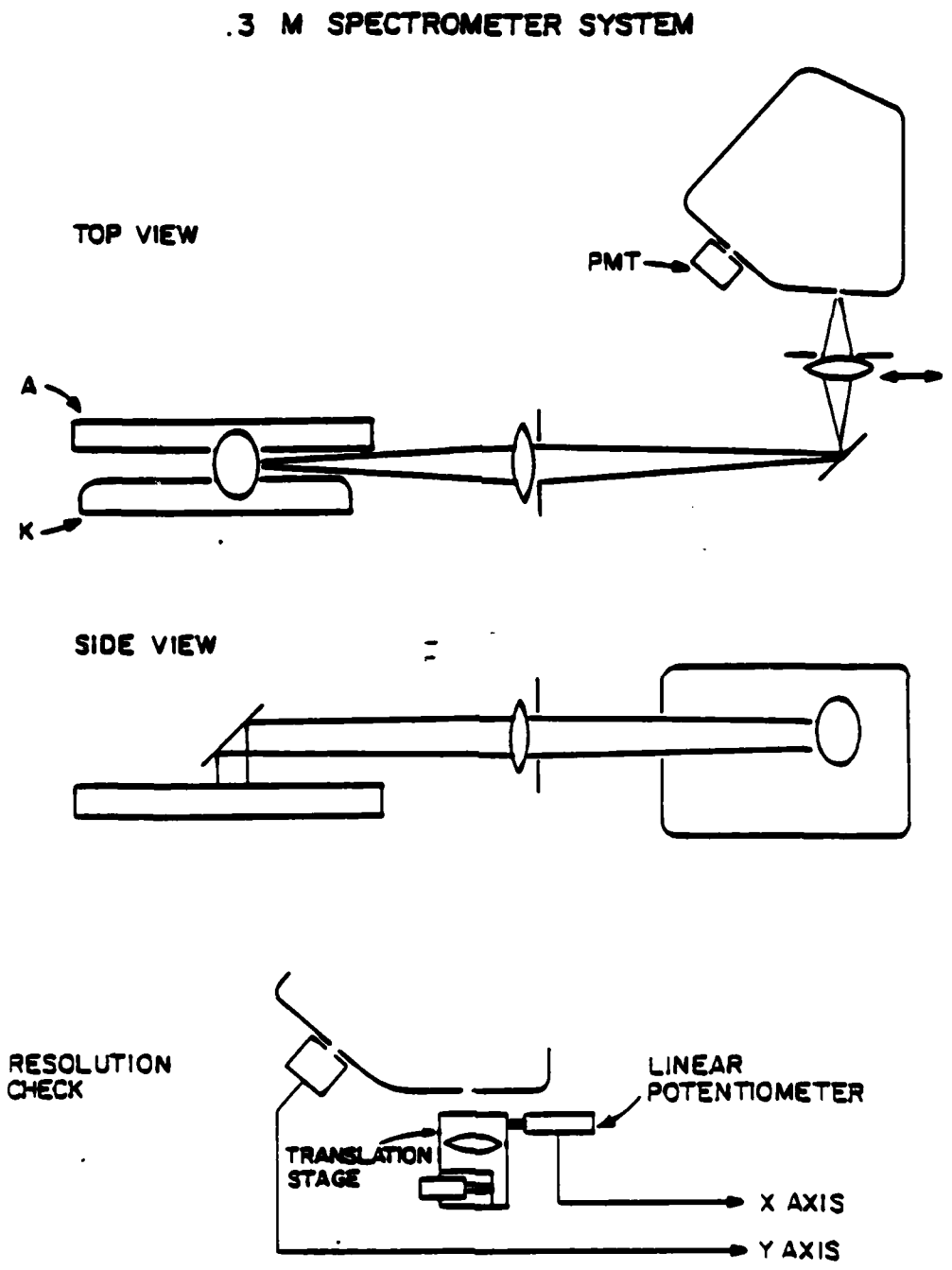

Fig. 8.3: 0.3 M monochromator system.

aberrations (primarily spherical), any misalignment between the axis of the slit image and the axis parallel to the electrodes, and the finite width of the entrance slit. The system resolution was checked by backlighting the gap and sweeping the slit image across it. The scanning lens was attached to a precision linear potentiometer as shown in Fig. 8.3 and the potentiometer and PMT outputs were displayed with an X-Y recorder. A typical recorder output is shown in Fig. 8.4. The slope of the electrode edge images is indicative of the system resolution, which can be seen to be better than 200 μm. Similar results were obtained by scanning the light emitted by a thin hot tungsten wire that was positioned parallel to the cathode surface.

The light intensity incident on the PMT was maintained in the linear range by varying the lens apertures and slit width, and by using Kodak neutral density filters (for visible lines). Typical parameters were a 10 μm entrance and 40 μm exit slit (giving 1.1 Å resolution), 4 mm slit height, and 1 cm lens apertures (the lenses were 3.8 cm in diameter). The typical system demagnification was 2.5×.

The 0.1 M monochromator was a PTR Optics Minichrom 1 with a dispersion of 60 Å/mm. The smallest slits availible were 150 μm wide, giving a fairly coarse resolution of 9 Å. This monochromator was generally left set on the strong C II 4267 Å line as a check for shot-to-shot reproducibility. The optical system consisted of a lens and two mirrors: the lens was mounted on a translation stage to sweep the slit image (also parallel to the cathode surface) across the gap, and the monochromator was mounted on precision sliding rails to focus the system for each wavelength.

8.4. Line Identification

In Figs. 8.5 and 8.6, a wavelength scan is shown for 9.6 mm Aerodagged aluminum cathodes. Lines from various ionization stages of carbon, aluminum and hydrogen can be seen as well as the Swan band from the C_2 molecule. This band is the only feature of the continuum that could be identified. In general the line intensities (and especially the continuum intensity) on the film were not very reproducible, probably due the the nonlinearity of the film, so that it is not possible to compare overall continuum intensities from different shots. Lines from

Fig. 8.4: Typical resolution scan.

hydrogen, carbon II, carbon III, and the C_2 molecule are observed for all cathodes used. When aluminum cathodes, both bare and aerodagged, are used, aluminum I, II and III lines are observed, as well as lines from magnesium. Copper I and zinc I and II lines are observed with brass cathodes. With stainless cathodes, many weak lines are seen, most of which could not be identified. All strong lines were identified with the exception of the two at 4716 and 4736 Å, which are observed with all cathodes.

There are several interesting points to note here. The aluminum emission from Aerodagged cathodes was unexpected since the coating was thick and no aluminum could be seen under the Aerodag, either before or after the shot. It is possible that the sandblasted surface has tips that poke through the Aerodag. To check this, smooth aluminum cathodes were covered with a fairly thick (many coats) coating of Aerodag, and aluminum was still observed.

It is also interesting that no silicon or oxygen light was observed, even though the former would be expected because of diffusion pump oil and the latter would be expected because of adsorbed water and silicone oil and oxide coatings. In Fig. 8.7 scans are shown for aluminum cathodes, one of which was coated before the shot with a layer of silicone pump oil that was thin on a macroscopic scale but presumably quite thick compared to any microscopic coatings. As can be seen, silicon light was observed in that case, so it may be that the line emission was normally too weak to be observed. Likewise, two weak oxygen II lines were seen in some cases, as shown in Fig. 8.7, so that oxygen was also presumably present.

Weak lines of sodium, calcium, and aluminum (with non-aluminum cathodes) were observed. In view of the surface analysis results in Ch. 5, which indicate the presence of many metallic impurities on all cathodes, this is not surprising.

In addition to the lines observed with the spectrograph, several lines were also seen to be present with the 0.3 M monochromator, by comparing the signal at the line with that just off the line. In this manner, the C IV lines at 5801 and 5812 Å were identified on shots with carbon cathodes. These lines were also observed with the spectrograph on some shots, as shown in Fig. 8.7. The C II line at 2836 Å was also observed with the monochromator.

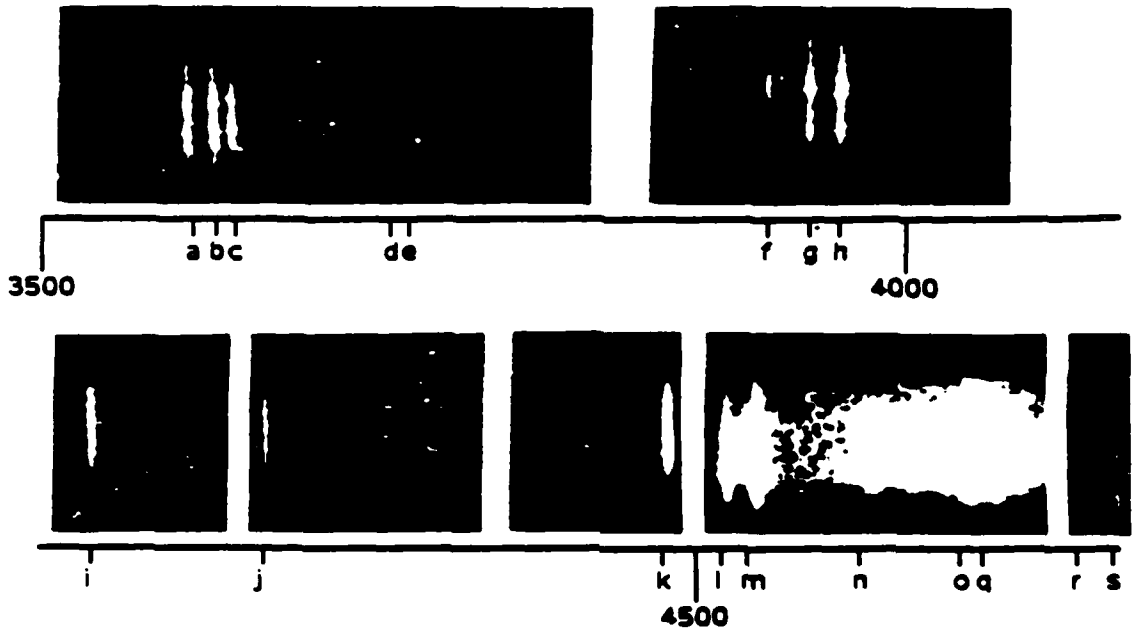

SPECTRAL LINES OBSERVED

a	Al II	3587.1 Å
b	Al III	3601.6 Å
c	Al III	3612.4 Å
d	Al III	3702.1 Å
e	Al III	3713.1 Å
f	C II	3920.7 Å
g	Al I	3944 Å
h	Al I	3961 Å
i	Al III	4149.8-4150.1 Å
j	C II	4267.2 Å
k	Mg II	4481.1-4481.3 Å
l	Al III	4512.5 Å
m	Al III	4529.2 Å
n	C III	2296.9 Å (second order)
o	C III	4647.4-4651.4 Å
q	Al II	4663.1 Å
r	??	4716 Å
s	??	4736 Å

Fig. 8.5: Spectrograph scan for shots with 9.6 mm Aerodagged cathodes.

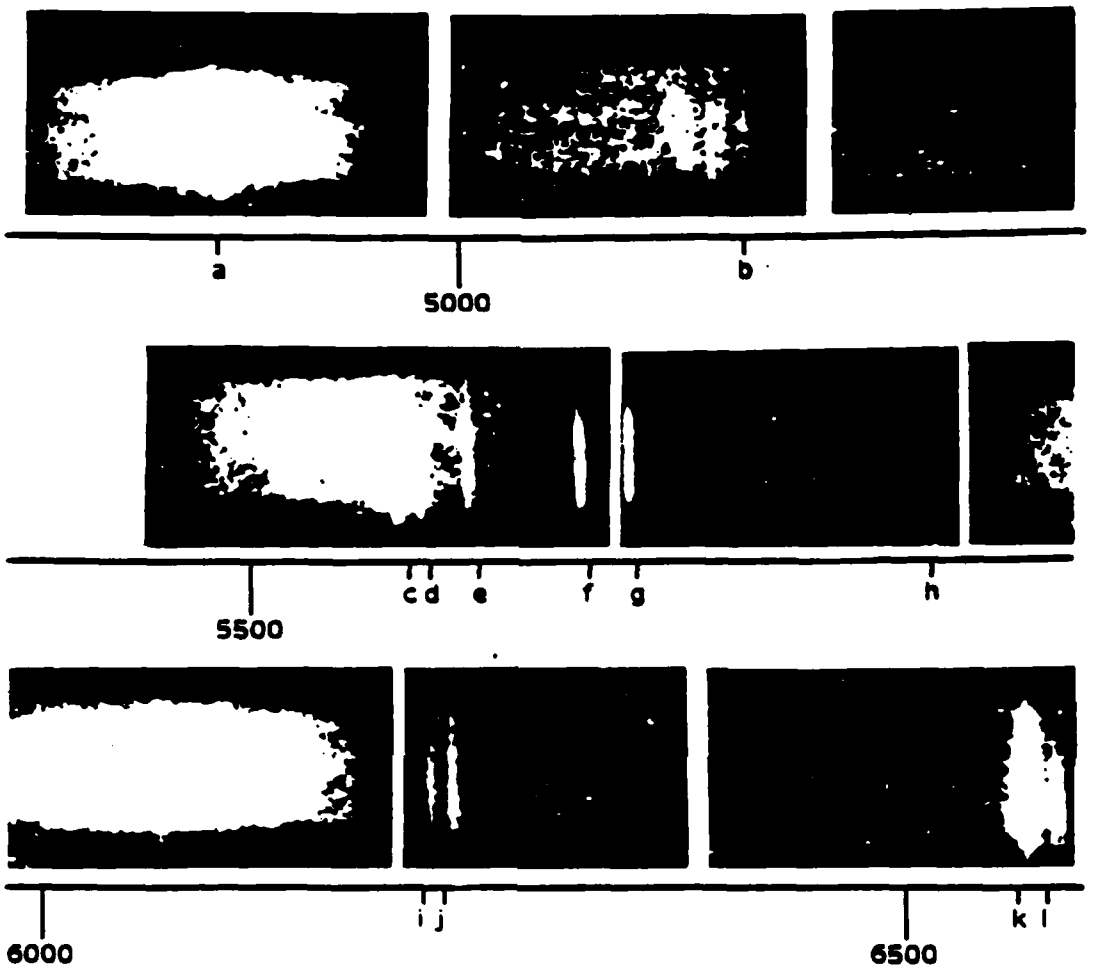

SPECTRAL LINES OBSERVED

a	H_β	4861.3 Å
b	C_2	5165.2 Å (Swan band)
c	Mg II	5593.2 Å
d	Mg II	2802.7 Å (second order)
e	Al II	2816.2 Å (second order)
f	C III	5695.9 Å and Al III 5696.5 Å
g	Al III	5722.6 Å
h	Na I	5889.9, 5895.9 Å
i	Al II	6226,6232 Å
j	Al II	6243 Å
k	H_α	6562.7 Å
l	C II	6578, 6581 Å

Fig. 8.6: Spectrograph scan for shots with 9.6 mm Aerodagged cathodes, con't.

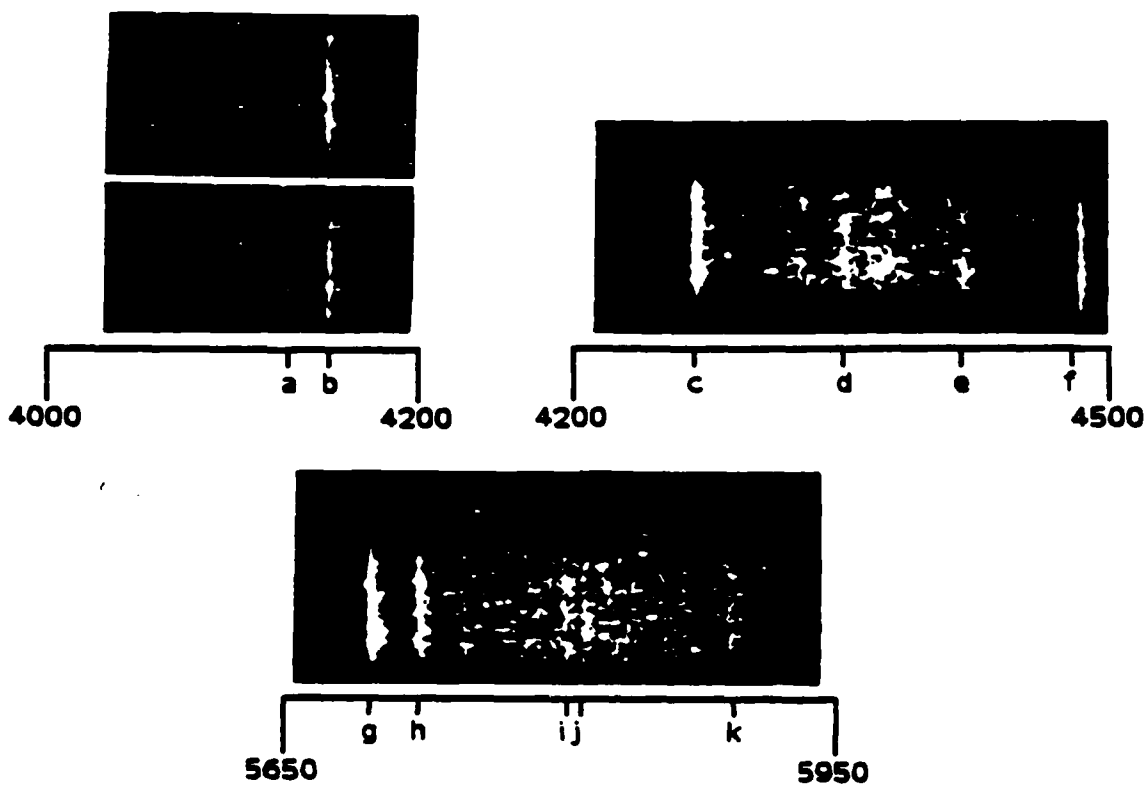

SPECTRAL LINES OBSERVED

a	Si II	4128.0, 4130.8 Å
b	Al III	4149.9-4150.1 Å
c	C II	4267.2 Å
d	O II	4349.4, 4351.3 Å
e	O II	4414.9, 4416.9 Å
f	Mg II	4481.1-4481.3 Å
g	C III	5695.9 Å and Al III 5696.5 Å
h	Al III	5722.6 Å
i	C IV	5801.3 Å
j	C IV	5812.0 Å
k	Na I	5889.9, 5895.9 Å

Fig. 8.7: Additional spectrometer scans: (top left) bare Al (upper) and silicone oil coated Al (lower); (top right) Oxygen line emission (6.4 mm Aerodagged cathode); (bottom) C IV line emission (1.6 mm Aerodagged cathode).

The cathode plasma is seen to be composed at least in part of surface impurity consituents. In view of the vacuum arc results in Ch. 2, which indicate that arcs on contaminated surfaces are associated with negligible metallic erosion, it is worth asking whether any of the cathode substrate material gets into the plasma. The presence of aluminum does not verify this since the aluminum could have come from a surface oxide. Since stainless steel is coated with a layer of chromium oxide, the presence of iron in the plasma would be significant. No iron lines could be positively identified on the spectrograph pictures, but the Fe III line at 4164 Å was definitely observed with the monochromator.

Since some lines were seen to be present even though they were not seen with the spectrograph (because of insufficient system sensitivity), there may well be other lines emitted that have not been observed.

8.5. General Characteristics of Line Intensities

Traces of the diode current, total light intensity, and spectral line intensities are shown in Figs. 8.8 and 8.9. On some of the traces, particularly the H_α trace, there appears to be a large amount of noise. This is not electrical noise since the PMT output was zero when the monochromator entrance slit was blocked. For traces with equal signal levels, this 'noise' is greater for weaker lines where the PMT is operated at a higher voltage to compensate for the reduced number of incident photons. Because of this, it is reasonable to assume that the spiky nature of the traces is due to statistical variations in the plasma output. From the calibrations described in Ch. 9, the signal levels on the H_α trace correspond to about 100 photons within the 2 ns integration time of the PMT. From this, a 10% statistical variation would be expected, so that this explanation is not unreasonable.

The traces all have two peaks which appear to correspond to the two peaks in the current trace. In general, the peaks are sharper for lines which have higher upper level energies (compare the C IV and C II traces), and this will be discussed further in Ch. 9. That the line intensity peaks are correlated with peaks in the current is shown by the slow switch traces in Fig. 8.9. In that case the current does not have the double humped shape and likewise the line intensity does not

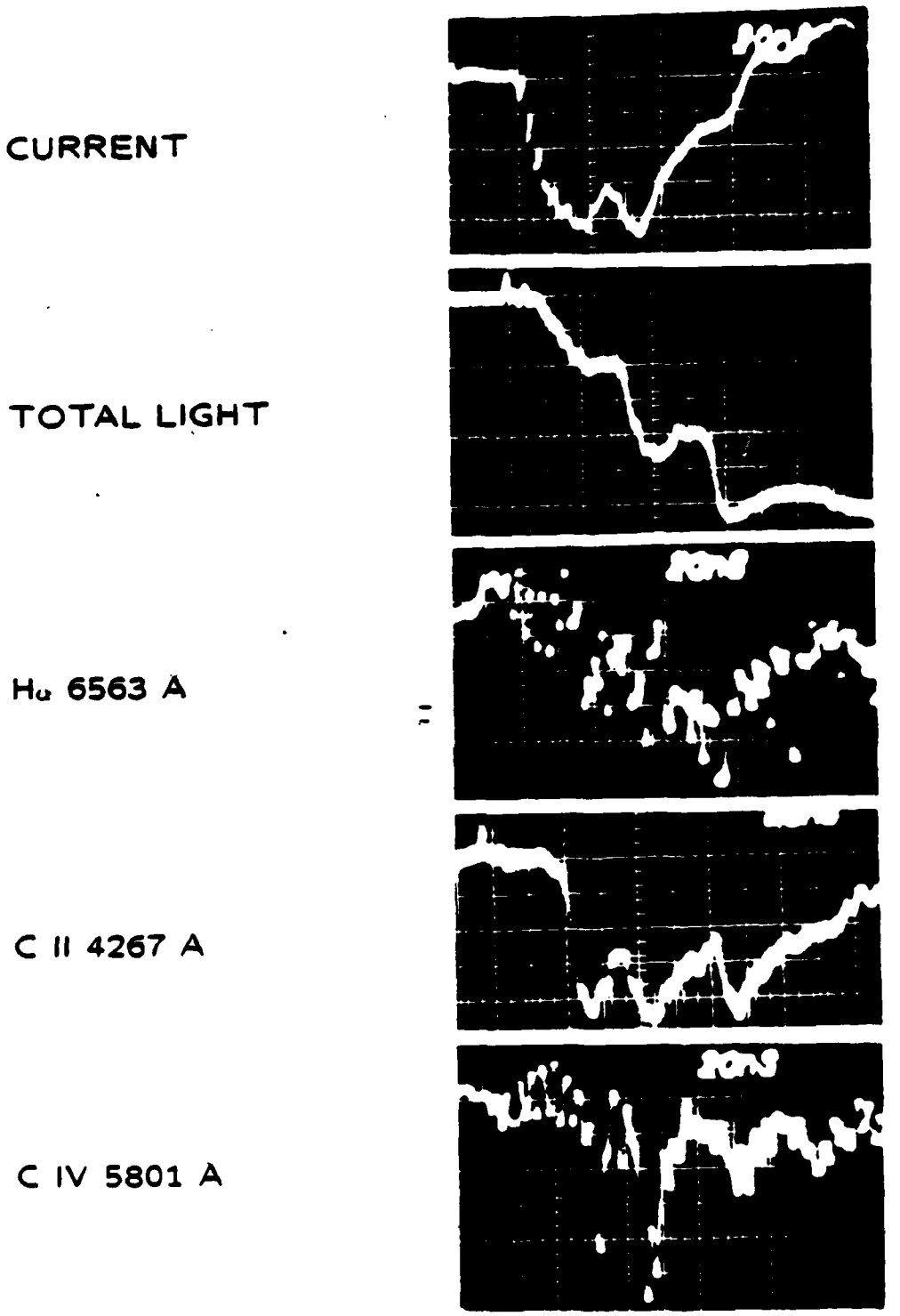

Fig. 8.8: Typical current and PMT traces.

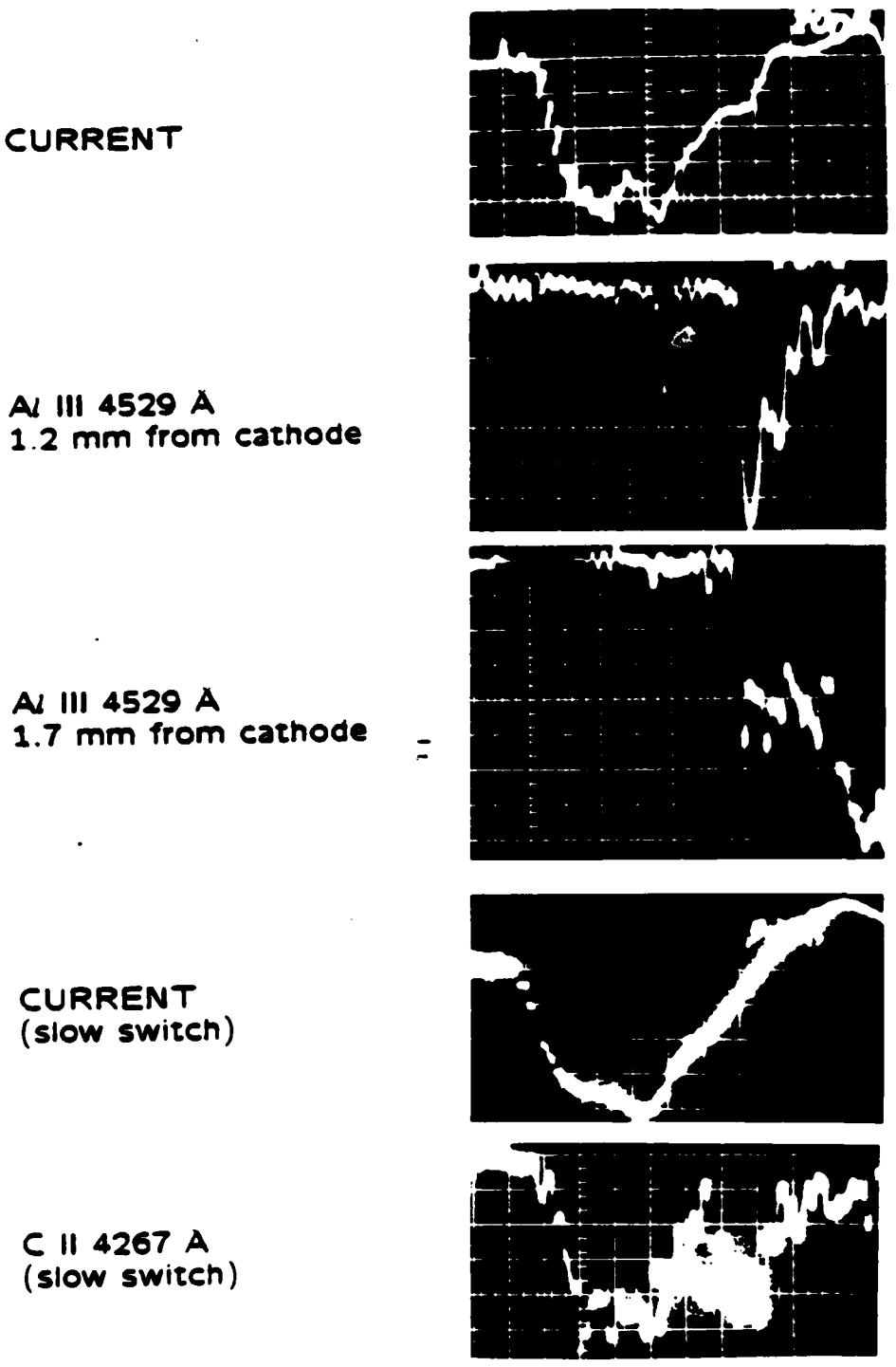

Fig. 8.9: Typical current and PMT traces. con't.

have the two peaks. Also, when flashover occurs during the shot and chops the current. the second peak is not observed.

The line intensities rise again at the end of the shot, which is seen more clearly in the line emission at locations out in the gap in Fig. 8.9. The intensity spike appears to be correlated with the time at which the voltage goes to zero (and presumably gap closure occurs), although as mentioned in Ch. 6 this time is difficult to determine precisely. The average times at which the spikes peak are 100, 120, and 140 ns for the 1.6 mm, 6.4 mm, and 9.6 mm cathodes, implying (average) closure velocities of 1.7, 1.8, and 1.9 cm/μs, respectively.

After the spike, the intensity sometimes drops back down again, sometimes it remaines high, and sometimes it drops and then rises again. The total light signal stays relatively constant for at least several μs (in this case the signal was well within the linear range). The line intensity behavior at distances out into the gap will be discussed further in Sec. 8.6.

The plasma is seen to be composed of materials obviously from surface contaminants (H) and from the cathode substrate (Fe). Some insight into the fundamental processes at the cathode can be gained by comparing the time dependence of impurity and bulk lines. In this experiment there is no obvious difference between the two. Shots were taken with the monochromator system gain set to the maximum in order to observe light as close to the beginning of the shot as possible. In this case. emission from H. C. Al. and Fe was observed within 10 ns. There is no reason to assume that light would not have been observed even sooner with a more sensitive system.

8.5.1. General Intensity Comparisons

In general. carbon lines are of roughly equal intensity for Poco and Aerodagged cathodes and about 8 times more intense than when aluminum. brass. and stainless cathodes (which all have similar carbon line intensities) are used. Aluminum lines are of equal intensity when either Aerodagged (aluminum) or aluminum cathodes are used. The H_α line and total light intensities are roughly the same for all cathodes.

When aluminum cathodes are coated with silicone oil, the intensity of the Si II line at 4130 Å increases, as was observed with the spectrograph.

The intensity of the C II line at 4267 Å increases by about 50% when aluminum cathodes were coated with either silicone or hydrocarbon oil. In this case, no change in aluminum line intensity is observed.

Glow discharge cleaning has no effect on carbon lines.

Heating Aerodagged stainless cathodes to about 500°C has no effect on C II line emission but reduces the H_α emission by about 50%.

8.6. Previous Species-Resolved Expansion Measurements

8.6.1. Experiments

Since vacuum arc plasmas consist solely of ions (and atoms) of the electrode material, these experiments are a good source of information concerning the expansion of different species. Vacuum arc cathodes have been known to be sources of high velocity (~2 cm/μs) particles since 1930.[184] These flows have been the subject of extensive experimental investigation; two significant studies are those reported by Plyutto *et al.*,[185] and Davis and Miller.[186] Further references are given in those papers, as well as in Refs. 32 and 187.

These flows are seen to consist of singly and multiply charged ions (usually, no neutrals with directed velocities are observed). In general, the high velocity ions are produced at a rate (as mentioned in Ch. 7) of about 0.1 ions for every current electron. The directed ion energies of ~20–100 eV exceed the thermal ion energies. The ion velocities generally increase with increasing ion charge and decrease with increasing ion mass.

These flows are interesting for two reasons. First, the ion directed velocities are in the 'wrong' direction, that is, from the cathode to the anode. Second, the ion energies often exceed the applied arc voltage.

Miller[187] studied the dependence of velocity on ion mass and charge in an arc with a Cu/Bi cathode, where velocities of ions with three charge states and two masses could be measured. The results are summarized in Table 8.1.

In fact, since (as mentioned in Ch. 2) needle cathode surfaces may be considered clean, the expansion measurements with needle cathodes reviewed in Ch. 6 may also be considered to be species-resolved. Again, typical velocities were 2 cm/μs for Al and Mo and 1 cm/μs for Pb.

Baksht *et al.*[183] observed (in a manner similar to the present experiment) the expansion of different species in a short-pulsed (75 ns) arc with a needle cathode. Velocities of ~2 cm/μs were observed for H, C II, and Cu I.

8.6.2. Theory

In the adiabatic expansion of a gas cloud into vacuum, the outer regions of the cloud expand inertially with the velocity[188]

$$v = \sqrt{\frac{4\gamma}{\gamma - 1}\epsilon_0} \tag{8.1}$$

where ϵ_0 is the initially supplied specific energy and γ is the adiabatic exponent. Mesyats[189] has suggested that the metal is superheated prior to explosion, and the initial energy is related to the metal's specific heat of sublimation. Agreement was found between the calculated and measured expansion velocities. In Ref. 183, it is suggested that the high current density in the spot regions heats the plasma to several tens of eV: in this case,

$$\epsilon_0 = \frac{1}{\gamma - 1}\frac{T_0}{M} \tag{8.2}$$

If energy is continually supplied to the plasma as it expands through Joule heating, then the ions can be accelerated to higher velocities. In particular, for the case of isothermal expansion, the final ion velocity V_i is given by[190]

$$\frac{MV_i^2}{2} \approx (1 - Z)T \ln(\frac{n_0}{n}) \tag{8.3}$$

where n_0 is the initial density, so that if the density falls off by several orders of magnitude, ions will be accelerated to energies greatly exceeding the electron temperature.

Table 8.1

Ion Velocities in a Cu/Bi Vacuum Arc

Ion	v(cm/μs)	E(eV)	V(volts)	E/M(eV/amu)
Cu II	1.21	48	48	0.75
Cu III	1.47	70	35	1.1
Cu IV	1.66	90	31	1.4
Bi II	1.01	110	110	0.52
Bi III	1.10	130	65	0.62
Bi III	1.18	150	50	0.72

Here is a summary of ion velocity measurements in a vacuum arc by Miller.[187] The observed ion velocities and energies are given in the first two columns. Also listed are the ion potentials (E Z) in V and energy mass in eV amu.

The above considerations still do not specify the exact mechanism by which electrons transfer their energy to the ions. Plyutto *et al.*[185] describe the mechanism as being ambipolar acceleration. The electrons tend to preferentially leave the spot region because of their higher thermal velocities, creating a positive electrostatic 'potential hump', off of which the ions are accelerated. Lyubimov[191] considers the mechanism to be a gas-dynamic acceleration based on electron-ion collisions.

These theories and others are reviewed by Miller,[187] who then compares the predictions with the results of his study mentioned above. A pure electrostatic acceleration would accelerate ions to equal potentials (with the ion energy independent of mass and proportional to charge) while a gasdynamic acceleration would accelerate ions to equal velocities (with the ion energy independent of charge and proportional to mass). As shown in Table 8.1, the dependence of ion energy on mass and charge is in between these two predictions.

Ion velocities can be equalized by ion-ion collisions. Anisimov *et al.*[192] have numerically simulated the expansion of a hydrogen plasma with aluminum impurity ions, and shown that if the plasma is dense enough, both species will be accelerated to similar velocities. Charge exchange processes can also equalize velocities of different charge states.[193]

The important point to this is that while the exact acceleration mechanism is undetermined as yet, all of those discussed above require the existence of regions of high energy density at the cathode. The directed ion energies are acquired in some way from the high energy density in the spot regions.

The existence of such fast ion flows in diodes would be important for two reasons. First, it would constitute further evidence of similarity between the microphysical processes of broad area diodes, needle cathodes, and vacuum arcs. Second, it would have significant ramifications in diode design, as will be discussed in Sec. 8.9.

8.7. Expansion

The motion of different species across the gap was investigated by positioning the slit image at a given distance from the cathode and measuring the time at which emission of the characteristic spectral line is first observed. A plot so obtained for the Al III 4529 Å line for shots with a 6.4 mm aluminum cathode is shown in Fig. 8.10. In that plot, the vertical axis represents the distance from the cathode surface of the slit image while the horizontal axis represents the time at which Al III line emission is first observed. Since each point represents the maximum time required for the ion to arrive at the slit image location, the minimum ion velocity is given by the slope of the line from the origin to that point (if the ions left the cathode at t>0, then the velocity would be greater). In other words, the actual motion of the Al III ion front can lie anywhere to the upper right of the curve defined by the points on the plot. On this plot, the highest minimum velocity is inferred from the points later in time, which give a minimum velocity for the Al III ions of 1.6 cm/μs.. This velocity corresponds to an aluminum ion energy of about 35 eV, which is typical of $\bar{v}$alues in vacuum arcs and significantly larger than the 4 eV electron temperature estimated in the next chapter. In fact, the inferred ion velocity is close to the *average* gap closure velocity of 1.7–2 cm/μs given in Ch. 6. It is concluded that the directed ion flows observed in vacuum arcs do indeed also exist in broad area diode plasmas. The calculated motion of the plasma (electron) emission layer from Ch. 6 is also shown on the plot.

In order to verify that the ions do indeed have such a velocity, it must be determined that: the light is actually emitted from the presumed spatial location; the light is indeed from Al III ions; these ions originate at the cathode. The first is determined from the resolution scan in Fig. 8.4. The other two conditions are shown to be true by comparing the line intensity with that of the background just off the line, and by comparing the line intensity with that on shots where brass cathodes were used. Photographs of such traces are shown in Fig. 8.11, for locations 1.9 mm from the cathode, and it can be seen that the light is definitely emitted by aluminum ions originating at the cathode.

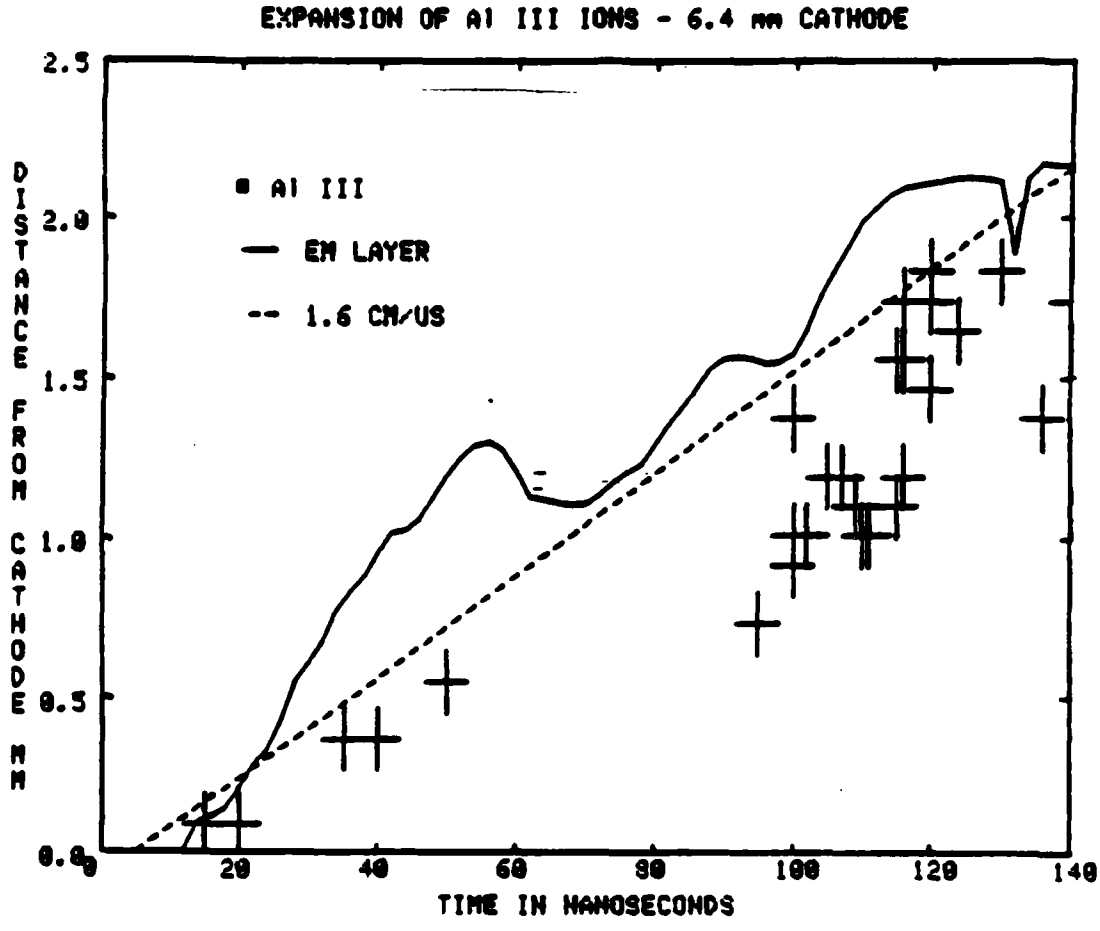

Fig. 8.10: Expansion plot for Al III ions on shots with 6.4 mm aluminum cathodes.

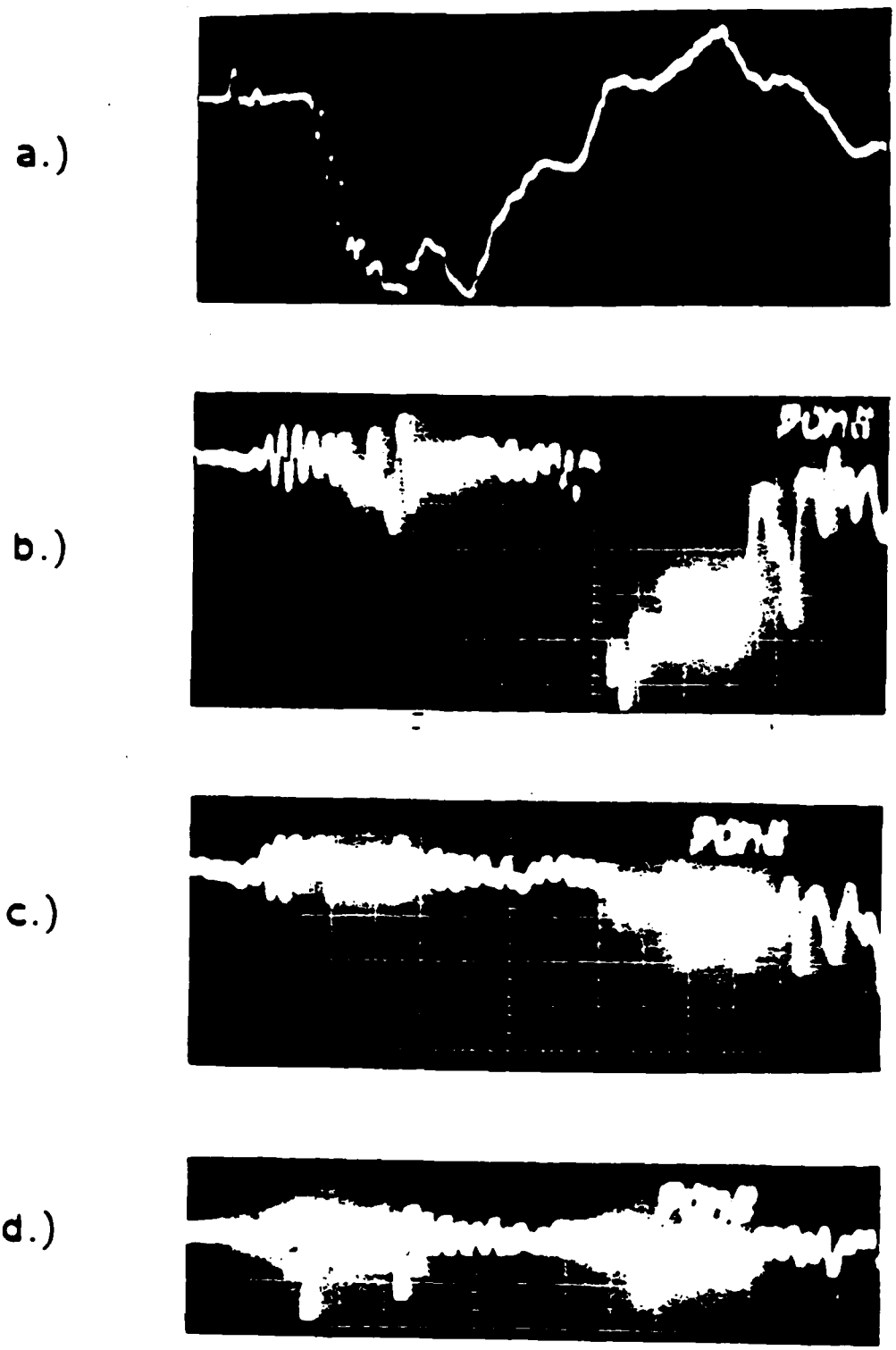

Fig. 8.11: Expansion verification checks: (a) on line; (b) off line: (c) on line with a brass cathode.

An explanation for the shape of the ion luminosity expansion plot will now be given. The ions are assumed to move with a velocity of about 1.6 cm/μs as indicated by the dashed line in Fig. 8.10. The sensitivity of the monochromator system limits the minimum ion density that can be observed; thus there is some delay before ions are observed at the cathode. As the ions expand out from the cathode, the motion of the plasma layer with observable ion density (henceforth referred to as the luminosity layer) lags behind the motion of the (electron) emission layer. Finally, at the end of the shot, the plasma rapidly heats (as will be suggested below), increasing the plasma emissivity and allowing lower densities to be observed. Because of this, at the end of the shot the calculated emission layer location and that of the luminosity layer approximately coincide.

Al III 4529 Å line intensity traces at different spatial locations are shown in Fig. 8.12. The temporal behavior of the line intensity as a function of distance from the cathode in this case is typical of all lines. Near the cathode the signal is like those in Fig. 8.8. At 0.3 mm, the leading edge of the first peak is eroded since about 20 ns is required for the ions to arrive. As the distance from the cathode is increased, the first peak is further eroded until only the second peak is observed. With a further increase in distance, the ion density is too low during the second peak and no light is observed until the spike at the end of the pulse. At distances close to the anode, the line intensities are weak at all times.

8.7.1. Expansion at Different Current Densities

Plots for the motion of Al III ions from 1.6 mm and 9.6 mm aluminum cathodes are shown in Fig. 8.13. These plots display the same behavior as those for the 6.4 mm cathode, with the calculated emission layer and the luminosity layer locations agreeing at the beginning and end of the shot, and the luminosity layer lagging behind at intermediate times. At the higher current density, the luminosity layer is closer to the emission layer from (40-100 ns) than at the lower current densities. This is reasonable since the emission layer density is higher at the higher current density. Also note the excellent agreement between the luminosity and calculated emission layers for the first 40 ns with the 9.6 mm cathode.

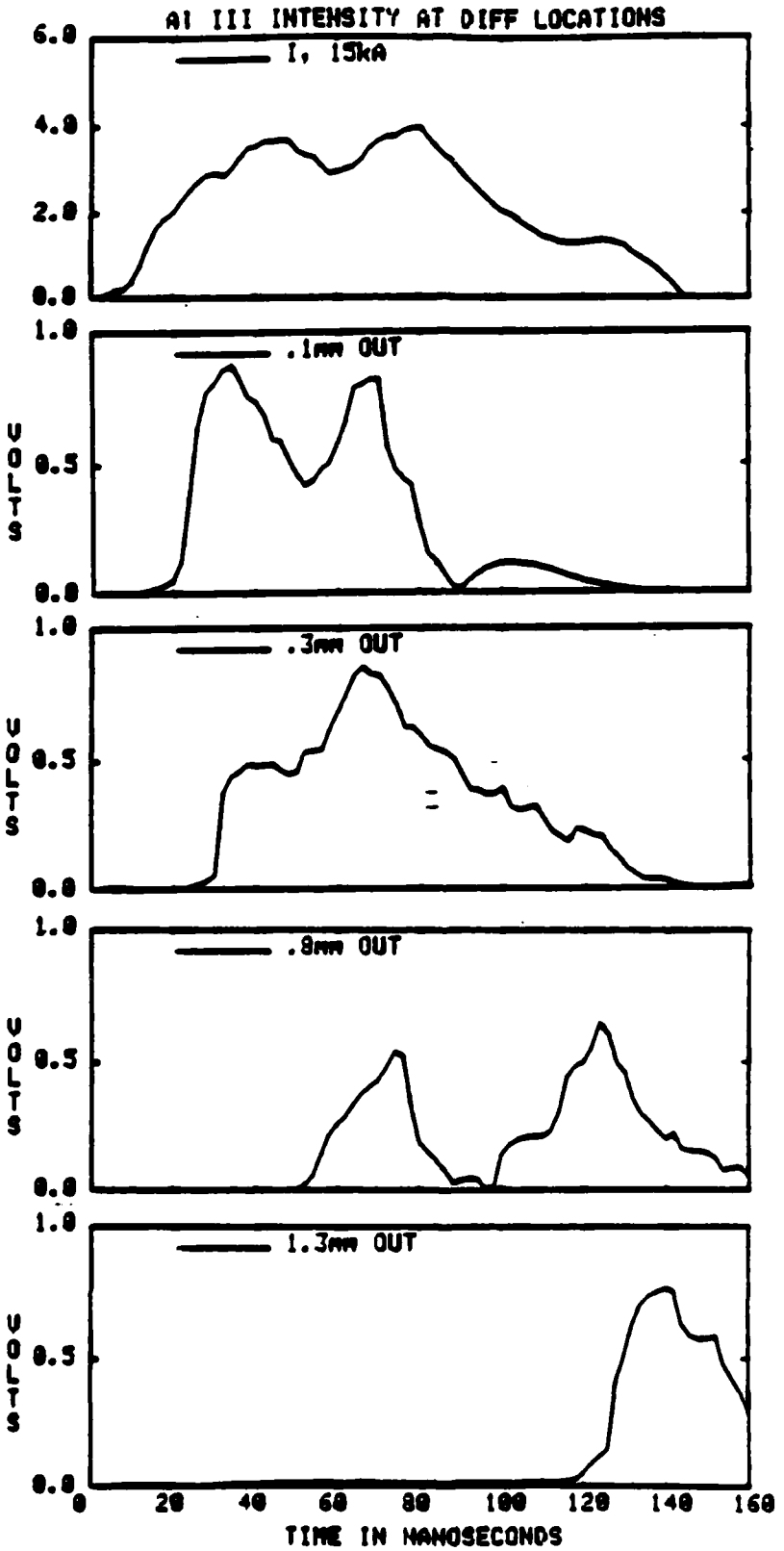

Fig. 8.12: Temporal behavior of the 4529 Å Al III line at different spatial locations for shots with a 9.6 mm aluminum cathode.

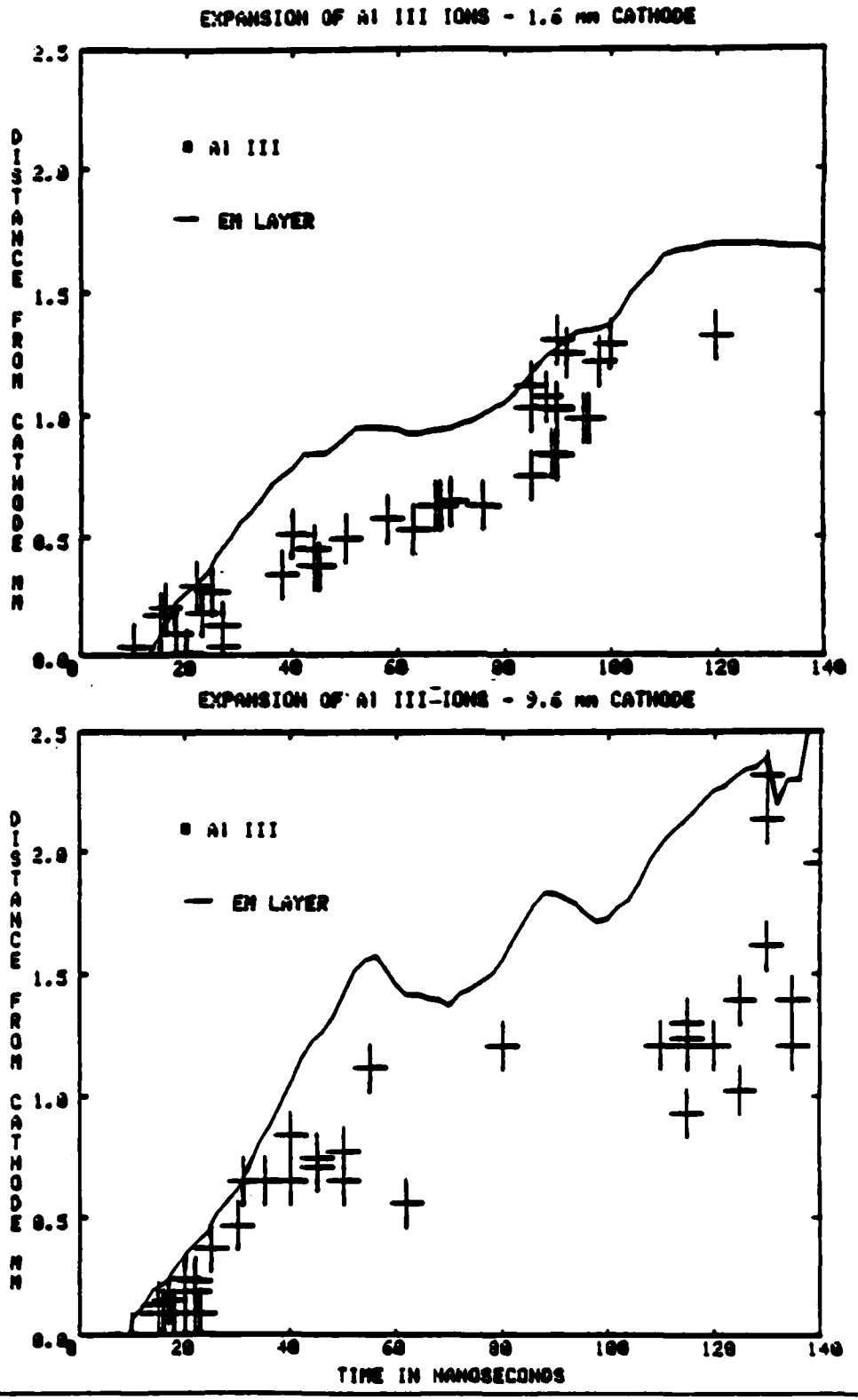

Fig. 8.13: Expansion plots for different current densities: (top) 39 kA. cm^2 (1.6 mm cathode): (bottom) 8 kA. cm^2 (9.6 mm cathdode).

8.7.2. Comparison With Interferograms

If the luminosity layer is correlated with a given density, then its motion should be correlated with some feature of the interferograms. The expansion plots are compared with the bend point motion obtained from the interferograms, for 1.6 mm and 6.4 mm aluminum cathodes, in Fig. 8.14, and the two are seen to agree within the error bars. This suggests that the luminosity layer corresponds to a plasma electron density of about $10^{16}/cm^3$.

8.7.3. Expansion of Different Species

The expansion of H, C II, and AL III are compared in Fig. 8.15. The hydrogen and carbon luminosity show the same behavior as that from Al III, and the three plots are seen to more or less overlay. As shown in the next chapter, the H_α upper level is assumed to be in equilibrium with the protons, so that measurement of hydrogen light is assumed to be a measurement of proton motion. It appears that all components of the cathode plasma expand at the same rate.

8.7.4. Expansion of Different Charge States

An expansion plot of Al I, Al II, and Al III is shown in Fig. 8.16. The expansion of Al II and Al III is similar, while the neutral aluminum is delayed. The neutral velocity is apparently about 0.7 $cm/\mu s$. As shown in the next chapter, the equilibrium concentration of Al I is expected to be negligible, and the light observed at the cathode is presumably due to a non-equilibrium injection of neutrals from the cathode. That neutral aluminum is seen out in the gap at much later times implies that rapid cooling occurs at the end of the shot. The neutral carbon line at 2478 Å shows similar behavior, as described in the next chapter.

8.7.5. Luminosity Spike

It remains to explain the reason for the sharp increase in light intensity at the end of the shot. An increase in current would be expected when the diode shorts but since closure occurs near the end of the power pulse the current shows no great increase. A possible explanation has been suggested,[194] as shown in Fig. 8.17. If the plasma has any local bumpiness, then closure will first occur at localized regions as shown. Because of the reduced resistance in these regions, the

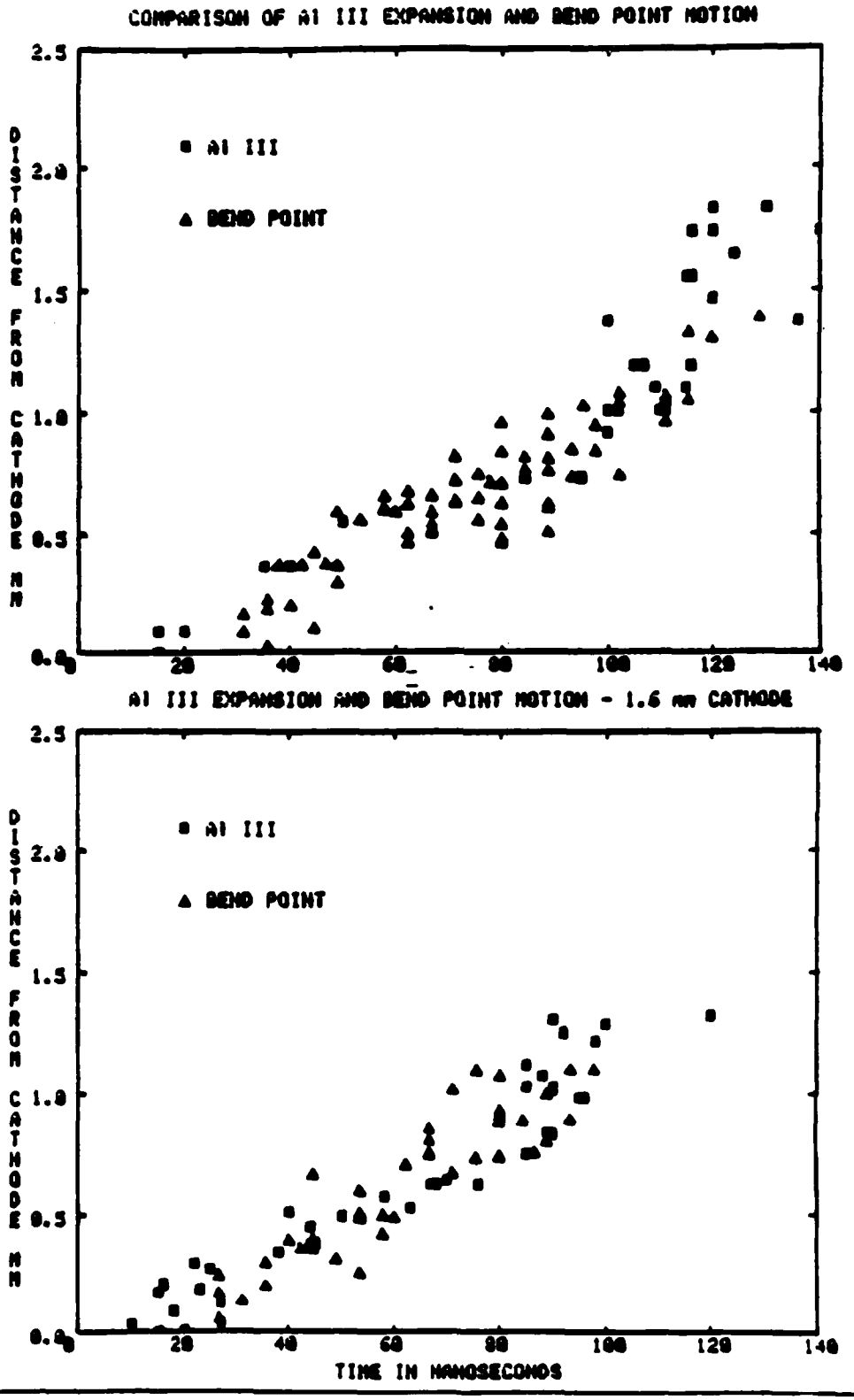

Fig. 8.14: Comparison of expansion plots with the bend point motion: (top) 13 kA cm^2 (6.4 mm cathode): (bottom) 39 kA cm^2 (1.6 mm cathode).

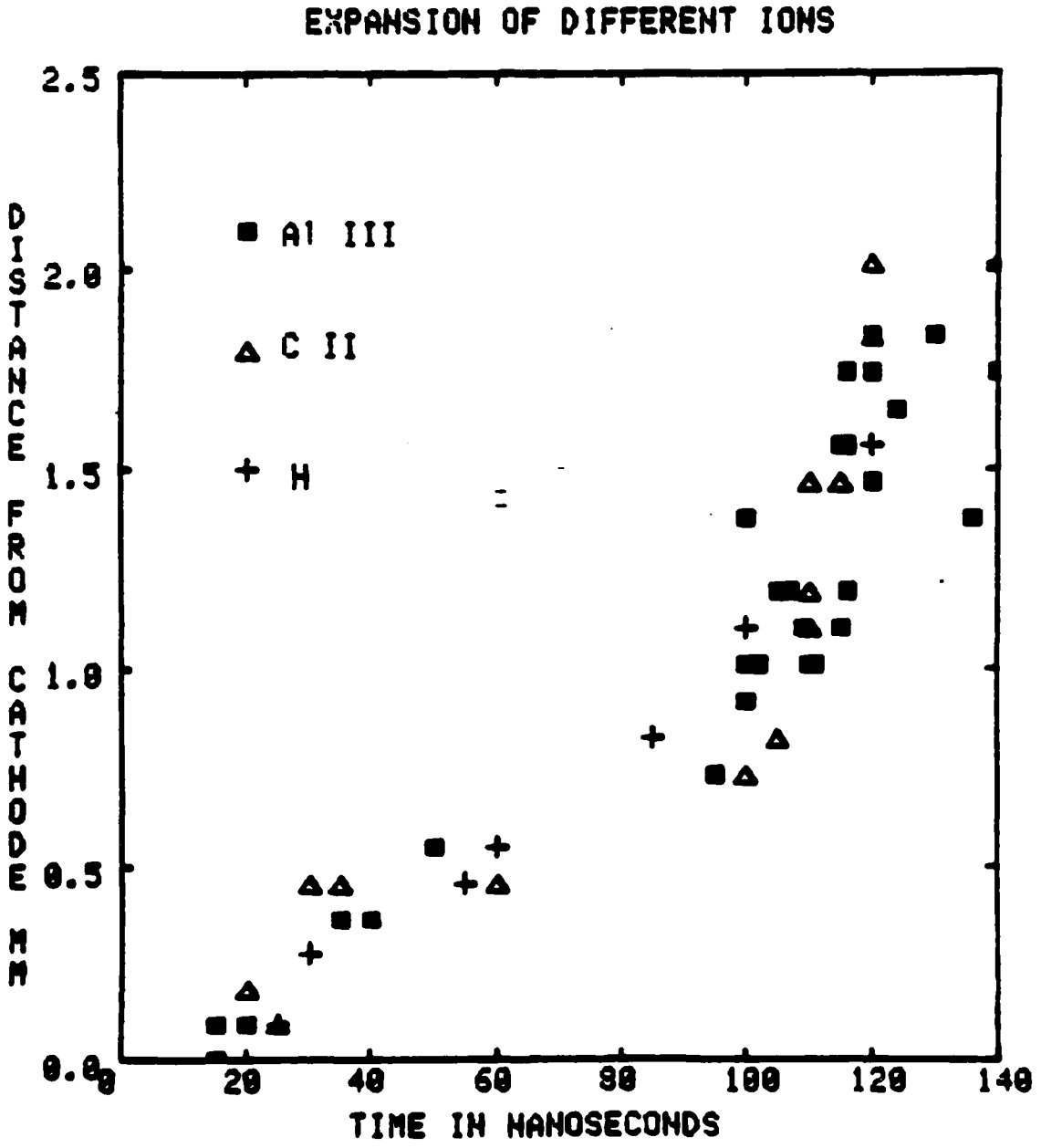

Fig. 8.15: Expansion plots for different lines with 6.4 mm aluminum cathodes.

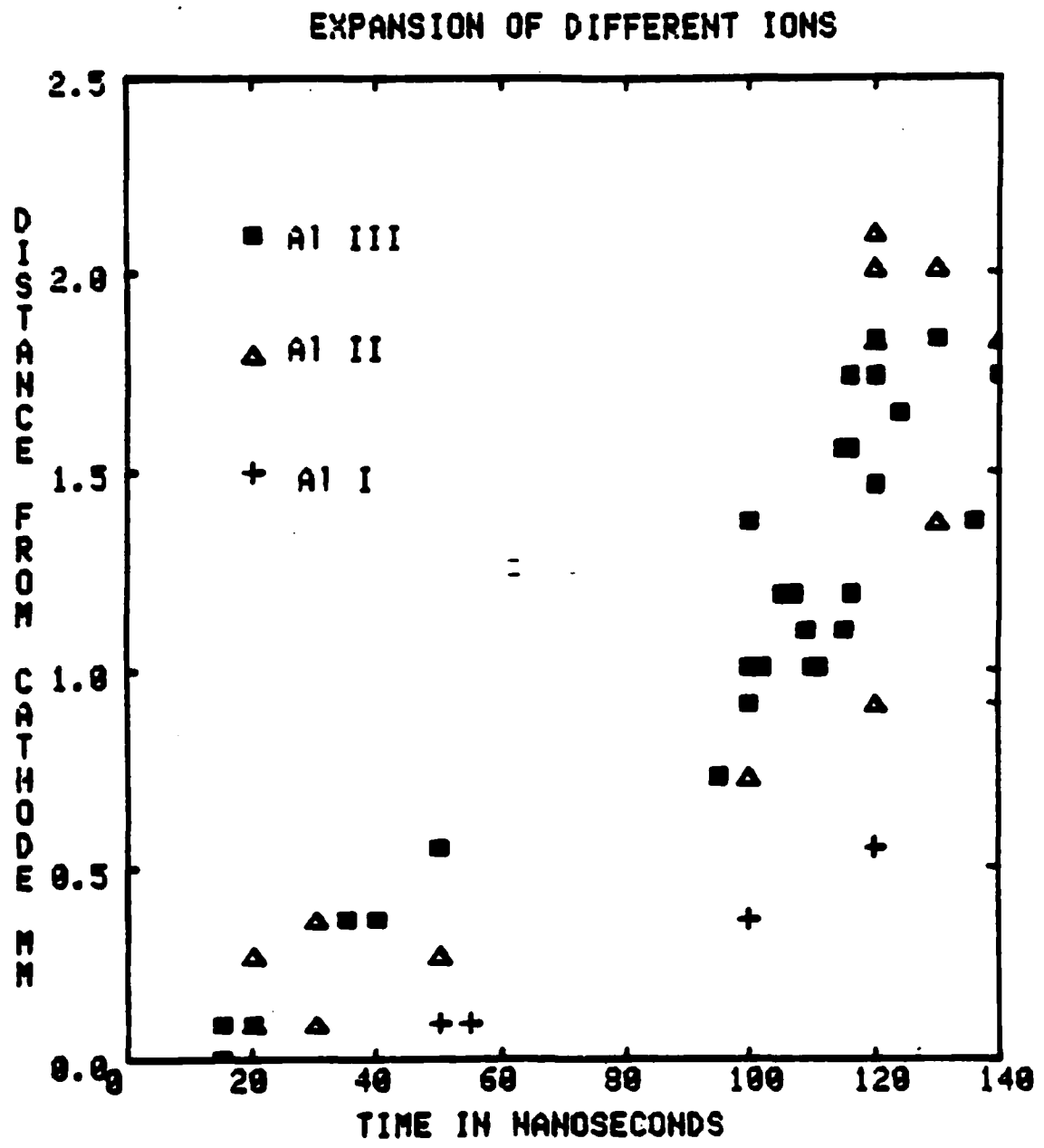

Fig. 8.16: Expansion plot for different charge states of aluminum.

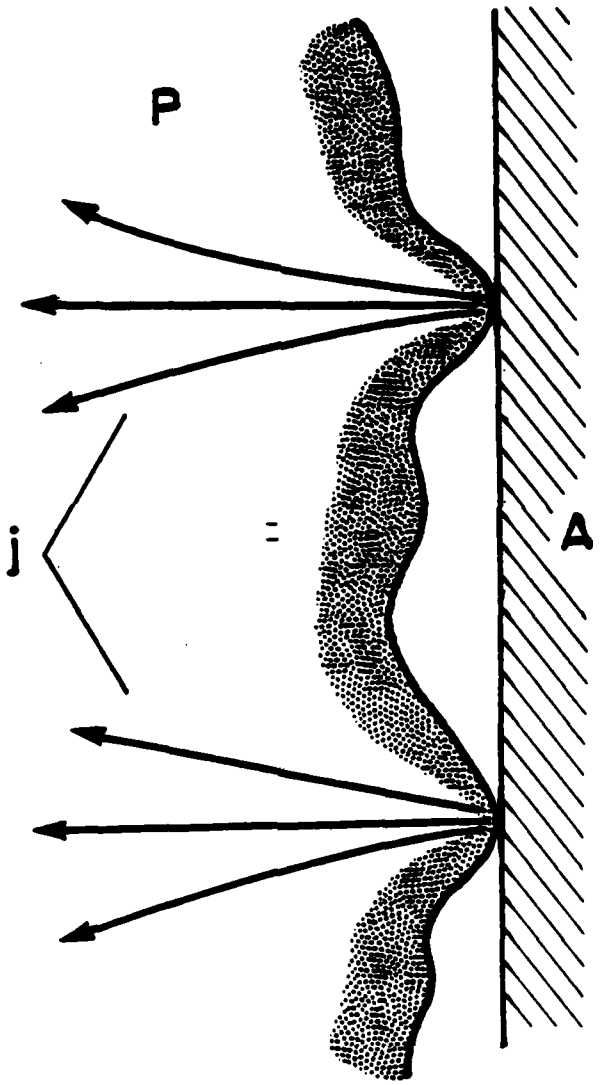

Fig. 8.17: Possible explanation for the luminosity spike.

current will tend to concentrate there, resulting in a high local current density, although the total current may not change, and this high local current density can result in heating and increased luminosity. Since the plasma resistivity varies as $T^{-3/2}$, the increase in temperature will tend to cause a further increase in current. This is the basis for the so-called thermal resistive instability, which was analyzed in Ref. 127. For the right initial conditions, growth can occur in a few ns.

The framing pictures presented in Ch. 4 also show increased luminosity at the end of the shot. Both the framing pictures and the PMT signals (at different locations) show that the luminosity spike is greatest near the middle of the gap. At distances further back into the plasma (toward the cathode), the current flow may spread out (with consequently reduced heating) as indicated in Fig. 8.17. Since the plasma emissivity is determined by both the plasma density and temperature, the maximum spike luminosity in the middle of the gap can be explained by a reduced density toward the anode and reduced temperature toward the cathode.

8.8. Discussion

The fact that hydrogen is observed, and carbon with non-carbon cathodes, shows that the cathode plasma is composed in part of materials from surface impurities, as was found in the previous investigations. The cathode plasma is also seen to be composed of material from the cathode bulk. Since iron is observed, this conclusion can be stated more definitely than in previous works where metal ions could have originated from surface oxide coatings. This conclusion is also indicated by the fact that carbon line emission is stronger with carbon than with non-carbon cathodes. Since line emission is observed from both impurity and substrate species early in time, it appears that both are involved in the fundamental processes of plasma formation.

The fact that aluminum is observed when Aerodagged cathodes are used is evidence of the violent nature of the emission process. The presence of triply ionized carbon is evidence of the existence of relatively hot, high density plasma regions at the cathode.

Since silicon and carbon line emission increase when an oil coating is used, and the H_α intensity decreases when the cathode is heated, it is possible to (in part) affect the plasma composition by altering the cathode coating.

The fact that neutrals are observed at the end of the pulse is consistent with the fringe shift reversal seen at that time on the interferograms. The observation of neutrals at the end of the shot suggests that plasma cooling also occurs at this time, interrupted temporarily by momentary heating at the time of the luminosity spike. The thermal behavior of the plasma will be discussed further in the next two chapters.

The results of the expansion measurements are particularly interesting. The aluminum ions have a minimum velocity that is close to the average velocity of the emission layer. Obviously, the expansion velocities of different components do not follow a $M^{-1/2}$ dependence; rather, it appears that all components expand at the same rate.

The results of this experiment are compared with relevant results from needle cathode, short pulsed arc, and long pulsed arc experiments in table 8.2. The velocities observed in this experiment are quite comparable to those observed in the other systems.

8.9. Conclusions

While the measurements presented in this chapter are qualitative, they do furnish information on the plasma composition and the process of plasma expansion. In addition, some insight is gained into the fundamental microprocesses at the cathode.

The cathode plasma is seen to be composed of both the cathode material and constituents of surface impurities. By varying the cathode coating it is possible to (only) partly affect the plasma composition. The fact that both substrate and impurity materials enter the plasma early in time implies that both are involved in the fundamental processes of plasma formation.

The directed ion flows observed in vacuum arcs are also seen to exist in a diode plasma. Thus, it is likely that the microprocesses at the cathode surface

Table 8.2

Comparison of Ion Velocity Measurements

Experiment	Ion	v (cm/μs)	Energy (eV)
Diode	H	>1.6	>1.4
(This exp.)	C II	>1.6	>16
	Al II	>1.6	>35
	Al III	>1.6	>35
Pulsed	H	2	2
Vacuum Arc	C II	2	25
(Ref. 183)	Cu I	1.5	75
Needle Cathode	Al	2	54
(Ref. 42)			
Arc	Al	1.7	37
(Ref. 186)			
Arc	C II	2.2	30
(Ref. 186)	Al II	1.9	50
	Al III	2.3	75

Comparison of measured ion velocities from different experiments.

in broad area diodes, needle cathode diodes, and vacuum arcs are similar. In particular, the fast ions point to the existence of (fairly hot) dense cathode spots, as does the existence of triply ionized carbon.

These fast ions have great practical relevance to diode design. If plasma expansion was dominated by protons (because of their reduced mass), then if a hydrogen-free surface could be obtained (which is reasonable at least in a repetitively pulsed diode) the expansion velocity would be reduced. Because of these anomalously large heavy species velocities, the expansion velocity would be expected to change little with a hydrogen-free surface.

Chapter 9

Quantitative Spectroscopy

After the measurements described in the last chapter were made, the 0.3 M monochromator system was absolutely calibrated. This chapter describes the resulting quantitative spectroscopic measurements of spectral line intensities, from which estimates of the electron temperature and (quantitative) plasma composition were obtained. Some background theory is discussed in the next section. Procedures used to calculate the various quantities are described in Secs. 9.2–9.4, and the calibration and experimental procedure are be described in Sec. 9.5. Temperature measurements are presented in Sec. 9.6, estimates of the total ionic populations are given in Sec. 9.7, and the time dependence of the spectral line intensities is discussed in Sec. 9.8. This work is compared with the results of previous studies in Sec. 9.9, and conclusions are given in Sec. 9.10.

9.1. Background Theory

9.1.1. Collision Rates

In all of this work it is assumed that the electron temperature is a well defined quantity, that is, the electrons have a Maxwellian velocity distribution. In order for this to be the case, the electron-electron collision time τ_{ee} must be small compared to the time scale on which the plasma parameters are changing, and small compared to the time scale on which free electrons are supplied by ionization. This collision time is given by[195]

$$\tau_{ee} = 3.3 \times 10^5 \frac{T^{3/2}}{n \ln \Lambda} \tag{9.1}$$

where T is the electron temperature, n the electron density, and $\ln \Lambda$, the Coulomb logarithm, is roughly 6 for the parameters of this experiment. (Again, unless noted, all units are cgs with the exception of temperatures, which are in eV). For example, at $n=10^{15}/\text{cm}^3$ and $T=4$ eV this time is 4.4×10^{-10} s, so that this condition is well satisfied and the electrons may be assumed to have a Maxwellian velocity distribution.

The ion velocity distribution is established on the time scale of the ion-ion collision time, which is given by

$$\tau_{ii} = 3.3 \times 10^5 \sqrt{\frac{M}{m}} \frac{T_i^{3/2}}{n \ln \Lambda Z^3} \tag{9.2}$$

where T_i, M, m, and Z are the ion temperature, ion mass, electron mass, and ion charge, respectively. For protons with $T_i \leq T$ this time is 1.8 ns at an electron density of $10^{16}/\text{cm}^3$, so that for the densities that are spectroscopically observed the ions are also expected to have a Maxwellian distribution (although it may well be a drifting Maxwellian). For heavier ions, the increase in Z (on the average) will tend to offset the effect of the increase in M on τ_{ii}.

The electron and ion temperatures will equilibrate on a time scale given by

$$\tau_{eq} = \tau_{ee} \frac{M}{3mZ^3} \tag{9.3}$$

For protons, this is about 3 ns at an electron density of $10^{17}/\text{cm}^3$, so that while the electrons and ions will presumably start out with the same temperature, once the plasma has expanded out to densities lower than this the temperatures may differ.[176]

9.1.2. Transition Processes

The transition processes between different levels and ionization stages that will be considered here are shown in Fig. 9.1. Different energy levels of the same ion are connected by collisional excitation ($C_{i,j}$) and de-excitation ($X_{j,i}$), spontaneous emission ($A_{j,i}$), and stimulated absorption ($\sigma_{i,j}$) and emission ($\sigma_{j,i}$). Each level is also connected with the ground state of the next ionization stage by collisional ionization (S_j) and recombination (α_j), radiative recombination (R_j), and dielectronic recombination (β_j). Photoionization will be neglected here because of the relatively small cross section ($\sim 10^{-17}$). The rates for these will now be discussed in turn.

The only radiative transitions relevant to this experiment are electric dipole transitions. For the relatively light ions considered here LS coupling is appropriate

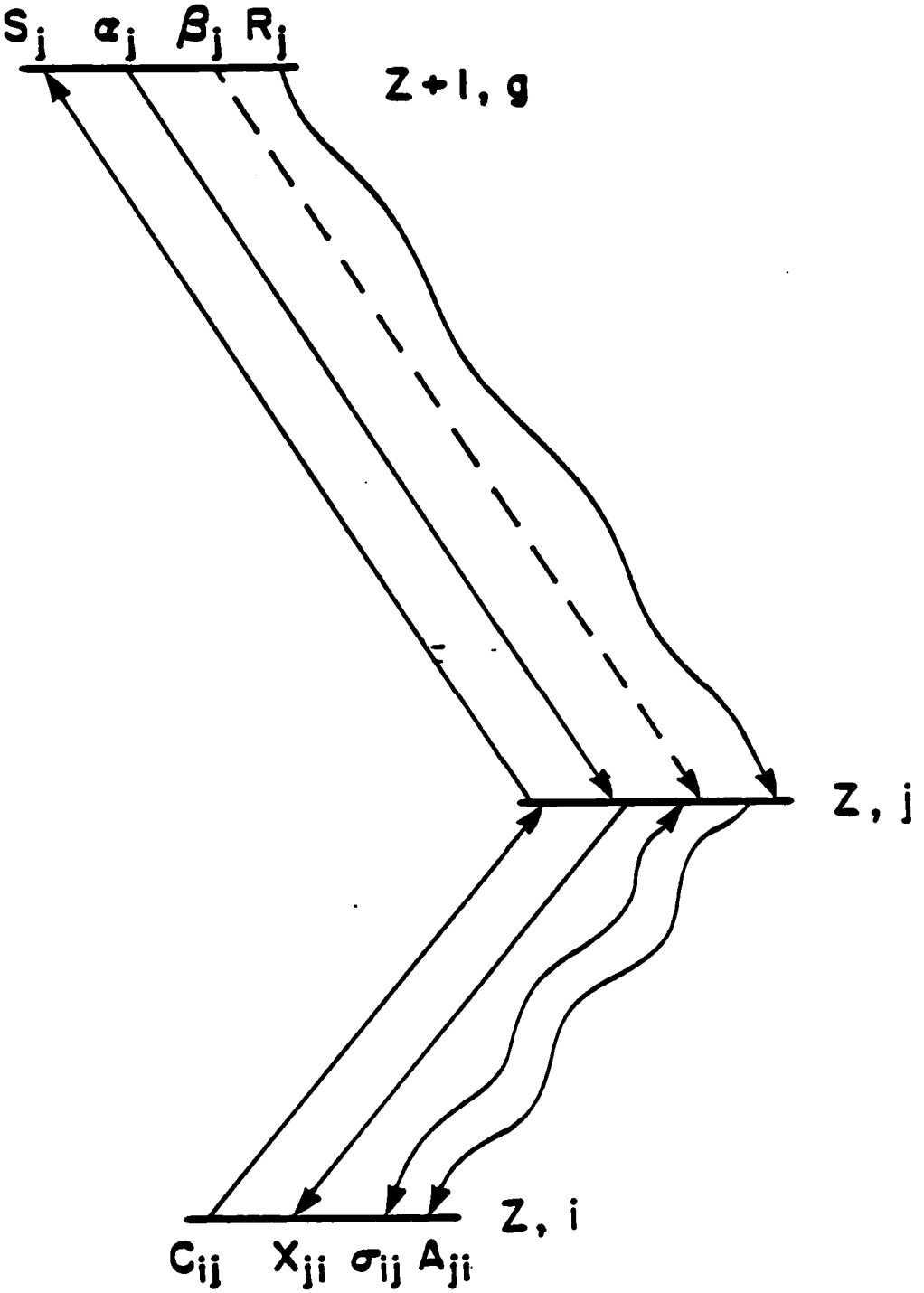

Fig. 9.1: Transition processes in a plasma.

(with the quantum numbers L, S, J, and m_j), and optically coupled transitions are those for which

$$\Delta L = \pm 1$$

$$\Delta S = 0$$

The spontaneous transition rate (in s^{-1}) and absorption cross section (in cm^2) are given by[196]

$$A_{ji} = 4.3 \times 10^7 \frac{g_i}{g_j} f_{ij} (\Delta E_{ij})^2 \tag{9.4}$$

$$\sigma_{ij}(\lambda) = 8.9 \times 10^{-13} f_{ij} \lambda^2 L(\lambda) \tag{9.5a}$$

$$\sigma_{ji} = \frac{g_i}{g_j} \sigma_{ij} \tag{9.5b}$$

where f_{ij} is the absorption oscillator strength, g_n is the statistical weight of level n, ΔE_{ij} is the energy difference between the levels, and $L(\lambda)$ is the normalized lineshape.

The remaining rates are discussed in several monographs.[197,198,199] In general, there are simple formulae for most of these rates but it should be pointed out that they are most applicable to hydrogen atoms and the applicability of these formulae to all ions or to all ranges of plasma parameters is not known. The rates for collisional excitation and ionization and radiative recombination (in s^{-1}) are given by[197]

$$nC_{ij} = n \frac{1.6 \times 10^{-5} f_{ij} \bar{g}}{\Delta E_{ij} T^{1/2}} e^{-\Delta E_{ij}/T} \tag{9.6}$$

$$nS_j = n \frac{1.1 \times 10^{-5} T^{1.2} \zeta}{(\Delta E_i)^2 (6 - T\ \Delta E_i)} e^{-E_i/T} \tag{9.7}$$

$$nR_j = 1.9 \times 10^{-14} n \frac{\Delta E_i}{T^{1/2}} \tag{9.8}$$

where ζ is the number of equivalent outer shell electrons, $\bar{g}$ is the averaged Gaunt factor, which is approximately equal to 0.2, and E_i is the ionization energy of level i. If two levels are not optically coupled, then calculation of the rate of collisional excitation becomes more complicated. However, this rate can be significant. Of particular importance are spin-flip transitions connecting lower levels of different

spin systems, as discussed in Ref. 200. In thermal equilibrium, level populations in a given ionization stage are related by the Boltzmann relation

$$\frac{N_j}{N_i} = \frac{g_j}{g_i} e^{-\Delta E_{ij}/T} \tag{9.9}$$

while level populations are related to the population of the ground state of the next higher ionization stage by the Saha equation

$$\frac{nN_{g,z+1}}{N_{j,z}} = 6.0 \times 10^{21} \frac{g_{g,z+1}}{g_{j,z}} e^{-E_i/T} \tag{9.10}$$

The rates for collisional de-excitation and (three body) recombination are determined from C_{ij} and S_j by the principle of detailed balance — in equilibrium, each process is balanced by its inverse, but the rates are independent of the existence of equilibrium. This gives (in s^{-1})

$$nX_{ji} = \frac{g_i}{g_j} e^{\Delta E/T} nC_{ij} \tag{9.11}$$

$$n^2\alpha_j = 1.7 \times 10^{-22} n^2 \frac{g_{j,z}}{g_{g,z+1}} e^{E_i/T} S_j \tag{9.12}$$

Dielectric recombination is a radiationless electron capture where the excess energy goes into excitation of a bound electron, resulting in a doubly excited, autoionizing state, which then undergoes a stabilizing radiative transition. The calculation of this process is complicated and there is at present no simple formula to describe it.[198,201]

9.1.3. Equilibria

As mentioned above, in complete thermal equilibrium each process is exactly balanced by its inverse and the level populations are related by the Saha and Boltzmann relations. Such an equilibrium state rarely exists in a plasma. However, if the rates of collisional processes are much larger than the radiative rates, the population distribution will be determined by collisions alone and the level populations will still be given by the Saha and Boltzmann relations. In local thermodynamic equilibrium (LTE) it is assumed that the collisional rates are large enough so that the level populations are constantly in equilibrium with the local electron temperature, which may vary with space and time. In this case the level

populations are determined only by the local temperature and density and the level statistical weights; no knowledge of the atomic parameters is required. In a steady state, homogeneous plasma it is only necessary for the collisional rates to exceed the radiative rates in order to have LTE; for example, for de-excitation, Eqs. (9.4), (9.6) and (9.11) place a limit on the minimum density:

$$n \geq 10^{14} T^{1/2} (\Delta E_{ij})^2 \tag{9.13}$$

in order for the collisional rate to exceed the radiative rate by a factor of ten. Since the required density goes up with the energy difference, this condition will be hardest to satisfy for lower levels and there will always be some level above which the condition is satisfied. For example, for the 1s–2p transition in hydrogen, a density of $2 \times 10^{17}/\text{cm}^3$ is required. A similar condition is necessary for the collisional recombination rate to exceed the radiative rate. Note that in LTE the level populations are independent of density while the ionization stage populations depend on the density.

At the other extreme from LTE is coronal equilibrium (CE). This arises when the electron density is so low that collisional de-excitation and recombination can be neglected compared to the radiative processes. In this case the level populations are determined by:

$$n N_i C_{ij} = N_j A_{ji} \tag{9.14a}$$

$$N_{z,j} S_j = N_{z=1,g} R_j \tag{9.14b}$$

Now the level populations depend on the density while the ionization stage populations do not. Also, in CE determination of the level populations requires the knowledge of all of the transition rates.

LTE and coronal equilibrium represent limiting cases of the more general collisional-radiative equilibrium[202] (CRE). In CRE, all of the processes in Fig. 9.1 are considered. In general, for the parameters of this experiment the lower levels of an ion will be in approximately coronal equilibrium while the upper levels will be in LTE.

9.1.4. Equilibration in a Transient Plasma

If the plasma is spatially uniform and time independent then the nature of equilibrium is determined by the electron density. However, spatial and temporal variations in the plasma parameters place additional constraints on the plasma equilibrium.

First the case of a single ionization stage will be considered, that is, ionization and recombination will be neglected. The time required to establish equilibrium in a two level system is determined by the fastest transition process. For the lower levels of most ions, this is radiative de-excitation and the radiative lifetime is generally a few ns or less. For the upper levels, where the radiative lifetimes are longer, collisional de-excitation is generally rapid. For example, from Eqs. (9.6) and (9.11), with an energy difference of 2 eV, an oscillator strength of 0.2, and an electron temperature of 4 eV, the collisional de-excitation time is only 2 ns at an electron density as low as $10^{15}/cm^3$. Thus all neighboring levels would be expected to be in equilibrium with one another. Equilibration between non-adjacent levels may be thought of as a 'diffusion' process, with the equilibration time being related to the longest adjacent level equilibration time involved. From this, it may be concluded that (in the absence of ionization) the level populations of a single ionization stage will equilibrate with the electron temperature within a few ns for the plasma parameters in the present experiment. There is one exception to this, and that occurs when the ion levels are divided into different spin systems, where the lower levels of each are connected only by collisional spin-flip transitions.

Next, equilibration between ionization stages will be considered. From Eq. 9.7, at a density of $10^{17}/cm^3$ and electron temperature of 4 eV, the ionization time from a given level is about 3 ns for an ionization energy of 10 eV and 160 ns for an ionization energy of 20 eV. Because of the strong dependence of ionization rate on ionization energy, ionization from the lower levels is generally a stepwise process of excitation to a higher level followed by ionization from that level. The total ionization rate is given by

$$nS_z = n \sum S_i \frac{N_i}{N_z} \tag{9.15}$$

where N_z is the total population of charge state z. (This assumes that the ionization rates for each level are less than the rate of transitions from that level to other levels of the same ionization stage. For hydrogen, the ionization rates [under the conditions of this experiment] for all levels above the ground state are greater than all rates of transitions from these levels to other hydrogen levels. In this case a level $j \geq 2$ will equilibrate with the continuum at a rate S_j and the ground state will equilibrate with the other levels and with the continuum at the rate X_{12} of collisional excitation to the n=2 level.) Calculated values of S are given in table 9.1. They range from about 1 ns to times much longer than the shot time scale.

Radiative recombination is much slower than ionization in this experiment. For example, from Eq. (9.8), with an ionization energy of 40 eV, electron temperature of 1 eV, and density of $10^{17}/\text{cm}^3$, the recombination time is still 10 microseconds. Recombination into the upper levels is dominated by collisional recombination, which is also much slower than ionization. With an ionization energy of 1 eV, temperature of 1 eV, and density of $10^{17}/\text{cm}^3$, the collisional recombination time is 300 ns. It can be seen that recombination will also consist of a stepwise cascade of recombination into upper levels followed by de-excitation.

If the the relative populations of neighboring charge states differ from the equilibrium distribution, there will be a net flow of ions from one ionization stage to the next. For example, in an ionizing plasma a given ionization stage will have a flux of ions into the ground state from the previous stage and a flux of ions out of the upper levels into the next stage. This will shift the equilibrium level populations from those in the absence of ionization, reducing the ratio of upper level to ground state populations. This shift in level populations will last until the ionization stages equilibrate, and the amount of this shift for a given ionization stage is determined by the relative rates of (1) transitions between levels in that ionization stage, and (2) transitions into and out of that stage.

If the rate of equilibration between stages (i.e., the inverse ionization time) is large, then the duration of this equilibrium shift will be brief and levels can be assumed to be in (steady state) equilibrium with each other and with the next

Table 9.1

Ionization Rates

Ion	E_i	$S_z(cm^3/s)$	T(eV)
H (n=1)	13.6	5.0×10^{-9}	4
H (n=3)	1.5	1.4×10^{-7}	4
C I	11.3	3.0×10^{-8}	4
C II	24.4	3.6×10^{-10}	4
C III	47.9	5.0×10^{-10}	7.4
		4.5×10^{-12}	4
C IV	64.5	5.0×10^{-12}	7.4
Al I	6.0	2.3×10^{-8}	4
Al II	18.8	3.0×10^{-9}	4
Al III	28.5	1.0×10^{-9}	4

The ionization rate given for the hydrogen ground state is the collisional excitation rate to the n=2 level (Eq. (9.6)). The ionization rate for the Hα upper level was calculated from Eq. (9.7). The rates for carbon were calculated from Eq. (9.15) with ionization rates from Ref. 203, and level populations obtained from the CRE code described in Sec. 9.[redacted] The rate for Al I is the ionization rate of the ground state, which is already large. The rates for Al II and Al III were estimated using Eq. (9.15) and a simple CRE calculation of the level populations.

ionization stage. If the ionization time is long, then the shift in equilibrium will be small (as the flux into a level from different stages will be small) and the ionization stages will be decoupled — no equilibrium can be assumed between stages but the levels in each stage will be in steady state equilibrium. For ionization times in between these cases, problems can occur,[204] with the equilibrium being (on the time scale of the shot) permanently shifted from that which would occur in the absence of ionization.

9.1.5. Optical Depth

If the plasma is optically thin to a given spectral line, the observed intensity I_{obs} (in W/cm^2) of that line over a path length d (in planar geometry) is simply

$$I_{obs} = 1.6 \times 10^{-19} d N_j A_{ji} \Delta E_{ij} \equiv I_0 \tag{9.16}$$

If the emitted photons have a finite probability of being reabsorbed before they escape the plasma, the situation is complicated in two ways. The intensity of light observed along the plasma I_{obs} will be less than I_0 given above so that the upper level population will be underestimated if this is not taken into account. In addition, the reabsorbed photons may actually alter the level populations.

The transport of radiation through a plasma is described by the radiation transfer equation[197]

$$\nabla I = \epsilon - \kappa I \tag{9.17a}$$

$$\epsilon = 1.6 \times 10^{-19} N_j A_{ji} \Delta E_{ij} \tag{9.17b}$$

$$\kappa = (N_i \sigma_{ij} - N_j \sigma_{ji}) d \tag{9.17c}$$

where I is the radiation intensity, ϵ is the plasma emissivity in W/cm^3, and κ is the absorption in cm^{-1}. Included in κ are both absorption and stimulated emission. Both ϵ and κ depend on the level populations and, to the extent that these populations are influenced by radiative transitions, ϵ and κ are themselves functions of I. The problem of radiation transfer is thus quite complicated and generally not amenable to simple analytic treatment.

The importance of optical depth is determined by the ratio of radiative to collisional decay rates for the transition in question. If radiative de-excitation dominates (i.e., coronal equilibrium) then an ion which has absorbed a photon will reradiate the photon before it undergoes collisional decay, so that the light is actually scattered rather than absorbed. In this case there will be no net reduction in intensity.

The effect of radiation trapping for general CRE is treated in Ref 197. The resulting rate equations are formally the same as those for an optically thin plasma, except that the radiative decay rate A_{ji} is replaced by $A_{ji}g(\tau_0)$, where τ_0 is the optical depth at line center along some typical plasma dimension (generally the shortest dimension) and $g(\tau_0)$, the escape factor, takes into account the effects of absorption and stimulated emission. This function has a value of 1 at τ_0=0 and decreases to zero for large τ_0. Once the level populations are determined then the radiated intensity may be determined from Eqs. (9.17).

This formalism makes clear the effects of optical depth for different equilibria. If the transition is coronal, the reduction in A_{ji} will result in a higher upper level population which will just compensate for the reduction in escaping intensity from Eqs. (9.17). If A_{ji} is reduced to the point where it is less than the collisional de-excitation rate, then self absorption will have the effect of shifting the equilibrium to LTE. Finally, if the levels are already in LTE, then the reduction in A_{ji} will have no effect on the populations.

If the plasma is in LTE then the level populations are maintained constant by collisions and so ϵ and κ are independent of I. In planar geometry Eq. (9.17a) has the solution

$$I = \frac{\epsilon}{\kappa}(1 - e^{-\kappa d}) \tag{9.18}$$

By Kirchoff's law, in LTE ϵ and κ are related by

$$\frac{\epsilon}{\kappa} = I_{bb} = \frac{2hc^2}{\lambda^5}\frac{1}{e^{\Delta E_{ij}/T} - 1} \tag{9.19}$$

where h is Planck's constant and I and ϵ are defined in terms of intensity and emissivity per interval of wavelength. From this it can be seen that an LTE

plasma with great optical depth radiates like a black body, as would be expected. From Eqs. (9.16), (9.17b), and (9.18) the observed intensity I_{obs} per wavelength interval may be expressed in terms of the optical depth τ as

$$I_{obs}(\lambda) = I_0(\lambda)\left(\frac{1 - e^{-\tau(\lambda)}}{\tau(\lambda)}\right) \tag{9.20a}$$

$$\tau \equiv \kappa(\lambda)d \tag{9.20b}$$

For small τ, $I_{obs} = I_0$.

From Eqs. (9.5b), (9.9), (9.17c), and (9.20b), the optical depth (in LTE) is given by

$$\tau = \tau_0 \frac{L(\lambda)}{L(\lambda_0)} \tag{9.21a}$$

$$\tau_0 \equiv 8.9 \times 10^{-13} f_{ij} \lambda^2 L(\lambda_0)(1 - e^{-\Delta E/T}) \tag{9.21b}$$

where τ_0 is the optical depth at line center. At line center $L(\lambda)$ is roughly equal to $1/\Delta\lambda$, so that the linewidth must be known in order to calculate the optical depth. From Eqs. (9.20) and (9.21), the reduction in intensity from that in the absence of absorption is given by

$$I_{obs} = D(\tau_0) I_0 \tag{9.22a}$$

$$D(\tau_0) \equiv \int \left(\frac{1 - e^{-\tau_0 L(\lambda)}}{\tau_0 L(\lambda)}\right) d\lambda \tag{9.22b}$$

For a Doppler broadened line (see Eqs. (9.27) this becomes

$$D(\tau_0) = \frac{1}{\sqrt{\pi}\tau_0} \int (1 - e^{-\tau_0 e^{-y^2}}) dy \tag{9.23}$$

In principle, the optical depth may be corrected for in the following way: From Eqs. (9.17), (9.21), and (9.27a) I_0 is related to I_{bb} by

$$I_0 = I_{bb} \sqrt{\pi} \Delta\lambda \tau_0 \tag{9.24}$$

and so, from Eq. (9.22a)

$$\frac{I}{I_{bb}\sqrt{\pi}\Delta\lambda} = \tau_0 D(\tau_0) \tag{9.25}$$

It can be shown that

$$\frac{I}{I_{bb}\sqrt{\pi}\Delta\lambda} = \tau_{calc} \tag{9.26}$$

where τ_{calc} is the 'first order' calculated optical depth which is calculated by: (1) determining the upper level population from I_{obs} assuming zero optical depth; (2) calculating the lower level population from this; and (3) calculating the optical depth from that. Thus, the procedure is to first calculate τ_{calc}, determine τ_0 from Eqs. (9.22b), (9.25), and (9.26), and finally determine I_0 from Eq. (9.22a). In Fig. 9.2, $D(\tau_0)$, the correction factor, is plotted as a function of τ_{calc}. It can be seen that the reduction in intensity is relatively small for values of τ_{calc} below 0.4 or so. As τ_{calc} increases, the intensity reduction increases rapidly. Physically this is because as the optical depth increases, the observed intensity is a weak function of the nominal intensity I_0. Thus, while in principle the effects of optical depth may be corrected for, the strong variation in $D(\tau_0)$ with τ_{calc} causes the derived upper level population to be very sensitive to calibration and measurement errors.

9.1.6. Line Broadening

It is necessary to know the width of a spectral line in order to determine the optical depth. (Of course, it is also necessary to make sure that the monochromator exit slit is set wide enough to include the entire lineshape). The two dominant line broadening mechanisms are Doppler broadening and Stark broadening.[205]

Doppler shifted radiation from an ensemble of ions having a Maxwellian velocity distribution results in a Gaussian lineshape

$$L(\lambda) = \frac{1}{\sqrt{\pi}\Delta\lambda} e^{-(\lambda-\lambda_0)^2/\Delta\lambda^2} \tag{9.27a}$$

$$\Delta\lambda = .72(T_i/\mu)^{1/2}\lambda_0 \tag{9.27b}$$

where λ_0 is the line center in microns. $\mu = M_i/M_p$, and $\Delta\lambda$ is in A. The linewidths in this experiment can only be estimated since the ion temperature is unknown. Doppler widths of the spectral lines relevant to this experiment, assuming an ion temperature of 2 eV, are given in table 9.2. The uncertainty in linewidth determination due to unknown T_i should be emphasized in the context of optical

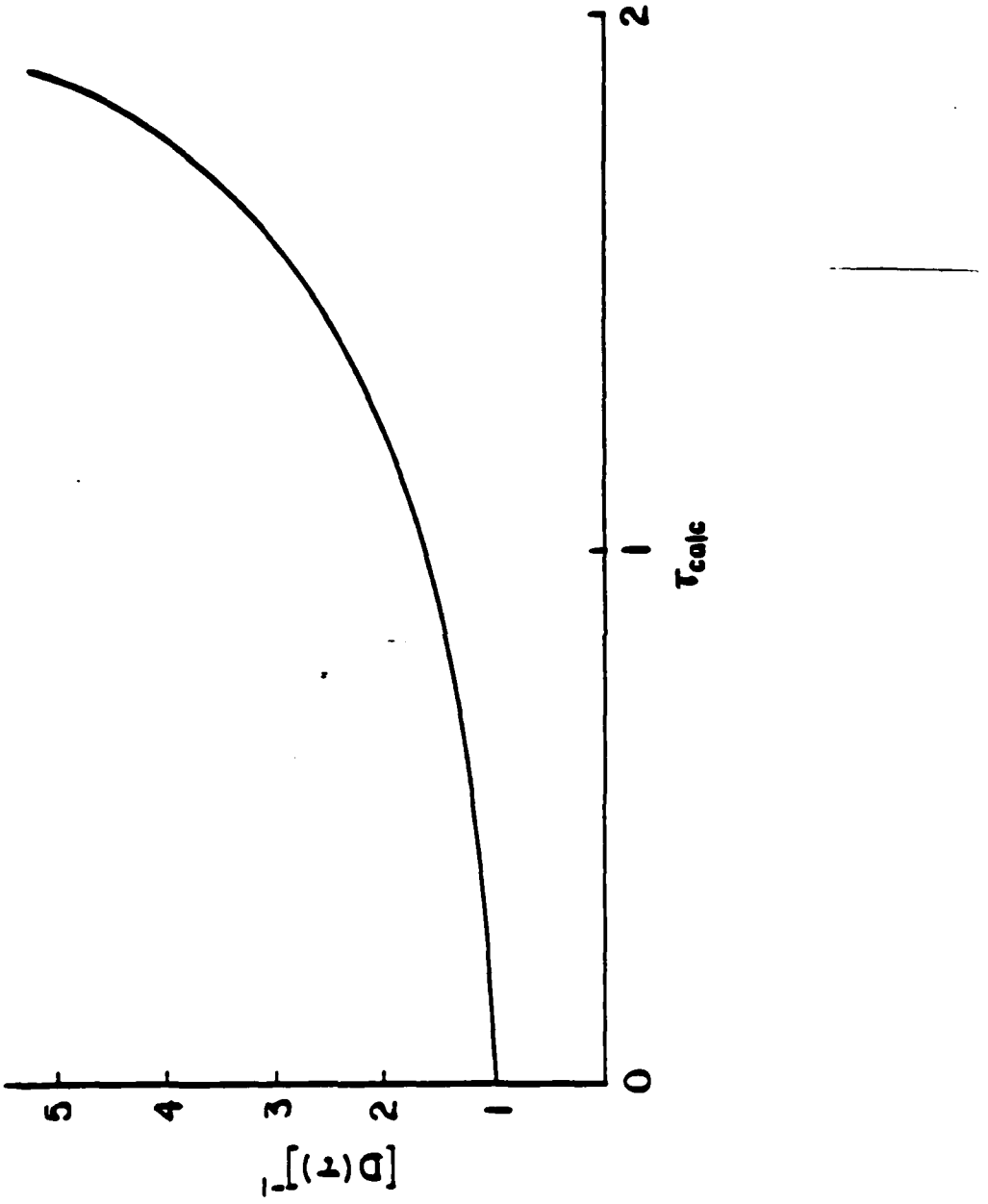

Fig. 9.2: Optical depth correction factor as a function of τ_{calc}. The upper level population obtained from the line intensity (assuming zero optical depth) must be multiplied by this to get the true upper level population.

depth correction — even if there were no calibration or measurement uncertainty, the uncertainty in linewidth would give an uncertainty in τ_{calc}.

Stark broadening arises from the fluctuating electric fields caused by Coulomb collisions. Calculation of Stark profiles and linewidths is a much more complicated problem than is Doppler broadening. The broadening is highly dependent on the particular spectral line, and no general formula is available. Stark broadening is discussed in several references.[205,206,207] Stark linewidths for most of the lines in this experiment are also given in table 9.2. The widths listed are the full width at half maximum, at an electron density of $10^{16}/cm^3$. The widths scale roughly linearly with electron density (for hydrogen they scale more as $n^{2/3}$) and are not strongly dependent on the electron temperature.

From this table it can be seen that the effects of Doppler and Stark broadening are of the same order. Even at the maximum electron densities of $\sim 2\times 10^{17}/cm^3$ the Stark broadening is less than 1 Å for all lines but the Hα line.

Another conceivable line broadening effect is Zeeman splitting due to the self magnetic field. While the calculated splitting is on the order of, or greater than, the linewidths given above, in this experiment the direction along which light is observed is mainly transverse to the magnetic field, so that the Zeeman splitting is expected to be negligible.

9.2. CRE Code

The spectroscopic measurements in this experiment were interpreted with the aid of a collisional-radiative equilibrium code developed at the Naval Research Laboratory. This code includes all of the processes shown in Fig. 9.1. and a description of the code, including the methods used to calculate the various rate coefficients, is given in Ref. 200. In particular, spin-flip transitions are included — as pointed out in Ref. 200, collisional excitation from the ground state is the dominant populating process for different spin systems.

Each ionization stage is represented by 4–12 levels: to simplify the computation, closely spaced levels are assumed to be in LTE with one another and are grouped together. Optical depth effects can be handled with this code but were

Table 9.2

Linewidths

Ion	λ	f_{ij}	E_j	$\Delta\lambda_d$	$\Delta\lambda_s$	Ref.
H	6563	12.1	0.64	0.47	1.2	206
C I	2478	0.09	7.7	0.07	0.02	208
C II	4267	0.94	21.0	0.12	0.03	208
C III	2296	0.47	18.1	0.07	0.001	208
C III	4647	0.42	32.2	0.13	0.01	208
C IV	2524	1.00	55.8	0.07	0.03	208
C IV	5801	0.32	39.7	0.17	0.04	209
Al I	3961	0.12	3.1	0.08	0.05	206
Al II	2816	0.15	11.8	0.06	0.01	206
Al III	3601	0.17	17.8	0.03	0.03	210
Al III	4529	1.17	20.6	0.04	0.11	210
Al III	4150	0.79	23.5	0.03		
C III	459	0.42	33.5	0.01		
C III	977	0.81	12.7	0.03		
C IV	312	0.20	39.7	0.01		

Wavelengths and widths are in A. The oscillator strengths and upper level energies were obtained from Ref. 211. The Doppler widths were calculated from Eq. (9.27b) assuming an ion temperature of 2 eV. The Stark widths were obtained from the references given in the last column. These widths are those at an electron density of $10^{16}/cm^3$. The Stark width scales approximately with electron density ($\propto n^{2/3}$ for H), and is roughly independent of temperature.

The last three spectral lines are those for which self absorption is potentially significant in determining the level populations.

not done so here. The code predicts steady state level populations for a given temperature and density. In addition to using the code as such, use was also made of the rate coefficients calculated by the code authors,[203] as these were deemed more accurate than the simple formulae given in Sec. 9.1.2.

9.3. Calculation Procedure

In determining the steady state level populations, the code results are compared with the predictions of LTE. If the two predict different population ratios for a given transition, then the optical depth of that transition is calculated *a posteriori*. If the transition is believed to be optically thick, then LTE is assumed, while if it is believed to be thin, the code result is assumed correct. In calculating the effect of self absorption on the population distribution, the distance used in Eq. (9.20b) was 1 mm, which was on the order of the smallest plasma dimension.

If the calculated ionization time between two stages is calculated to be short, then the stages are assumed to be in equilibrium, while if the time is very long then the stages are assumed to be completely decoupled. In either case the levels are assumed to be in steady state equilibrium. If the ionization time is in between these extremes, then it is assumed that the level populations may not be in the predicted steady state equilibrium.

9.4. Spectral Lines Observed

The spectral lines investigated in this experiment are listed in table 9.2, along with the upper level energy and oscillator strength of each line, obtained from Ref. 211. The ionization potentials and calculated ionization times for each ion are given in table 9.1. From this it can be seen that hydrogen and neutral aluminum and carbon would be expected to be in equilibrium with the next higher stage. Carbon III and IV will clearly be decoupled from the next higher ions, and carbon II will probably be decoupled from carbon III. However, aluminum II and III have ionization times that are calculated to be marginal.

9.5. Calibration and Experimental Procedure

9.5.1. Photomultiplier Tube Adjustments

The linear response range of the PMT's was extended prior to making the measurements described in this chapter. The primary factor that causes saturation in PMT's is the space charge limit on the current that may be drawn between dynodes. To reduce this problem, the dynode chain resistive divider was changed to increase the voltage across the last two stages, where the current is greatest. Satisfactory performance was obtained with 180 kΩ resistors across the last two stages and 100 kΩ resistors across the other stages. The linearity was checked by exposing the PMT to a small light emitting diode and observing the effect on the PMT output signal when an ND 0.3 filter (2× attenuation) was inserted in between the two. The LED was pulsed to produce a pulse length of light similar to that which occurred during the shots. The results of this are shown in Fig. 9.3. With the lowest PMT bias voltage used, (and thus the most restricted linear range) the response was linear (to within 10%) at a 1.4 V output signal.

The PMT transit time delay was also checked with the nitrogen laser. An output beam was split between the PMT and a photodiode which had a subnanosecond transit time. The measured delay was equal to the quoted value of 22 ns to within the 3 ns accuracy of the measurement. The PMT gain-bias voltage dependence was also carefully checked periodically throughout the experiment, as was the output of the bias voltage power supply.

9.5.2. System Calibration

The monochromator system was calibrated immediately after these measurements were made. The calibration procedure consisted of first using an absolutely calibrated tungsten ribbon lamp (Optronics model 550GA[212]) to obtain an absolute system calibration over the range of 3500–6600 A. and then obtaining a relative calibration over the entire range using a pencil mercury lamp.[213] By comparing the two it was possible to get an absolute calibration over the whole range. The tungsten lamp current was maintained at the specified 15 A with a regulated curent source: this current was also measured with a precision ammeter. The lamp was positioned with the filament in the same position as the cathode

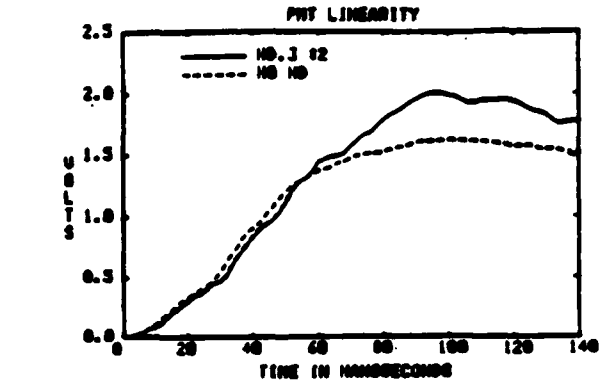

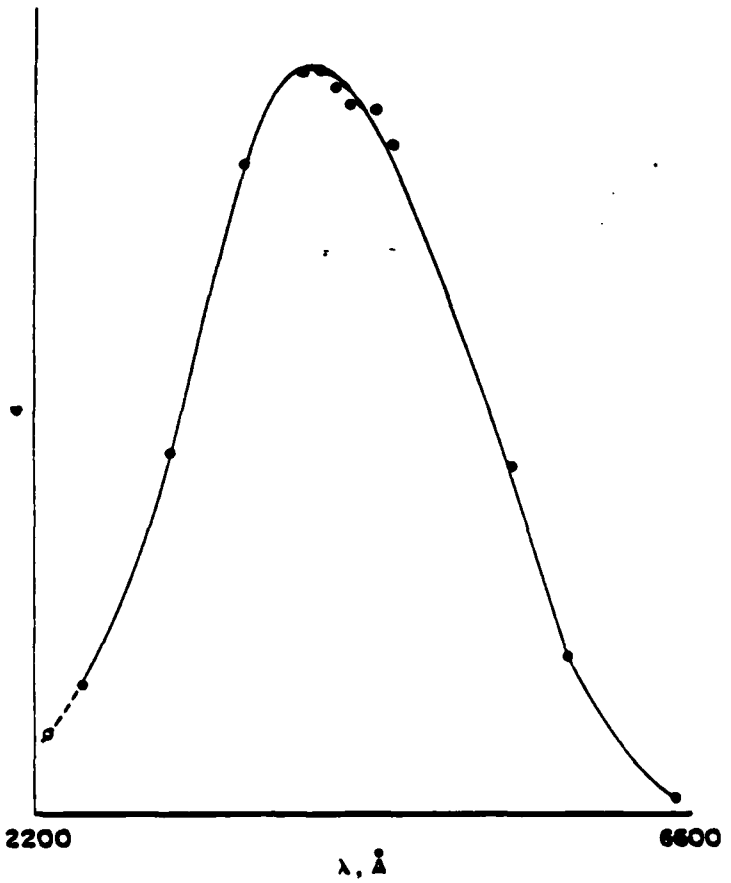

Fig. 9.3: (top) PMT linearity. The dashed curve is the PMT output signal: the solid curve is twice the PMT output obtained when the input signal was reduced by half (i.e.. the solid curve represents the 'true' signal). The linear range is seen to be about 1.4 V. (bottom) Total monochromator system sensitivity (arbitrary units). The sensitivity at 2296 Å was obtained by extrapolation.

and the optical system during calibration was the same as that used for the shots. The slit image was positioned in the center of the filament (the lamp intensity was seen to vary over the filament area by less than 5%). Under the conditions of this calibration (with regulated current and looking normal to the filament within a small solid angle) the accuracy of the lamp is quoted as being a few percent. A precision microammeter was used to measure the PMT current. That the PMT response was linear was verified by observing the signal change as the lens aperture was changed. As the lamp is a continuum source, it is necessary to know the wavelength spread that is passed through the monochromator, which is determined in this case by the exit slit width. Because of play in the slit adjustment, this is probably the biggest source of error, with an estimated uncertainty of about 10%.

This calibration was performed on two separate occasions and the two results differed by less than 5%. In addition, the system sensitivity obtained from this calibration procedure was consistent with that calculated using the properties of the optical system and estimates of PMT and monochromator sensitivities.

This calibration was extended down to 2536 Å with the pencil mercury lamp. The utility of a similar lamp as a calibration source was examined in Ref. 214. It was found that the relative intensities of different lines were quite reproducible and virtually independent of the lamp current and viewing angle. Seven lines between 5799 Å and 2536 Å were used. In this case also the lamp was placed in the cathode position and the optical system was the same as that used for the shots. The lamp was allowed to warm up for 40 min prior to the calibration and the lamp current remained constant during the calibration. The off-line background intensity was negligible for all of the lines used. This calibration was repeated several times to make sure that there was no drift in the lamp output.

Three methods were used to determine the relative Hg lamp irradiance at the different lines. Typical values are given in the manufacturer's catalogue, although these are only approximate and the accuracy is not specified. Values were also given for a similar lamp in Ref. 214. Finally, the lamp was taken to an absolutely calibrated monochromator system and calibrated there. This last

method would have been sufficient by itself but the monochromator used was of such low resolution that only the strongest lines could be measured. The relative intensities quoted in the catalogue and in Ref. 214 and those measured with the second monochromator system all agreed within 30%. In addition, the relative intensities of the visible Hg lines determined by the above methods agreed with those inferred by comparing the monochromator system response to these lines with that to the tungsten lamp.

The above procedures absolutely calibrated the system for all spectral lines measured in this work except for the C III 2296 Å line. While there are Hg lines nearby, they were to weak to be used. The sensitivity at this wavelength was estimated by extrapolation. The system sensitivity is shown in Fig. 9.3. The calibration uncertainty is conservatively assumed to be 30% above 3500 Å, 60% below that, and a factor of two at 2296 Å.

9.5.3. Experimental Procedure

The system was focussed for each line as described in the previous chapter. A hollow cathode platinum lamp, which had a line at 2292 Å, was used to focus the system for the 2296 Å line. The 0.1 M monochromator was set to the C II 4267 Å line to check shot-to-shot reproducibility.

Because of play in the monochromator slits, the entrance slit was left fixed at 20 μm throughout these experiments. The exit slit was normally set at 70 μm (2.3 Å), except when the Hα line was being observed, in which case the slit was set wide enough to pass the entire (Stark broadened) line. The wavelength calibration was checked repeatedly.

During the measurements the PMT signal was maintained within the linear range by adjusting the PMT bias voltage and by varying one of the lens apertures (the signal levels changed as expected when this was done). The uncertainty in the aperture area was estimated at less than 20%.

9.6. Experimental Results — Temperature

9.6.1. Typical Traces

Typical PMT signals for different lines on shots with a Poco cathode are shown in Figs. 9.4 and 9.5. These are given in units of calculated upper level population assuming zero optical depth. As mentioned in the previous chapter, each trace has two peaks which correspond to the two peaks on the current trace.

Signals are shown for two spatial locations — 0.1 mm and 0.8 mm from the cathode surface. The signals at the two locations are seen to peak at the same time, indicating that this variation in signal is due to a change in the electron temperature rather than to a change in the ion density due to an increased flux of ions from the cathode.

As mentioned in Ch. 8, the peaks are more pronounced for lines with higher upper level energies, being very sharp for the C IV and C III lines, less pronounced for the C II line and very slight for the neutral lines. Also, the lines with higher upper level energies have little intensity after the second peak while those for the neutrals actually increase. The neutral carbon and aluminum lines viewed at the cathode start later, and they are not seen until after the shot at distances away from the cathode. In contrast, the Hα line is seen out in the gap.

Because the signals are so spiky, line intensity comparisons were confined to measurements of the two peak heights. The combined effects of the previously mentioned calibration uncertainty and shot to shot variations are about a factor of two.

The calculated upper level populations at the time of the second peak are summarized in table 9.3. As mentioned in the previous chapter, the Hα line intensity is about the same for all cathodes. The carbon lines are about equally intense with Poco and Aerodag cathodes, and about 8 times stronger than when aluminum cathodes are used. Aluminum lines are equally intense with Aerodag and aluminum cathodes.

The optical depths of all lines are calculated to be negligible, with the exception of the 2296 A C III line.

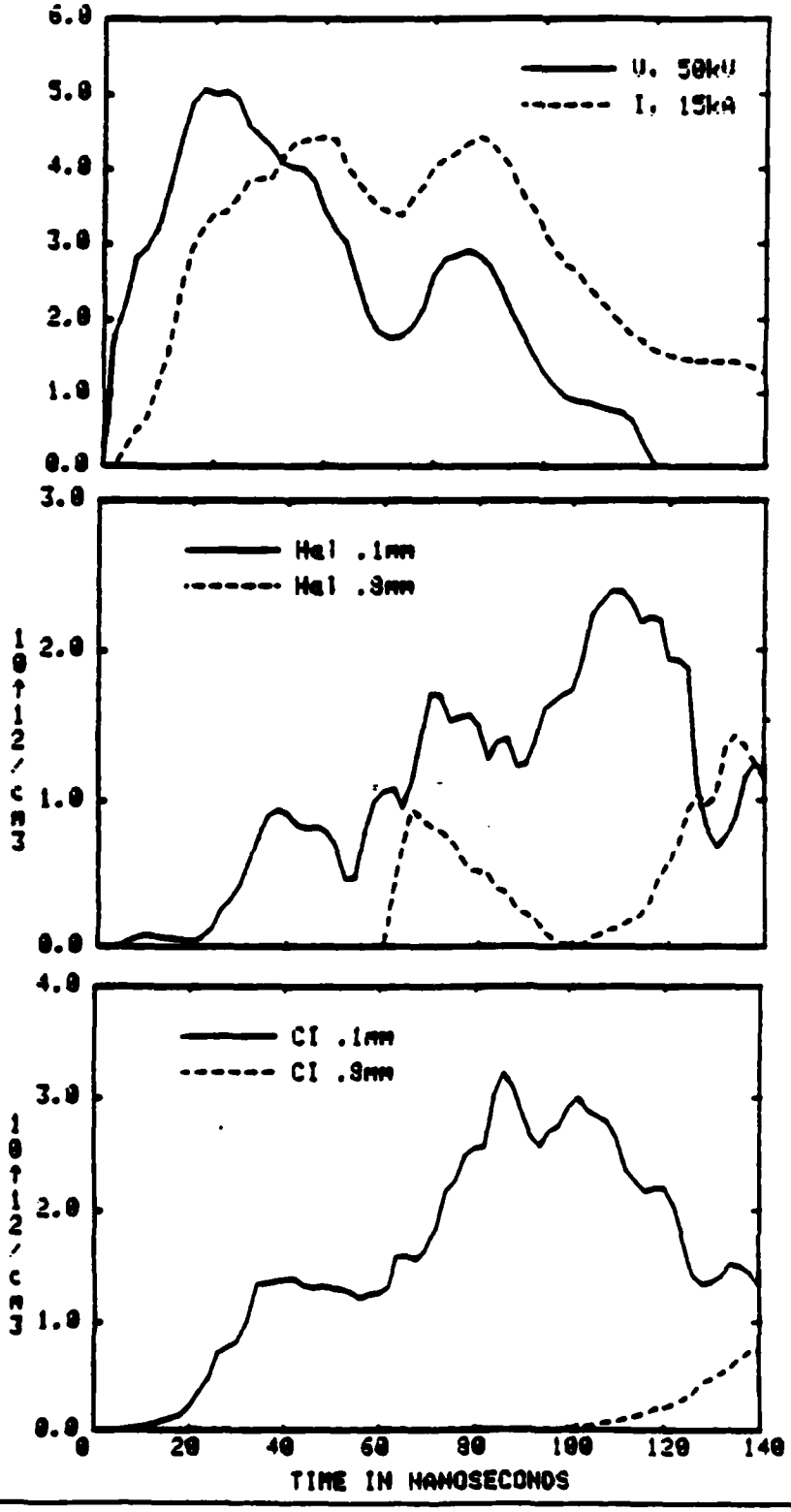

Fig. 9.4: Spectral line intensities, in units of calculated upper level populations (assuming zero optical depth). The top trace is the diode current. The solid lines are intensities 0.1 mm from the cathode surface and the dashed lines are intensities at 0.8 mm away.

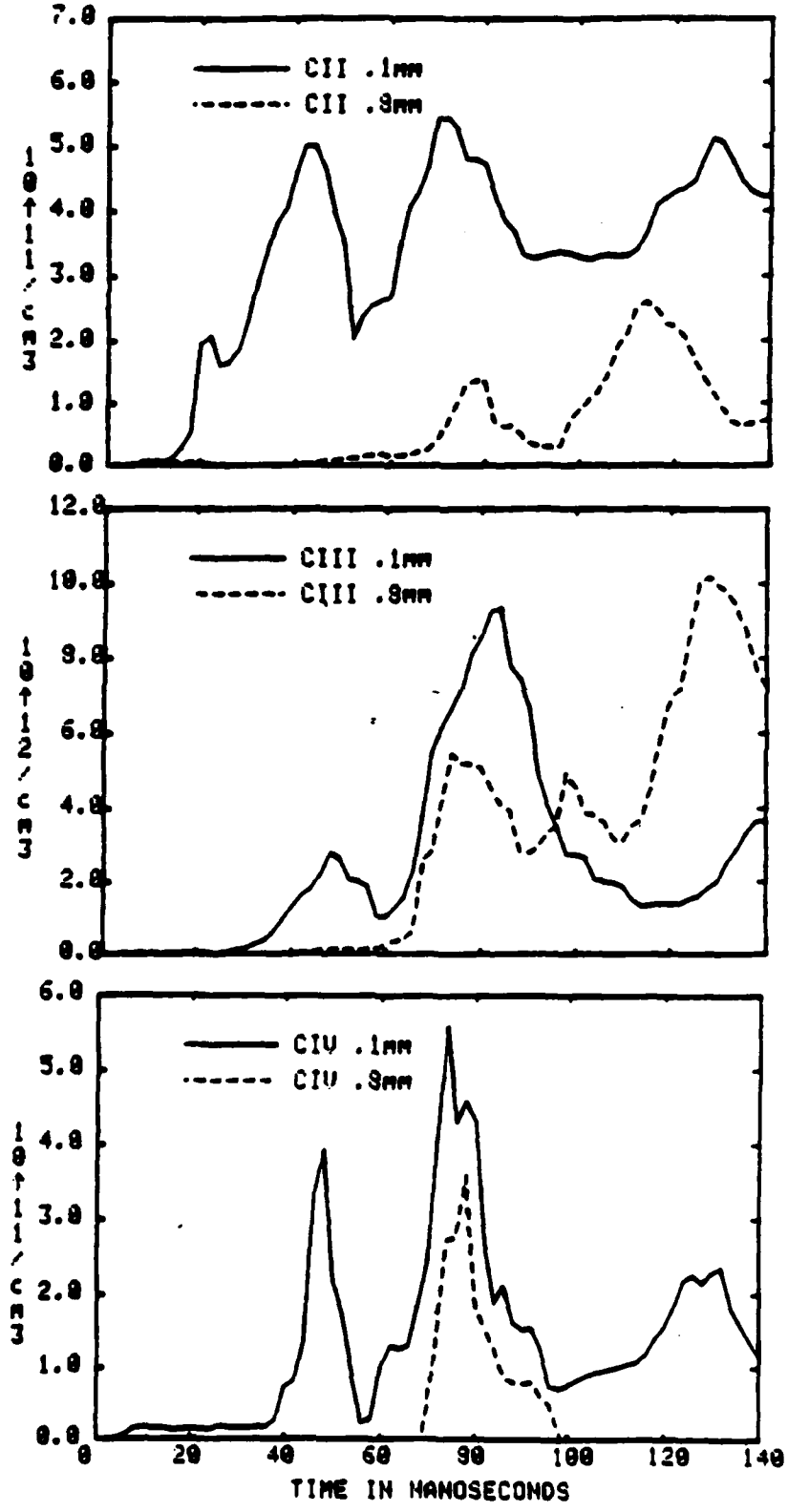

Fig. 9.5: Spectral line intensities, con't.

Table 9.3

Upper Level Populations at 70 ns

Line	λ	Poco cathode	Aerodag cathode	Aluminum cathode
H_α	6563 Å	1.7×10^{12}	1.3×10^{12}	1.7×10^{12}
C I	2478 Å	1.9×10^{12}		
C II	4267 Å	5.3×10^{11}	3.4×10^{11}	4.6×10^{10}
C III	2296 Å	7.7×10^{12}	6.8×10^{12}	2.6×10^{12}
C III	4647 Å	1.3×10^{12}	1.5×10^{12}	1.5×10^{11}
C IV	2524 Å		9.6×10^{9}	
C IV	5801 Å	5.5×10^{11}	3.3×10^{11}	
Al I	3961 Å			2.0×10^{11}
Al II	2816 Å			2.0×10^{10}
Al III	3601 Å		1.2×10^{12}	1.2×10^{12}
Al III	4529 Å		2.8×10^{11}	2.8×10^{11}
Al III	4150 Å		2.4×10^{11}	2.4×10^{11}

These are the upper level populations, in units of cm^{-3}, calculated at the time of the second peak assuming zero optical depth.

9.6.2. Temperature measurements

Normally, temperature measurement based on line intensity ratios involves lines from different ionization stages since the difference in upper level energies, and hence the variation in intensity ratio with temperature, is the greatest. In the present experiment, however, lack of equilibrium between ionization stages required that the lines be from the same ion. Also, the mixed ionic composition precluded the use of continuum methods.[206]

Initially the most suitable ratio was thought to that involving the two C III lines at 2296 Å and 4647 Å, as the lines were fairly strong and observed with all cathodes, and have a reasonable difference of upper level energies. These lines are shown in the partial Grotrian diagram for C III, taken from Ref. 215, in Fig. 9.6. The upper level population ratios predicted by both the code and by LTE are shown in Fig. 9.7. Examination of the code results shows that the code and LTE agree on all levels except the for ratio between levels separated by the 977 Å resonance line and between those separated by the 460 Å and 538 Å lines.

The measured population ratios (assuming zero optical depth) and calculated optical depths are given in table 9.4 for a variety of cathodes. Based on the measured line intensities, the 977 Å and 460 Å lines are calculated to be thin for shots with aluminum cathodes and marginal for carbon cathode shots. With aluminum cathodes, the intensity ratio is about 20, implying a temperature of about 5 eV in the LTE case and 8 eV if the code predictions are appropriate. With carbon cathodes the ratios are lower than those predicted at any reasonable temperature.

The first thing to notice is that the ratio is least for those shots with the highest calculated optical depth of the 2296 Å line. Corrected ratios based on Eq. (9.22a) are also given in table 9.4. The correction apppears to be small but it must be noted that the calculated depth is in the range where the correction is extremely sensitive to variations in τ_{calc} which is itself prone to error. Thus, the optical depth of the 2296 Å line might be the reason for the abnormally low ratios for carbon cathodes.

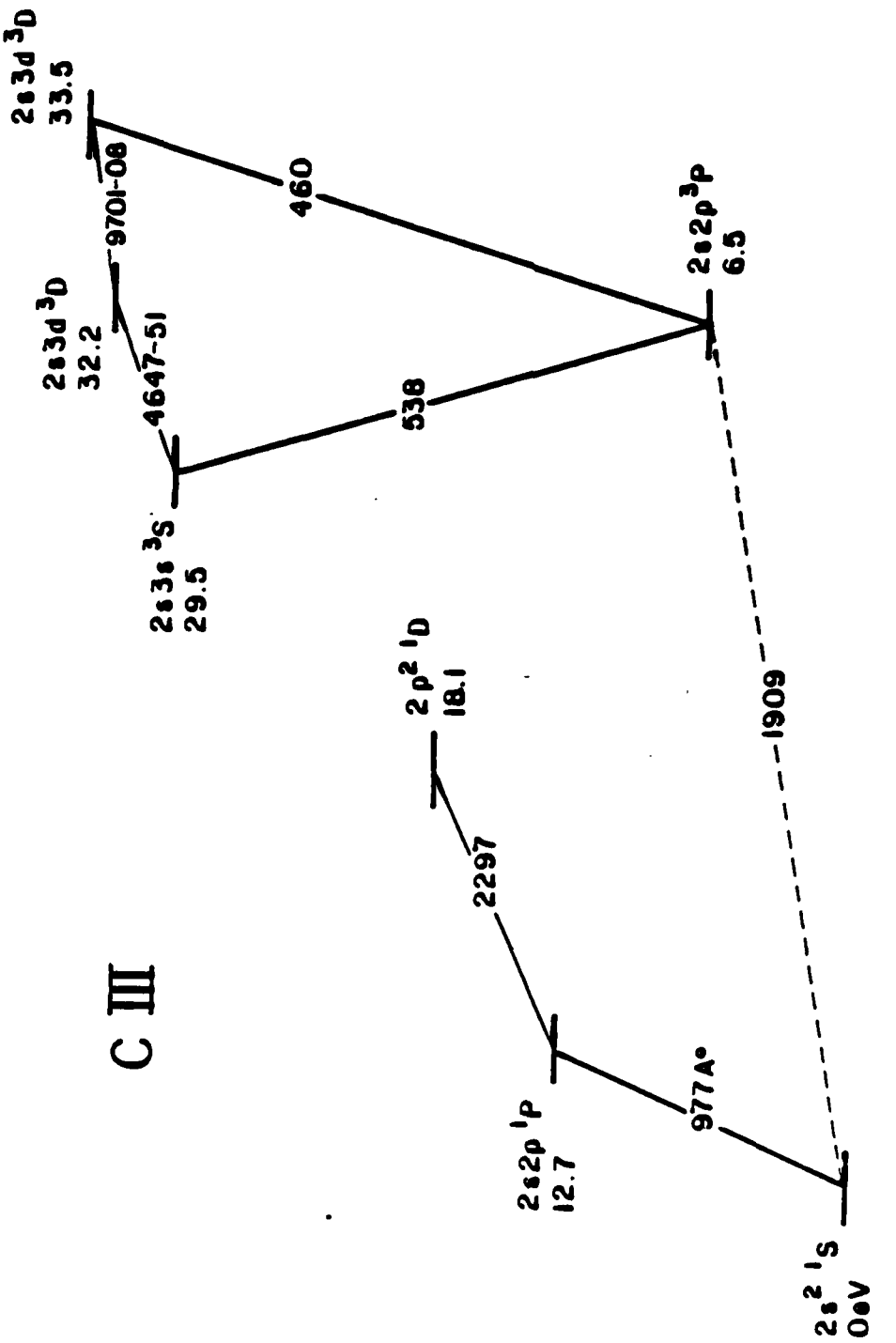

Fig. 9.6: Partial Grotrian diagram for C III.

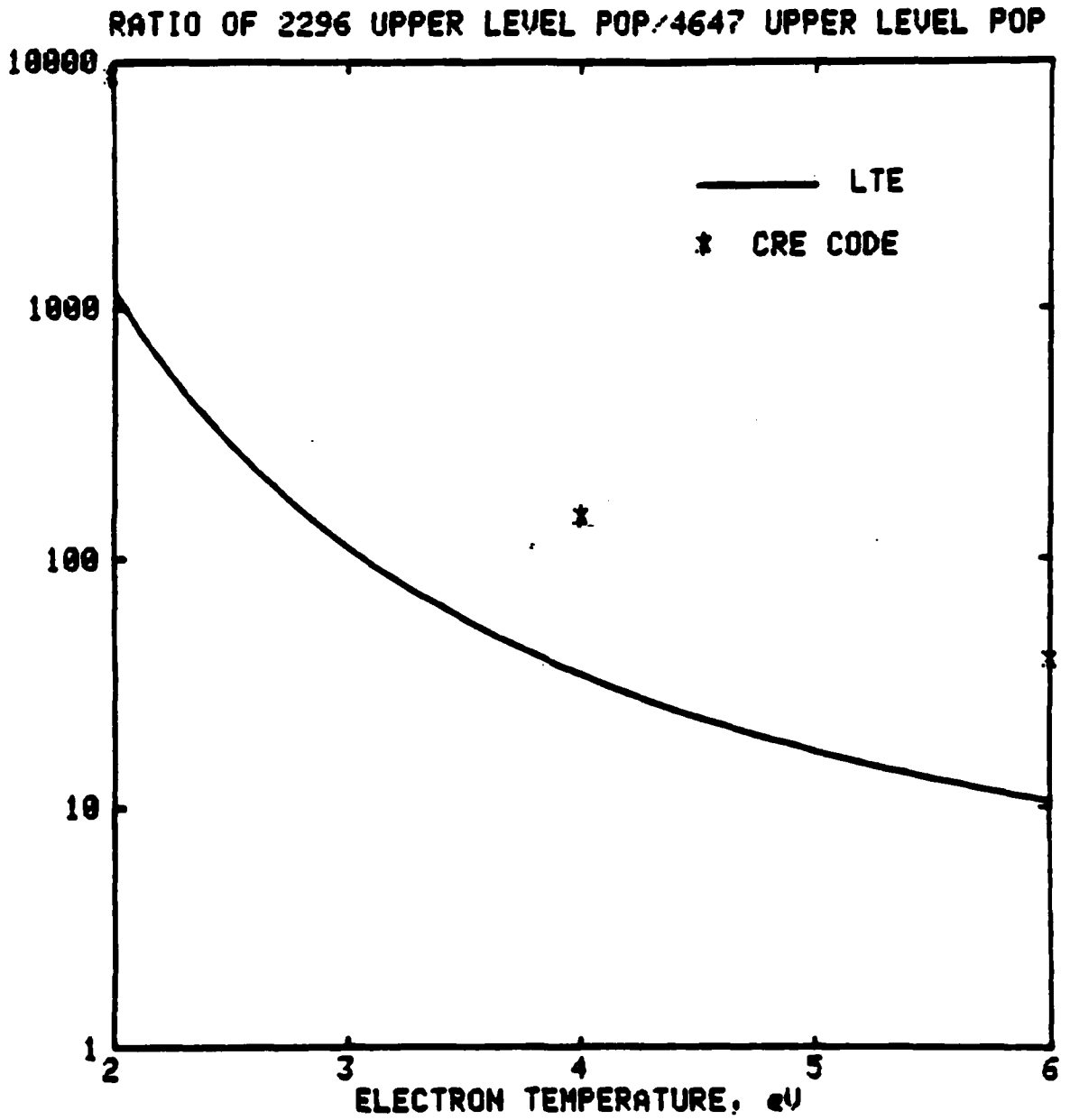

Fig. 9.7: Predicted ratio of C III upper level populations as a function of electron temperature.

Table 9.4

C III Population Ratios

	40 ns		70 ns	
Cathode	**Ratio**	τ_{calc}	**Ratio**	τ_{calc}
Poco	13 (14)	0.5	6 (9)	1.2
Aerodag	5 (7)	0.7	5 (9)	1.1
Aluminum	50	0.2	17 (19)	0.4
Al (1.6 mm)	15 (16)	0.4	12 (14)	0.4
Al (9.6 mm)	22	0.5	24 (26)	0.4
Poco (out)	—	—	4 (6)	0.8

These are the ratios of the calculated upper level population of the 2296 Å line to that of the 4647 Å line at the times of the two peaks, assuming zero optical depth. Ratios corrected for the optical depth of the 2296 Å line are given in parenthesis. These ratios were measured at 0.1 mm from the cathode surface, with the exception of the last, which was measured at 0.8 mm out.

Another effect would be the optical depth of the resonance lines. If they are thick, then the equilibrium will be shifted towards LTE and the ratio will be less for a given temperature. All in all, these effects make interpretation of the results with carbon cathodes difficult. With the aluminum cathodes, optical depth effects do not seem to be a problem.

However, there is another problem with the use of these lines; as seen in Fig. 9.6, the two upper levels are in different spin sustems; at the densities in this experiment, the equilibration time between the spin systems is calculated to be about 50 ns, based on the rates of collisionally induced spin-flip transitions.[203]

Thus, the problems of optical depth and spin system equilibration make interpretation of these results subject to uncertainty. Also, in the range of the suggested 5–8 eV temperature, the intensity ratio is not so strong a function of temperature. In particular, an increase or decrease in the intensity ratio by a factor of two changes the calculated temperature from 8 eV to 5 eV, or from 8 eV to very hot, respectively..

A better ratio was found to be that between the C IV lines at 5801 Å and 2524 Å. The partial Grotrian diagram and ratio predictions are shown in Figs. 216 and 217. The upper levels are closely connected so that rapid equilibration can be assumed, yet there is a large difference in upper level energies. Also, the upper levels are high enough so that optical depth is not a problem. This means not only that the measured intensities need no correction, but that there is no uncertainty about whether to use the code or LTE. The disadvantage of these lines is that they were weak. and only strong enough to be observed with carbon cathodes. Even then. the intensities were lost in the continuum at locations away from the cathode. and at the second peak with the 1.6 mm cathode (line intensities were significantly greater than the continuum background in the other cases). Thus. measurement of this ratio is confined to three points: with a 6.4 mm Aerodagged cathode at the two peaks, and at the first peak with a 1.6 mm Aerodagged cathode.

The ratios for these cases are given in table 9.5. Within the experimental uncertainty, the ratio is about 25 in all cases. From the code. this predicts a temperature of slightly less than 4 eV. In this case the ratio varies strongly with

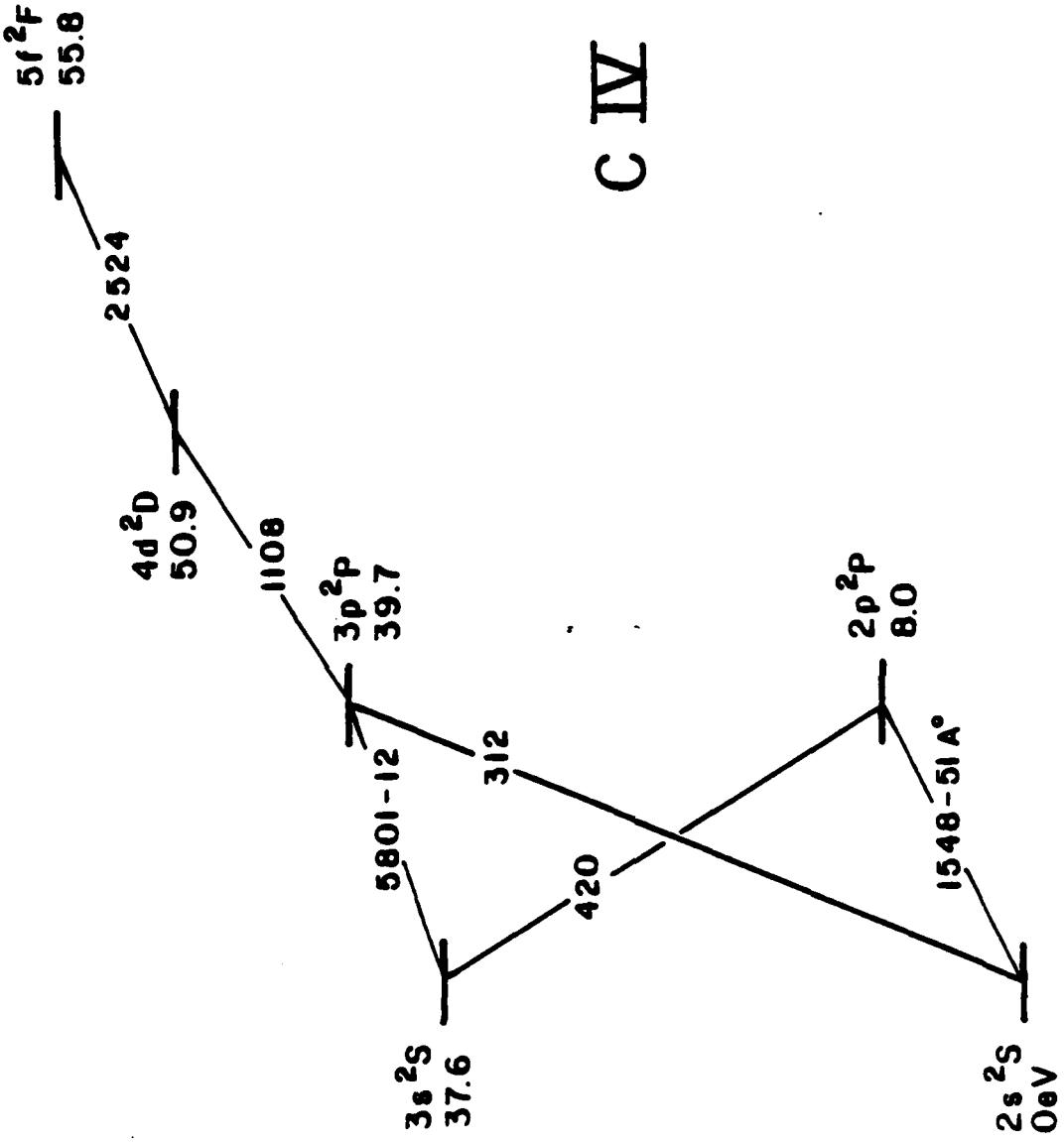

Fig. 9.8: Partial Grotrian diagram for C IV.

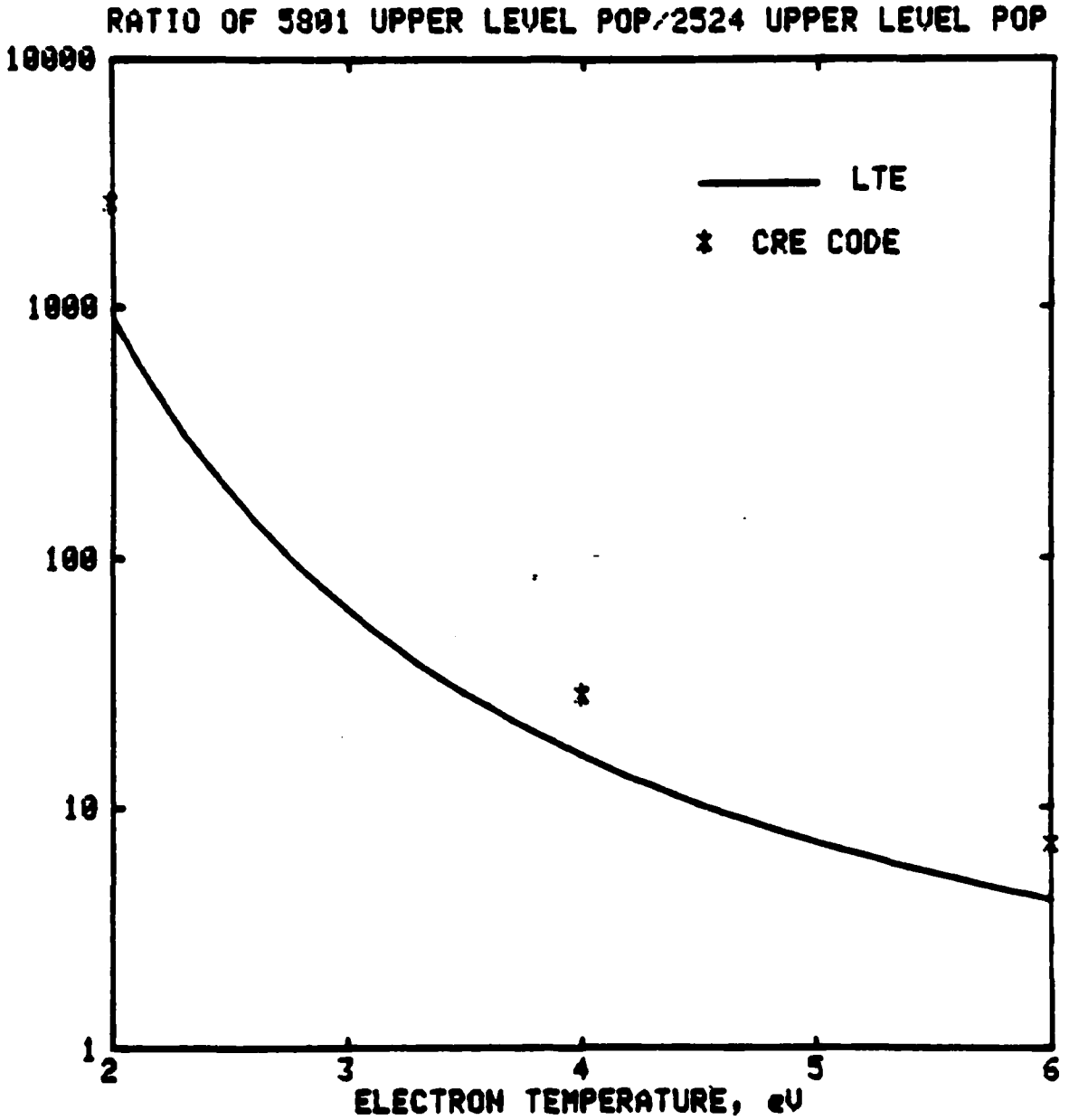

Fig. 9.9: Predicted ratio of C IV upper level populations as a function of electron temperature.

Table 9.5

C IV Population Ratios

Cathode	40 ns	70 ns
6.4 mm Aerodag	23	34
1.6 mm Aerodag	19	

Ratios of the upper level population of the 5801 Å line to that of the 2524 Å line at the times of the two peaks.

temperature — at a temperature of 6 eV, the ratio would be 4 times less, while at 2 eV, the ratio would increase by a factor of 10^3!

These data points, though few, yield some interesting information. For one thing, an increase in the current density of a factor of three does not seem to change the temperature. Also, the fact that the ratio was similar at 40 and 70 ns with the 6.4 mm cathode shows that there is no steady heating of the cathode plasma.

So, while the signals were weak, and only 3–4 shots were taken per line per cathode, the strong variation in ratio with temperature make this a useful diagnostic. Another desirable feature is that the higher transition rate and statistical weight of the 2524 Å line compensates for the effects of energy separation so that the two signals are of about the same size. It is suggested that this line ratio would be useful for many other experiments.

As another check, the intensities of the aluminum lines at 3601, 4529, and 4150 Å were examined. The Grotrian diagram is shown in Fig. 9.8. The code and LTE agreed for all levels of Al III. The intensities are similar for both aluminum and Aerodag cathodes and similar at both peaks, and the observed level populations are shown in a Boltzman diagram in Fig. 9.9. In this diagram, the logarithms of the upper level populations divided by their statistical weights are shown as functions of the upper level energies. Ideally, this would give a straight line with a slope equal to $1/T$. The populations are not observed to lie on such a line, although the error is within the factor of two experimental uncertainty, so this may not be too significant. However, the best fit gives an electron temperature of about 2 eV, which contradicts the results of the previous measurement.

One possible explanation for this discrepancy is the effect of partial ionization equilibrium mentioned earlier. If Al II ions are steadily being ionized and thus populating the Al III ground state, and Al III ions are steadily being ionized and thus depopulating the Al III upper levels, then the distribution temperature would be lower than the electron temperature. (In the steady state, at a 4 eV electron temperature 98% of the aluminum ions would be in the Al IV ground state, according to the code.)

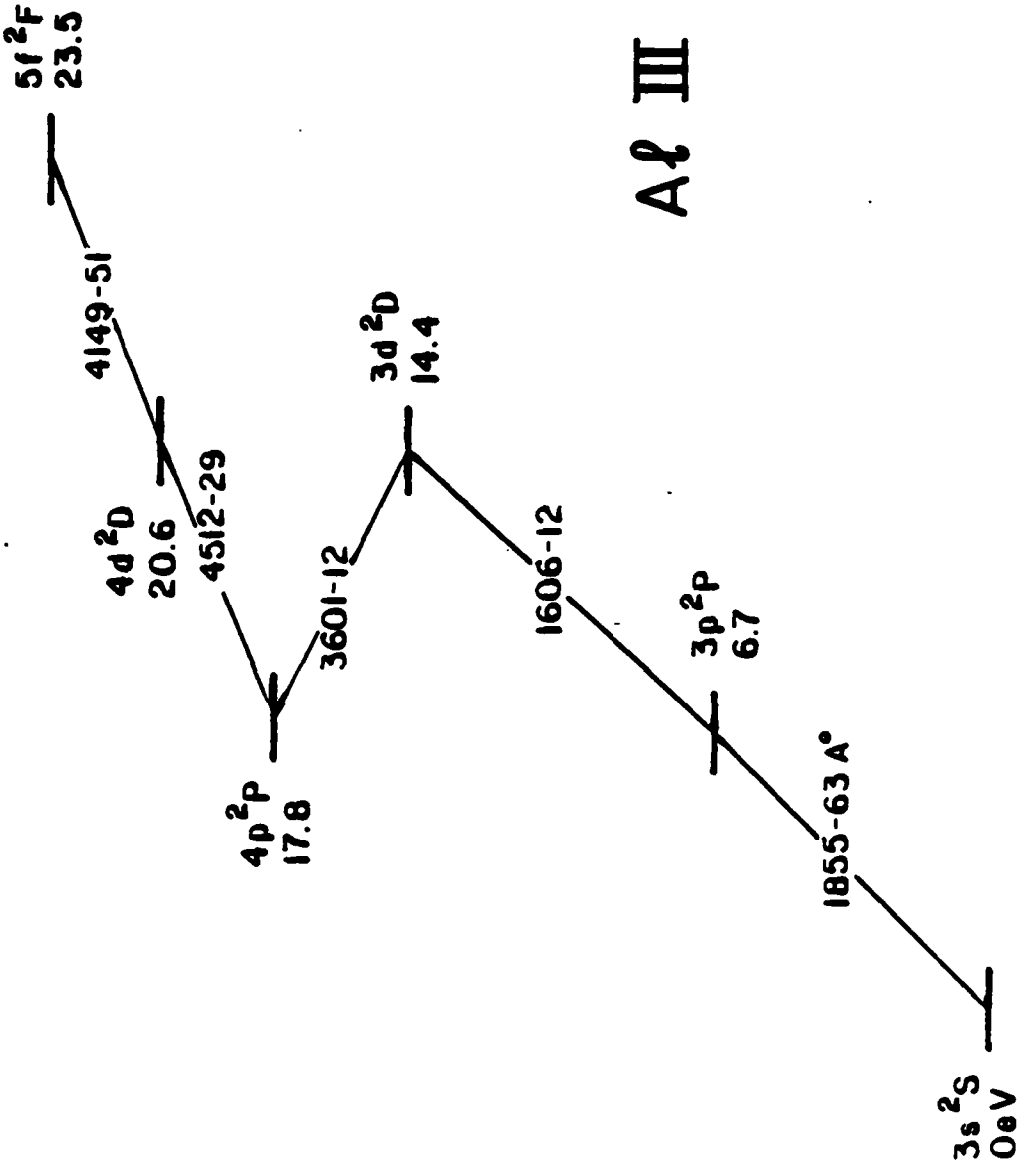

Fig. 9.10: Partial Grotrian diagram for Al III.

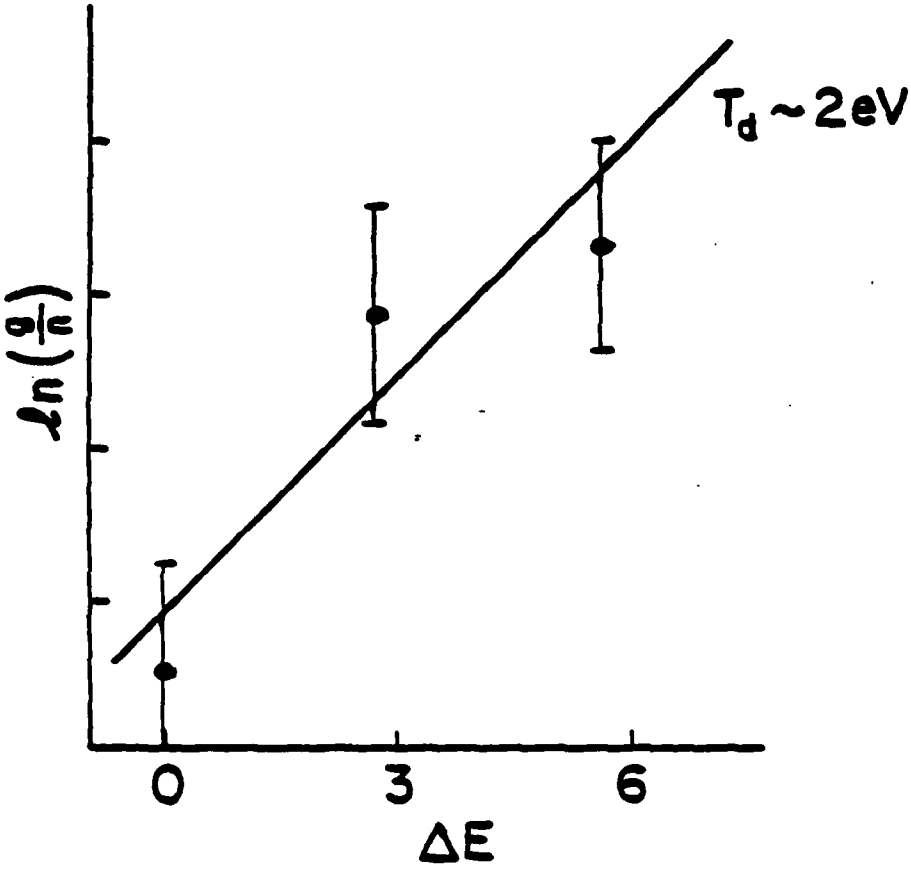

Fig. 9.11: Experimental Al III Boltzmann plot.

There are two previous studies that are relevant to this.[218,219] Both involved spectroscopic studies of aluminum arcs coupled with CRE modeling, and the codes used included transient effects (unlike the code used here). In both cases a distribution temperature of 2 eV was predicted, independent of the electron temperature. Now, these experiments involved $10^{14}/cm^3$ plasma densities, so that the results may not be relevant to the present case. However, from the code predictions presented in Ref. 217, it can be inferred that a distribution temperature of 2 eV would be predicted at $10^{16}/cm^3$, if the plasma parameters were changing on a 10 ns time scale.

In conclusion, electron temperature estimates were obtained by three methods. That involving C III ratios suggests a temperature of above 5 eV but is subject to many uncertainties. That involving C IV ratios has a smaller data base but because of the strong variation in ratio with temperature, the temperature can be assumed to be between about 3–6 eV (with a factor of two uncertainty, the temperature lies between 3.5–5 eV). The ratio involving aluminum lines disagrees with this, but in light of the results from Refs. 216 and 217, this may be due to by an incomplete ionization equilibrium, which would not be a problem with the C IV lines since in that case ionization can be completely neglected.

9.6.3. Temperature Spatial dependence

As stated, no temperature measurements with C IV lines were obtained at points out in the gap. It is seen that the line intensities at points away from the cathode do not decrease as fast as the (interferometrically measured) density decreases, implying that the temperature is higher away from the cathode. The line intensities out in the gap are consistent with a temperature rise of an eV or so.

9.7. Total Ionic Populations

In principle, once the electron temperature is known, it is possible to determine the total population of an ionization stage from the population of one level.

However, the same strong dependence of level population on temperature that allows a fairly accurate temperature measurement also gives rise to great uncertainty in the determination of total populations.

The calculated total proton, C IV, and C III densities, based on the measured upper level populations of the Hα, 5801 Å, and 4647 Å lines when carbon cathodes are used, are shown as a function of electron temperature in Fig. 9.10. The densities are plotted in units of electron density, that is, ZN_z, and the (interferometrically) measured electron density is indicated by the dotted line. These values correspond to the time of the second peak, or about 70 ns. At this time, the area viewed by the monochromator is inside the opaque region on the interferograms mentioned in Ch. 7, so that the density quoted is that at the opaque edge. As mentioned in Ch. 7, comparisons of line intensities inside and just outside the opaque region indicate that the density inside the opaque region is not greatly different than that just outside.

The proton density was calculated using the Saha equation (radiative recombination is negligible compared to collisional recombination). For the carbon ions, the points on the graphs are the code results. The solid lines are for the LTE case. With C IV, this occurs when the 312 resonance line is optically thick, and with C III, this occurs when the 977 and 460 Å lines are optically thick. All of these lines are calculated to be marginally thick, and thus considering the aforementioned uncertainties in this calculation, it is not possible to say which (LTE or code) model is applicable.

The first thing to note is that it is that for any temperature, the spectroscopically calculated electron densities exceed those measured from interferometry. This is not surprizing in light of the uncertainty caused by the opaque region. Also, at 4 eV this error is only about a factor of two, which is within the range of the spectroscopic and interferometric uncertainties. If the LTE calculations are assumed to be valid, then the discrepancy is least at about 4 eV, which is the temperature inferred from the C IV line ratios. In any event, these calculations place bounds on the possible electron temperature. If the electron temperature was 3 eV, the C IV ions would contribute an electron density ten times greater

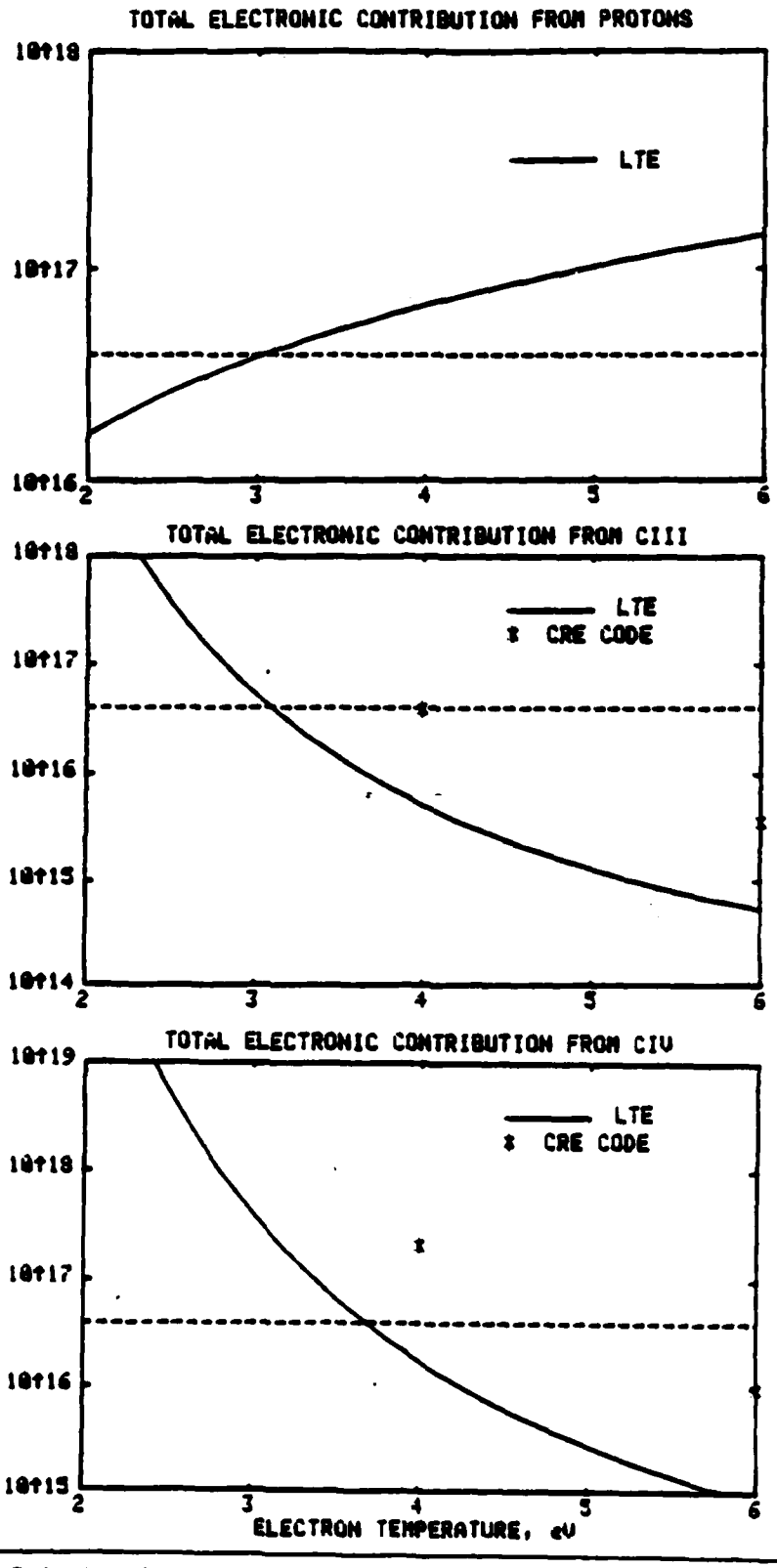

Fig. 9.12: Calculated total densities of protons. C III and C IV ions in units of ZN_z. The interferometrically measured electron density is indicated by the dashed line.

than that measured interferometrically. If the electron temperature was 10 eV, the measured hydrogen densities would imply an electron density that is ten times too large.

Without a precise knowledge of the electron temperature, much cannot be said concerning the ratios of ionic densities. It appears that the C IV density is at least as great as that for C III — if the LTE calculation is applicable to each ion then this is true at all electron temperatures. (According to the code, in equilibrium the C IV density is about one tenth the C III density at 4 eV and 5 times the C III density at 6 eV.) If the electron temperature is 4 eV then the proton density would exceed the total carbon density by about a factor of ten, but the strong variation in calculated carbon densities with temperature, plus the uncertainty about the applicability of the LTE calculation, do not permit this to be definitely stated.

The H, C I and C II densities can also be calculated. The total population density of the first five levels of hydrogen is calculated to be about $1\text{-}2\times10^{13}/\text{cm}^3$ based on a simple CRE calculation. The C I and C II densities are calculated based on the code (the calculated densities for these ions were much lower than C III and C IV so that self absorption effects were assumed negligible); at 4 eV the densities of C I and C II are $3\times10^{14}/\text{cm}^3$ and 5×10^{14} cm^3, respectively.

When Aerodagged cathodes are used, the densities of Al I and Al II are estimated to be in the range of a few $\times 10^{12}$ cm^3, with an uncertainty of a factor of five or so. Determining the Al III density is more difficult because of the uncertain applicability of any equilibrium model, as mentioned above. If the distribution temperature is 2 eV, as it seemed to be from the measured level populations, then the Al III (electron, i.e., $2\times N_i$) density is about 10^{16} cm^3, which is comparable to the carbon densities. The situation with aluminum is further complicated by the fact that in the steady state, over 90% of the total aluminum population is predicted by the code to be in the Al IV ground state for electron temperatures between 3–8 eV.

As mentioned before, shots with aluminum cathodes have roughly equal $H\alpha$ and aluminum line intensities, and about 8–10 times lower carbon line intensities.

than shots with carbon cathodes. Since the carbon IV lines are too weak to be observed with the aluminum cathodes, less can be said about the electron temperature in this case. However, the fact that the C III 4647 Å and C II 4267 Å lines, which have upper level energies differing by 12 eV, are diminished by about the same amount (compared to their intensities when carbon cathodes were used) when aluminum cathodes were used suggests that the temperature is not too different in this case. If this is true, then plasmas on aluminum cathodes will have equal proton and aluminum, and 8–10 times lower carbon, concentrations than plasmas on Aerodag cathodes.

From these calculations it appears that the proton/carbon ratio in aluminum cathode plasmas (if not also in carbon cathode plasmas) is significantly greater than the 2/1 ratio that would be expected if the hydrogen comes from desorption of hydrocarbons. This could be caused by absorbed hydrogen gas (although hydrogen is relatively insoluble in aluminum), by desorption of water, or by a mechanism of hydrogen desorption from hydrocarbons proposed by Halbritter that will be discussed in the next chapter.

The high proton/carbon ratio in aluminum cathode plasmas is also implied by the following bit af handwaving. Since Aerodag and Poco cathode plasmas have similar (interferometrically measured) electron densities, proton densities, and carbon densities, it can be argued that aluminum is not a major component of Aerodag cathode plasmas (since if it was, then its absence in Poco cathode plasmas would make a noticeable difference in the electron density). Since the aluminum densities with Aerodag and aluminum cathodes are similar, it can also be argued that aluminum is not a major component of aluminum cathode plasmas. And by the same logic as above, it can be argued that carbon is not a major component of aluminum cathode plasmas, since the electron density of aluminum cathode plasmas is not much less than that in carbon cathode plasmas, but the carbon densities differ greatly.

There remains one further question concerning ionization which must be cleared up. The neutral atoms are expected, by virtue of their short ionization times, to be in equilibrium with the singly ionized ions, and in fact this is

used to calculated the proton density. Doing the same for aluminum and carbon, however, results in calculated Al II and C II densities that are orders of magnitude larger than those observed. One clue as to the discrepancy comes from the fact that while hydrogen is observed out into the gap, the neutral carbon and aluminum lines are only observed near the cathode surface during the shot. If a sizable fraction of carbon and aluminum ions come off as relatively fast (i.e., ~0.5 cm/μs) neutrals (these velocities would be typical for either reflected or desorbed neutrals, as discussed in Ch. 10), then they will reach the slit image location in about 10–20 ns. With an ionization time of a few ns, there could still be a finite neutral fraction at that time.

9.8. Line Intensity Time Dependence

The spikes in the line intensity traces can be explained by increased heating when the current rises. This is consistent with the fact that the change in line intensity is greater for lines with higher upper level energies. The fact that the signals increase and decrease with changes in the current (rather than steadily increasing with time) implies that the temperature 'follows' the current (rather than steadily increases with time). This is born out by the fact that the temperature inferred by the C IV line ratio was the same at both peaks. The change in temperature which accompanies changes in the current does not have to be great: a change in temperature of less than 1 eV will change the 5801 Å line intensity by a factor of ten.

However, there appears to be a major inconsistency here. On the one hand, the temperature seems to increase slightly with only a 20% increase in curent density (this is the amount by which the current changes during the humps on the current trace). On the other hand, a factor of three increase in current density (that occurs when 1.6 mm cathodes are used) apparently results in little, if any, change in temperature. This point is discussed further in the next chapter.

9.8.1. Late Time Neutrals

In Ch. 7 it is suggested that a large flux of neutrals comes off the cathode late in the shot. Since no large increase in the neutral line intensities at that time

is observed, it would be concluded that rapid plasma cooling occurs at the end of the shot. For example, a drop in the electron temperature to 1 eV would increase the ratio of hydrogen ground state to Hα upper level populations by about four orders of magnitude.

9.9. Comparison With Previous Work

9.9.1. Temperature

In the spectroscopic study of aluminum needle cathode plasmas in Ref. 182, Baksht *et al.* report an electron temperature of 4.5 $\pm$0.8 eV. This was determined from intensity ratios of Al III lines, but since the upper levels in this case differed by only a few eV, the accuracy of this measurement is questionable.

The only other (known) relevant attempts at temperature measurement have been with vacuum arcs, such as those by Boxman and Goldsmith in Refs. 218 and 216. This experiment involved an aluminum arc with a current density of about 1 kA/cm^2, and a temperature of 6–9 eV is quoted. Electrostatic probe temperature measurements by Webster *et al.* are reviewed in ref. 34; temperatures of 3–6 eV are stated. Schellekens[219] obtained similar temperature estimates from a spectroscopic examination of a copper arc with a current density of a few hundered A/cm^2. Arc temperatures of a few eV are also quoted in Ref. 32.

It can be seen that temperature data is lacking for all of these relevant systems, and that broad area cathode plasma temperatures, as estimated here, are not obviously different from those in needle cathode or vacuum arc experiments.

9.9.2. Ionic Composition

The studies of ion flows in Ref. 186 also involved measurements of the relative fractions of ions in different ionization stages. In that experiment, carbon arc plasmas were found to consist mainly of singly ionized carbon ions, and aluminum arc plasmas consisted of roughly half Al II and half Al III. This is to be compared with the present experiment where most of the carbon is triply ionized and the fraction of Al III apparently greatly exceeds that of Al II. It is suggested that the difference arises because of the higher plasma density in this exeriment, which allows ionization to higher stages.

9.10. Conclusions

The vast quantity of information which may, in principle, be determined from the results of spectroscopic measurements is reduced in this experiment by experimental and theoretical uncertainties, the latter caused in particular by the short time scale involved and the unknown effects of self absorption, especially of resonance lines. However, several general conclusions may be drawn. The electron temperature is definitely between 3 and 10 eV, most likely between 3 and 6 eV, and the best guess is 4 eV. This refers to the electron temperature with Aerodag cathodes at a current density of 13 kA/cm^2, but there is evidence that the temperature is similar for Poco and aluminum cathodes. The temperature seems to change as the current changes during a shot, but shows no steady increase with time, and no major increase with increasing current density on different shots. Evidently, rapid cooling occurs at the end of the shot, interrupted temporarily by heating at the moment of closure.

The protonic contribution to the plasma density is significant, and there is evidence that it is dominant. The carbon ions are mostly doubly and triply ionized. The plasma is not in ionization equilibrium; in particular, close to the cathode the neutral concentration is too high.

One final point should be mentioned — all of these calculations are based on the assumption that the volume of plasma observed by the monochromator is uniform. This volume is about 50 μm perpindicular to the cathode surface and 6×10 mm parallel to it. In view of the results of Ch. 4, the assumption of uniformity may not be valid. If the electron temperature is constant but the ion and electron densities are nonuniform, then to first order the conclusions stated here are valid in an average sense. If the electron temperature is also nonuniform (so that, for instance, the Hα light is emitted from cooler, and C IV light from hotter, regions) then the conclusions regarding electron temperature are modified to: there is some region of the plasma of at least 3.5 eV temperature, and some region of at most 6 eV temperature. As shown in the next chapter, heat conduction will limit the spatial variations of electron temperature.

Chapter 10

Cathode Plasma Model

The objective of this chapter is to develop a simple global picture of the cathode plasma. An attempt will be made to relate and explain the observations of density, composition and temperature described in the previous chapters.

A basic first order model is proposed in Sec. 10.1. The density, composition, and temperature results of the last few chapters are summarized and compared with the model predictions in Sec. 10.2.

These are seen to be in fair agreement, but there are some discrepancies, and modifications to the model are discussed in Secs. 10.3, 10.4, and 10.5. Sec. 10.3 consists of a discussion of plasma-surface interactions and their impact on the supply of material to the plasma. Sec. 10.4 consists of a simple calculation of thermal processes in the plasma. Electric pressure effects are discussed in Sec. 10.5.

The modified model of cathode plasma behavior is described in Sec. 10.6. Finally, in Sec. 10.7, the resulting picture of the cathode plasma is given. This picture draws on the experimental measurements of the previous chapters, the simple calculations in this chapter, and the results of previous experiments.

10.1. First Order Model

The following model will be used as a reference point in analyzing the plasma properties. This model is motivated by the results of the needle cathode and vacuum arc studies described previously, and is similar to the (steady state) multi-cathode spot vacuum arc model presented by Boxman *et al.*[34]

A schematic of the cathode plasma is shown in Fig. 10.1. The plasma is divided into cathode spot regions and a more or less uniform 'bulk' region, which extends from some tens of microns off of the cathode surface out to the emission layer (i.e., this is the region viewed by the diagnostics in these experiments). The spots are treated as "black boxes" that: (a) facilitate current transfer from the cathode to the plasma, and (b) supply streams of ionized material to the plasma.

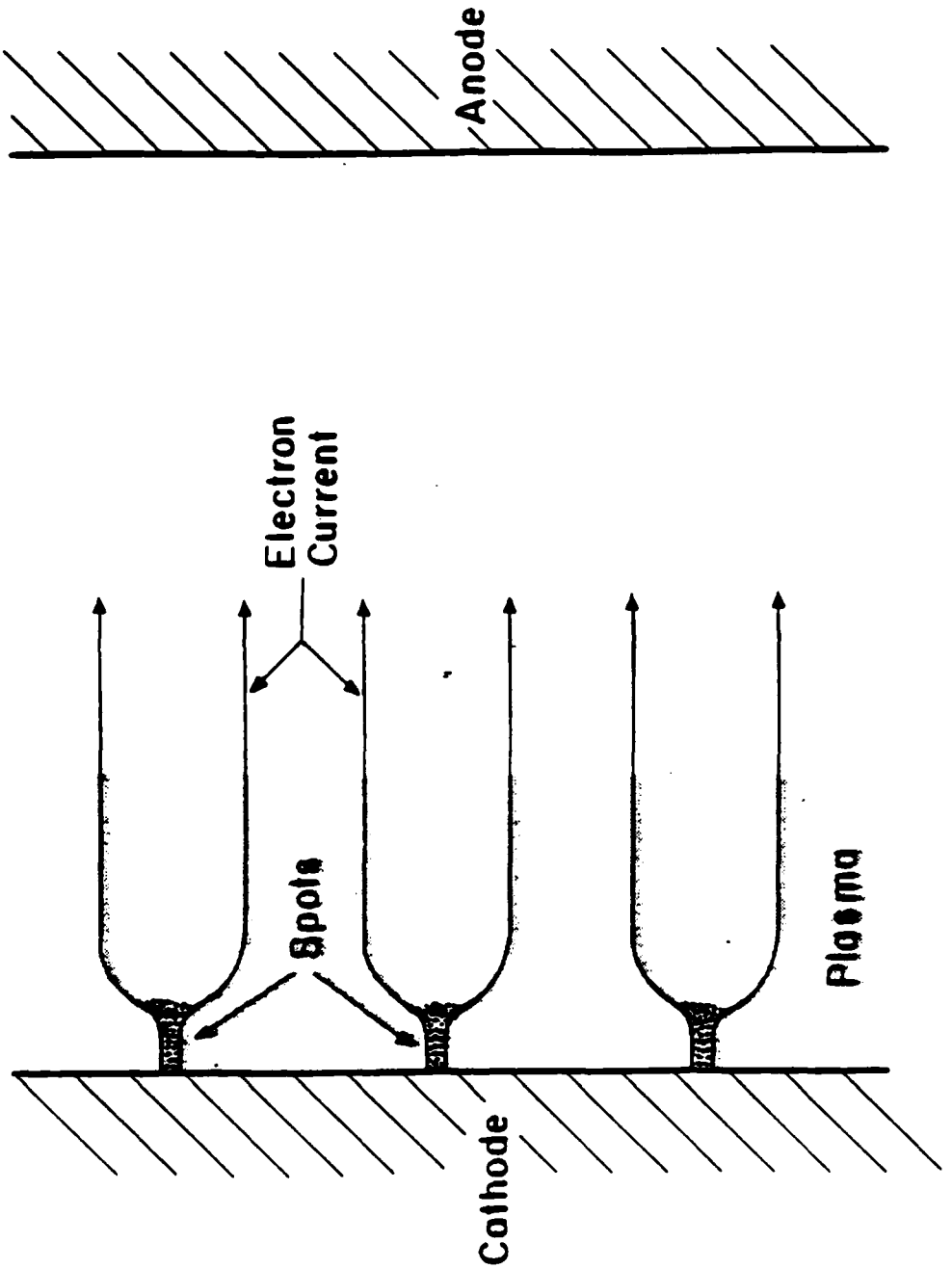

Fig. 10.1: Schematic of the Cathode Plasma

The number of spots per unit area is proportional to the current density, and the spot properties are constant in some average sense.

The material supplied to the plasma is characterized by an electron temperature of a few eV and some distribution of ionization stages. In the simple model, ionization, recombination, and thermal processes are neglected in the bulk region, so that the temperature stays constant. The material is supplied with a directed velocity of a few cm/μs, and streams out toward the anode.

Interaction between the plasma and the cathode surface outside of the spot regions is neglected.

The density, temperature and expansion velocity predictions of this model are then

$$e \int n dx \propto \int j dt \tag{10.1}$$

that is, the inventory is proportional to the charge transfer, and

$$T_e = constant \tag{10.2a}$$

$$v_{exp} = constant \tag{10.2b}$$

that is, the temperature is independent of current density and time, and all species move toward the anode with some constant (directed) velocity.

In other words, the essential feature of this model is that as the current density is varied, the (increasing or decreasing number of) cathode spots supply more or less of the 'same kind' of plasma. This model is appealing because it offers an explanation as to why plasmas in diodes with current densities differing by four orders of magnitude have similar expansion velocities (as discussed in Ch. 6), and why plasmas in broad area diodes are apparently similar in many ways to those in needle cathode diodes and vacuum arcs.

10.2. Summary of Plasma Measurements

The results of the density, composition, and temperature measurements of the previous chapters will now be summarized and compared with the predictions of the simple model above.

10.2.1. Density

The density profile has a maximum near the cathode and decreases out to the emission layer. The density at a given point increases with time, and at a given point and time is roughly proportional to the current density. On a given shot, the plasma inventory increases with time, and the inventory is very roughly proportional to the charge transfer, and weakly dependent on the cathode material. On shots with different current densities, the inventory (at a given time) is roughly proportional to the current density. The electron transport coefficient so determined is about 0.1–0.5 plasma electrons/current electron.

This proportionality of plasma inventory to charge transfer is in agreement with the model prediction (Eq. 10.1). However, as stated in Ch. 7, the measurement uncertainties do not allow a precise determination of the relationship between inventory and current density. In particular, the inventory increases more rapidly with time than predicted by Eq. (10.1). Also, the presence of the opaque region and its motion with time indicate the existence of an additional process of plasma formation.

10.2.2. Temperature

The electron temperature close to the cathode is between 3–6 eV, with 4 eV as the best guess. No variation in temperature is observed over a factor of t.. e variation in current density. This also is in agreement with the model prediction.

However, an odd fact is observed. On the one hand, the temperature shows no increase with a factor of three increase in current density. On the other hand, the 20% change in current density at the times of the current humps is seen to have a large effect on the line intensities, and this effect is consistent with a slight temperature increase of about 1 eV. Also, there is some evidence that the plasma is a bit hotter, on the order of an eV, at points out in the gap than it is at 100 μm from the surface.

10.2.3. Composition

The plasma is composed of materials from both the cathode and impurity constituents. The ionization stage populations are not in equilibrium: in particular,

there is a larger than expected population of neutrals at the cathode surface. The plasma includes both (relatively) highly ionized (C IV; the C III ionization energy is 50 eV) species and molecular species (C_2). The plasma contains a significant, and possibly dominant, fraction of protons.

The model makes no predictions concerning the plasma composition. The existence of CIV is definite evidence of the existence of high density cathode spot regions. On the other hand, it is difficult to imagine how neutrals could survive these regions.

10.2.4. Expansion

The expansion velocity is independent of cathode material and current density. This includes a range of current densities of a factor of ten in this experiment; analysis of the literature shows that velocity shows no dependence on current density over a factor of 10^4.

Spectroscopic measurements presented do not show any difference in the expansion velocities of different plasma species. In particular, aluminum ions with energies exceeding 35 eV are observed. While it cannot be stated that expansion is dominated by these directed flows (for example, a 4 eV protonic plasma undergoing simple thermal expansion at the sound speed would have a velocity of about 3 cm/μs, in the range of the observed velocity), the velocities so inferred are comparable to the expansion velocity calculated from the electrical characeristics.

The apparent independence of expansion velocity on species is in agreement with the model (Eq. 10.2b). More than any other experimental observation, the fast ions are also direct evidence of the existence of dense, hot, spot regions. On the other hand, the expansion velocity inferred from the electrical characteristics decreases after 40–50 ns, which is not in agreement with the model prediction.

10.2.5. Summary

In general, the experimental measurements are in rough agreement with the first order model: the plasma inventory is related to the charge transfer, the electron temperature (at a given time on different shots) shows no dependence on

current density, all species move with similar velocities, and the ion velocities and existence of C IV are both evidence of high energy density spot regions.

On the other hand, there are some discrepancies, and modifications to the model are discussed in the next three sections to account for these. The plasma inventory increases faster than predicted from Eq. (10.1), and it is suggested that plasma-surface interactions can explain this. The electron temperature apparently changes somewhat during the shot, and thermal proceeses in the plasma bulk are calculated and can explain this. Electric pressure effects can explain the decrease in expansion velocity that occurs during the shot.

10.3. Plasma-Surface Interaction

The only sources of material to the cathode plasma that have been considered up until now are the cathode spots, where it is assumed that some number of ions are supplied to the plasma for every current electron that is drawn from the cathode. However, a plasma in contact with a surface can 'boil off' material from that surface without necessarily turning-on new emission sites. The processes of plasma-surface interaction that cause material to be supplied to the plasma are the subject of this section.

The motivation for this is as follows. Consider for the moment a protonic plasma (with no directed velocity) in contact with a surface. The plasma is assumed to have a thickness l and density n. The flux of protons to the surface will depend somewhat on the cathode potential drop but is approximately given by[77]

$$\Gamma = 0.5 n \sqrt{\overline{T_e M_p}} \tag{10.3}$$

Each proton is assumed to desorb G ions from the surface, and so the plasma inventory (in electrons $\cdot$ cm^2) $N = nl$ increases according to

$$\frac{dN}{dt} = \Gamma(G-1) = .5 \sqrt{\overline{T_e M_p}} \frac{(G-1)N}{l} \tag{10.4}$$

Thus, the effect of plasma-surface interaction is to exponentially increase the plasma inventory with a time constant of

$$\tau = \frac{2l}{(G-1)\sqrt{\overline{T_e M_p}}} \tag{10.5}$$

With a temperature of 4 eV and plasma thickness of 1 mm (i.e., on the order of the diode gap), the e-folding time of the plasma inventory is then $70/(G-1)$ ns.

Thus, if the gain is on the order of 5, a significant increase in the plasma inventory due to plasma-surface interaction would be expected.

This effect can explain the difference between the observed inventory and the model prediction. Since Eq. (10.4) predicts exponential growth, the plasma inventory would be expected to increase more rapidly than predicted by the model (Eq. (10.1)), which is in agreement with the experimental results. It will also be shown that plasma-surface interactions can explain the neutrals observed near the cathode and the opaque layer observed interferometrically.

The remainder of this section is devoted to an estimation of G and a characterization of the desorbed materials.

10.3.1. Characterization of Impurities

First it is necessary to characterize the surface coverage expected in this experiment. To begin with, the metallic cathodes will be coated with a layer of oxide(s). The oxide thickness depends on the metal and on the surface preparation. For aluminum, the layer thickness is roughly 100 Å on a diamond turned surface and roughly 1 μm on a rough surface, although in the latter case, most of the thickness is a metal-oxide mixture.[29] Oxide surfaces on aluminum of 200 Å are quoted in Ref. 220. It will be assumed that the thickness of the 'pure' oxide layer is roughly 100 Å.

In this experiment, an untrapped oil diffusion pump was used to produce a vacuum of $\sim 10^{-4}$ T, so that the surface coating is expected to include both hydrocarbon (from the roughing pump) and silicone (from the diffusion pump) oils. Also, water is expected, particularly due to outgassing from the plexiglass rings in the water-vacuum interface (see Ch. 3). Another potential source of contamination is the diffusion of any machining oils absorbed in the metal.

Estimates of impurity concentrations may be obtained from the results of surface physics studies. In Ref. 221, the electron stimulated desorption yields from unbaked stainless steel surfaces were examined. These surfaces were initially vapor

degreased and placed in ultra-high vacuum. Up to 10^{17} mol/cm^2 were released, principally CO, with lesser quantities of H_2, CO_2, CH_4 and H_2O. In Ref. 68, the results of DC arc cleaning of Al electrodes were given and a total gas release of $\sim 4 \times 10^{17}$ cm^{-2} occurred. This was a lower limit as any gas reabsorbed on the chamber walls would not have been measured. In this case also a clean vacuum system was used and the electrodes were cleaned beforehand. In Ref. 222, similar coating levels were observed, and it is suggested that such high coating levels are due to adsorption in a porous oxide "sponge".

Since the background pressure in these experiments is higher than in those above, and the system is oil pumped, it is reasonable to assume that the surface coverage in the present experiments will be greater than that in the above experiments, or about 10^{18} atoms/cm^2. Assuming a typical monolayer coverage of 10^{16}/cm^2 implies that this coating will be about 100 layers, or about 100 Å, thick.

10.3.2. Incident Particle Fluxes

A surface adjacent to a plasma will in general be bombarded by ions, electrons and photons from the plasma. These may remove surface contaminants (as well as the bulk material) either by heating the surface, or by various single particle mechanisms. In this section the effects of electron and ion bombardment will be examined.

For now, any directed motion of the ions will be neglected, and the ions will be assumed to have an isotropic Maxwellian distribution of velocities. In that case, the flux of ions, Γ_i, is given by

$$\Gamma_i \approx 0.5 n_i \sqrt{T_e / M_i} \tag{10.6}$$

where the exact coefficient is determined by a version of the Bohm criterion that is related to the cathode sheath drop.[77]

The flux of electrons, Γ_e, can be calculated assuming that the electrons follow a Boltzmann distribution in the sheath

$$\Gamma_e = 1/4 n_e v_{the} e^{-eV_c/T} \tag{10.7}$$

AD-A147 917 PLASMA STUDIES IN ION DIODES(U) MASSACHUSETTS INST OF TECH CAMBRIDGE RESEARCH LAB OF ELECTRONICS G BEKEFI SEP 84 N00014-83-K-2024 4/4

UNCLASSIFIED F/G 20/9 NL

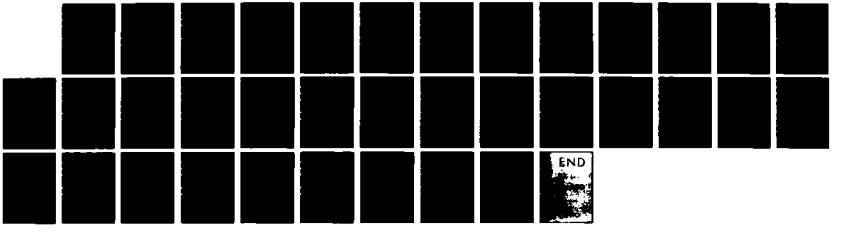

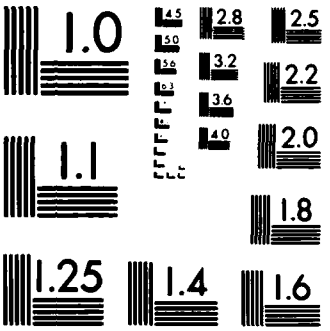

where V_c is the sheath drop. The ratio of incident ion to electron fluxes depends on the cathode sheath drop. In a thermal sheath, the drop is adjusted to make these fluxes equal. However, in the case of a cathode plasma, the drop will be higher to facilitate current transfer, and so the incident ion flux will exceed the incident electron flux.

Heating will be considered first. Let j_i and j_e be the ion and electron currents from the plasma to the surface through the sheath. The incident ion power density P_i (in this chapter, all powers are given in W, power flux densities in W/cm^2, and so on) is given by

$$P_i = 1.6 \times 10^{-19}\Gamma_i\left(\frac{E_i}{Z} + eV_c + \frac{T_i}{Z} + \frac{E_b}{Z} - e\phi\right) \tag{10.8}$$

where T_i is the ion temperature, Z_i is the ion charge, V_c is the sheath voltage, E_b is the binding (i.e., evaporation) energy and ϕ is the electronic work function (as electrons must be supplied from the metal to neutralize the ion). The incident electron power density P_e is given by

$$P_e = 1.6 \times 10^{-19}\Gamma_e(T + e\phi) \tag{10.9}$$

since the electrons, assumed to be Maxwellian in the sheath. deposit an average kinetic energy of T regardless of V_c. Now, the terms in parenthesis in Eq. (10.8) will be larger than those in Eq. (10.9). Since $\Gamma_i \geq \Gamma_e$, P_e will be neglected. With a 4 eV protonic plasma, $T_i = 1$ eV, $V_c = 25$ V, $E_i = 13.6$ eV, $E_b = 2$ eV and $\phi = 4$ eV then

$$P_i = 6.6 \times 10^{-12}n_i \tag{10.10}$$

The scale length l_{th} for thermal diffusion on a timescale τ is given by[223]

$$l_{th} = 2\sqrt{\frac{\kappa\tau}{\rho C_p}} \tag{10.11}$$

where κ, ρ and C_p are the heat conductivity, density and heat capacity, respectively, of the surface. If the penetration depth of the ions is much less than this length, then the ion energy may be assumed to be deposited in an infinitely thin layer. As will be shown later, the ions are stopped within a few tens of Å, which

is significantly less than the thermal diffusion length. In this case, the energy deposition at the surface ΔE in J/gm may be found from the solution of the semi-infinite heat equation[223]

$$\Delta E = P_i \sqrt{\frac{4}{\pi} \frac{tC_p}{\rho\kappa}} \tag{10.12}$$

Whether the relevant thermal properties are those of the coating or those of the substrate depends on the ratio of coating thickness to thermal scale length. The thermal characteristics and calculated diffusion lengths on a 10 ns timescale for water, hydrocarbon oils, aluminum oxide, aluminum and Poco graphite are given in table 3.1.

As can be seen, the thermal scale lengths are all greater than any reasonable coating thickness, so that the energy deposition is determined by the substrate, which in these experiments is generally aluminum or graphite. The energy deposition necessary to desorb significant quantities of contaminants on a rapid (~10 ns) timescale can be found from studies of anode plasma formation,[136,152] where it is concluded that an energy deposition of 500–2000 J/gm is required. From the values in table 10.1 and Eqs. (10.10) and (10.12), the energy deposition (in aluminum or graphite) in 70 ns is roughly

$$10^{-15} n \tag{10.13}$$

It can be seen that a plasma density of $\sim 10^{18}/\text{cm}^3$ is necessary in order to desorb significant material through bulk heating.

Next, individual particle effects will be considered. The following phenomena are of interest here:

1. backscattering
2. electron stimulated desorption (ESD)
3. ion stimulated desorption (ISD)
4. sputtering

Table 10.1

Thermal Quantities

Material	ρ	C_p	κ	l_{th}
H_2O	1	4.2	6.0×10^{-3}	0.1
HC Oil	1	0.3[2,3]	1.3×10^{-3}[†]	0.2
Al_2O_3	3.8	1.1[2]	0.3	0.8
Al	2.7	0.9	1.3[5]	2.3
Poco[1]	1.8	0.8	1.2	2.8

[1] From manufacturer's data sheet.

[2] From Ref. 225

[3] Estimate for various hydrocarbons.

[†] Values for silicone, transformer, and petroleum oils, ±20%.

[5] Value for 2024 alloy; varies from 1.2–2.2 for different alloys.

These thermal quantities are from Ref. 224 unless noted. This table gives the density (g/cm^3), heat capacity (J/°K·g), and thermal conductivity (W/cm·°K). Also shown is the calculated thermal diffusion length in μm for a timescale of 10 ns.

The distinction between 3 and 4 is that 3 refers to removal of adsorbed contaminants while 4 refers to removal of the bulk material.

A discussion of backscattering is given by McCracken and Stott.[226] For 20 V protons incident on carbon or aluminum, the reflection coefficient is roughly 50%. The reflected particles are primarily neutrals with typical energies of 50% of the initial energy, and roughly cosine distributions of reflected velocities.

Backscattering cannot increase the plasma inventory ($G < 1$) but it can explain the presence of a nonequilibrium concentration of neutrals near the cathode. Ions will be accelerated in the plasma sheath, neutralized and reflected with energies of roughly half the sheath potential. These neutrals will rapidly ionize, but the neutral concentration will remain finite close to the cathode and this can explain why neutral aluminum and carbon are observed near the cathode but not out in the gap during the shot. The relatively high energy of the reflected particles can also explain the $\sim$1cm/μs neutral aluminum velocities at the end of the shot that were observed in Ch. 8.

(Another possible effect of the reflected neutrals concerns plasma expansion, if the plasma is cold and dense enough so that the neutrals can escape without being ionized. A mode of plasma expansion against a magnetic field would then be possible where the neutrals move out into the gap, unimpeded by the field, to be ionized in the gap by the electron beam. Fast neutral dominated expansion in magnetically insulated diodes has been suggested previously.[227] and reflection can account for the fast neutrals.)

Theories of ESD are given in Refs. 228 and 229. Generally, the particles desorb as neutrals, with the yields being about two orders of magnitude higher than for desorption as ions. Although there is much data in the literature, most of this data is for well defined adsorber-adsorbate systems with low surface coverages. ESD of gasses from unbaked metals in UHV for 600 eV incident electron energies were measured in Refs. 221 and 222, and found to range from 1–10, dropping rapidly after the metals were baked. In a series of papers,[230–232] Halbritter discusses the (more relevant to this experiment) case of $\leq$30 eV incident electrons on "dirty" (i.e., oil and water covered) surfaces. The dominant process is desorption

of hydrogen from saturated hydrocarbons, resulting in polymerization and dehydrogenation. A threshold energy of about 5 eV is quoted, with a yield of roughly unity. The significance of this process is that it permits a higher ratio of protons to carbon in the plasma than that predicted from a CH_2 dependence.

ISD is discussed in Refs. 233–235. As in the case of ESD, data for low incident energies is lacking. Generally, the yield goes up with the mass of the incident ion, the coating thickness (if less than the particle range) and the ion energy (at low energies). Achard[222] studied ESD and ISD of gasses on stainless steel with similar (~1kV) ion and electron incident energies, and found that the ISD yields were about 20, ten times greater than those for ESD.

Since the flux of ions from the plasma will be equal to or greater than the flux of of electrons, and since the ions will have been accelerated in the sheath to energies greater than the (presumed) electron energy of a few eV, ESD will be neglected compared to ISD. Based on the ESD measurements of Halbritter, and comparisons of ESD and ISD yields at higher energies, an ISD yield of 1–10 will be assumed. (Also, the coatings in this experiment are relatively thick, which will tend to increase the yield.)

Generally, the desorption products come off as molecules, although presumably (according to Ref. 230–232) ISD can also desorb protons from saturated hydrocarbons. Sputtering of the electrode materials is expected to be negligible. For sputtering to occur at all, the incident ion range must be greater than the coating thickness. At the low energies corresponding to the sheath voltage, nuclear stopping dominates the energy loss. Calculations of this loss are given in Ref. 236: for protons the range is about 1 Å/eV, and for carbon ions the range is about 0.1 Å/eV. Thus, for a sheath drop of 10–30 V, carbon ions are not expected to penetrate past the coating, and penetration of the protons will be marginal. In addition, sputtering yields for various ions on graphite and aluminum[237] are 0.01–0.1 at 100 eV and drop rapidly with decreasing energy. The yields for sputtering of aluminum oxide are lower still.[238]

10.3.3. Desorption by Photons

It remains to examine desorption due to photons from the plasma. In order to calculate the photon flux from the plasma it is necessary to know the plasma composition, average ion charge, density and electron temperature. In addition, optical depth effects must be taken into account. Calculations of power radiated by a plasma, assuming collisional-radiative equilibrium, are given in Ref. 127. The energy loss is predominately due to line radiation and reaches a peak at an electron temperature of about 6 eV. From the calculations in that paper, the estimated flux of photons (for the plasma densities in these experiments) will be about equal to the ion flux.

An experiment by Enloe *et al.*,[239] is particularly relevant here. In that experiment, an electrically stressed insulator was irradiated with UV and the effect of this irradiation on flashover was examined. It was concluded that the effect of the photons was of a single particle nature (PSD), rather than a bulk heating.

PSD is discussed in Refs. 231 and 240. In general, the yields are similar to or slightly less than those for ESD. Hence, PSD will also be neglected here in comparison to ISD, as the photonic and ionic fluxes are presumed to be roughly equal. This is in line with the results of Ref. 241, which involved a study of anode plasma formation in a diode driven by a Nereus accelerator. It is stated that "the electrodes were illuminated with a source producing a UV flux equal to that of the diode, with no effect".

So, in conclusion, ion stimulated desorption is seen to be the dominant desorption mechanism. From Eq. (10.5), a yield of about 5 desorbed particles/incident particle is necessary for this process to contribute to the plasma inventory, and such a yield is seen to be reasonable.

The nature of plasma-surface interaction is as follows: Initially, the plasma consists of directed ion flows from the cathode spots. Some fraction of these ions[190] flow from the spots parallel to the cathode, impinge at grazing incidence, and desorb surface contaminants. This starts a 'bootstrap' mechanism where some of the desorbed material returns to the cathode, desorbing more material, and so on. The desorbed material consists of protons desorbed from saturated

hydrocarbons as well as various molecular species. The protons (and ions from molecules that have undergone dissociative ionization) move out with the cathode plasma and cause the inventory to increase faster than would occur if the only sources of plasma were the cathode spots. The molecular species stay closer to the surface and perhaps in some way are responsible for the opaque layer that is seen on the interferograms. Desorption of molecules can explain the observation of C_2 in the cathode plasma. Some of the aluminum and carbon ions from the cathode spots return to the cathode and are reflected as neutrals — these neutrals are eventually ionized, but a finite nonequilibrium neutral population exists close to the plasma surface.

10.4. Thermal Processes

A simple calculation of the thermal processes in the cathode plasma is presented here. A detailed calculation is beyond the scope of this work; the attempt here is to explain the results of the previous chapter.

10.4.1. Bulk Processes

Heat is supplied to the plasma by Joule heating. The power generated P_J in W/cm^3 is given by[195]

$$P_J = \eta j^2 \tag{10.14a}$$

$$\eta = \frac{1.0 \times 10^{-2} Z \ln \lambda}{T^{3/2}} \tag{10.14b}$$

where η is the resistivity in Ω-cm. With $\ln \lambda = 6$, $Z \approx 1.5$, and $T = 4$ eV, (appropriate considering the results of Ch. 9), the power is about 2×10^6 W/cm^3 at 13 kA cm^2, and 1.7×10^7 W/cm^3 at 39 kA/cm^2.

This is all assuming that the resistivity is classical, that is, described by Eq. (10.14b). If the electron drift velocity is high enough then an increased resistivity will result.[242] According to Ref. 242, under the conditions of these experiments the electron drift velocity will be below the critical value for anomalous resistivity everywhere but at the very edge of the plasma, and so the assumption of classical resistivity is reasonable.

The temperature rise due to Joule heating is given by

$$\frac{3}{2}nT = 6 \times 10^{18} \int P_J dt \tag{10.15}$$

Clearly, thermal processes in the bulk region are important. If the current is approximated by a linear ramp for 40 ns, then the $1 \times 10^{16}/\text{cm}^3$ plasma layer will be heated (in the absence of loss mechanisms) to 8 and 20 eV at that time, for peak current densities of 13 kA/cm^2 and 39 kA/cm^2, respectively. The plasma will get even hotter with further passage of time.

The heat supplied by Joule heating is balanced by elastic electron-ion collisions, inelastic electron-ion collisions, and heat conduction. The rate of energy loss P_e due to elastic collisions is given by[195]

$$P_e = 4.8 \times 10^{-19} \frac{m_e}{M_i} \frac{n}{\tau_e} (T_e - T_i) \tag{10.16a}$$

$$\tau_e = 3.5 \times 10^5 \frac{T^{3/2}}{nZ \ln \lambda} \tag{10.16b}$$

With an electron density of $3 \times 10^{16}/\text{cm}^3$, electron temperature of 4 eV, and ion (proton) temperature of 1 eV, this power is 2.3×10^6 W/cm^3.

Part of the energy transfered to ions is radiated; the remainder (in the transient case) goes into increased ionization. As mentioned in Sec. 10.3.3, the radiated power is difficult to calculate. From the calculations in Ref. 127, it is estimated that the maximum loss rate at a carbon ion density of 10^{16} cm^3 and electron density of $3 \times 10^{16}/\text{cm}^3$ is about 10^6 W/cm^3.

The radiative loss rate can also be estimated from the results of Ch. 9. It is assumed that the major non-protonic species is C IV. As stated in Ch. 9, the population of all levels except the ground state and 2P level is negligible (see Fig. 9.6). These two levels are expected to be in LTE, and if the CIV ion density is $3 \cdot 10^{15}$ cm^3 as calculated in Ch. 9, then the loss rate is about 7×10^5 W cm^3.

In addition to radiation, energy supplied to the ions by inelastic collisions can go into increased ionization. If recombination is neglected, the loss rate is given by

$$1.6 \cdot 10^{-19} \sum_i n_i N_e S_i E_i \tag{10.17}$$

where S_i is the ionization rate and E_i is the ionization energy (in eV) of species i. From the ionization rates and ionic populations given in Ch. 9, it can be seen that this loss is negligible — S_i is too low for the higher ionization stages and n_i is too low for the lower stages.

Thus, the combined effects of elastic and inelastic collisional losses can equal the energy input at 13 kA/cm^2, but not at 39 kA/cm^2.

Since the specific heating is inversely proportional to the density, in the absence of heat conduction the outer layer of the plasma will get extremely hot. The power loss due to heat conduction P_c is given by[195]

$$P_c = -\kappa \frac{d^2T}{dx^2} \tag{10.18a}$$

$$\kappa = \frac{320T^{5/2}}{Z \ln \lambda} \tag{10.18b}$$

If the temperature profile is assumed to be parabolic for simplicity

$$T(x) = T_0 + \delta T\left(1 - (\frac{x}{x_0})^2\right) \tag{10.19}$$

where x is the distance from the cathode, T_0 is the temperature near the cathode, and $x_0 \approx 1$ mm, then the conduction loss is approximately

$$P_c = 7.1 \times 10^3 \overline{T}^4 \delta T \tag{10.20}$$

where $\overline{T}$ is the average temperature.

From this equation and Eqs. (10.14), the temperature rise at the emission layer necessary to balance the ohmic power with conduction can be calculated. With T_0=4 eV, this temperature rise is about 2 eV at 13 kA/cm^2 and 4 eV at 39 kA/cm^2.

This assumes steady state conditions. In the transient case, it is necessary to calculate the equilibration time τ_{equil}. By analogy with Eq. (10.11), this time can be seen to be

$$\tau_{equil} = 4.0 \cdot 10^{-20} \frac{l^2 n}{\kappa} \tag{10.21}$$

For a length l of 1 mm, temperature of 4 eV, and density of $3\times10^{16}/cm^3$, this time is about 10 ns. Thus, the plasma temperature profile can be approximated by the steady state value.

Another possible loss mechanism is adiabatic cooling. For example, during adiabatic expansion, the temperature decreases according to

$$T \propto n^{2/3} \tag{10.22}$$

However, this effect is expected to be negligible once the density has dropped below about $10^{17}/cm^3$. The total internal energy of a 4 eV plasma at $10^{17}/cm^3$ is $\sim$0.1 J/cm^3. At 39 kA/cm^2, this energy is supplied to the plasma by Joule heating in about 5 ns.

The above calculations are modified by the magnetic field caused by the diode current. The effect of this field is to increase the resistivity and decrease the heat conduction, thus causing a larger temperature gradient. The magnitude of this correction is on the order of $(\omega_c\tau)^2$, where ω_c is the cyclotron frequency eB/mc. At 4 eV, $3\times10^{16}/cm^3$ and at the diode midplane at peak current, this quantity is about 1. At higher densities and lower currents, it is lower. Because of variations in the field along the diode edge, magnetic field effects will be neglected, although this neglect is not strictly justified.

In conclusion, neither elastic nor inelastic collisions are sufficient to balance the ohmic heating. Heat conduction tends to equalize the temperature within the plasma, although the plasma away from the cathode is expected to be somewhat hotter than the plasma near the cathode, which is consistent with the results of Ch. 9.

Since the thermal equilibration time within the plasma bulk is so short, it is possible to examine the balance between the total heat supplied to the bulk and heat transfer back to the cathode from the bulk plasma. If the plasma is assumed to be about 1 mm thick, then the total ohmic power deposited in the plasma is about 2×10^5 W/cm^2 at a current density of 13 kA/cm^2 and 2×10^6 W/cm^2 at a current density of 39 kA/cm^2. One form of heat loss is the flow of ions across the sheath to the cathode. If each ion is assumed either to be reflected as a neutral or

to desorb a neutral which then becomes ionized, the ion essentially carries away an amount of energy equal to its ionization energy. From Eq. (10.6), with protons this gives a value of about $2\times10^{-12}n$ in W/cm^2. In order to balance the total ohmic input at the highest current density, a density of 10^{18}/cm^3 is required. Since the plasma density (at 100 μm from the cathode) on these shots is about 10^{17}/cm^3 at the time of the first peak, it seems unlikely that this can account for the loss. However, if each ion desorbs several neutrals, which then become ionized, the heat loss will be greater. At a plasma density of 10^{17}/cm^3, the input ohmic power at peak current can be balanced if the yield is 10.

Another possibility is radiation. An upper limit to the radiated power is given by that for a black body (in W/cm^2)[243]

$$I_{bb} = 1.0 \times 10^5 T^4 \tag{10.23}$$

Now, at plasma densities below 10^{19}/cm^3, the plasma is quite thin to either Bremstrahlung or recombination radiation,[243] so that in order for the radiation output to be close to that of a black body, the plasma must be so thick to line radiation that the lines are broadened considerably. For a 4 eV plasma, from Eqs. (10.15) and (10.23), the total black body radiation output exceeds the ohmic input by about a factor of ten. This means that on the average one tenth of the spectrum must be taken up by the broadened spectral lines, or with, say, one strong line every 100 Å. each line must be broadened to 10 Å. In view of the results of Ch. 9, this seems unlikely.

In conclusion, then, these very simple calculations of the plasma thermal processes suggest that Joule heating in the plasma bulk is balanced by conduction back to the cathode: there is a cooler plasma right at the cathode surface (closer than the 100 μm distance where temperature measurements were made) which acts as a heat sink. The outer regions do get slightly hotter, on the order of a few eV.

The input power is proportional to j^2 and the loss power due to conduction is proportional to n. If the plasma density is indeed proportional to the current

density, then the plasma would be expected to be hotter at higher current densities. That no temperature difference is observed when the current density is increased by a factor of three can be due to either of two possibilities. It may be that in the present experiments, the loss rates exceed the ohmic input, with the result that the plasma temperature is dominated by the initial temperature of the plasma emerging from the spot regions. In this case an increase in plasma temperature would be expected at sufficiently high current densities. The other possibility is that the plasma density is not strictly proportional to the current density, particularly close to the cathode. For example, if the plasma density is proportional to j^2, the loss rate would increase proportionately to the increased rate of heating. As mentioned previously, the uncertainties in the interferograms do not permit the relationship between current density and plasma density to be determined exactly.

It remains to explain the time dependence of the temperature. As mentioned before, there is an apparent contradiction in that a change in current density of a factor of three makes no difference in the plasma temperature, but the 20% change in current density at the times of the current peaks makes a noticeable difference in line intensities which is consistent with a change in temperature of an eV or so. The constancy of temperature on different shots is explained above as being due to the fact that at the higher current densities, the plasma density near the cathode is higher and so the loss increases. When the current density increases, more material is supplied to the plasma. However, when the current falls (on a given shot), the material remains, so that the loss rate stays constant while the input power drops. In addition, if the decrease in current causes spots to die out, one would expect a flux of neutrals from the still hot cathode surface under the spot. Thus, cooling is expected when the current falls. This can explain the cooling that results in between the two peaks in the current, and the rapid cooling that occurs at the end of the shot.

In other words, there is a difference between variations in current density (at a given time) on different shots, and variations in current density with time on a particular shot. In the latter case, there is a finite response time for the amount

of material in the plasma to equilibrate with the current density. New material can be supplied quickly when the current density increases, but material leaves the plasma quite slowly when the current falls.

10.5. Electric Pressure Effects

According to the perveance measurements in Ch. 6, the plasma expands at a constant velocity for ~40 ns, after which the velocity decreases and in some cases the gap appears to open temporarily. This is attributed to electric pressure effects, which place a minimum on the emission layer density n_{el}:

$$n_{el} = 4j/v_{the} \tag{10.24}$$

If the plasma density at the emission layer falls below this value, the resulting electric pressure will push back the plasma, piling up the density until Eq. (10.24) is satisfied once more. In order for electric pressure to have a noticeable effect on plasma motion, it is necessary to have both a rising power (current) pulse and a shallow density gradient. In the present experiment, electric pressure effects are believed to be accentuated by the shape of the current pulse. When the current falls, free expansion of the plasma is possible and the density gradient flattens, so that when the current rises again, the increased requirements on emission layer density push the plasma back.

If the plasma expansion is greater than one dimensional, then electric pressure effects will also be accentuated, since the fall off in density will be greater. This has also apparently been observed in these experiments, where on shots with highly nonuniform plasma formation, the reduction in expansion velocity is more pronounced. Also, on these shots the luminosity consists of spherical spots of light rather than a uniform layer, and plasma expansion from these spots will be greater than one dimensional.

Electric pressure effects as described above can not permanently stop the plasma motion because new material is continually supplied to the plasma: the emission layer can be temporarily pushed back but eventually the plasma density will be high enough to allow resumed expansion. However, as mentioned in

Ch. 6, very long pulse lengths ($\gg \mu s$), where the inferred plasma emission layer remains stationary, have been observed in experiments with needle cathodes.[244] In this case the electric pressure effects apparently were brought about by another cause.[245] These experiments involved low current densities, with the current per (needle) cathode being close to the minimum threshold described in Ch. 2. At these low currents and long timescales, the supply of material into the plasma apparently decreases. If the rate of new plasma production is no more than the rate of plasma flow back to the cathode, then the total amount of material in the gap will remain constant. In this case, the volume occupied by the plasma is limited by the fixed quantity of plasma and by Eq. (10.24). This phenomenon was not investigated in these experiments, and is mentioned here only to point out that the electric pressure effects in this experiment are believed to have a different cause than those in the low current density, long pulse experiments.

10.6. Corrections to the Model

The previous sections show that interactions between the plasma and the cathode surface, and thermal processes in the plasma bulk, both of which were neglected in the first order model, do play an important role in the plasma behavior. Plasma-surface interaction gives another source of material to the cathode plasma, and explains many of the interferometric observations. Thermal processes in the plasma bulk are also important and can explain many of the observations made in Ch. 9. Electric pressure effects can explain the inferred reduction in expansion velocity.

The plasma inventory, then, may not be exactly that given by Eq. (10.1), but it is true that the inventory increases with increasing charge transfer. The temperature may not be exactly constant, but is relatively so over the conditions varied in this experiment. This constancy is believed to be due to increased losses at higher current densities that result from the higher plasma densities. So, in an approximate sense, the key feature to the first order model is still apparently valid: cathodes in diodes with different current densities (and to a degree, at different times on a given shot), have more or less of the 'same kind' of plasma.

10.7. Cathode Plasma Description

The experimental results presented in the previous chapters, the simple calculations in this chapter, and the results of previous measurements all give rise to a relatively complete picture of the cathode plasma:

Upon the initial imposition of an electric field to the cathode, emission sites are formed by an as yet undetermined mechanism. Breakdown may originate at metallic protrusions, although there is evidence that impurities play a role in emission site formation. With time, more sites are formed, however, the space charge from current emitted from the initial sites retards the formation of subsequent sites. If the rate of rise of the applied field is great enough, this effect will be minimized. If not, then a bumpy plasma surface will result, increasing the electron beam emittance.

As plasma expands from the emission sites, new sites can form under the plasma cloud, and this formation is known to be facilitated by impurities.

Current flows from the cathode to the plasma in cathode spots — localized regions of high plasma (and energy) density. The high energy density in the spot regions facilitates current transfer. The number of spots increases with increasing current density.

These spots also supply material to the plasma in the form of directed streams of ions with a velocity on the order of 2 cm/μs. The hot, dense, spot regions give rise to multiply ionized species and cause the acceleration of ions to the relatively high velocities.

Material is also supplied to the plasma as a result of interaction between the plasma and the cathode surface. This material consists of both ions (presumably these are dominated by protons) and molecular species. This desorption is initiated by some of the material ejected from the spots which returns to the cathode: at this point the desorbed plasma density can increase exponentially.

The plasma inventory increases by these two mechanisms with time and with increasing current density.

The plasma is composed of constituents of both surface impurities and of the cathode substrate material. By altering the surface coating (for example, by adding a thick coating of silicone oil) it is possible to modify the plasma composition somewhat.

Ions emitted from the spots move toward the anode, and all species move with similar velocities. Thus, to a degree, plasma expansion is dominated by the physics at the cathode surface, that is, in the spot regions.

Expansion is also affected by electric pressure effects at the plasma-vacuum interface, which can retard or advance expansion, depending on the shape of the current pulse.

Plasma in the spot regions is presumably quite hot; the rapid density decrease as material moves out into the plasma bulk cools the plasma to about 4 eV. The bulk plasma is heated by the diode current and this heating is balanced by heat conduction back to the cathode, where cold material near the cathode surface can act as a heat sink. Outer regions of the plasma are slightly hotter (on the order of a few eV). The increase in plasma inventory with current density tends to keep the temperature constant; however, it is possible that at sufficiently high current densities the temperature will increase. (It could be argued that the needle cathode experiments with very high current densities (but apparently similar temperatures) contradict this. However, in these experiments, the 3-D expansion will result in increased adiabatic cooling.) The plasma temperature can also effect the expansion by way of Eq. (10.24), since a higher electron thermal velocity reduces the demands on the emission layer density.

At the end of the shot, the decrease in current causes rapid plasma cooling, and at this point large fluxes of neutrals come off of the cathode. This cooling is temporarily interrupted by momentary rapid heating when the cathode plasma comes into contact with the anode (or anode plasma) at localized points.

In general, the plasma properties in all manner of broad area diodes, needle cathode diodes, and vacuum arcs are similar, differing only in the quantity of

plasma (and in the fact that plasmas in the latter two cases are composed primarily of the cathode substrate material). The cathode spot is fundamental to the behavior of all of these related systems.

Chapter 11

Conclusions

In these experiments, the cathode plasma in a broad area planar diode has been characterized as a function of several experimental parameters. Particular attention has been devoted to the uniformity of plasma formation and the rate of plasma expansion, since these are the plasma properties most important to diode performance. The objectives of this work were to: (a) investigate the fundamental physics of cathode plasma behavior, and (b) identify practical steps which can be taken in diode design to optimize the plasma behavior. To a large degree these objectives have been met. The key processes that determine plasma formation uniformity and the rate of plasma expansion have been identified, aspects of the previous diode folklore have been critically examined, and several practical implications for diode (and driving circuit) design can be stated. In addition, the results of this work have cast some light on the fundamental microprocesses of cathode plasma formation.

The experimental results are summarized in Sec. 11.1, the implications of these results for diode design are discussed in Sec. 11.2, and suggestions for future work are given in Sec. 11.3.

11.1. Experimental Results

11.1.1. General Plasma Properties

Cathode plasma production occurs during the entire pulse, and the rate of plasma production increases with increasing current density. The density is highest at the cathode and decreases toward the emission layer. After the pulse, the material in the gap is dominated by neutrals that remain for about 100 μs.

The cathode plasma is composed of both the cathode substrate material and constituents of surface impurities. The plasma includes singly, doubly, and (at least) triply ionized species, neutrals, and molecular species. The electron temperature is about 3–6 eV, and shows no dependence on current density over a

factor of three change in the latter. Rapid cooling occurs at the end of the pulse, although there is a temporary period of rapid heating when the cathode plasma comes into contact with the anode or anode plasma.

A global model of the cathode plasma has been proposed. This model involves plasma production from independent cathode spots, with modifications to take into account plasma-surface interactions, thermal processes in the plasma bulk, and electric pressure effects. The essential feature of this model is that cathodes in all diodes produce more or less of the 'same kind' of plasma.

11.1.2. Uniformity

The cathode plasma uniformity, as inferred from luminosity observations, is correlated with both the electron beam source brightness uniformity and reduced beam divergence. This uniformity is determined by the rate of rise of the (local microscopic) electric field. A slowly rising field impairs uniformity by the screening effect of electrons emitted from initial emission sites. As the microscopic field is determined by both the applied macroscopic field and the local field enhancement, performance can be improved by using a rough cathode surface and by increasing the rate of rise of the diode field.

11.1.3. Expansion

Motion of the cathode plasma is affected by two processes. The high energy density in the cathode spot regions accelerates ions to velocities of about 2 cm/μs, (relatively) independent of the ion mass. In this sense plasma expansion is controled by phenomena at the cathode surface.

The other influence on plasma motion arises from electric pressure effects at the plasma-vacuum boundary. Magnetic pressure also inhibits plasma expansion, although in a non-magnetically insulated diode there will always be a part of the cathode plasma where there is no field. Electric pressure effects are significant when the plasma density profile is shallow and during times when the current is rising.

Electric pressure may also be partially responsible for the improved uniformity that results from a high dE/dt. If the current rises rapidly, the resulting electric pressure will tend to flatten any bumps in the plasma surface.[246]

11.1.4. Microprocesses

The results of these experiments have implications concerning the cathode plasma microprocesses. The observed fast ion flows and triply ionized carbon ions are direct evidence of the existence of high energy density cathode spots. The luminosity patterns described in Ch. 4 are similar to erosion pattens in contaminated surface vacuum arcs and are believed to be evidence of plasma induced emission site formation, and propagation of site formation along grain boundaries. The composition and density measurements also point to the importance of interactions between the plasma and the cathode surface outside of the spot regions.

11.2. Implications for Diode Design

11.2.1. Uniformity

Graphite cathodes produce the most uniform plasma. If design considerations mandate metallic cathodes, the surfaces should be roughened (e.g., by sandblasting). Coating with Aerodag helps, but not greatly. If an Aerodag coating is used, the coated surface should not be polished but should be left as is. It is most important to have a high $dE\ dt$: with sandblasted or graphite surfaces (at least in these experiments), a value of 2×10^{14} V/cm·s is necessary.

11.2.2. Expansion

There is apparently little that can be done concerning acceleration of ions in the spot regions, since similar velocities are observed in systems (vacuum arcs, needle cathode diodes, and broad area diodes) with widely varying parameters. (Also, there is apparently no advantage to having a hydrogen free surface.) If some sort of diffuse discharge could be set up so that (in some undetermined way) current could be transferred from the cathode to the cathode plasma without high energy density cathode spot formation, then ion acceleration should not occur. It is not known how this could be accomplished.

Electric pressure effects do offer the possibility of (temporarily) reducing the plasma expansion velocity. They are accentuated both by a rising power pulse and a diode geometry (such as point cathode–plane anode) where the cathode plasma expansion is greater than one dimensional. Such geometries, however, are usually associated with increased beam divergence. An array of points could be used, but once the plasma clouds from each merge, the greater dimensionality will be lost.

11.2.3. Short Pulse Diodes

Light ion beam target design considerations demand a short (~10 ns) ion beam pulse. For such pulse lengths gap closure is not a concern but rapid plasma formation is of paramount importance, especially for those ion beam diodes (e.g., the pinch reflex diode) that depend on electron flow for the diode operation. The results of this work show that if the rise time decreases along with the pulse length, then rapid, uniform plasma formation should be no problem.

11.2.4. Long Pulse Diodes

The external circuit should supply a pulse with a high dE/dt. If the diode is designed for a low current density (and thus a low electric field), then the pulse should consist of a sharp, high voltage spike to aid in turn-on, followed by the lower voltage main pulse. The shape of the main pulse will affect the plasma motion, and the optimum shape depends on whether the goal is constant voltage, constant current, or constant impedance. Plasma expansion tends to increase the current; a rising power pulse tends to reduce the rate of decrease of the impedance.

11.2.5. Inductively Driven Diodes

Inductive storage circuits tend to produce output power pulses that rise quickly, followed by a gradual fall. The falling power pulse will tend to increase the gap closure velocity and could be a concern, depending on the desired pulse length.

A leading candidate for the output (opening) switch of an inductive storage circuit is the plasma erosion switch.[24] This switch is characterized by a fast rise time (~5 ns); however, in order for switching to occur a low current must be

carried by the load for tens of ns.[248] This low current (and hence low voltage) 'foot' to the pulse could degrade the plasma formation uniformity. To remedy this, a high impedance diode with a low turn-on voltage (e.g., two sharp points) could be placed in parallel with the primary load. The turn-on voltage and impedance of the shunt diode would be adjusted so that during the low current 'foot', only the shunt diode turns on, with the primary diode turning on during the rapidly rising portion of the pulse. With a sufficiently large shunt impedance, very little of the total energy would be lost to the shunt diode. With such a scheme, a high degree of plasma uniformity would be expected due to the fast rise time of the switch.

11.2.6. Repetitively Pulsed Diodes

If a diode is pulsed with an interpulse spacing less than the monolayer formation time, then the electrode surfaces will eventually be clean, and, as stated above, this is not expected to significantly reduce the expansion velocity. Since surface impurities facilitate plasma-induced emission site formation and thus aid the process of filling in the plasma layer, diode performance is expected to improve when impurities are intentionally added to the cathode (e.g., oil impregnated brass), and, as mentioned in Ch. 2, this was indeed observed by Buttram.[104]

A potential limitation on pulse rate is the time required for the plasma to clear out of the gap. This time is seen to be lower in these experiments when the geometry allows for easy diffusion out of the gap volume. Since plasma densities on oil coated electrodes are slightly higher than on uncoated electrodes, it seems likely that by limiting the amount of surface impurities, the quantity of material in the gap will be reduced, so in light of the preceding paragraph, there is presumably some optimum amount of added impurities. Also, material supply can be reduced by limiting the pulse length and chopping the diode current at the end of the (useful portion of the) shot.

11.2.7. Magnetically Insulated Diodes and MITL's

MID's and in particular MITL's tend to have lower charge transfers per unit area than non-insulated planar diodes. On the other hand, electrons can return to the cathode with non-zero energies: a fraction of the electrical energy supplied

to the diode can be deposited on the cathode in this fashion.[249] Because of these differences, one would expect MID and especially MITL plasmas to be more affected by plasma-surface interactions and less affected by the cathode spots than uninsulated diode plasmas. MID plasmas were studied by Bekefi *et al.*,[176] and an investigation of MITL plasmas similar to the experiments described here is presently being carried out by Stinnett *et al.*[250] In both experiments the plasma densities are observed to be lower than in the present case, which may be explained in terms of the reduced charge transfer. Also, in both experiments (in contrast to this work), the strongest spectral line emission comes from hydrogen, and no doubly or triply ionized species are observed. This can be explained by the increase in plasma 'boiled off' by plasma-surface interactions (such as ESD) and a decrease in plasma supplied by the spots, since hydrogen is expected to dominate the 'boil off' plasma while spots are needed to produce higher ionization states.

Concerning expansion, it should be pointed out that in a MID or MITL, magnetic pressure effects can impede plasma expansion (since all or the plasma area is exposed to the field), and they can play the same role that electric pressure does in uninsulated diodes. In fact, this has been observed in both experiments and numerical studies involving MID's,[176] and in numerical studies of an MITL.[251] Thus, the external circuit considerations are the same for MID's and MITL's as for non-insulated diodes. (Expansion of MID plasmas is also discussed in Refs. 252 and 253.)

11.3. Suggestions for Future Work

These experiments provide some information on the plasma thermal processes, but the temperature measurements are incomplete. Further work in this area would be beneficial, particularly measurements of the temperature at various distances from the cathode, and further measurements of the temperature dependence on current density.

The cathode plasma is composed in part of constituents of surface impurities, impurities are known to assist new spot formation under the plasma cloud, and they are linked to initial emission site formation. Further experiments to clarify the role of impurities would be useful. In particular, experiments with repetitively

pulsed diodes, where a clean surface can be obtained, are necessary. In these experiments, known types and quantities of impurities can be introduced and their effects determined.

Finally, further computational and theoretical modeling of the cathode plasma, including the microprocesses, will be useful. As mentioned in Ch. 2, at least one such effort is presently underway.[102]

References

1. S. E. Graybill and S. V. Nablo, *Appl. Phys. Lett.* 8, 18 (1966).
2. R. B. Miller, *Intense Charged Particle Beams* (Plenum, New York 1982).
3. R. Gillette, *Science* 188, 30 (1975).
4. J. A. Nation, *Appl. Phys. Lett.* 17, 491 (1970).
5. L. P. Bradley, *Inst. Phys. Conf. Series* 29, 58 (1976).
6. See, for example R. F. Fernsler, D. Conte, and I. M. Vitkovitsky, *IEEE Trans. Plasma Sci.* PS-18, 176 (1980).
7. R. B Oswald, Jr., F. B. McLean, D. R. Schallhorn, and L. D. Buxton, *J. Appl. Phys.* 42, 3463 (1971).
8. F. Winterberg, *Phys. Rev.* 174, 212 (1968).
9. M. V. Babykin, E. K. Zavoisky, A. A. Ivanov, L. I. Rudakov, *Proc. Conf. Plasma Phys. and Contr. Nuc. Fusion Res. (Madison, WI), Nuc. Fusion Suppl. 1972*, p. 75.
10. M. J. Clauser, *Phys. Rev. Lett.* 35, 848 (1975).
11. J. P. VanDevender, *Proc. Fifth Int. Conf. High-Power Part. Beams (San Fransisco, CA) 1983*, p. 17; G. Yonas, *Proc. Conf. Plasma Phys. and Cont. Nuc. Fusion Res. (Baltimore, MD) 1982, Nuc. Fusion. Suppl. 1983*, p. 353.
12. G. Cooperstein, S. J. Stephanakis, J. R. Boller, D. G. Colombant, S. A. Goldstein, D. D. Hinshelwood, R. A. Meger, J. M. Neri, W. F. Oliphant, P. F. Ottinger, T. J. Renk, B. V. Weber, and F. C. Young, *Proc. Fifth Int. Conf. High-Power Part. Beams (San Fransisco, CA) 1983 (abstracts)*, p. B3 ; G. Cooperstein, R. J. Barker, D. G. Colombant, A. Drobot, Shyke A. Goldstein, R. A. Meger, D. Mosher, P. F. Ottinger, F. L. Sandel, and F. C. Young, *Proc. Conf. Plasma Phys. and Cont. Nuc. Fusion Res. (Baltimore, MD) 1982, Nuc. Fusion. Suppl. 1983*, p. 361.
13. D. A. Hammer, B. R. Kusse, J. Maenchen, A. Manovsky, J. Neri, T. J. Renk, R. N. Sudan, *Proc. Fifth Int. Conf. High-Power Part. Beams (San Fransisco, CA) 1983*, p. 56 ; H. Bluhm, J. B. Greenly, D. A. Hammer, B. R. Kusse, J. Maenchen, A. Manovsky, J. Neri, R. Pal, T. J. Renk, G. N. Rondeau, and R. N. Sudan, *Proc. Conf. Plasma Phys. and Cont. Nuc. Fusion Res. (Baltimore, MD) 1982, Nuc. Fusion. Suppl. 1983*, p. 371.
14. J. C. Arnoud, R. Bailly-Salins, A. Bernard, C. Bourgeois, N. Camarcat, J. Chevallier, G. D'Agnostini, A. Devlin, E. Pasini, C. Patou, and C. Peugnet, *Proc. Fifth Int. Conf. High-Power Part. Beams (San Fransisco, CA) 1983 (abstracts)* , p. B5
15. S. Nakai, K. Imasaki, S. Miyamoto, S. Higaki, T. Ozaki, A. Yoshinouchi, T. Yabe, K. Nishihara, K. Mima, C. Yamanaka, *Proc. Fifth Int. Conf. High-Power Part. Beams (San Fransisco, CA) 1983*, p. 28; K. Imasaki, S. Miyamoto, S. Higaki, T. Ozaki, K. Nishihara, S. Ido, S. Nakai, C. Yamanaka, *Proc. Conf. Plasma Phys. and Cont. Nuc. Fusion Res. (Baltimore, MD) 1982, Nuc. Fusion. Suppl. 1983*, p. 383.

16. K. Yatsui, Y. Araki, K. Masugata, M. Ito, M. Matsui, *Proc. Fifth Int. Conf. High-Power Part. Beams (San Fransisco, CA) 1983*, p. 34.

17. W. Naiyan, Z. Niagong, W. Wenchang, Y. Dawei, W. Chunhou, D. Shigang, L. Tuming, G. Kung, W. Shumao, Z. Rongsheng, W. Bidan, L. Weiren, W. Ganchang, *Proc. Fifth Int. Conf. High-Power Part. Beams (San Fransisco, CA) 1983*, p. 63.

18. H. U. Karow, KFK, Fed. Rep. Germ., personal communication.

19. L. I. Rudakov, *Proc. Fifth Int. Conf. High-Power Part. Beams (San Fransisco, CA) 1983*, p. 23; L. E. Aranchuk, *et al.* (40 coauthors), *Proc. Conf. Plasma Phys. and Cont. Nuc. Fusion Res. (Baltimore, MD) 1982, Nuc. Fusion. Suppl. 1983*, p. 393.

20. S. Humphries, Jr., *Nuc. Fusion* 20, 1549 (1980).

21. E. Ott and R. N. Sudan, *Appl. Phys. Lett.* 29, 5 (1976).

22. J. M. Finn and R. N. Sudan, *Nuc. Fusion* 22, 1443 (1982).

23. W. M. Manheimer and N. K. Winsor, NRL Rep. 4213 (1980).

24. G. A. Mesyats, D. I. Proskurovsky, V. P. Rotshtein and N. I. Lebedeva, *Sov. Phys. Dokl.* 25, 650 (1980).

25. R. T. Hodgson, J. E. E. Baglin, R. Pal, J. Neri, and D. A. Hammer, *Appl. Phys. Lett.* 37, 187 (1980).

26. W. W. Destler and M. Reiser, IEEE Cat. 82CH1770-7, p. 28 (1982).

27. M. S. Di Capua, *IEEE Trans. Plasma Sci.* PS-11, 205 (1983).

28. See, for example C. W. Mendel, Jr., D. B. Seidel, and S. A. Slutz, *Phys. Fluids* 26, 3628 (1983); J. P. VanDevender, *J. Appl. Phys.*, 50, 3928 (1979).

29. R. W. Stinnett, SNL, personal communication.

30. W. D. Coolidge, *Am. Jour. Roentgenol. Rad. Ther.* 19, 313 (1928).

31. K. T. Compton, *Phys. Rev.* 32, 492 (1928).

32. G. A. Lyubimov and V. I. Rakhovskiĭ, *Sov. Phys. Usp.* 21, 693 (1978).

33. J. M. Lafferty, ed., *Vacuum Arcs, Theory and Application* (Wiley, New York 1980).

34. R. L Boxman, S. L. Goldsmith, I. Izraeli, and S. Shalev, *IEEE Trans. Plasma Sci.* 11, 138 (1983).

35. W. P. Dyke, J. K. Trolan, E. E. Martin, and J. P. Barbour, *Phys. Rev.* 91, 1043 (1953).

36. W. W. Dolan, W. P. Dyke, J. K. Trolan, *Phys. Rev.* 91, 1054 (1953).

37. J. P. Barbour, W. W. Dolan, J. K. Trolan, E. E. Martin, and W. P. Dyke, *Phys. Rev.* 92, 45 (1953).

38. D. Alpert, D. A. Lee, E. M. Lyman, and H. E. Tomaschke, *J. Vac. Sci. Tech.* 1, 35 (1964).

39. J. C. Martin, AWRE, SSWA/JCM/704/49, (1970). See also R. A. Fitch and V. T. S. Howell, Proc. IEE, 111, 849 (1964).

40. S. P. Bugaev, E. A. Litvinov, G. A. Mesyats, and D. I. Proskurovsky, *Sov. Phys. Usp.* 18, 51 (1975).

41. G. A. Mesyats, *J. Appl. Mech. Tech. Phys.* 5, 690 (1981).

42. E. A. Litvinov, G. A. Mesyats, and D. I. Proskurovsky, *Sov. Phys. Usp.* 26, 138 (1983).

43. R. K. Parker, R. E. Anderson, and C. V. Duncan, *J. Appl. Phys.* 45, 2463 (1974).

44. G. A. Mesyats, *Tenth Int'l. Conf. Phen. Ion. Gasses (Oxford, UK) 1971*, p. 333.

45. G. A. Farrall in Ref. 33.

46. R. J. Noer, *Appl. Phys. A* 28, 1 (1982).

47. W. Schottky, *Physik. Z.* 15, 872 (1914).

48. R. H. Fowler and L. Nordheim, *Proc. Roy. Soc* 119, 183 (1928).

49. E. L. Murphy and R. H. Good, Jr., *Phys. Rev.* 102, 1464 (1956).

50. F. M. Charbonier, R. W. Strayer, L. W. Swanson, and E. E. Martin, *Phys. Rev. Lett.* 13, 397 (1964).

51. L. W. Swanson, L. C. Crouser, and F. M. Charbonier, *Phys. Rev.* 151, 327 (1966).

52. W. B. Nottingham, *Phys. Rev.* 59, 906 (1941).

53. G. N. Fursei and P. N. Vorontsov-Vel'yaminov, *Sov. Phys. Tech. Phys.* 12, 1370 (1968).

54. G. N. Fursei and P. N. Vorontsov-Vel'yaminov, *Sov. Phys. Tech. Phys.* 12, 1377 (1968).

55. G. K. Kartsev, G. A. Mesyats, D. I. Proskurovsky, V. P. Rotshtein, and G. N. Fursei, *Sov. Phys. Dokl.* 15, 475 (1970).

56. E. A. Litvinov, G. A. Mesyats, and A. F. Shubin. *Sov. Phys. J.* 13, 537 (1970).

57. E. A. Litvinov, G. A. Mesyats. D. I. Proskurovsky, V. F. Puchkarev, and S. I. Shkuratov, *Sov. Phys. Dokl.* 27. 73 (1982).

58. V. M. Zhukov. G. N. Fursei. E. I. Giuargizou. I. D. Ventova. and N. V. Egarov. *Sov. Phys. Tech. Phys.* 21. 1110 (1976).

59. G. N. Fursei and V. M. Zhukov. *Sov. Phys. Tech. Phys.* 19. 804 (1974).

60. M. M. Martynyuk, *Sov. Phys. Tech. Phys.* 23. 877 (1978).

61. A. S. Dmitriev and O. A. Sinkevich. *Sov. Phys. Tech. Phys.* 27. 1015 (1982).

62. R. P. Little and W. T. Whitney. *J. Appl. Phys.* 34. 3142 (1963).

63. W. S. Boyle. P. Kisliuk. and L. H. Germer. *J. Appl. Phys.* 26. 720 (1955).

64. R. E. Hurley. *J. Phys. D* 13. 1121 (1980) and references therein.

65. R. V. Latham. *IEEE Trans. Elec. Insul.* EI-18. 194 (1983).

66. A. S. Pokrovskaya-Sobeleva, V. V. Kraft, T. S. Borisova. and L. K. Mazurova. *Proc. Fifth Intl. Symp. Disch. Elec. Insul. Vac. (Poznan, Poland) 1972*, p. 105.

67. G. A. Farrall, F. G. Hudda. and R. H. Johnston. *J. Appl. Phys.* 50. 3608 (1979).

68. J. Achtert, B. Altrichter, B. Jüttner, P. Pech, H. Pursch. H.-D. Reiner, W. Rohrbeck, P. Siemroth, and H. Wolff, *Beitr. Plasma Phys.* 17, 419 (1977).

69. G. A. Mesyats, *Proc. Sixth Intl. Symp. Disch. Elec. Insul. Vac. (Swansea, UK) 1974*, p. 21.

70. F. G. Zheleznikov, *Sov. Phys. Tech. Phys.* 23, 684 (1978).

71. L. V. Tarasova, *Sov. Phys. Dokl.* 167, 330 (1966).

72. L. P. Babich and M. D. Tarasov, *Rad. Phys. Quant. Elec.* 23, 914 (1980).

73. G. Dearnaley, A. M. Stoneham, and D. V. Morgan, *Rep. Prog. Phys.* 33, 1129 (1970).

74. D. Adler, H. K. Henisch, and N. Mott, *Rev. Mod. Phys.* 50, 209 (1978).

75. D. V. Morgan, *Elec. Lett.* 12, 454 (1976).

76. S. S. Mackeown, *Phys. Rev.* 34, 611 (1929).

77. C. Lejeune in *Applied Charged Particle Optics, C*, A. Septier, ed. (Academic, New York 1983).

78. G. P. Bazhenov, E. A. Litvinov, G. A. Mesyats, D. I. Proskurovsky, A. F. Shubin, and E. B. Yankelevich, *Sov. Phys. Tech. Phys.* 18, 795 (1973).

79. G. P. Bazhenov, E. A. Litvinov, G. A. Mesyats, D. I. Proskurovsky, A. F. Shubin, and E. B. Yankelevich, *Sov. Phys. Tech. Phys.* 18, 799 (1973).

80. E. A. Litvinov, G. A. Mesyats, D. I. Proskurovsky, and E. B. Yankelevich, *Sov. Phys. Tech. Phys.* 23, 319 (1978).

81. E. A. Litvinov, G. A. Mesyats, and A. G. Parfenov, *Sov. Phys. Dokl.* 28, 272 (1983).

82. G. N. Fursei and V. M. Zhukov, *Sov. Phys. Tech. Phys.* 21, 176 (1976).

83. V. M. Zhukov and G. N. Fursei, *Sov. Phys. Tech. Phys.* 21, 182 (1976).

84. V. M. Zhukov and G. N. Fursei, *Sov. Phys. Tech. Phys.* 21, 1112 (1976).

85. V. A. Koval', D. I. Proskurovsky, V. F. Tregubov, and E. B. Yankelevich. *Sov. Tech. Phys. Lett.* 5, 246 (1979).

86. G. A. Mesyats, D. I. Proskurovsky, E. B. Yankelevich, and V. F. Tregubov, *Sov. Phys. Tech. Phys.* 21, 228 (1979).

87. B. Jüttner. *Beitr. Plasma Phys.* 19, 259 (1979).

88. G. A. Mesyats. *Sov. Tech. Phys. Lett.* 9, 384 (1983).

89. B. Jüttner. *Beitr. Plasma Phys.* 21, 217 (1981), and references therein.

90. E. Hantzsche, *Beitr. Plasma Phys.* 23, 77 (1981), and references therein.

91. G. P. Bazhenov and S. M. Chesnokov. *Sov. Phys. J.* 19, 1500 (1976).

92. D. I. Proskurovsky and V. F. Puchkarev. *Sov. Phys. J.* 18, 1687 (1975).

93. G. P. Bazhenov, O. B. Ladyzhenskii, S. M. Chesnokov, and V. G. Shpak. *Sov. Phys. Tech. Phys.* 24, 67 (1979).

94. M. A. Lutz. *IEEE Trans. Plasma Sci.* PS-2, 1 (1974).

95. G. P. Bazhenov, R. B. Baksht, G. A. Mesyats, D. I. Proskurovsky, and V. F. Puchkarev. *High Temp.* 13, 160 (1975).

96. D. I. Proskurovsky and V. F. Puchkarev, *Sov. Phys. Tech. Phys.* 24, 1474 (1979).

97. D. I. Proskurovsky and V. F. Puchkarev, *Sov. Phys. Tech. Phys.* 24, 1479 (1979).

98. B. Jüttner, *Beitr. Plasma Phys.* 19, 266 (1978).

99. I. I. Beilis, *Sov. Phys. Tech. Phys.* 19, 251 (1974).

100. V. A. Nemchinskii, *Sov. Phys. Tech. Phys.* 24, 764 (1979).

101. G. Ecker in Ref. 33.

102. D. P. Bacon. E. L. Kane, and A. T. Drobot, IEEE Cat. 84CH1958-8, p. 110 (1984).

103. G. B. Frazier, *Proc. Second IEEE Int'l. Pulsed Power Conf. (Lubbock, TX) 1979*, p. 127.

104. M. Buttram, SNL, personal communication.

105. K. R. Prestwich, *IEEE Trans. Nuc. Sci.* NS-17, 278 (1970).

106. R. S. Clark, Sandia Dev. Rep. SC-DR-710216 (1971).

107. Physics International, San Leandro, CA.

108. Poco Graphite, Decatur, TX.

109. Acheson Colloids, Port Huron, MI.

110. ARI Industries, Franklin Park, IL.

111. W. B. Herrmannsfeldt, SLAC Rep. 226, (1979).

112. Pulsar Associates, San Diego, CA.

113. Pearson Electronics, Palo Alto. CA.

114. Cablewave Systems, North Haven. CT.

115. Varo. Inc.. Garland. TX.

116. S. P. Bugaev. A. M. Iskol'dskii. G. A. Mesyats. and D. I. Proskurovsky, *Sov. Phys. Tech. Phys.* 12. 1625 (1968).

117. G. A. Mesyats and D. I. Proskurovsky, *JETP Lett.* 13, 4 (1971).

118. R. B. Baksht. S. P. Bugaev, V. I. Koshelev, G. A. Mesyats. V. P. Stas'ev, K. N. Sukhushin. and M. N. Timofeev, *Sov. Tech. Phys. Lett.* 3, 243 (1977).

119. S. Ya Belomyttsev. S. D. Korovin. and G. A. Mesyats. *Sov. Tech. Phys. Lett.* 6. 466 (1980).

120. D. I. Proskurovsky and V. F. Puchkarev. *Sov. Phys. Tech. Phys.* 25, 1235 (1980).

121. L. P. Bradley. *Rev. Sci. Inst.* 46. 673 (1975).

122. Kent Humphries. Far West Technologies. Goleta. CA.

123. G. P. Bazhenov. G. A. Mesyats. and D. I. Proskurovsky, *Sov. Phys. J.* 13. 1054 (1970).

124. A. J. Toepfer and L. P. Bradley. *J. Appl. Phys.* 43. 3033 (1972).

125. G. S. Murty. *Ark. Fysik.* 19. 499 (1961).

126. A. P. G. Kutty, *J. Appl. Phys.* 50, 6139 (1979).

127. V. K. Tripathi, P. F. Ottinger, and J. Guillory, *J. Appl. Phys.* 54, 3043 (1983).

128. O. Milton, *IEEE Trans. Elec. Insul.* EI-9, 68 (1974).

129. W. Bostick, Stevens Inst. Tech., personal communication.

130. H. Bischel in *Am. Inst. Phys. Handbook*, D. E. Gray, ed. (McGraw-Hill, New York 1982) pp. 8-179ff.

131. H. Helava, PI, personal communication.

132. Yu. A. Vasilivskaya, M. A. Vasilevskii, I. M. Roife, V. I. Engelko, S. P. Yakolev, and E. G. Yankin, *Sov. Phys. Tech. Phys.* 28, 429 (1983).

133. H. H. Anderson and J. F. Ziegler, *Stopping Powers and Ranges in All Elements, Vol. 3* (Pergammon, New York 1977).

134. L. Dehghanmanesh, NRL 1968 (unpublished).

135. J. W. Poukey, *Appl. Phys. Lett.* 26, 145 (1975).

136. D. W. Swain, S. A. Goldstein, L. P. Mix, J. G. Kelly, and G. R. Hadley, *J. Appl. Phys.* 48, 1085 (1977).

137. J. R. Boller, NRL, personal communication.

138. D. D. Hinshelwood, NRL Rep. 5185 (1983).

139. H. F. Ivey, *J. Appl. Phys.* 24, 1466 (1953).

140. G. A. Mesyats, V. P. Rotshtein, G. N. Fursei, and G. K. Kartsev, *Sov. Phys. Tech. Phys.* 15, 1202 (1971).

141. S. P. Vavilov, *Sov. Phys. J.* 15, 1360 (1972).

142. S. P. Bugaev, G. A. Mesyats, and D. I. Proskurovsky, *Sov. Phys. Dokl.* 14, 605 (1969).

143. D. A. Phelps, D. Markins, V. Fargo, and A. C. Kolb, *IEEE Trans. Plasma Sci.* PS-4, 190 (1976).

144. J. J. Ramirez and D. L. Cook, *J. Appl. Phys.* 51, 4602 (1980).

145. S. V. Lebedev, V. V. Chikonov, and M. A. Shcheglov, *Sov. Tech. Phys. Lett.* 8, 302 (1982).

146. R. B. Baksht, S. P. Vavilov, and A. P. Kudinov, *Sov. Phys. J.* 17, 5 (1974).

147. C. D. Child, *Phys. Rev.* 32, 492 (1911).

148. I. Langmuir, *Phys. Rev.* 2, 450 (1913).

149. I. Langmuir and K. T. Compton, *Rev. Mod. Phys.* 3, 191 (1931).

150. S. A. Goldstein, R. C. Davidson, J. G. Siambis, and R. Lee, *Phys. Rev. Lett.* 33, 1471 (1974).

151. S. A. Goldstein and R. Lee, *Phys. Rev. Lett.* 35, 1079 (1975).

152. A. E. Blaugrund, G. Cooperstein, and S. A. Goldstein, *Phys. Fluids* 20, 1185 (1977).

153. G. A. Mesyats and E. A. Litvinov, *Sov. Phys. J.* 17, 1235 (1972).

154. G. P. Bazhenov, G. A. Mesyats, and S. M. Chesnokov, *Radio Eng. Elec. Phys.* 20, 150 (1975).

155. D. I. Proskurovsky, V. P. Rotshtein, A. F. Shubin, and E. B. Yankelevich, *Sov. Phys. Tech. Phys.* 20, 1342 (1976).

156. G. P. Bazhenov, O. B. Ladyzhenskii, E. A. Litvinov, and S. M. Chesnokov, *Sov. Phys. Tech. Phys.* 22, 1212 (1977).

157. A. V. Gurevich, L. V. Parĭlskaya, and L. P. Pitaevskiĭ, *Sov. Phys. JETP* 22, 449 (1966).

158. P. Mora and R. Pellat, *Phys. Fluids* 22, 2300 (1979), and references therein.

159. M. Born and E. Wolf, *Principles of Optics* (Pergammon, Oxford 1970).

160. J. D. Jackson, *Classical Electrodynamics* (Wiley, New York 1975).

161. A. R. Striganov and S. V. Sventitiski, *Tables of Spectral Lines of Neutral and Ionized Atoms* (IFI/Plenum, New York 1968).

162. R. A. Alpher and D. R. White in *Plasma Diagnostic Techniques*, Huddlestone and Leonard, ed. (Academic, New York 1965).

163. E. E. Bergmann, *Rev. Sci. Inst.* 48, 545 (1977).

164. E. E. Bergmann, *Appl. Phys. Lett.* 31, 661 (1977).

165. R. A. Fitch and V. T. S. Howell, *Proc. IEE* 111, 849 (1964).

166. Microcoatings, Inc., Burlington, MA.

167. Heraeus-Amarsil, Sayreville, NJ.

168. C. W. Kimblin, *J. Appl. Phys.* 44, 3074 (1973).

169. J. E. Daalder, *Jour. Phys. D* 9, 2379 (1976).

170. S. Shalev, S. Goldsmith, and R. L. Boxman, *IEEE Trans. Plasma Sci.* PS-11, 146 (1983).

171. D. I. Proskurovsky and E. B. Yankelevich. *Rad. Eng. Elec. Phys.* 24, 99 (1979).

172. B. E. Djakov, G. A. Lyubimov, and V. I. Rakhovskiĭ. *IEEE Trans. Plasma Sci.* PS-12, 150 (1984).

173. S. P. Bugaev, R. B. Baksht, E. A. Litvinov, and V. P. Stas'ev. *High Temp.* 14, 1027 (1976).

174. L. P. Mix, J. G. Kelly, G. W. Kuswa, D. W. Swain, and J. N. Olsen, *J. Vac. Sci. Tech.* 10, 951 (1973).

175. J. G. Kelly and L. P. Mix, *J. Appl. Phys.* 46, 1084 (1975).

176. G. Bekefi, T. J. Orzechowski, and K. D. Bergeron. *Intl. Top. Conf. Elec. Beam Res. Tech. (Albuq., NM) 1975*, p. 303.

177. R. Pal, D. A. Hammer, and R. N. Sudan. IEEE Cat. 81CH1640-2, p. 81 (1981).

178. J. W. Maenchen, F. C. Young, R. Stringfield, S. J. Stephanakis, D. Mosher, S. A. Goldstein, R. D. Genaurio, and G. Cooperstein. *J. Appl. Phys.* 54, 89 (1983)

179. J. D. Craggs and H. S. W. Massey in *Encyclopedia of Physics, Vol. 37/1*, S. Flugge, ed. (Springer-Verlag, Berlin 1959).

180. R. C. Weast, ed., *Handbook of Chemistry and Physics* (CRC, Cleveland 1979) p. E356

181. B. Fell, R. J. Commisso, V. E. Scherrer, and I. M. Vitkovitsky, NRL Rep. 4714 (1982).

182. R. B. Baksht, A. P. Kudinov, and E. A. Litvinov, *Sov. Phys. Tech. Phys.* 18, 94 (1973).

183. R. B. Baksht, N. A. Ratakhin, and A. P. Kablambaev, *Sov. Phys. Tech. Phys.* 25, 294 (1980).

184. R. Tanberg, *Phys. Rev.* 35, 1080 (1930).

185. A. A. Plyutto, V. N. Ryshkov, and A. T. Kapin, *Sov. Phys. JETP* 20, 328 (1965).

186. W. D. Davis and H. C. Miller, *J. Appl. Phys.* 40, 2212 (1969).

187. H. C. Miller, *J. Appl. Phys.* 52, 4523 (1981).

188. Ya. B. Zel'dovich and Yu. P. Raĭzer, *Physics of Shock Waves and High Temperature Hydrodynamic Phenomena* (Academic, New York 1967) p. 103.

189. G. A. Mesyats, E. A. Litvinov, and D. I. Proskurovsky, *Fourth Intl. Symp. Disch. Elec. Insul. Vac. (Waterloo, Ont.) 1970*, p. 82, also, Refs. 40–42.

190. B. Ya. Moizhes and V. A. Nemchinskii, *Sov. Phys. Tech. Phys.* 25, 43 (1980).

191. G. A. Lyubimov, *Sov. Phys. Tech. Phys.* 22, 173 (1977); G. A. Lyubimov, *Sov. Phys. Dokl.*, 20, 830 (1975); M. P. Zekster and G. A. Lyubimov, *Sov. Phys. Tech. Phys.*, 24, 1 (1979).

192. S. I. Anisimov, M. F. Ivanov, Yu. V. Medvedev, and V. F. Shvets, *Sov. J. Plasma Phys.* 8, 591 (1982).

193. I. I. Aksenov, V. G. Bren', V. G. Padalka, and V. M. Khoroshikh. *Sov. Tech. Phys. Lett.* 7, 497 (1981).

194. G. Cooperstein, NRL, personal communication.

195. S. I. Braginskii in *Reviews of Plasma Physics Vol. 1.* M. A. Leontovich, ed. (Consultants Bureau, New York 1965).

196. R. W. Nicholls and A. L. Stewart in *Atomic and Molecular Processes*. D. R. Bates, ed. (Academic, New York 1962).

197. R. W. P. McWhirter in Ref. 162.

198. R. C. Elton in *Methods of Experimental Physics. Vol. 9.* Griem and Lovberg, ed. (Academic Press, New York, 1970).

199. H. W. Drawin in *Plasma Diagnostics*, Lochte-Holtegreven, ed. (North Holland, Amsterdam, 1968).

200. D. Duston and J. Davis, *Phys. Rev. A* 23, 2602 (1981).

201. V. L. Jacobs and J. Davis, *Phys. Rev. A* 18, 697 (1978).

202. D. R. Bates, A. E. Kingston, and R. W. P. McWhirter, *Proc. Roy. Soc. A* 257, 297 (1962).

203. D. Duston, NRL, personal communication.

204. W. Engelhardt, *Phys. Fluids* 16, 217 (1973).

205. M. L. Weise in Ref. 162.

206. H. R. Griem, *Plasma Spectroscopy* (McGraw-Hill, New York 1964).

207. H. R. Griem, *Spectral Line Broadening in Plasmas* (Academic, New York 1974).

208. G. S. Romanov, K. I. Stepanov, and M. T. Syrkin, *Opt. Spectr.* 47, 476 (1979).

209. M. A. El-Farra and T. P. Hughes,, *J. Quant. Spectr. Rad. Trans.* 30, 335 (1983).

210. M. A. Mazing and N. A. Vrublevskaya, *Opt. Spectr.* 16, 6 (1964).

211. W. Weise, M. Smith, and B. Miles, *Atomic Transition Probabilities* (US GPO, Washington 1969).

212. Optronics Labs, Orlando, FL.

213. Oriel Corp., Stratford, CT.

214. C. B. Childs, *Appl. Opt.* 1, 711 (1962).

215. R. B. Bashkin and Stoner, *Atomic Energy Levels and Grotrian Diagrams* (North Holland, Amsterdam 1975).

216. S. Goldsmith and R. L. Boxman, *J. Appl. Phys.* 51, 3649 (1980).

217. F. M. Bacon and H. A. Watts, *J. Appl. Phys.* 46, 4758 (1975).

218. R. L. Boxman and S. Goldsmith, *J. Appl. Phys.* 51, 3644 (1980).

219. H. Schellekens, *J. Appl. Phys.* 54, 144 (1983).

220. P. Vouros, J. I. Masters, and R. J. Starble, *Rev. Sci. Inst.* 39, 741 (1968).

221. G. M. McCracken, R. S. Barton, and W. Dillon, *Nuovo Cim. Suppl.* 5, 146 (1967).

222. M. H. Achard. R. Calder, and A. Mathewson, *Vacuum* 29, 53 (1979).

223. H. S. Carslaw and J. C. Jaeger, *Conduction of Heat in Solids* (Clarendon. Oxford 1959).

224. G. T. Furukawa. T. B. Douglas. and N. Pearlman in Ref. 130; R. L. Powell and G. E. Childs in Ref. 130.

225. Ref. 180. pp. D-64 and D-141ff.

226. G. M. McCracken and P. E. Stott, *Nucl. Fusion* 19, 889 (1979).

227. R. Pal and D. A. Hammer. Cornell Rep. LPS-302 (1983).

228. P. A. Redhead. J. P. Hobson, and E. V. Kornelsen. *The Physical Basis of Ultra-High Vacuum* (Chapman & Hall. London 1968).

229. P. J. Feibelman and M. L. Knotek. *Phys. Rev. B* 18. 6531 (1978).

230. J. Halbritter. *IEEE Trans. Elec. Ins.* EI-18. 253 (1983).

231. J. Halbritter. *Scanning Electron Microscopy* II. 511 (1983).

232. J. Halbritter. *J. Appl. Phys.* 53. 6475 (1982).

233. G. M. McCracken. *Vacuum* 24. 463 (1974).

234. A. Sagara and K. Kamada. *Jour. Nuc. Mat.* 111-112. 812 (1982).

235. E. Taglaur and G. Heiland. *Jour. Nuc. Mat.* 93-94. 823 (1980).

236. J. Lindhard and M. Scharff. *Phys. Rev.* 124. 128 (1961).

237. R. A. Anderson and H. L. Bay in *Sputtering by Particle Bombardment*, R. Behrisch, ed. (Springer-Verlag, Berlin 1981).

238. R. Kelly and N. Q. Lam, *Rad. Effects* 19, 39 (1973).

239. C. Enloe, R. Blaher, M. Coffing, and R. Reinovsky, *Tenth Intl. Symp. Disch. Elec. Insul. in Vac. (Columbia, S. C.) 1982*, p. 308.

240. J. G. Kelly, S. A. Goldstein, and D. W. Swain, *J. Appl. Phys.* 46, 4726 (1975).

241. M. Knotek, V. O. Jones, and V. Rehn, *Phys. Rev. Lett.* 43, 300 (1979).

242. B. D. Fried and R. W. Gould, *Phys. Fluids* 4, 139 (1961).

243. G. Bekefi, *Radiation Processes in Plasmas* (Wiley, New York 1966).

244. É. N. Abdullin, G. P. Bazhenov, S. P. Bugaev, and O. B. Ladyzhenskii, *Sov. Tech. Phys. Lett.* 7, 148 (1981).

245. M. A. Vasilevskii, I. M. Roife, and V. I. Éngel'ko, *Sov. Phys. Tech. Phys.* 26, 671 (1981).

246. D. P. Bacon, SAI, personnal communication.

247. C. W. Mendel and S. A. Goldstein, *J. Appl. Phys.* 48, 1004 (1977).

248. R. A. Meger, R. J. Commisso, G. Cooperstein, and S. A. Goldstein, *Appl. Phys. Lett.* 42, 943 (1983).

249. A. Palevsky, G. Bekefi, and A. T. Drobot, *J. Appl. Phys.* 52, 4938 (1981).

250. R. W. Stinnett, M. A. Palmer, R. B. Spielman, and R. Bengtson, *IEEE Trans. Plasma Sci.* PS-11, 216 (1983).

251. T. W. Hussey, SNL, personnal communication.

252. S. P. Bugaev, A. A. Kim, A. I. Klimov, and V. I. Koshelev, *Sov. J. Plasma Phys.* 7, 286 (1981).

253. S. P. Bugaev, A. A. Kim, V. I. Koshelev, and P. A. Khryapov, *Sov. J. Plasma Phys.* 9, 743 (1983).

DISTRIBUTION LIST

	DODAAD Code	
Dr. Gerald Cooperstein Attn: Code 4770 Naval Research Laboratory 4555 Overlook Avenue, S.W. Washington, D.C. 20375	N00173	(1)
Administrative Contracting Officer ONRRR - E19-628 Massachusetts Institute of Technology Cambridge, Massachusetts 02139	N6617	(1)
Director Naval Research Laboratory Attn: Code 2627 Washington, D.C. 20375	N00173	(6)
Defense Technical Information Center Bldg. 5, Cameron Station Alexandria, Virginia 22314	S47031	(12)

END

FILMED

12-84

DTIC